N° d'ordre NNT : 2019LYSEI093

THESE de DOCTORAT DE L'UNIVERSITE DE LYON
opérée au sein de
INSA Lyon

Ecole Doctorale 512
Infomaths

Spécialité/ discipline de doctorat : Informatique

Soutenue publiquement le 08/11/2019, par :
Audrey Denizot

Simulation de la signalisation calcique dans les prolongements fins astrocytaires

Devant le jury composé de :

Dupont, Geneviève	Directeur de recherche	ULB	Rapporteure
Savtchenko, Leonid	Senior research scientist	UCL	Rapporteur
Henneberger, Christian	Assistant Professor	Uni. Bonn	Examinateur
Venance, Laurent	Directeur de recherche	CNRS	Examinateur
Beslon, Guillaume	Professeur	INSA Lyon	Examinateur
Panatier, Aude	Chargée de recherche	INSERM	Examinatrice
Berry, Hugues	Directeur de recherche	INRIA	Directeur de thèse
Soula, Hédi	Professeur	UPMC	Co-directeur de thèse, invité

Département FEDORA – INSA Lyon - Ecoles Doctorales – Quinquennal 2016-2020

SIGLE	ECOLE DOCTORALE	NOM ET COORDONNEES DU RESPONSABLE
CHIMIE	**CHIMIE DE LYON** http://www.edchimie-lyon.fr Sec. : Renée EL MELHEM Bât. Blaise PASCAL, 3e étage secretariat@edchimie-lyon.fr INSA : R. GOURDON	M. Stéphane DANIELE Institut de recherches sur la catalyse et l'environnement de Lyon IRCELYON-UMR 5256 Équipe CDFA 2 Avenue Albert EINSTEIN 69 626 Villeurbanne CEDEX directeur@edchimie-lyon.fr
E.E.A.	**ÉLECTRONIQUE, ÉLECTROTECHNIQUE, AUTOMATIQUE** http://edeea.ec-lyon.fr Sec. : M.C. HAVGOUDOUKIAN ecole-doctorale.eea@ec-lyon.fr	M. Gérard SCORLETTI École Centrale de Lyon 36 Avenue Guy DE COLLONGUE 69 134 Écully Tél : 04.72.18.60.97 Fax 04.78.43.37.17 gerard.scorletti@ec-lyon.fr
E2M2	**ÉVOLUTION, ÉCOSYSTÈME, MICROBIOLOGIE, MODÉLISATION** http://e2m2.universite-lyon.fr Sec. : Sylvie ROBERJOT Bât. Atrium, UCB Lyon 1 Tél : 04.72.44.83.62 INSA : H. CHARLES secretariat.e2m2@univ-lyon1.fr	M. Philippe NORMAND UMR 5557 Lab. d'Ecologie Microbienne Université Claude Bernard Lyon 1 Bâtiment Mendel 43, boulevard du 11 Novembre 1918 69 622 Villeurbanne CEDEX philippe.normand@univ-lyon1.fr
EDISS	**INTERDISCIPLINAIRE SCIENCES-SANTÉ** http://www.ediss-lyon.fr Sec. : Sylvie ROBERJOT Bât. Atrium, UCB Lyon 1 Tél : 04.72.44.83.62 INSA : M. LAGARDE secretariat.ediss@univ-lyon1.fr	Mme Emmanuelle CANET-SOULAS INSERM U1060, CarMeN lab, Univ. Lyon 1 Bâtiment IMBL 11 Avenue Jean CAPELLE INSA de Lyon 69 621 Villeurbanne Tél : 04.72.68.49.09 Fax : 04.72.68.49.16 emmanuelle.canet@univ-lyon1.fr
INFOMATHS	**INFORMATIQUE ET MATHÉMATIQUES** http://edinfomaths.universite-lyon.fr Sec. : Renée EL MELHEM Bât. Blaise PASCAL, 3e étage Tél : 04.72.43.80.46 infomaths@univ-lyon1.fr	M. Luca ZAMBONI Bât. Braconnier 43 Boulevard du 11 novembre 1918 69 622 Villeurbanne CEDEX Tél : 04.26.23.45.52 zamboni@maths.univ-lyon1.fr
Matériaux	**MATÉRIAUX DE LYON** http://ed34.universite-lyon.fr Sec. : Stéphanie CAUVIN Tél : 04.72.43.71.70 Bât. Direction ed.materiaux@insa-lyon.fr	M. Jean-Yves BUFFIÈRE INSA de Lyon MATEIS - Bât. Saint-Exupéry 7 Avenue Jean CAPELLE 69 621 Villeurbanne CEDEX Tél : 04.72.43.71.70 Fax : 04.72.43.85.28 jean-yves.buffiere@insa-lyon.fr
MEGA	**MÉCANIQUE, ÉNERGÉTIQUE, GÉNIE CIVIL, ACOUSTIQUE** http://edmega.universite-lyon.fr Sec. : Stéphanie CAUVIN Tél : 04.72.43.71.70 Bât. Direction mega@insa-lyon.fr	M. Jocelyn BONJOUR INSA de Lyon Laboratoire CETHIL Bâtiment Sadi-Carnot 9, rue de la Physique 69 621 Villeurbanne CEDEX jocelyn.bonjour@insa-lyon.fr
ScSo	**ScSo*** http://ed483.univ-lyon2.fr Sec. : Véronique GUICHARD INSA : J.Y. TOUSSAINT Tél : 04.78.69.72.76 veronique.cervantes@univ-lyon2.fr	M. Christian MONTES Université Lyon 2 86 Rue Pasteur 69 365 Lyon CEDEX 07 christian.montes@univ-lyon2.fr

Remerciements

Je tiens tout d'abord à remercier celui qui, par son ouverture d'esprit, m'a ouvert les portes de la modélisation, à moi, expérimentaliste de formation. Hugues, merci pour ta confiance, ton soutien et ta patience. Merci aussi à toi Hédi pour avoir su trouver les mots justes quand tout n'était pas au beau fixe dans mon parcours. I would also like to thank all of the other members of my PhD committee for accepting to examine my thesis: Dr Geneviève Dupont, Dr Leonid Savtchenko, Pr Christian Henneberger, Dr Laurent Venance, Pr Guillaume Beslon and Dr Aude Panatier. Merci à Aude et Geneviève, membres de mon comité de suivi de thèse. Elles ont su me conseiller avec bienveillance et rigueur et ont contribué à l'amélioration du travail présenté dans cette thèse.

Merci à l'ENS Lyon pour le financement de cette thèse. Merci à mon laboratoire, le LIRIS pour le financement de mon voyage au Japon afin de collaborer avec l'équipe d'Erik de Schutter ainsi que des mois de travail qui séparaient la fin de mon contrat de thèse de la date de ma soutenance. Merci enfin à INRIA, qui a financé mes déplacements, sans lesquels ma thèse aurait très certainement perdu en couleurs.

I am highly grateful to my collaborators. I would like to thank OIST university and more particularly Erik De Schutter and his team for their welcoming during my 4 months-long stay in their lab. Special thanks to Weiliang and Iain, for their patience to teach me STEPS, their help to debug and improve my code as well as collaborative work for designing new simulations. I thank Corrado Calì for his availability for visioconferences and for the exciting collaborative work started together. Thank you Misa and Valentin for our joint fruitful work. Hopefully the first of a long series. Special thanks to you Misa, for your rigorous work, patience, positiveness and support.

Merci également à toute l'équipe pédagogique Biosciences de l'INSA pour leur aide. Je tiens à remercier tout particulièrement Charlotte, Marion et Céline pour leurs précieux conseils. Merci mille fois Baptiste pour ta disponibilité, ton aide et pour tes réparations multiples au cours des TPs ! Merci également à l'équipe pédagogique de la préparation à l'agrégation de l'ENS de Lyon et plus particulièrement à Déborah, pour la confiance et la liberté qui m'ont été accordées pour l'élaboration

de mes corrections de leçons et cours.

Merci à l'antenne INRIA de la Doua pour les sourires et blagues (plus ou moins grasses de bon matin), la bienveillance, les déjeuners, le café, les sorties montagne et musique, les discussions politiques, existentielles, les bonnes recettes partagées. Nico et tes jeux de mots, Victor et nos discussions qui m'ont fait grandir (même si ça ne se voit pas trop en grimpe !), Aurel et nos cafés existentiels, Simon, Lois et Charles et nos débats animés, Kiki et tes sourires, Alex et ta bienveillance, Alvaro et ta générosité sans bornes, et tous les autres, merci pour votre gentillesse. Gracias Carlos pour ton enthousiasme for astrocytes and constant emulation.

Un grand merci aux Bordelais, qui ont su m'accueillir chaleureusement lors de mon stage de Master 2. Merci Aude pour tout ce que tu m'as appris, tant scientifiquement qu'humainement. Merci à Dylan, Mark, Silvia et Valentin pour les bons moments passés en paillasse et au bureau. Merci à mes amis de toujours m'y accueillir les bras ouverts: Silvia, Scarlett, Nadia, Gio, Nico, Lisa et tous les autres ! Merci, thank you, grazie Nadia et Gio de m'avoir permis de découvrir votre belle Sicile et Palermo, un voyage riche en couleurs et en saveurs. Thank you Orsi for your kind supportive messages and for all those sportive moments shared together, you have made Bordeaux feel like home for me too.

To my friends met in Okinawa: I think there are no words to thank you enough for all that you have done for me. Thank you for welcoming me, helping me and showing me around. Thank you my climbing, diving, workout, yoga, cooking, photography buddies. Neil, my stay would have been so different without you around, thank you for your kindness, I feel very lucky to be your friend. Thank you Leonidas for the scientific discussions and emulation on astrocytes. Thank you Anna, Natasha, Ales, Georgiy, Will, Nico, Xavi and Jo for broadening my horizons. I am very happy to have met you. I miss you and will hopefully see you all very soon! Thanks also to those crazy people met in OCNC: Vasha, Dorian, Aurelio and Caleb. I hope we'll meet again!

Merci à tous mes amis pour leur soutien inconditionnel. Merci à Tristan et Fantine pour votre présence quand tout va bien comme dans les moments difficiles, pour nos expéditions et aventures en tous genres, pour vos bons petits plats et votre gentillesse ! Merci aux autres copains grimpeurs pour toutes nos aventures et en attendant les suivantes : Yuri, Math, Alban, Ben. Thomas, Ralbol, Guillaume, Jean Loup, Théo : quelle coloc ! Merci pour ces moments de partage truffés d'étourderies et de blagues plus ou moins réussies (on sait à qui je fais référence ;)). Léa et nos discussions pour refaire le monde (et nos vies). Thomas et ton sarcasme acéré. Pacôme, merci d'être toujours présent. Que d'aventures partagées, qui ont largement contribué à mon épanouissement ! Albane et nos discussions décousues et chaotiques (un peu comme ces remerciements), rythmées au fil des voyages. Pierre et nos échanges écolos bobos gauchiasses et nos beaux voyages. Merci Ziyad de m'avoir ouvert tes

portes à la Réunion, merci pour ces moments d'échanges et de découvertes. Grégoire et nos discussions montagnardes, musicales et politiques. Merci de m'avoir permis de découvrir la Chine et ton quotidien là-bas. Aurélie et tes anecdotes croustillantes. Juliette et nos discussions toujours enrichissantes. Thib et Judith, votre gentillesse et votre bonne humeur. Merci aux zicos pour avoir rythmé mes années à Lyon: Félix, Jason, Pacôme, Lucas, le club jazz et la fanfare de l'ENS et tous ceux que j'ai oubliés. Alice et ta détermination détonnante, tes tractions impressionnantes et autres Top Top. Mon Jéjé et notre amitié inconditionnelle et bienveillante, tu me manques beaucoup. Ma Pata, ta folie et ta curiosité sans limites. Anh Thy et nos moments de folies et de partage. Paug et nos échanges musico-existentiels. Rémi et nos discussions thésardes et autres aventures démesuriennes.

Qu'aurait été cette thèse sans une petite touche DéMesurée... J'ai failli louper le coche, heureusement, Jean Loup a eu l'oeil ! Que de moments d'échanges, de fous rires, de sourires, d'apprentissage et de remises en question. En espérant que l'aventure n'en soit qu'à ses balbutiements. Jean Loup, Anissa, Nico, Rémi, Anaïs, Nadège, Marylou, Lucile, Sonia, Camille et tous les autres: merci pour votre enthousiasme DéMesuré.

Une rencontre inopinée dans une salle d'escalade fort occupée. Alexis, je ne sais comment te remercier pour ta bienveillance, ta gentillesse et ton soutien intarissable. Que de beaux moments partagés et de projets (à) réalisés(er). Vivement la suite, qui sait où nos petites têtes pleines d'idées vont nous mener !

Last but not least, merci à ma famille, toujours présente et acceptant avec patience mes excentricités et autres lubies. Merci Quentin pour les blagues mais aussi pour ton soutien quand mes jambes refusaient d'avancer. Merci maman et papa pour votre accueil chaleureux et bienveillant et pour m'avoir toujours laissé la liberté de poursuivre mes rêves et mes passions. Un amour non sans appréhension mais sans bornes. J'ai de la chance de vous avoir. Merci, merci, merci.

Résumé

Les astrocytes sont les cellules gliales les plus abondantes du système nerveux central et sont essentiels à son fonctionnement, intervenant notamment dans la formation des synapses et de la barrière hémato-encéphalique, dans le maintien de l'homéostasie métabolique et ionique ainsi que dans la régulation des concentrations extracellulaires en neurotransmetteurs. Récemment, les astrocytes ont également été identifiés comme des partenaires essentiels des neurones dans le cadre du traitement de l'information dans le système nerveux central. Les astrocytes peuvent entrer en contact avec les neurones au niveau des synapses ($\approx$ 60-90% des synapses de l'hippocampe sont contactées par des astrocytes [1, 2]) et moduler la communication neuronale via la libération de gliotransmetteurs et l'absorption de neurotransmetteurs [3]. Les interactions au niveau de ces synapses dites tripartites sont nécessaires au développement et impliquées dans le fonctionnement normal du système nerveux central.

L'excitabilité des astrocytes résulte de fluctuations de la concentration cytosolique en calcium : les signaux calciques. Ces signaux sont altérés dans de nombreuses pathologies dont les maladies neuro-développementales, neurodégénératives et neuropsychiatriques. Le recours dans un nombre croissant d'études à la microscopie à super-résolution [4] et aux indicateurs calciques encodés génétiquement (GECI) [5] a permis de révéler une complexité jusqu'alors insoupçonnée des signaux calciques astrocytaires. Ces derniers présentent une grande diversité spatio-temporelle, avec notamment des différences majeures entre les signaux observés dans le corps cellulaire (le soma) et dans les prolongements fins périphériques [6]. Par rapport aux signaux somatiques, les signaux des prolongements sont caractérisés par une cinétique plus rapide, ont des amplitudes de pics d'un ordre de grandeur inférieur et sont fortement confinés spatialement. La majorité des signaux calciques mesurés *in vivo* et *in vitro* surviennent dans ces prolongements, qui représentent la majorité ($\approx$ 75%) du volume des astrocytes [7]
.

Historiquement, les signaux calciques ont été modélisés avec des modèles déter-

ministes parfaitement mélangés, qui supposent que le système comprend un grand
nombre de molécules qui sont uniformément distribuées. Ces méthodes ne prennent
pas en compte la stochasticité inhérente aux interactions moléculaires ainsi que les
effets de diffusion, qui sont prépondérants dans les petits volumes. De fait, ces
méthodes permettent d'étudier les signaux calciques à l'échelle de la cellule ou du
réseau de cellules mais sont peu adaptées à l'étude des signaux dans de petits vol-
umes comme ceux des prolongements fins astrocytaires. Les travaux présentés dans
cette thèse étudient l'effet des propriétés spatiales (comme la géométrie cellulaire,
les distributions spatiales des molécules et la diffusion) sur les signaux calciques dans
les prolongements fins astrocytaires, en collaboration avec des expérimentateurs.

Le Chapitre IV présente notre modèle de signaux calciques en 2 dimensions
spatiales. Comme les canaux calciques IP$_3$R sont supposés être responsables de
la majorité des signaux dans les astrocytes, nous proposons un modèle de signaux
calciques IP$_3$R-dépendants. Pour prendre en compte la stochasticité inhérente aux
petits volumes sub-cellulaires et au faible nombre de molécules supposé dans les
prolongements fins, le modèle est à la fois spatialement explicite et individu-centré.
La cinétique des canaux IP$_3$R est modélisée par une version simplifiée du modèle
de De Young et Keizer [8] (voir la section III.1 pour plus de détails). Cette implé-
mentation en 2D, bien que moins réaliste qu'un équivalent en 3D, est plus rapide
et mieux adaptée à une analyse extensive de la diversité de comportements que le
modèle peut exhiber. Les principales conclusions de cette étude sont les suivantes :

- Les signaux calciques spontanés du modèle émergent d'une interaction entre
  l'excitabilité et la stochasticité du système.

- Le modèle reproduit les principales formes de signaux calciques reportées dans
  la littérature.

- La fréquence des signaux calciques dépend de l'organisation spatiale des canaux
  calciques. Les simulations du modèle montrent notamment que deux prolonge-
  ments astrocytaires exprimant exactement les mêmes canaux calciques peuvent
  être caractérisés par différents types de signaux en fonction de l'organisation
  spatiale des canaux.

Comme le paramétrage en 2 dimensions spatiales ne permet pas d'établir une
relation exacte entre le nombre de molécules dans les simulations et les concentra-
tions mesurées expérimentalement, nous avons décidé de développer notre modèle
en 3 dimensions spatiales. Le modèle est stochastique, utilisant des méthodes dites
"voxel-based" (voir la section III.4 pour plus de détails). Ce travail a été effectué

en collaboration avec l'équipe d'Erik De Schutter, OIST (Japon), qui a développé le logiciel STEPS, avec lequel le modèle a été implémenté. Ce modèle permet de plus d'étudier l'impact de la localisation des canaux IP$_3$R, qui sont présents à la surface (2D) du reticulum endoplasmique (ER), sur les signaux calciques dans le volume cytosolique (en 3D). Dans ce modèle, les concentrations moléculaires et les volumes peuvent être ajustés avec précision pour décrire au mieux les données expérimentales. Les données expérimentales en question ont été obtenues par nos collaborateurs : l'équipe d'U. V. Nägerl de l'Institut interdisciplinaire des neurosciences de l'Université de Bordeaux (France) pour les mesures de signaux calciques en microscopie à super-résolution et en confocal et C. Cali, KAUST University (Arabie Saoudite) pour la reconstitution en 3D de la géométrie d'un astrocyte de l'hippocampe àpartir d'images de microscopie électronique. Les résultats de cette étude sont présentés dans le Chapitre V. Brièvement, les principales conclusions de cette étude sont que :

- Notre modèle en 3D, avec un volume et des concentrations calciques réalistes, reproduit les données expérimentales de signaux calciques spontanés, obtenues dans des microdomaines calciques dans les prolongements fins.

- Les simulations du modèle prédisent que des variations locales de la concentration et de la cinétique des indicateurs fluorescents, utilisés dans les expériences d'imagerie calcique, pourraient contribuer à la diversité des signaux observée au sein d'un même astrocyte.

- Des interactions entre l'organisation spatiale des canaux calciques et la géométrie cellulaire permettent de moduler la fréquence et l'amplitude des signaux spontanés.

Les résultats de nos collaborateurs [9] ainsi que de nombreuses études révèlent la présence de signaux induits par l'activité des neurones avoisinant l'astrocyte. Dans le but de mieux comprendre cette communication entre neurones et astrocytes, nous avons simulé l'induction de signaux calciques astrocytaires en réponse à une stimulation neuronale. Les simulations ainsi que les données expérimentales associées sont présentées dans le Chapitre VI et permettent de mieux comprendre les paramètres qui peuvent influencer le déclenchement ainsi que la propagation des signaux au sein des prolongements fins. Les principales conclusions de cette étude sont :

- La géométrie des prolongements astrocytaires, qui sont le site des interactions entre neurones et astrocytes, influence la probabilité ainsi que la vitesse de propagation des signaux. Notamment, les structures observées par nos collaborateurs, constituant une alternance de renflements cellulaires et de ramifications plus fines, semblent isoler les renflements de la diffusion de molécules

tout en favorisant la propagation des signaux calciques.

- La présence de ramifications se refermant en anneaux semble diminuer la prob-
abilité ainsi que la vitesse de propagation des signaux calciques, pouvant poten-
tiellement favoriser une communication locale entre l'astrocyte et les synapses
en contact avec ladite structure en anneaux.

- Des simulations de notre modèle révèlent que la distance entre une synapse
neuronale et le plus proche ER astrocytaire influe sur la variabilité en am-
plitude et en fréquence des signaux calciques, pour une intensité de stimulus
neuronal donnée.

En résumé, les simulations présentées dans cette thèse indiquent que (1) la diffu-
sion moléculaire, fortement modulée par la concentration et la cinétique des buffers
endogènes et exogènes, (2) l'organisation spatiale des molécules au sein de la cel-
lule, notamment la co-clusterisation des canaux calciques, (3) la géométrie de l'ER
et sa localisation dans la cellule et (4) la géométrie cellulaire influencent fortement
les signaux calciques et pourraient contribuer à la diversité des signaux calciques
astrocytaires.

Mots-clés: Système nerveux central, astrocytes, signalisation, calcium, neuro-
sciences computationnelles, modélisation stochastique, réaction-diffusion.

Abstract and keywords

Abstract

Astrocytes are predominant glial cells in the central nervous system, which are essential for the formation of synapses, participate to the blood-brain barrier and maintain the metabolic, ionic and neurotransmitter homeostasis. Recently, astrocytes have emerged as key elements of information processing in the central nervous system. Astrocytes can contact neurons at synapses and modulate neuronal communication via the release of gliotransmitters and the uptake of neurotransmitters. The use of super-resolution microscopy [4] and highly sensitive genetically encoded Ca^{2+} indicators (GECIs) [5] have revealed a striking spatiotemporal diversity of Ca^{2+} signals in astrocytes. Most astrocytic signals occur in processes, which are the sites of neuron-astrocyte communication, and strongly differ from somatic signals. Those processes are too fine to be resolved by conventional light microscopy so that super-resolution microscopy and computational modeling remain the only methodologies to study those compartments. The work presented in this thesis aims at investigating the effect of spatial properties (as e.g cellular geometry, molecular distributions and diffusion) on Ca^{2+} signals in those processes, which are deemed essential in such small volumes.

Historically, Ca^{2+} signals were modeled with deterministic well-mixed approaches, which enabled the study of Ca^{2+} signals in astrocytic networks or whole-cell events. Those methods however ignore the stochasticity inherent to molecular interactions as well as diffusion effects, which both play important roles in small volumes.

In this thesis, we present the spatially-extended stochastic model that we have developed in order to investigate Ca^{2+} signals in fine astrocytic processes. This work was performed in collaboration with experimentalists that performed electron (C. Cali, KAUST University, Saudi Arabia) as well as super-resolution microscopy (Nägerl team, Institut interdisciplinaire des neurosciences de l'Université de Bordeaux, France). The model was validated against experimental data. Simulations of

the model suggest that (1) molecular diffusion, strongly influenced by the concentration and kinetics of endogenous and exogenous buffers, (2) intracellular spatial organization of molecules, notably Ca^{2+} channels co-clustering, (3) ER geometry and localization within the cell, (4) cellular geometry strongly influence Ca^{2+} dynamics and can be responsible for the striking diversity of astrocytic Ca^{2+} signals. This work contributes to a better understanding of astrocyte Ca^{2+} signals, a prerequisite for understanding neuron-astrocyte communication and its influence on brain function.

Keywords : Central nervous system, astrocytes, signaling, calcium, computational neuroscience, stochastic modeling, reaction-diffusion.

List of scientific productions

Publications

K. Ceyzériat, L. Ben Haim, <u>A. Denizot</u>, D. Pommier, M. Matos, O. Guillemaud, M.-A. Palomares, L. Abjean, F. Petit, P. Gipchtein, M.-C. Gaillard, M. Guillermier, S. Bernier, M. Gaudin, G. Aurégan, C. Joséphine, N. Déchamps, J. Veran, V. Langlais, K. Cambon, A. P. Bemelmans, J. Baijer, G. Bonvento, M. Dhenain, J.-F. Deleuze, S. H. R. Oliet, E. Brouillet, P. Hantraye, M.-A. Carrillo-de Sauvage, R. Olaso, A. Panatier, and C. Escartin, "Modulation of astrocyte reactivity improves functional deficits in mouse models of Alzheimer's disease," Acta Neuropathologica Communications, vol. 6, p. 104, Oct. 2018.

<u>Denizot, A.</u>, Arizono, M., Nägerl, U.V., Soula, H., and Berry, H. (2019). Simulation of calcium signaling in fine astrocytic processes: Effect of spatial properties on spontaneous activity. PLOS Comput. Biol. 15, e1006795.

<u>Denizot, A.</u>, Berry, H., Venugopal, S. Computational Modeling of Intracellular Ca^{2+} Signals in Astrocytes. in Encyclopedia of Computational Neuroscience, 2019. **Submitted**.

<u>Denizot, A.</u>, Arizono, M., Chen, W., Hepburn, I., Soula, H., Nagerl, U. V., De Schutter, E., Berry, H. Investigating the effect of the nanoscale architecture of astrocytic processes on the propagation of calcium signals, accepted to the 28th Annual Computational Neuroscience Meeting, CNS 2019, Barcelona, Spain. **In Press**.

Communications

A. Denizot, M. Arizono, W. Chen, I. Hepburn, H. Soula, V. U. Nägerl, E. De Schutter, H. Berry. Investigating the effect of the nanoscale architecture of astrocytic processes on the propagation of calcium signals, *Annual Computational Neuroscience Meeting*, July 2019, Barcelona, Spain. (poster)

A. Denizot, H. Soula, and H. Berry, Simulation of calcium signaling in fine astrocytic processes, *OIST Computational Neuroscience Course*, Okinawa, Japan, July 2018. (poster)

A. Denizot, H. Soula, and H. Berry, Simulation of calcium signaling in fine astrocytic processes, *LyonSysBio*, Lyon, France, November 2017. (poster)

A. Denizot, H. Soula, and H. Berry, Simulation of calcium signaling in fine astrocytic processes : effect of spatial properties on spontaneous activity, *LyonSysBio*, Lyon, France, November 2017. (oral presentation)

A. Denizot, H. Soula, and H. Berry, Simulation of calcium signaling in fine astrocytic processes, *OIST Computational Neuroscience Course*, Okinawa, Japan, July 2017. (poster)

A. Denizot, Towards simulation of calcium signaling in fine astrocytic processes, *International Astrocyte School*, Bertinoro, Italy, March 2017. (oral presentation)

A. Denizot, H. Soula, and H. Berry, Simulation of calcium signaling in fine astrocytic processes, *CompSysbio*, Aussois, France, March 2017. (poster)

Contents

List of Figures

List of Tables

Abbreviations

AAV: Adeno-associated virus
AD: Alzheimer's disease
ANP: Atrial natriuretic peptide
ATP: Adenosine-triphosphate
BD: Brownian dynamics
BDNF: Brain-derived neurotrophic factor
cAMP: Cyclic adenosine monophosphate
CB_1: Cannabinoid receptor type 1
CICR: Calcium-induced calcium release
CME: Chemical master equation
CNS: Central nervous system
DREADD: Designer receptors exclusively activated by designer drugs
DYK: De Young-Keizer
EM: Electron microscopy
ER: Endoplasmic reticulum
FDF: Fire-diffuse-fire
FIB: Focused ion beam
FRET: Fluorescence resonance energy transfer
FWHM: Full width at half maximum
GABA: Gamma-Aminobutyric acid
GECI: Genetically encoded calcium indicator
GFAP: Glial fibrillary acidic protein
GPCR: G protein-coupled receptors
GFRD: Green's function reaction dynamics
IP_3R: Inositol 3-Phosphate receptor
LTP: Long term potentiation
mGluR: metabotropic glutamate receptor
NMDA: N-Methyl-D-aspartic acid
NCX: Na^+-Ca^{2+} exchanger
NPC: Neural precursor cell
ODE: Ordinary differential equation

OPC: Oligodendrocyte precursor cell
PALM: Photo-activated localization
PAP: Peripheral astrocytic process
PD: Parkinson's disease
PDE: Partial differential equation
PDF: Probability density function
PDMP: Piecewise deterministic markov processes
PIP_2: Phosphatidylinositol 4,5-bisphosphate
PKA: Protein kinase A
PLC: Phospholipase C
PM: Plasma membrane
RDME: Reaction-diffusion master equation
ROS: Reactive Oxygen Species
RyR: Ryanodine receptor
SEM: Scanning electron microscopy
SERCA: Smooth endoplasmic calcium ATPase
SMFM: Single-molecule fluorescence microscopy
SOCE: Store-operated Ca^{2+} entry
SSA: Stochastic Simulation Algorithm
STED: Stimulated emission depletion
STORM: Stochastic optical reconstruction
TIRF: Total internal reflection fluorescence
TRPV: Transient receptor potential cation channel subfamily V
TTX: Tetrodotoxin
WT: Wild type

"If our small minds, for some convenience, divide this glass of wine, this universe, into parts — physics, biology, geology, astronomy, psychology, and so on — remember that nature does not know it! So let us put it all back together, not forgetting ultimately what it is for."

Richard Feynman

Part A

Modeling astrocyte excitability and Ca^{2+} signaling

Chapter I

Astrocyte characteristics and functions within the CNS

I.1   What are astrocytes?

I.1.1   Historical considerations

Astrocytes are a type of glial cells of the central nervous system (CNS). The first report of glial cells was done by Virchow in 1846, describing a highly connected substance, cementing the brain, that he named "neuroglia" [10]. Camillo Golgi has first identified them as cells that differ from neurons [11, 12] and observed, using silver-chromate staining, a huge diversity of glial cells, which were organized in networks. He also observed that many of their cellular ramifications were heading towards blood vessels. Michael von Lenhossek has named those cells 'astrocytes', literally "star-shaped" cells, referring to their ramifications from the soma [13]. In the beginning of the XX$^{\text{th}}$ century, Ramón y Cajal has developed a method to stain astrocytes: gold and mercury chloride-sublimate, which labels only glial fibrillary acidic protein (GFAP), a marker that is mostly expressed in astrocytes [14]. He has suggested their role in regulating blood flow [15]. Few researchers a century ago even speculated that glia might play a central role for information processing in the CNS [16, 17].

I.1.2   Astrocyte characteristics

Astrocyte morphology

Deiters has first reported the ramified shape of some neuroglia, later confirmed by Michael von Lenhossek [18]. Astrocyte morphology consists in a big soma ($\approx 6 \times 10^3 \mu m^3$ [19]), containing the nucleus, and cellular ramifications/branches referred to as astrocyte processes.

The first studies of astrocytic morphology were performed with stainings such as Golgi staining and with dyes that were loaded in the cell. Later studies have rather performed immunostaining, which relies on the selective visualization of proteins that are specific to the cell type of interest. For example, astrocytes have been traditionally characterized by their expression of GFAP and anti-GFAP immunostaining has yield to the concept of astrocytes being star-shaped cells (see Fig I.1A). Modern tools beyond those techniques have been developed to visualize astrocyte morphology in physiological conditions. Transcriptomics studies [20, 21, 22] have identified astrocyte-specific promoters such as GFAP or S100β [23, 24, 25]. Those promoters can be used to express genetically encoded Ca^{2+} indicators (GECIs) specifically in astrocytes [26]. Assuming that all regions of astrocytes can display Ca^{2+} signals, those tools allow for a better resolution of astrocyte morphology *in vivo* and *in vitro* compared to e.g GFAP staining, which marks 15% of the total astrocytic volume [27]. GECIs, similarly to dyes (see Fig I.1), actually reveal a shape that is more spongiform than star-shaped , with a volume of $\approx 10^4$ μm^3 [28]. $\approx 80\%$ of the total surface area belongs to processes [29]. Specialized and polarized ramifications that are in contact with blood vessels are called endfeet [30]. Electron microscopy (EM) has been important for characterizing astrocytic morphology at the nanometer scale [31, 32, 33, 2, 1], revealing extra-thin sheets and processes near the neuropil and enwrapping synapses, often referred to as peripheral astrocyte processes (PAPs). Fig I.1 presents the typical morphology of astrocytes, revealed by different imaging techniques.

Interestingly, an astrocyte in the adult rodent brain can cover from 20 000 to 80 000 μm^3 [27, 35, 36]. Each astrocyte only contacts neighboring ones at its peripheral processes so that astrocytes occupy non-overlapping territories [27] (see also Fig I.1C). A single astrocyte can also wrap several neuronal somata and can interact with 300 to 600 neuronal dendrites [35]. Finally, it has been demonstrated that astrocytes in the rat hippocampus can contact simultaneously up to 100 000 synapses [27]. Since the volume of human astrocytes is 15 to 20 fold larger than in rodents, a single astrocytic domain could cover up to 2 000 000 synapses [37].
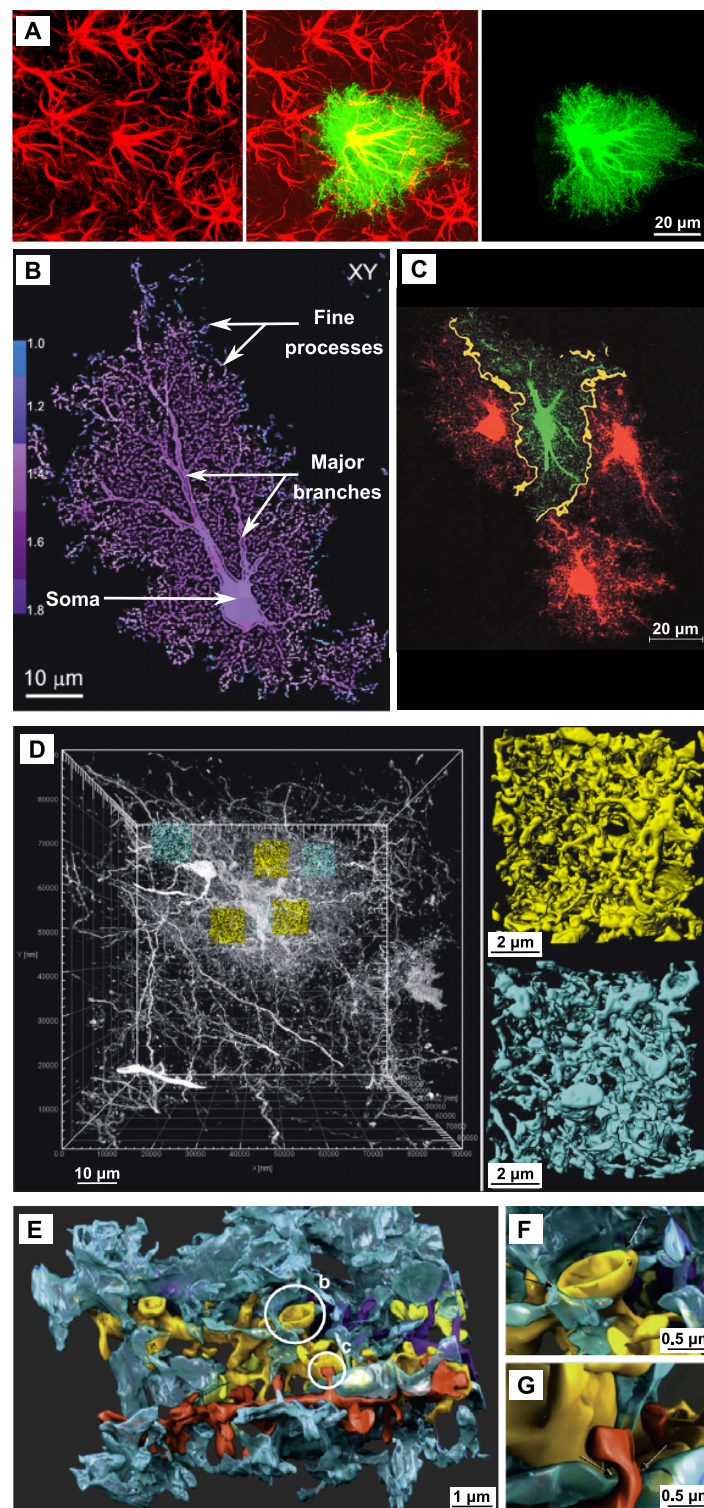
Figure I.1: Typical morphology of astrocytes. High resolution electron and light microscopy revealing the ramified, spongiform structure of astrocytes. (*A*) Comparison of astrocyte images obtained by glial fibrillary acidic protein (GFAP) immunostaining (red) and 3d reconstructions of dye-filled astrocytes (green). The images illustrate the higher morphological complexity that can be visualized with dye-filled compared to GFAP-labeled astrocytes, which is more spongiform than star-shaped. (*B*) Confocal image of a dye-filled astrocyte, revealing its discrete morphological compartments: the soma, major branches and distal finer processes). (*C*) Optical slice through the interface region of neighboring astrocytes (yellow), illustrating the restricted region in which astrocytes interdigitate.

Figure I.1: Typical morphology of astrocytes (continued). (*D*) Electron microscopic image of an entire astrocyte that was stained with Golgi (left). Yellow zones represent three peri-somatic sub-volumes and cyan regions, three peripheral ones (680 μm^3 each). The right panel illustrates the dense networks of fine astrocytic processes. (*E*) 3D reconstruction of astrocytic processes (blue) from a single astrocyte of the rat hippocampus. Their apposition to neuronal dendrites are clearly visible (four dendrites are reconstructed in gold, yellow, red and purple). Presynaptic neuronal elements are not reconstructed here. $\approx$ 50% of the surface of mushroom spines was apposed to peripheral astrocyte processes (PAPs) (*F*), while only the neck of thin dendrites was in contact with processes (*G*, arrows). Panel A was taken from Pekny et al [34], B from Shigetomi et al [26], C from Bushong et al [27] and D, E, F, G from Reichenbach et al [29].

Neuron/astrocytes ratio

The number of glial cells in the central nervous system has for long been a controversial subject (see [38]). New stereological studies [39] have revealed a ratio of the total number of glia and neurons in macaque monkeys and human brains that is roughly 1:1, although the glia/neurons ratio depends on brain region: from 11:1 in the brain stem to 0.2:1 in the cerebellum [40]. Astrocytes most probably account for 20-40% of all glial cells [18], thus accounting for 10-20% of neural cells in the human CNS.

Expression identity of astrocytes

In order to better characterize astrocyte gene expression identity and the possible variability of the latter depending on brain region, genetic screens have been performed. Astrocytes have first been characterized by the expression of glial fibrillary acidic protein (GFAP) [18]. GFAP is however not the best astrocytic marker as it is expressed late in development and fails at labelling protoplasmic astrocytes [41]. Recent transcriptomic studies on populations of astrocytes have revealed that the use of ALDH1L1 gene marker should be favoured instead [42, 43]. Other markers for astrocytes have been identified by Zhang et al [21]. No universal marker for staining all astrocytes in the CNS has been identified yet but the most commonly used are GFAP, Vimentin, S100β, EAAT-1 (GLAST), EAAT-2 (GLT-1), Glutamine synthetase, ALDH1L1, CX43, CX30, AQP4 and SOX9 (see [18] for more details). Importantly, cultured astrocytes do not express the same genes as *in vivo* astrocytes [42].
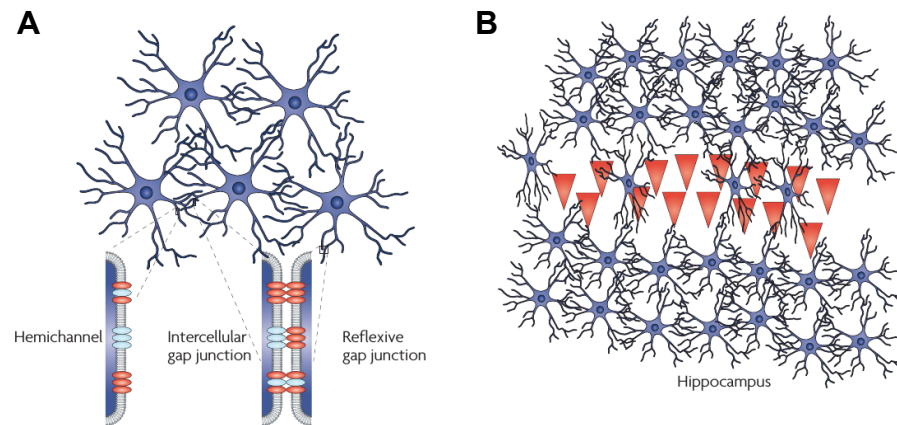
Figure I.2: Astrocytic networks (*A*) Astrocytes are connected to each other via connexin (Cx) channels. Specific domains characterize each astrocyte and astrocytes communicate via gap junction channels only at the interface between their territories. Note that 2 processes from the same astrocyte can contact each other and form 'reflexive' gap junctions. (*B*) Representation of the organization of the astroglial network in the hippocampus, in which the layer of pyramidal neurons (red) influences the number and morphologies of astrocytes. This figure was taken from Giaume et al [51].

Astrocyte networks

Astrocyte coupling has first been demonstrated by injecting Lucifer yellow or bio-cytin in a single astrocyte, resulting in the staining of nearly a hundred of adjacent astrocytes. This connection between the cytosol of several astrocytes is orchestrated by gap junctions on astrocytic membranes. Gap junctions are composed of hundreds of channels named connexons, which, when open, enable the intercellular transport of all ions and molecules that are smaller than 1000 Da. There, two adjacent membranes come close together, with an intercellular space of $\approx$ 2-3 nm [44]. Astrocytes coupling is highly variable as it can involve networks of hundreds of cells [45, 46] to only 2-5 of them [47, 48] and as coupling is not ubiquitous so that neighboring cells may not be coupled even if closely apposed [49, 50]. The organization of astrocytic networks does not look random as they often follow anatomical structures such as barrels of the somatosensory cortex [51]. Interestingly, $\approx$ 25% of gap junctions have been reported to connect processes from the same cell [52], potentially enabling the coupling of different subcellular compartments [52].

Astrocyte electrophysiological signature

Mature astrocytes are hyperpolarized with a resting potential of $\approx$ -80 mV, due to high membrane permeability to K^+ [53]. They are also characterized by a nearly linear relationship of current to voltage [54]. Although astrocytes display a huge variability in their morphology, their electrophysiological properties are remarkably similar. For more details on the ion channels responsible for ion currents and resting membrane potential in astrocytes, see [18].

Astrocyte diversity

Although astrocytes share a similar ramified structure, they display a remarkable morphological heterogeneity, which was already reported by Ramón y Cajal [55]. The diversity of astrocytic morphology is presented in Fig I.3. Nine main astrocyte subtypes have emerged from morphological studies, including protoplasmic VS fibrous astrocytes, which are found in gray and white matter respectively, and the more specific Müller glia of the retina and Bergmann glia in the cerebellum [56]. Notably, cultured astrocytes display a very different morphology from *in situ* or *in vivo* astrocytes (Fig I.3F,G). Depending on brain region, astrocytes display various protein expression levels [57], transcriptionally distinct intracellular regions [43, 58, 59] as well as distinct Ca^{2+} signals and electrophysiological properties [45, 60, 61]. Although the morphology of astrocytes is as heterogeneous as that of neurons, the functional implications of this diversity is still poorly understood and requires further investigation.

The proportion of synapses that are in contact with astrocytes processes also displays both intra-regional and inter-regional diversity (see section I.2.7 for more details).

Better understanding the subregional and regional diversity of astrocytes is important as it might underlie selective neuronal degeneration in brain diseases such as Parkinson's disease [62]. For more detailed reviews on regional morphological and functional diversity of astrocytes and potential approaches that could uncover the diversity of astrocytes, see [63, 64, 18, 65].
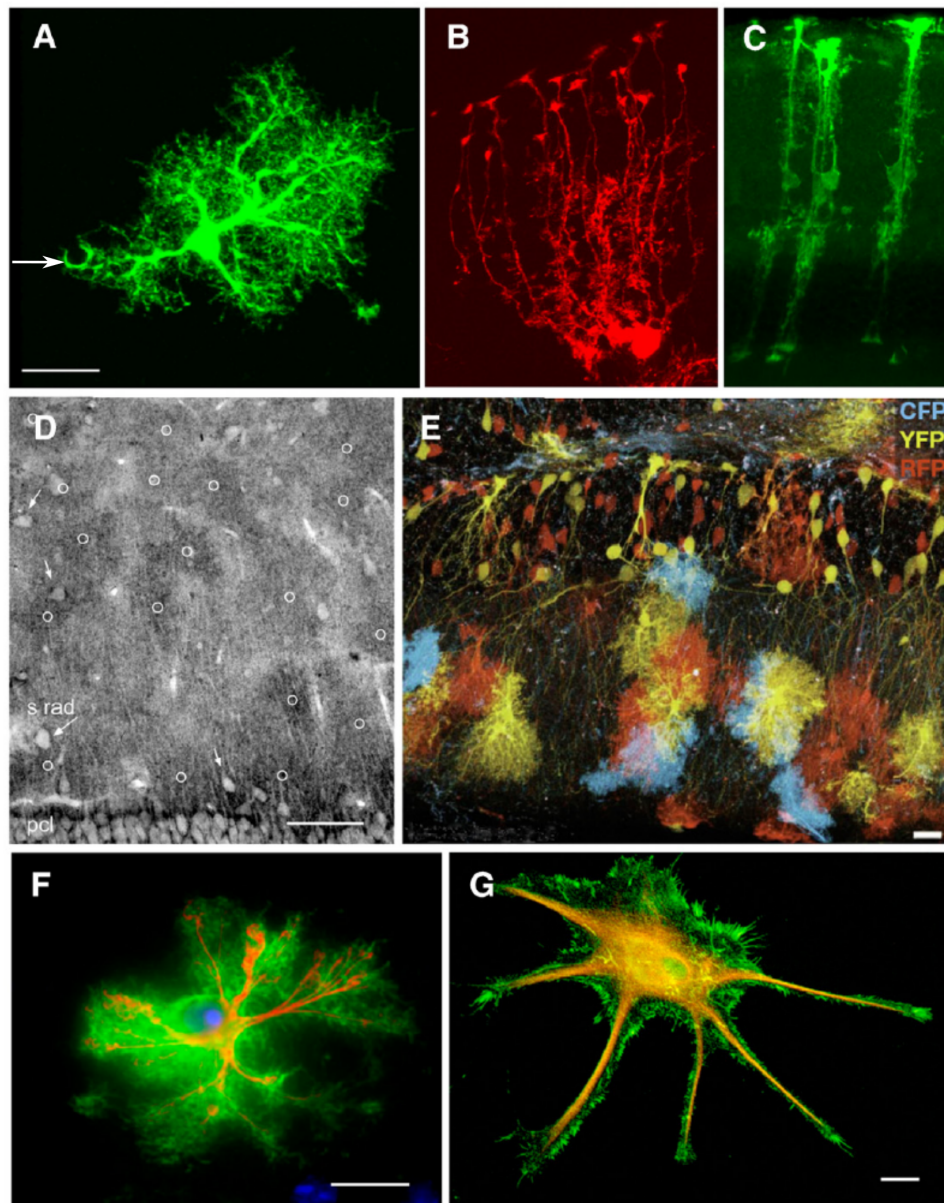
Figure I.3: Morphological diversity of astrocytes. Astrocytes are polarized and highly ramified cells that can display various morphologies depending on brain region. (*A*) Astrocyte of the mouse neocortex. Note that one process on the left is contacting a blood vessel (white arrow). (*B*) Bergmann glial cells from mouse cerebellum. Those astrocytes display a specific polarization: cell bodies are localized at one end while the other end contacts the pia mater. (*C*) Müller glial cells of the mouse retina also display an elongated morphology. (*D*) Staining of ezrin, an actin-binding protein in PAPs, in the stratum radiatum of the rat hippocampus. This staining labels the tips of astocytic processes and enables the visualization of astrocyte territories. Somata are labelled with white circles. Arrows represent pyramidal cells and interneurons. (*E*) Brainbow Cre/LoxP transgenic mice also revealing astrocyte territories and spongiform structures. (*F–G*) Co-immunostaining for GFAP (red) and ezrin (green), respectively labelling major processes and more distal ones and illustrating the lack of precision of morphological structure observed with GFAP staining. Also note the striking difference in morphology of acutely isolated (*F*) VS cultured (*G*) astrocytes. Cultured astrocytes appear less ramified, displaying a less complex morphological architecture. Scale bars (μm): 20 (A), 100 (D), 20 (E), 15 (F), 10 (G). Figure from Reichenbach et al [29].

I.2   Physiological functions of astrocytes

Although they were first considered to be mainly responsible for brain tissue cohesion, the roles of astrocytes in the functioning of the central nervous system are now better documented. The main roles of astrocytes in the CNS are presented in Fig I.4 and in the next paragraphs.

I.2.1   Brain development

The critical role of astrocytes for synaptogenesis has first been observed in culture. Indeed, astrocyte-neuron co-cultures displayed seven times more synapses than classical neuronal cultures [66]. Astrocytes induce synapse formation via the release of diverse molecules including thrombospondins and chordin-like 1 [67, 68]. Astrocytes modulate neighboring dendritic spines morphology [69], synapse-astrocyte contact is correlated to the maturation and to the lifetime of dendritic spines [70] and movements of astrocytic processes are observed during synapse formation [70]. Interestingly, metabotropic glutamate receptors (mGluRs) are expressed in astrocytes as early as the first postnatal week [71], enabling them to detect synaptic activity at early stages of brain development. For a review on the roles of astrocytes in synapse formation, maturation, pruning, as well as synapse elimination, which are synthesized in the concept of the astroglial cradle [72, 73], see Dallerac et al [74].

Astrocytes are also involved in promoting the myelination of active neurons by oligodendrocytes [75]. For reviews on the roles of astrocytes in CNS development, see [76, 41].

I.2.2   Homeostasis

Astrocytes regulate ionic homeostasis of the extracellular space, including K^+, Na^+ and Ca^{2+}, which is essential for the propagation of electrical signals within neurons [81]. Astrocytes are essential for uptaking and catabolizing neurotransmitters, including GABA, adenosine, monoamines and glutamate. Astrocytes also release precursors of neurotransmitters to neurons. For example, around 80% of glutamate is taken up by astrocytes in the CNS [82], which prevents neuronal and synaptic damage caused by high glutamate concentration [83]. Astrocytes also regulate the pH and water homeostasis of the extracellular space, thus also regulating its volume. Finally, astrocytes regulate the homeostasis of reactive oxygen species (ROS) [18].

INFORMATION PROCESSING

Synapse

1. Neurotransmitter
4. Modulation of neurotransmission

2. Ca²⁺ signals

Astrocyte   3. Gliotransmitters

- Modulation of neuronal communication

BRAIN DEVELOPMENT

- neuronal migration
- myelination
- synapse development
- pruning

METABOLISM

- Metabolic support (glucose, lactate)
- Glycogen stores

ROLES OF ASTROCYTES

HOMEOSTASIS

- Ionic homeostasis
- Neurotransmitter clearance
- Water balance and pH regulation
- ROS homeostasis

BLOOD BRAIN BARRIER

- Regulate the interface between blood vessels and neurons

BRAIN INJURY REPAIR

- Formation of the glial scar
- Astrocyte reactivity
- Immune modulation (with microglia)
- Controversial roles for neuronal regeneration
- Regulation of homeostasis at lesion site

Figure I.4: Roles of astrocytes in brain development and function. Astrocytes are essential for brain development (figure from Schiweck et al [77]), homeostasis, information processing and metabolism (figure from Amaral et al [78]). They are key elements of the blood brain barrier (figure from Kandel et al [79]) and participate to the repair of the injured brain tissue (figure from Lee-Liu et al [80]). For more detailed discussion and references on the physiological roles of astrocytes, please refer to section I.2 and to Verkhratsky et al [18].

Astrocytes are thus chemosensing cells that are responsible for systemic homeostasis of ions and metabolites in the CNS.

I.2.3   Metabolic support

Astrocytes possess most of the brain glycogen reserves and can metabolize it through glycogenesis, before providing neurons with energy substrates such as glutamine [78, 84]. Glycogenesis is important for long term potentiation (LTP) and for memory consolidation [18]. Most importantly, astrocytes utilize glucose to perform aerobic glycolysis, which produces lactate [84]. The astrocyte-neuron lactate shuttle hypothesis (ANLSH) has been formulated by Pellerin et al [85] and proposes that neuronal activity relies on lactate that is released from astrocytes. Astrocytes can produce, release as well as take up extracellular lactate [86] so that astrocytes can support metabolic needs of neurons by producing as well as uptaking lactate.

I.2.4   Blood Brain Barrier

Astrocytes contribute to the blood-brain barrier, which protects the brain from homeostatic changes and from most of the pathogens (although a few pathogens such as e.g the human immunodeficiency virus, HIV, can cross this barrier) [87]. Endfeet are enriched in ion channels and Kir K^+ transporters [87], which contribute to systemic homeostasis in the brain by regulating its pH, Na^+ and K^+ concentrations. Astrocyte activity in response to neuronal activity can induce vasomodulation [88, 89, 90], illustrating potential roles of astrocytes for mediating interactions between active neurons and blood vessels.

I.2.5   Brain injury

The involvement of glial cells in the diseased brain has been speculated since the beginning of the XIXth century by Alzheimer, Nissl and Fromman. However, the XXth century has been characterized by a neuro-centric investigation of the diseased brain [91].

As astrocytes play key roles in brain function, their functions are altered in various brain diseases such as epilepsy [91], brain tumours [91], neurodegenerative diseases [92], Down syndrome [93], major depressive disorder [91] and schizophrenia

[94]. The involvement of astrocytes in brain diseases is represented in Fig I.5A.

When the brain is injured, astrocytes migrate to the injured site and get activated. Astrocyte activation, also called astrogliosis, is characterized by an up-regulation of GFAP and by a modified pattern of gene expression. The beneficial and detrimental effects of reactive astrocytes are detailed in refs [95, 96, 34] and represented in Fig I.5B. After their activation, astrocytes often form a glial scar that isolates damaged from intact tissue [95] and assists recovery of the damaged tissue. The glial scar consists in astrocytes interacting with different cell types and only isolates severely damaged tissues such as tumours, necrosing tissue, neurodegenerative regions, infected or inflamed regions, both in brain and spinal chord injuries or following a stroke [97]. The glial scar is thus a hallmark of various brain diseases such as traumatic spinal cord and brain injuries, chronic (e.g multiple sclerosis (MS) and amyotrophic lateral sclerosis (ALS)) and acute neurodegenerative diseases (e.g Alzheimer's disease (AD) and Parkinson's disease (PD)) and stroke [98]. Recent studies have demonstrated that the glial scar is essential for the regeneration of stimulated axons within injured spinal cord [99]. However, the glial scar is also associated with some detrimental effects such as inhibition of neuronal growth and of synaptic transmission at the injury site [100] and consists in an impermeable barrier for regeneration, thus compromising neuronal repair [97].

My master's internship consisted in investigating the effect of astrogliosis in the hippocampus on neuronal communication. We have demonstrated that astrocyte reactivity impairs long term potentiation and is associated with learning and memory defects [101].

Astrocytes, especially reactive astrocytes, thus emerge as new therapeutic targets for the diseased brain. For reviews on astrogliosis, see [102, 103, 104, 34]. For more details on the involvement of astrocytes in the diseased brain, see dedicated reviews [94, 105, 91, 106].

I.2.6   Information processing

As they do not exhibit electrical excitability [108], astrocytes were first characterized as non-excitable cells of the CNS, although they express voltage-gated channels [109] and membrane receptors for neurotransmitters such as glutamate, γ-aminobutyric acid (GABA) or adenosine triphosphate (ATP) [18]. Astrocyte excitability instead results from variations of cytosolic Ca^{2+} concentration [110], which can activate signals that modulate neuronal communication [111, 112, 113, 114]. The diversity and functional roles of astrocytic Ca^{2+} signals will be further developed in Chapter II and the interactions of astrocytes with neurons for information processing in the brain in section I.2.7.
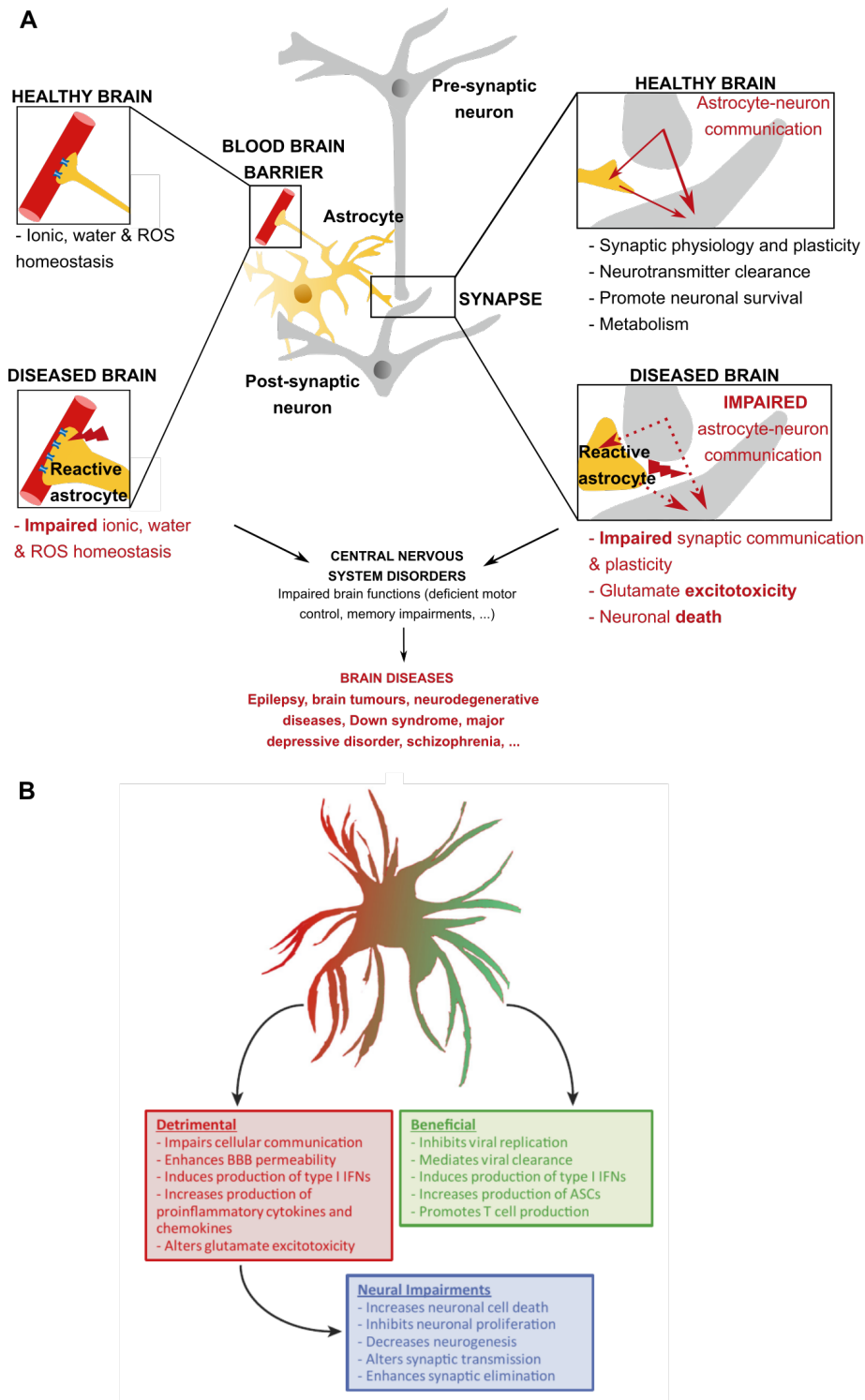
Figure I.5: Impaired functions of astrocytes in the diseased brain. Panel (*A*) is a schematic representation of the impaired functions of astrocytes in the diseased brain. For more details and references, see section I.2.5. For simplicity, only interactions with neurons and blood vessels are represented, although other cell types interact with astrocytes such as microglia and oligodendrocytes. Astrocytes in the diseased brain are responsible for glutamate excitoxicity, altered brain homeostasis, impaired synaptic communication and plasticity and can trigger neuronal death. Note that only adult brain functions are represented in this cartoon but that impaired astrocytic functions in the developing brain lead to neurodevelopmental

Figure I.5: Impaired functions of astrocytes in the diseased brain (continued). disorders that can be lethal [41]. Panel (*B*) is a figure taken from Soung et al [107] and represents the beneficial and detrimental effects of reactive astrocytes, which are a hallmark of many brain diseases.

I.2.7 Focus on the tripartite synapse

Electron microscopy has revealed that astrocytic processes can tightly wrap synapses [27]. At least half of the CNS synapses are indeed ensheathed by an astrocytic process, also referred to as peripheral astrocytic processe (PAP) [18]. The proportion of ensheathed synapses varies depending on brain region, from $\approx 90\%$ in layer IV of the somatosensory cortex to 60-90% in the hippocampus and 29-56% in the neocortex [115], and also varies depending on the type of synapse [116, 117]. The synaptic surface that is contacted by astrocytes varies from being the whole synaptic cleft [117] to only a fraction of it [2] (see Fig I.6C). Electron microscopy reveals that PAPs are very thin, ≈ 200 nm in diameter on average, often < 100 nm [29]. 80% of the plasma membrane of an astrocyte belongs to its PAPs, resulting in a high surface/volume ratio of $\approx 25 \mu m^{-1}$ [118].

When apposed to synapses, astrocytes can sense neurotransmitters and neuromodulators released from pre-synaptic neurons: glutamate through metabotropic glutamate receptors (mGluRs) [119], γ-aminobutyric acid (GABA) through GABAB receptors [120], acetylcholine [114, 121] and dopamine [122]. They can also sense purines released by neurons such as adenosine-triphosphate (ATP) and adenosine [123, 124]. Astrocytes have also been shown to respond to post-synaptic activity [125], including endocannabinoids through cannabinoid CB1 receptors (CB1Rs) [126, 127, 128] and ectopic release of glutamate from glutamatergic fibers in the case of Bergmann glia in the cerebellum [129]. Those stimuli trigger Ca^{2+} signals in astrocyes that can activate the release of molecules, referred to as gliotransmitters, such as glutamate, D-Serine, ATP, tumor necrosis factor-α (TNFα), brain-derived neurotrophic factor (BDNF) or atrial natriuretic peptide (ANP) [130], which can modulate synaptic transmission [111, 112, 113, 114] and vasoconstriction/vasodilatation [88, 89, 90, 131]. Detailed neuron-astrocytes signaling pathways at the tripartite synapse are presented in Fig I.7. For recent reviews on tripartite synapses and the associated controversies, see [3, 132, 133, 134, 135, 136].

The morphology of PAPs is highly dynamic and synapse coverage by astrocytic processes varies within minutes depending on physiological conditions [29] (see Fig I.6A,B). Long term potentiation (LTP) induction in hippocampal slices and sen-
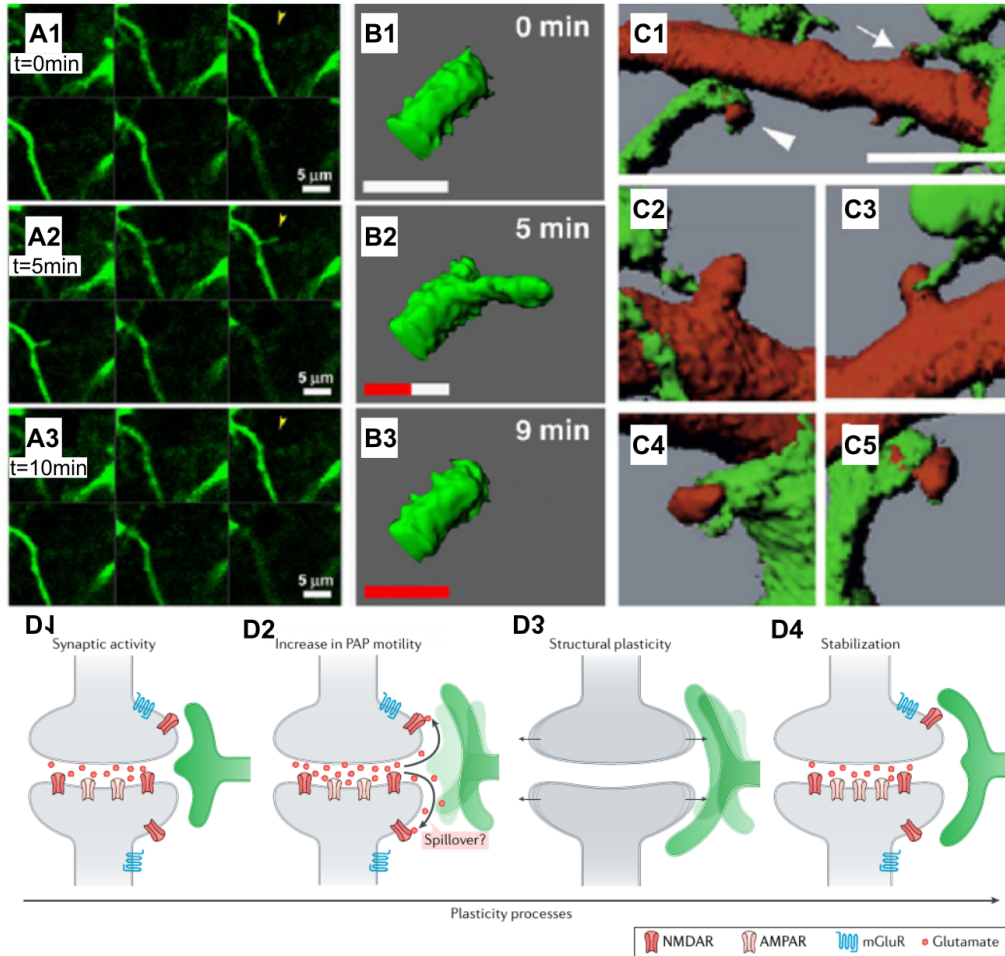
Figure I.6: Dynamic remodeling of PAPs. (*A*) Spontaneous transient extension and protrusion of an astrocytic process in the brainstem (arrowhead). (*A1*), (*A2*) and (*A3*) represent a stack of 6 images recorded respectively at time 0, 5 and 10 min in the same acutely isolated brainstem slice. (*B*) 3D-reconstruction revealing the transient extension of the PAP pointed by the arrowhead in panel A. Scale bar: 5 μm. (*C*) Diverse morphologies of neuron/astrocyte contact sites revealed by 3d reconstructions from two-photon image stacks. Contact sites can ensheath dendritic necks (arrowhead in C1; zoom in C4, C5) or contact a small fraction of the dendrite (arrow in C1; zoom in C2, C3). Scale bar in C1: 5 μm. (*D*) Schematic representation of the variations of synaptic coverage by astrocytes during synaptic plasticity. Increased synaptic activity at glutamatergic synapses (D1) is associated with the release of glutamate that triggers a temporary increase in the motility of PAPs (D2). If this transient motility results in a decrease of synaptic coverage, glutamate spillover occurs, activating both structural (D3) and functional (D4) synaptic plasticity. mGluR: metabotropic glutamate receptor. Panels A-C were taken from Reichenbach et al [29] and panel D from Dallerac et al [74].
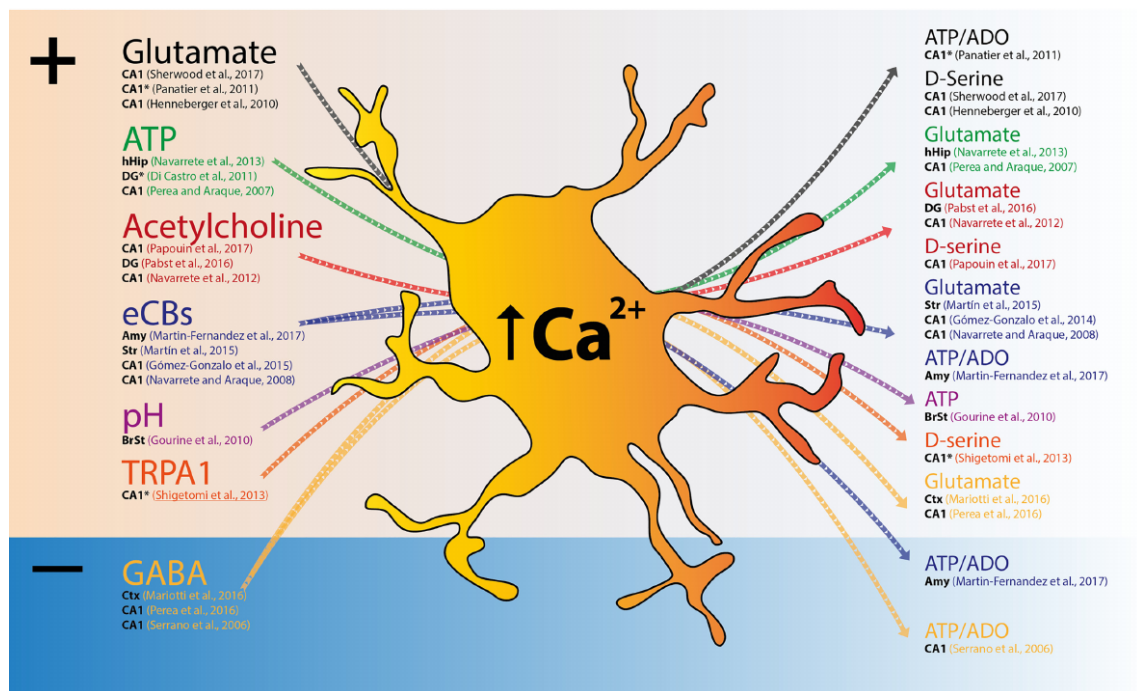
Figure I.7: Neuron-astrocyte interactions at the tripartite synapse. Representation of the diverse signals that are exchanged between astrocytes and neurons at the tripartite synapses, both excitatory (+, orange) and inhibitory (-, blue). The left panel of the figure presents the different neurotransmitters that can be released by active neurons and that trigger Ca^{2+} signals in astrocytes. The right panel presents the gliotransmitters that can be released by astrocytes in response to neuronal activity-induced Ca^{2+} signals. The corresponding references for each signaling molecule is given in parenthesis. The abbreviations correspond to the regions studied: Amy: Amygdala; BrSt: brainstem; CA1: CA1 region of the hippocampus; Ctx: cortex; DG: dentate gyrus; hHip: human hippocampus; Str: Striatum. The * symbol indicates that in the given study, Ca^{2+} signals involved in gliotransmission were local rather than global. This figure was taken from Guerra-Gomez et al [137].

sory stimulation *in vivo* both result in changes of synapse coverage by PAPs [138]. Under stimulation, astrocytic processes retract from the synapse, possibly favoring glutamate and ions clearance from the synaptic cleft [139].   The close association both structurally and functionally of astrocytes to pre- and post- synaptic elements presented in this section is referred to as the tripartite synapse. For more details on synaptic micro-environment associated with PAPs, see refs [139, 140, 115]. For a review on the involvement of astrocytes in synaptic plasticity, see Theodesis et al [139].

Chapter II

Astrocyte excitability: Ca^{2+} signals

Astrocytes have recently emerged as essential partners of neurons for information processing in the brain. Chemical or mechanical stimulation of cultured astrocytes have revealed that astrocyte excitability results from variations of cytosolic Ca^{2+} concentration [141, 142, 143, 144, 145]. In this chapter, the roles, characteristics and mechanisms of Ca^{2+} signals in astrocytes are presented.

II.1 General considerations on Ca^{2+} signals

II.1.1 Ca^{2+}, ubiquitous intracellular messenger

Ca^{2+} is an ubiquitous intracellular messenger in eukaryotic cells, playing key roles in signal transduction for cell growth, apoptosis, differentiation, secretion, metabolism, gene transcription, muscle contraction, fertilization, immunity, learning and memory [146]. Because of their central roles for cellular physiology, Ca^{2+} signals are altered in a lot of diseases, including cancer [147, 148].

Ca^{2+} signals correspond to variations of cytosolic Ca^{2+} concentration in response to stimuli. The encoding of signals depends on the cell and on the stimulus. For example, the main mechanism of Ca^{2+} signals in astrocytes is believed to rely on the opening of type 2 IP_3R. After agonists bind to $G_{q/11}$-GPCRs, IP_3 synthesis is activated and the resulting IP_3 molecules, together with Ca^{2+}, activate the opening of IP_3R channels, resulting in an influx of Ca^{2+} ions in the cytosol (see section II.2.3.2 for more details). Ca^{2+} signals can differ by their amplitude, duration, frequency and by their propagation range and speed. Those signals rely on the existence of Ca^{2+} stores and on the activity of Ca^{2+} channels and pumps that enable the generation of Ca^{2+} signals as well as the restoration of basal concentrations, respectively.
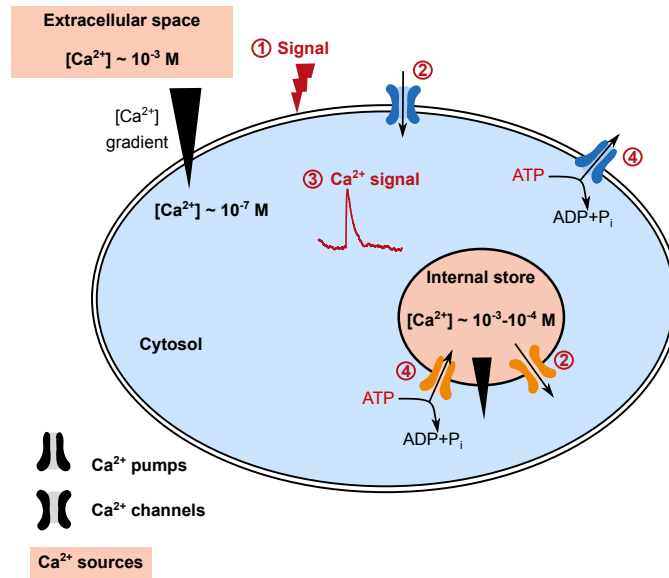
Figure II.1: Principles of Ca^{2+} signaling. Ca^{2+} signals correspond to transient increases in Ca^{2+} concentration in the cytosol (blue), $[Ca^{2+}]_{cyt}$. Resting $[Ca^{2+}]_{cyt}$ is $\approx$ 100 nM while $[Ca^{2+}]$ in Ca^{2+} sources (orange) (i.e the extracellular space and internal stores: ER, mitochondria, lysosomes) is $\approx$ 0.1-1 mM. The $[Ca^{2+}]$ gradient between the cytosol and Ca^{2+} sources is maintained at steady state, corresponding to equilibriated fluxes in and out of the cytosol. When a signal is sensed by the cell (1), Ca^{2+} influx to the cytosol is performed by Ca^{2+} channels (2), which results in a Ca^{2+} signal (3). Basal $[Ca^{2+}]$ in the cytosol and in stores are then restored by the ATP-dependent activity of Ca^{2+} pumps (4).

The detailed mechanisms are described in Fig II.1. Ca^{2+} channels and pumps as well as the proteins responsible for Ca^{2+} transport (i.e diffusive Ca^{2+} buffers) strongly vary depending on cell type or even on subcellular localization, which contributes to the variability of Ca^{2+} signals [149].

Fig II.2 presents the molecular mechanisms responsible for the contraction of heart cells, the cardiomyocytes, which are mediated by Ca^{2+} signals.

For detailed reviews on Ca^{2+} signals and the molecules involved, see [146, 150]. For a detailed review on the roles of Ca^{2+} signaling throughout the evolutionary tree, see Plattner et al [151].

II.1.2 Experimental methods to investigate Ca^{2+} signaling

In this section, the main experimental methods that can be used for investigating Ca^{2+} signaling are presented, mostly focusing on techniques based on electron and
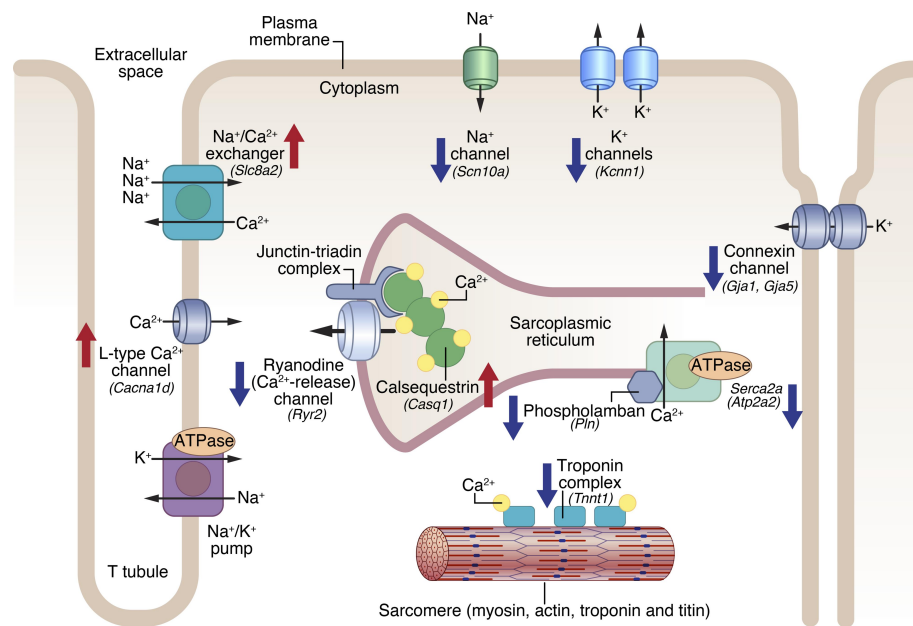
Figure II.2: Role of Ca^{2+} **in cardiomyocytes contraction.** Schematic representation of the molecular interactions that mediate Ca^{2+} signals in cardiomyocytes, which are necessary for normal cardiac contractility, taken from Baskin et al [152]. After an action potential depolarizes the plasma membrane of cardiomyocytes via a Na^+ influx into the cytosol, voltage-gated L-type Ca^{2+} channels are activated, resulting in an increase of [Ca^{2+}]$_{cyt}$. This triggers the activation of Ca^{2+}-gated Ryanodine Receptors (RyRs) on the sarcoplasmic reticulum, increasing further [Ca^{2+}]$_{cyt}$. Ca^{2+} ions then interact with troponin, which conformational change enables the binding of myosin to actin, resulting in cellular contraction. Muscle relaxation is regulated by Ca^{2+} pathways that restore the concentration of Ca^{2+} in both the cytosol and the SR, notably via the activity of energy-dependent membranous pumps and Na^+/Ca^{2+} exchangers (NCX). Red and blue arrows refer to up- and down-regulated genes in Med12cKO hearts (see Baskin et al [152] for more details).

fluorescent microscopy.

II.1.2.1 Molecular approaches to trigger Ca^{2+} signals

The most common tools that are used to trigger Ca^{2+} signals in astrocytes are depolarization, mechanical stimuli, photolysis of caged IP$_3$ or Ca^{2+} and the activation of astrocytic G protein-coupled receptors (GPCRs) by the application of agonists. The Designer receptors exclusively activated by designer drugs (DREADDs) are a family of engineered GPCRs created by Armbruster et al [153] that can selectively modulate signal transduction pathways *in vitro* and *in vivo*. Finally, optogenetics

[154] allow the investigation of Ca^{2+} signals with a high control of both spatial and temporal characteristics of the stimulation. For example, photo-activable Ca^{2+} channels can be used for triggering astrocytic Ca^{2+} [155] in specific sub-populations of astrocytes in a given physiological condition. For more details on molecular approaches to investigate Ca^{2+} signals in astrocytes, see [156, 157].

II.1.2.2   Fluorescent microscopy for monitoring Ca^{2+} signals

Fluorescing techniques involve the use of fluorescent indicators, I, to track molecules/ions of interest within the cell. Indicators fluoresce when bound to the molecule of interest and the variations of fluorescence with time are measured and normalized over the basal level of fluorescence ($\Delta F/F_0$). Importantly, imaging fluorescent Ca^{2+} indicators does not measure the exact $[Ca^{2+}]$ variations but rather the variations of $[Ca^{2+}$-I] so that the signals measured strongly depend on the concentration and kinetics of the indicator.

The available fluorescent indicators for studying Ca^{2+} signals, which kinetics are presented in Table II.1, are:

- **Ca^{2+} dyes**
  The first molecules that have been used to perform Ca^{2+} imaging were Ca^{2+} organic dyes such as Fluo4, BAPTA and EGTA. Those dyes are delivered by bulk loading or by dialysis of the cytosol with a patch pipette. They have been essential for studying astrocytic Ca^{2+} signals in live tissues, including their discovery, their relationship with neuronal activity [158, 159, 116, 111, 160] and their first recordings *in vivo* [47]. However, the loading of Ca^{2+} dyes in astrocytes in brain slices is often problematic and can result in cell death. Moreover, those dyes get diluted out of the cell with time so that they only reveal the soma and the major branches [161]. Importantly, a recent study has also demonstrated that BAPTA inhibits 30-80% of the activity of the Na^+,K^+-ATPase and suppresses spontaneous Ca^{2+} activity in astrocytes [162] so that its use should be avoided for monitoring Ca^{2+} signals.

- **GECIs**
  In order to improve the spatial resolution of Ca^{2+} imaging, Hires et al [163] have engineered some fluorescent proteins, which comprise a single polypeptide chain and a Ca^{2+}-binding motif, called genetically-encoded Ca^{2+} indicators (GECIs). GECIs can be used in live tissues to monitor Ca^{2+} dynamics. Two main types of GECIs have been used to study astrocytes: single-wavelengths GECIs, as e.g GCaMPs, and FRET-based ratiometric GECIs (for more details see Tian et al [164]). GCaMPs are molecular constructs derived from

the fluorescent protein GFP and the Ca^{2+} buffer calmodulin (Fig II.3A1,A2). GCaMPs have been optimized for brightness, dynamic range, photostability and Ca^{2+} affinity. They display high signal/noise ratio (Fig II.3A4). The emergence of these tools have improved considerably our understanding of Ca^{2+} dynamics in astrocytes, notably by revealing the existence of local signals in fine processes (see Fig II.6). GECIs are constantly being improved and display various kinetics and resolutions, which are suited to different biological questions (spatial VS temporal resolution notably). For example, GCaMP6f is more suited to the study of spatially restricted compartments such as microdomains than GCaMP3 [165]. Some GECIs are targeted to plasmalemmal [166] or organellar [167, 168] membranes (-Lck membrane-tethering domain [169], see Fig II.3A3)) or to subcellular compartments such as mitochondria and the ER (e.g CEPIAS) [170, 171, 172, 173, 174, 175], which enables a higher spatial resolution of Ca^{2+} signals.

GECIs can be targeted to be expressed specifically in astrocytes (Fig II.3B). This targeting further increases signal/noise ratio compared to classical Ca^{2+} dyes, enabling stable *in vivo* recordings and resolving the entire cellular ultrastucture [161]. Note that long-term expression of GECIs may cause astrogliosis and/or decreased health of neurons [176]. For a detailed review on GECIs, see Shigetomi et al [177].

- **Biosensors of molecules of the Ca^{2+} pathway**
  In order to refine our understanding of Ca^{2+} signaling, another strategy consists in tracking molecules that belong to the Ca^{2+} signaling pathway such as GCPRs [178], IP_3 [179, 180, 181], PKA [182] or cAMP [183].

- **Nanobodies**
  A recent study has developed plasmids that encode nanobodies against fluorescent proteins fused to functional modules [184]. Those nanobodies can be used as fluorescent sensors for visualizing Ca^{2+}, H^+ and ATP/ADP dynamics or can be targeted to the lumen of sub-compartments of interest. This toolkit could be useful for investigating Ca^{2+} fluxes e.g between the ER and mitochondria or at ER-plasma membrane contact sites.

Examples of the use of super-resolution microscopy techniques and electron microscopy for studying astrocytic sub-compartments are presented in Fig II.4. For further reading on the importance of super-resolution microscopy for studying Ca^{2+} dynamics in astrocytes, see dedicated reviews [158, 140, 4].
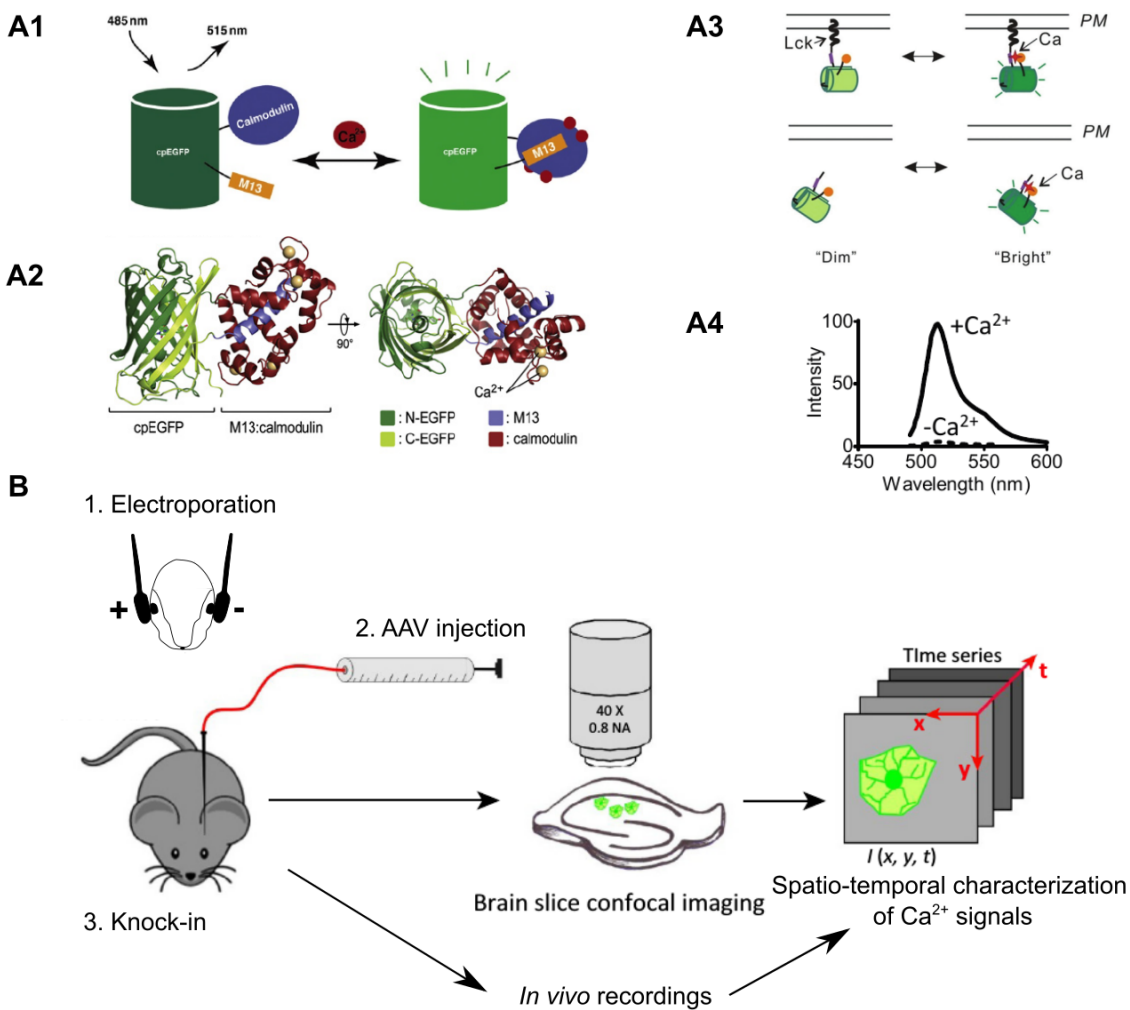
Figure II.3: Genetically encoded Ca^{2+} indicators (GECIs). (*A*) Molecular structure of GCaMP-like GECIs. GECIs are constructs based on GFP and calmodulin, which encounter a conformational change when binding Ca^{2+}, resulting in fluorescent emissions at 515nm (*A1*). Panel (*A2*) represents 2 orthogonal views of the crystal structure of the GECI GCaMP2DRSET in the Ca^{2+}-bound state. The M13 helix is represented in blue, calmodulin in red and cpEGFP in green. Some constructs can diffuse within the cytosol while Lck- variants are anchored to the plasma membrane (*A3*). Panel A4 represents the typical modification in emission spectrum of GCaMP-like GECIs when binding Ca^{2+}. (*B*) Astrocyte-specific expression of GECIs can be induced by electroporation (1), AAV injection (2) or Knock-in (3). Ca^{2+} signals can then be investigated either in acute brain slices or *in vivo*. Panels A1, A2, A3 & A4 were taken from [161, 164, 188] and B was adapted from Shigetomi et al [177]
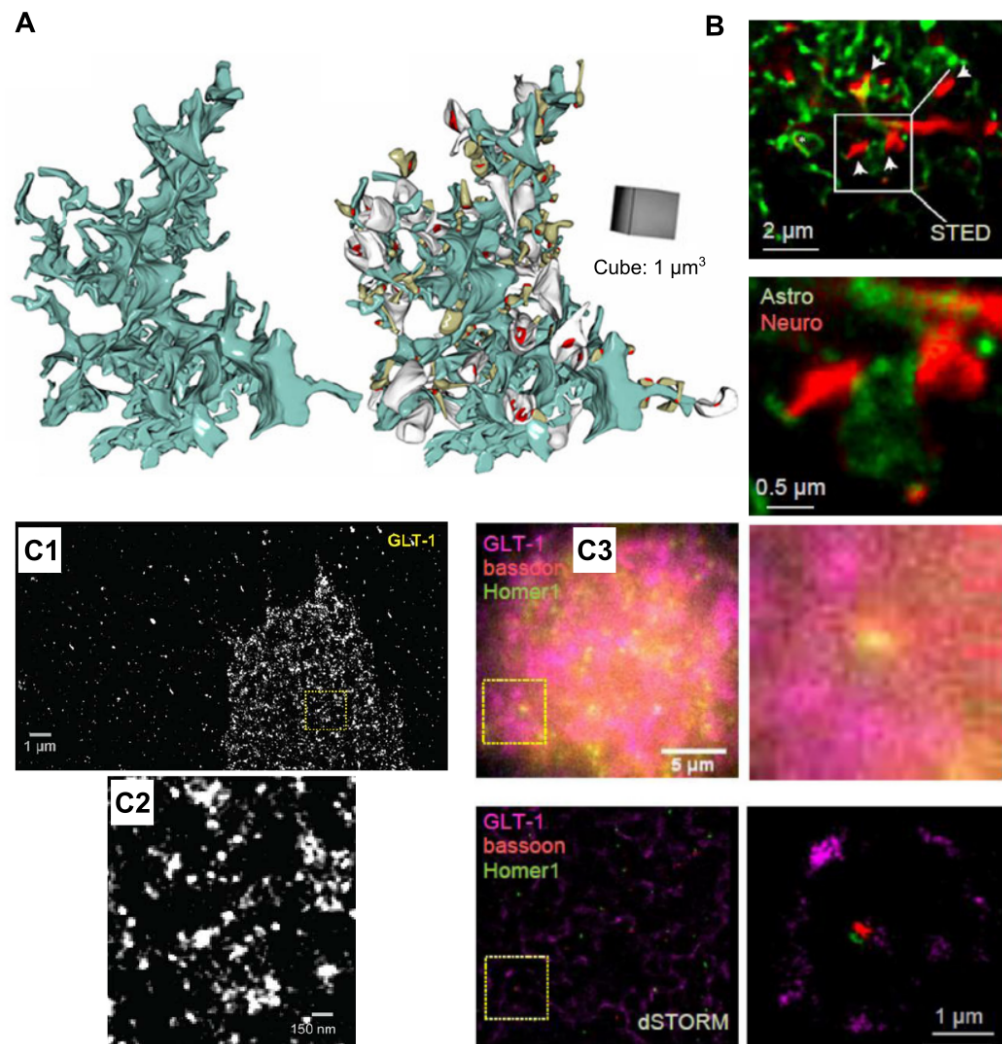
Figure II.4: Super-resolution and electron microscopy for better resolving Ca^{2+} **signaling at the nanoscale in astrocytes.** (*A*) 3D reconstruction of an astrocyte (blue) from electron microscopy shown without (left) and with (right) neighboring dendritic spines (thin in grey, mushroom spines in yellow) containing PSDs (red). (*B*) STED images displaying astrocytic processes (green) in CA1 stratum radiatum of hippocampal organotypic slices and the neighboring synaptic structures (red). Arrows point dendritic spines. Top and bottom panels correspond respectively to lower and higher (square in top panel) magnification. (*C*) dSTORM imaging of GLT-1 from cultured glial cells from rat hippocampus shown at lower (C1) and higher (C2, yellow squared region in C1) magnification. Panel C3 presents a comparison of confocal (top) with dSTORM (bottom) imaging of Bassoon (red), Homer1 (green) and GLT-1(magenta) in CA1 region from thick hippocampal slices. This figure was adapted from Heller et al [4, 140].

Table II.1: Kinetics of the major Ca^{2+} indicators. Note that the 2 components of k_{off} for GCaMP7s refer to the fast (61%) and slow (39%) components [185]. The values of k_{on} and k_{off} for a given indicator vary slightly depending on the study, although the order of magnitude is the same (see e.g kinetics of GCaMP6s and GCaMP6f in refs [185, 186]).

Indicator	$k_{on}(M^{-1}.s^{-1})$	$k_{off}(s^{-1})$	References
Fluo4	$6 \cdot 10^8$	210	[187]
Mag-Fura-2	$7.5 \cdot 10^8$	26760	[187]
GCaMP3	$7.45 \cdot 10^6$	2.57	[186]
GCaMP6s	$4.3 \cdot 10^6$	0.69	[185]
GCaMP6f	$9.44 \cdot 10^6$	4.01	[185]
jGCaMP7f	$1.34 \cdot 10^7$	5.86	[185]
jGCaMP7s	$2.15 \cdot 10^7$	2.86 & 0.26	[185]
jGCaMP7c	$3.56 \cdot 10^6$	2.79	[185]
jGCaMP7b	$1.6 \cdot 10^7$	4.48	[185]

II.2   Astrocytic Ca^{2+} signals

This section presents the main functional roles and impairments of astrocytic Ca^{2+} signals, their spatiotemporal diversity as well as the main molecular mechanisms from which they can emerge.

II.2.1   Functional roles of Ca^{2+} signals in astrocytes

After the discovery of Ca^{2+} signals in astrocytes in response to stimuli, a lot of studies have investigated their physiological roles, which are presented in next paragraphs and summarized in Fig II.5.

II.2.1.1   In the developing CNS

Ca^{2+} signals in radial glia, precursors of astrocytes, control cell proliferation and neurogenesis [189, 190]. Yang et al [191] have demonstrated that if type 2 inositol 1,4,5-triphosphate receptor (IP$_3$R2), which is the Ca^{2+} channel responsible for the majority of astrocytic signals (see section II.2.2), is not expressed then redundant synapses are observed in 2-weeks old mice. This suggests an essential role of astrocytic Ca^{2+} signals for developmental synapse elimination [191]. Astrocytic Ca^{2+} signals are also critical for dendritic spine maturation [192, 193]. Altogether, those data suggest strong implications of Ca^{2+} signals in astrocytes and their precursors for the development of the central nervous system (CNS).

II.2.1.2   In the adult brain functioning

In this section, the main brain functions that have been associated with Ca^{2+} signals in astrocytes are presented.

At the cellular level
For long, astrocytic Ca^{2+} signals have been considered too slow and to require sustained stimulation to impact synaptic communication [194, 195]. The use of superresolution microscopy [4] and of highly sensitive genetically encoded Ca^{2+} indicators (GECIs) [5] (see section II.1) has yet revealed the existence of faster Ca^{2+} events in peripheral synaptic processes (PAPs) *in vivo* or in slices, with an onset and duration

CELLULAR LEVEL

Blood brain barrier
- K+ homeostasis
- blood vessels diameter
- angiogenesis

Cellular interactions in the developing brain
- cell proliferation
- neurogenesis
- synaptic pruning
- dendritic spines maturation

Synaptic physiology & plasticity
- gliotransmission
- neurotransmitter uptake
- PAPs movements
- modulation of action potential propagation

NETWORK LEVEL

Synchronized neuronal firing

BRAIN LEVEL

Cognition
- memory consolidation
- spatial learning
- memory retrieval

Motor
- motor coordination
- rapid eye movement
- obsessive-compulsive-like behavior

Emotion
- anxiety ?
- depressive disorders ?
- fear

Sensory
- integration of visual stimuli
- somatosensory cortex plasticity

Figure II.5: Functional roles of astrocytic Ca^{2+} **signals.** Representation of the main functional roles of Ca^{2+} signals in astrocytes that have been demonstrated so far. Astrocytic Ca^{2+} signals emerge as essential components of brain function, from cellular functioning to neural networks coupling and behavior. For more details and references, see section II.2.1.

of the same order of magnitude than those of neuronal signals [111, 160, 6, 196] (see
Fig II.6). Those signals can trigger the release of gliotransmitters that modulate
synaptic physiology and plasticity (see section I.2.7). Astrocytic Ca^{2+} signals are
also essential for neurotransmitter uptake by astrocytes [197], modulating K^+ home-
ostasis [198], controlling blood vessels diameter [199], the movements of astrocytic
processes [200, 138, 201], glutamate spillover [202] or even modulate the propagation
of action potentials [203]. Ca^{2+} signals in astrocytes are thus crucial for synaptic
physiology and plasticity.

At the neural network level
One astrocyte can contact thousands of synapses that can project locally and/or to
long distances. As Ca^{2+} signals can propagate within astrocytic networks through
gap junctions (see section I.1.2), astrocytic Ca^{2+} signals could be involved in brain
function at a higher spatial scale: neural networks. Ca^{2+} signals are indeed associ-
ated to and seem necessary for synchronized neuronal firing in slices [204, 205, 206,
207, 208] and *in vivo* [209]. Ca^{2+} signaling from astrocytes in specific brain regions
thus support local neuronal synchronization states. Further investigation is needed
to refine our understanding of those processes.

At the brain level
Astrocytic Ca^{2+} signals are essential for brain physiology, including cognition, emo-
tion, motor and sensory processing. For a review, see Oliveira et al [210].

- **Cognition**
  A deficiency in the expression of IP$_3$R2 in astrocytes impairs memory consol-
  idation during non-theta periods in the hippocampus [211]. This observation
  is however in contradiction with a previous study that found no impact of
  IP$_3$R2 impairment on spatial memory [212]. Another study has also reported
  the necessity of astrocytic exocytosis, which relies on Ca^{2+}, for spatial learning
  and memory [213]. A recent *in vivo* study has demonstrated that activating
  astrocytes during memory acquisition is enough to improve memory retrieval
  [214]. Interestingly, transplanting human astrocyte progenitor cells within
  mouse brain resulted in an increased performance of the transplanted mice
  in learning and memory tasks [215]. Astrocytic Ca^{2+} signals thus emerge as
  key features of memory and learning, although further investigation is needed
  to resolve the apparent controversies. For a detailed review on the roles of
  astrocytes in cognition, see Santello et al [216].

- **Sensory processing**
  Fast Ca^{2+} signals have been observed in astrocytes in response to sensory
  stimulation *in vivo* [217, 196]. The intracellular localization of those events

as well as the molecular pathways involved vary depending on brain region [218, 219]. Two-photon imaging of Ca^{2+} signals in ferret visual cortex *in vivo* has demonstrated that astrocytic Ca^{2+} signals display distinct spatial receptive fields depending on the visual stimuli [220]. IP$_3$R2-dependent astrocytic Ca^{2+} signals are necessary for somatosensory cortex plasticity *in vivo* [114] and for the integration of visual stimuli [221]. Finally, astrocytic Ca^{2+} signals are responsible for an enhancement of evoked cortical responses by transcranial direct current stimulations [222]. Thus, astrocytic Ca^{2+} signals are associated with sensory processing.

- **Emotion processing**
  IP$_3$R2-dependent Ca^{2+} signaling does not seem to be involved in anxiety-related behaviors according to several studies [223, 202, 212]. Results on depressive-like behaviors are controversial depending on the genetic model [224, 212]. Astrocytic Ca^{2+} activity however reduces fear expression in fear-conditioning paradigm according to a recent study [225]. Overall, further investigation with more specific tools, notably that do not only trigger IP$_3$R2-dependent Ca^{2+} signals, are needed to refine our understanding of the roles of astrocytic signals in emotion processing.

- **Motor processing**
  Exploratory behavior does not seem to depend on IP$_3$-dependent astrocytic Ca^{2+} signals [224, 202, 212], although the activation of astrocytic GPCRs suggests a role of Ca^{2+} signaling in motor coordination in an IP$_3$R2-independent manner [226]. Tran et al [227] have demonstrated that the amplitude of Ca^{2+} signals in cortical astrocytes endfeet during neurovascular coupling is potentiated by the movement of the mouse. Finally, striatal microcircuits are altered *in vivo* in response to reduced Ca^{2+} signals in astrocytes, causing obsessive-compulsive-like behavior in mice (excessive self-grooming) [228]. Taken together, those results demonstrate an important role of astrocytic Ca^{2+} signals in motor circuits, although the detailed mechanisms require further investigation.

To conclude, astrocytic Ca^{2+} signals are essential for brain physiology, although the detailed mechanisms often remain controversial, probably because of the different techniques used. For example, studies with IP$_3R2^{-/-}$ mice are compared with studies using IP$_3$ sponge, which inhibits all IP$_3$-mediated Ca^{2+} signals, not to mention that most studies ignore IP$_3$R2-independent Ca^{2+} signals in astrocytes. More specific tools are needed to better investigate the involvement of astrocytic Ca^{2+} activity in brain physiology.

II.2.1.3   In the diseased brain

As a result of their roles in brain physiology, astrocytic Ca^{2+} signals are impaired in numerous brain injuries and diseases. Astrocytic Ca^{2+} signals are impaired in brain disorders such as neurodegenerative diseases including Alzheimer's disease (AD) [229, 230, 231, 232, 91, 233] and Parkinson's disease [234], epilepsy [235, 91, 236], schizophrenia [237], hyperactivity, attention deficit, and related psychiatric disorders [238], brain tumours [91], major depressive disorders [91], autism [239], Down syndrome [91, 93] and psychiatric disorders [240]. Aberrant Ca^{2+} signals have also been reported in reactive astrocytes, which are a hallmark of many brain diseases [241]. For reviews on the involvement of astrocytic Ca^{2+} signaling in CNS pathology, see [242, 105, 232, 91].

Alexander's disease (AxD) is directly associated with a deficiency in astrocytes. It is triggered by a mutation in the astrocytic intermediate filament GFAP. Its symptoms are diverse, from delays in mental and physical development, myelination deficits, focal lesions, macrocephaly and seizures. Interestingly, only specific brain regions are vulnerable to the effect of this mutation although GFAP is widely expressed throughout the CNS in astrocytes [243]. A recent study has generated iPSCs from 2 AxD patients and demonstrated that astrocytes displayed abnormal organellar morphology and distribution coupled with impaired Ca^{2+} wave propagation, while correcting the GFAP mutation restored functional phenotype [244]. Further investigation is needed to understand the causal relationship between impaired organelle localization, astrocytic Ca^{2+} signaling and AxD. This discovery however highlights the importance of subcellular spatial distributions of organelles for functional Ca^{2+} signaling.

II.2.2   Characteristics of astrocytic Ca^{2+} signals

The first Ca^{2+} signals in astrocytic networks (see section I.1.2) have been observed in cell culture and consisted in a wave propagating at a velocity of $\approx 20\mu m.s^{-1}$ [110, 245]. Few years later, Ca^{2+} waves have been observed *in situ* in the retina [246] and in the corpus callosum [247] and more recently observed *in vivo* in response to locomotion and startle [6, 248, 249]. Ca^{2+} waves can propagate in astrocytic networks over long distances ($300 - 400\mu m$). They propagate either by the cellular release of ATP and the activation of purinergic receptors [250, 251, 252] or directly through gap junctions [253]. A representative recording of an astrocytic Ca^{2+} wave measured with two-photon microscopy is presented in Fig II.6A.

The use of super-resolution microscopy [4] and of genetically encoded Ca²⁺ indicators (GECIs) [5] has revealed a striking spatiotemporal diversity of Ca²⁺ signals in astrocytes, notably demonstrating striking differences between signals in the soma and in the peripheral astrocytic processes (PAPs) [6] (see Fig II.6B). Ca²⁺ signals in PAPs are indeed highly localized, uncorrelated, characterized by faster kinetics and an order of magnitude smaller amplitude ($\Delta F/F_0$) compared to somatic signals. Most Ca²⁺ signals detected both *in vitro* and *in vivo* occur in processes [7].

As depicted in the schematic in Fig II.7, the different spatial patterns of astrocytic Ca²⁺ signals consist of:

- Spatially-restricted Ca²⁺ signals in microdomains (Fig II.7A) in thin processes. They are extremely diverse and can correspond to fast events that can be TTX-sensitive (neuronal activity-induced) [254, 111] or spontaneous [255, 197, 254, 248, 160]. The longer lasting events ($\approx$ 70s) are referred as Ca²⁺ twinkles [218].

- Endfeet-localized Ca²⁺ signals (Fig II.7B), that are mediated by IP₃R2 and plasmalemmal Transient receptor potential cation channel subfamily V member 4 (TRPV4) [256, 257].

- Local Ca²⁺ waves that propagate in larger processes, which sporadically propagate bidirectionally to and from the soma (Fig II.7C) [254, 7]. Local Ca²⁺ waves could also emerge from Ca²⁺ propagation across the intracellular network of processes via gap junction coupling (Fig. II.7D) [52]. Although $\approx$ 25% of gap junctions have been reported to connect processes from the same cell [52], intracellular network propagation has not been characterized yet.

- Global Ca²⁺ signals (Fig II.7E), which are IP₃R2-dependent and propagate within the whole astrocyte .

- Intercellular Ca²⁺ waves (Fig II.7F) that propagate throughout astrocytic networks.

Taken together, the spatiotemporal diversity of astrocyte Ca²⁺ signals concerns their spatial extent (from localized microdomains to intercellular Ca²⁺ waves), their timescales (from ms to tens of seconds).
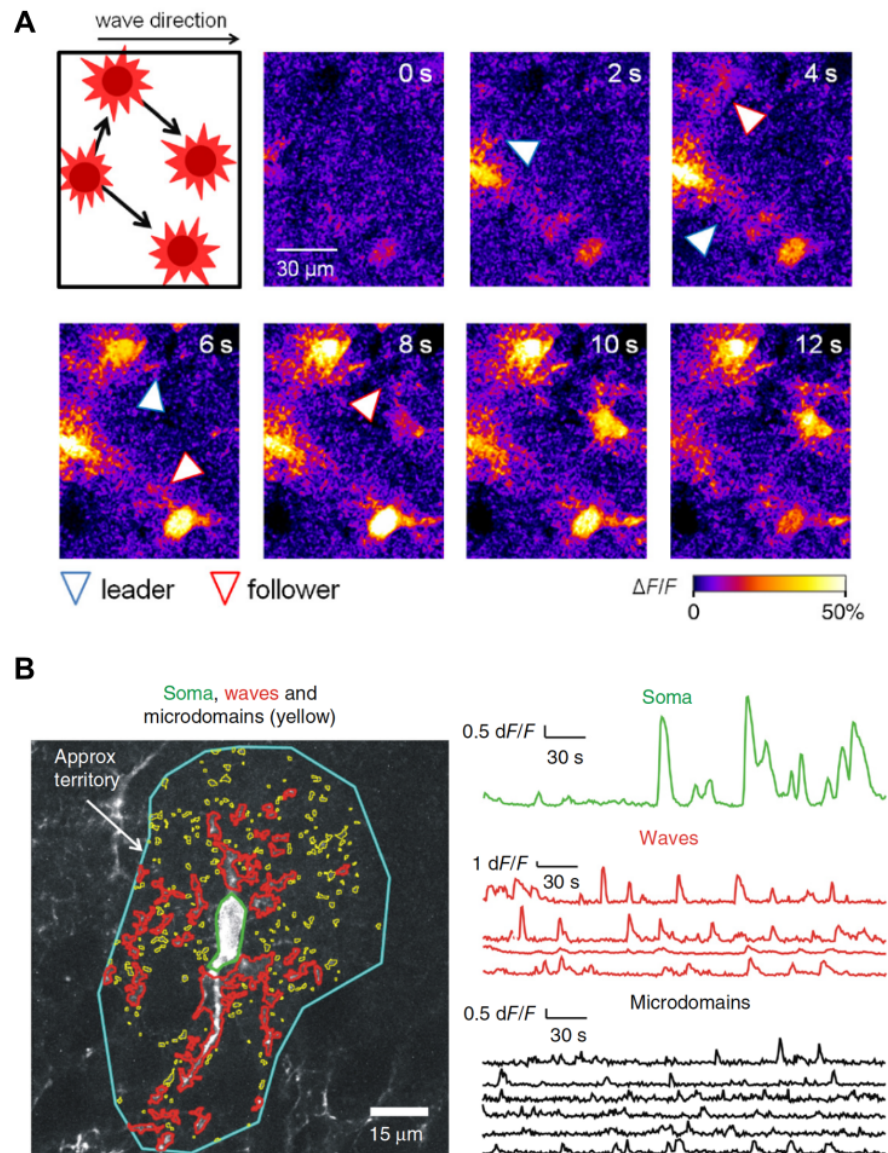
Figure II.6: Spatiotemporal diversity of Ca^{2+} signals in WT and $IP3R2^{-/-}$ astrocytes. (*A*) Two-photon imaging reveals that Ca^{2+} activity propagates from one astrocyte to another via gap junctions. The blue and red arrowheads correspond respectively to cells from which the wave comes and cells to which the wave is propagating. Taken from Kuga et al [46]. (*B*) This panel, taken from Srinivasan et al [6], illustrates the diversity of Ca^{2+} signals (amplitude, frequency, duration) in WT astrocytes depending on sub-cellular localization (soma in green, waves in red and microdomains in yellow). The blue line illustrates the approximate territory of the astrocyte.
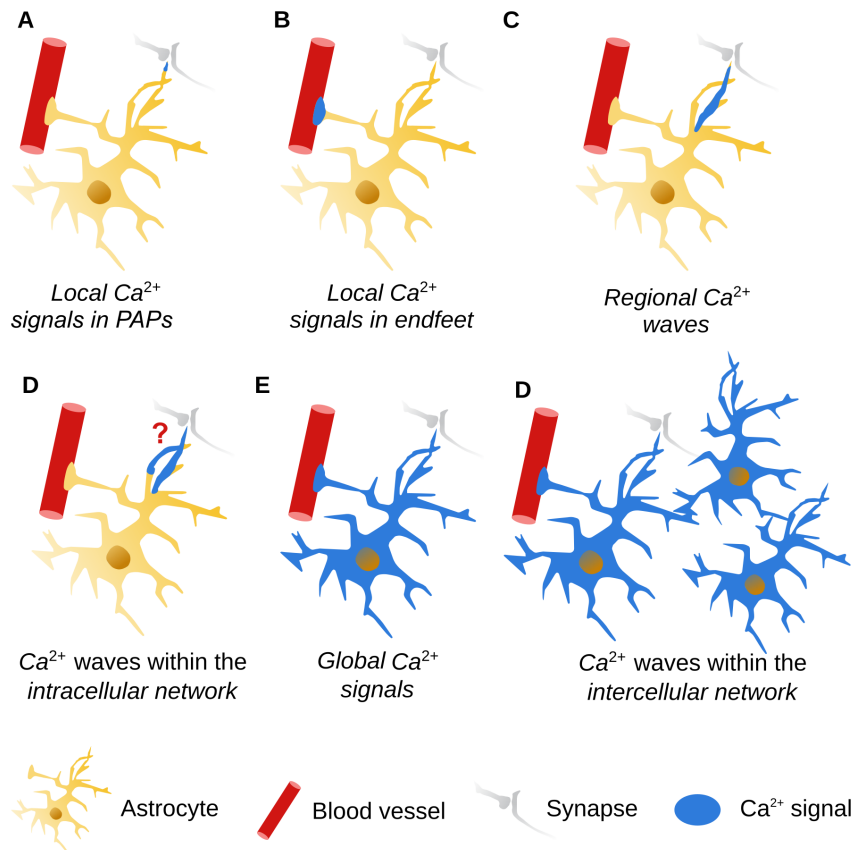
Figure II.7: Spatial diversity of Ca^{2+} signals in astrocytes. Ca^{2+} signals in astrocytes display various spatiotemporal forms. Some signals can be localized at the vicinity of synapses (A), either spontaneous or induced by neuronal activity, in endfeet (B) or they can propagate via regionalized (C), intracellular (D), global (E) or intercellular (F) Ca^{2+} waves. Note that the propagation of intra- and inter-cellular Ca^{2+} waves occurs via gap junction coupling, although intracellular propagation through gap junctions has not been reported yet.

II.2.3   Mechanisms of Ca^{2+} signals in astrocytes

In the next paragraphs, the main molecules that are involved in Ca^{2+} signaling in astrocytes are described, with a particular emphasis on the IP_3R pathway and on the kinetics of IP_3R channels.

II.2.3.1   Ca^{2+} signaling molecules in astrocytes

Spatial and temporal dynamics of Ca^{2+} signals in astrocytes emerge from different processes involving cytosolic uptake and release to either extracellular space or intracellular Ca^{2+} stores, as well as Ca^{2+} buffering and diffusion (see Fig II.1). Several channels, pumps and transporters of Ca^{2+} are expressed in astrocytes, that are presented in Fig II.8. Their contribution to Ca^{2+} signals is not clear and might depend on intracellular localization (e.g soma, endfeet or processes) or on brain region. For reviews on the different mechanisms of Ca^{2+} signals in astrocytes, see [177, 258, 259, 3]

II.2.3.2   The IP$_3$R pathway

Ca^{2+} signals in astrocytes are considered to rely mainly on the IP$_3$R Ca^{2+} channel pathway. Indeed, type-2 IP$_3$R (IP$_3$R2) Ca^{2+} channel is enriched in astrocytes [42] and knocking-out IP$_3$R2 channels abolishes all Ca^{2+} signals in astrocytic soma and about half of those in processes [6]. The molecular origin of the IP$_3$R2-independent signals in processes remains a matter of debate and could involve Ca^{2+} fluxes through the plasma membrane [6] and/or other IP$_3$R channel subtypes [260] and/or other intracellular stores [177] (see also Fig II.8). In the next paragraphs, the IP$_3$R pathway is presented as well as the structure, kinetics and molecular interactions of IP$_3$R channels. For reviews on the controversies associated with IP$_3$R-dependent signals in astrocytes, see [3, 135, 136].

Pathway description
The binding of agonists to G$_{q/11}$-GPCRs activates IP$_3$ synthesis via the cleavage of the membranous phosphatidylinositol bisphosphate (PIP2) by phospholipase C. IP$_3$ molecules then diffuse and the binding of both IP$_3$ molecules and Ca^{2+} ions to IP$_3$R channels on the membrane of the endoplasmic reticulum (ER) triggers a Ca^{2+} influx from the ER to the cytosol [261, 262]. [Ca^{2+}] gradient between the ER and the cytosol is maintained by energy-dependent sarcoplasmic/endoplasmic reticulum Ca^{2+}-ATPase (SERCA) pumps (see also Fig II.8).

Parker et al [263] have demonstrated that photolysis of caged IP$_3$ in Xenopus oocytes triggered Ca^{2+} release from the ER while simultaneous injection of Ca^{2+} inhibited Ca^{2+} release, demonstrating a bell-curve relationship between the probability of IP$_3$R opening and [Ca^{2+}]. The initiation and propagation of IP$_3$R-dependent Ca^{2+} signals then relies on Ca^{2+}-induced-Ca^{2+} release (CICR) mechanism: an increase, even small, of the local [Ca^{2+}] increases the probability of IP$_3$R opening
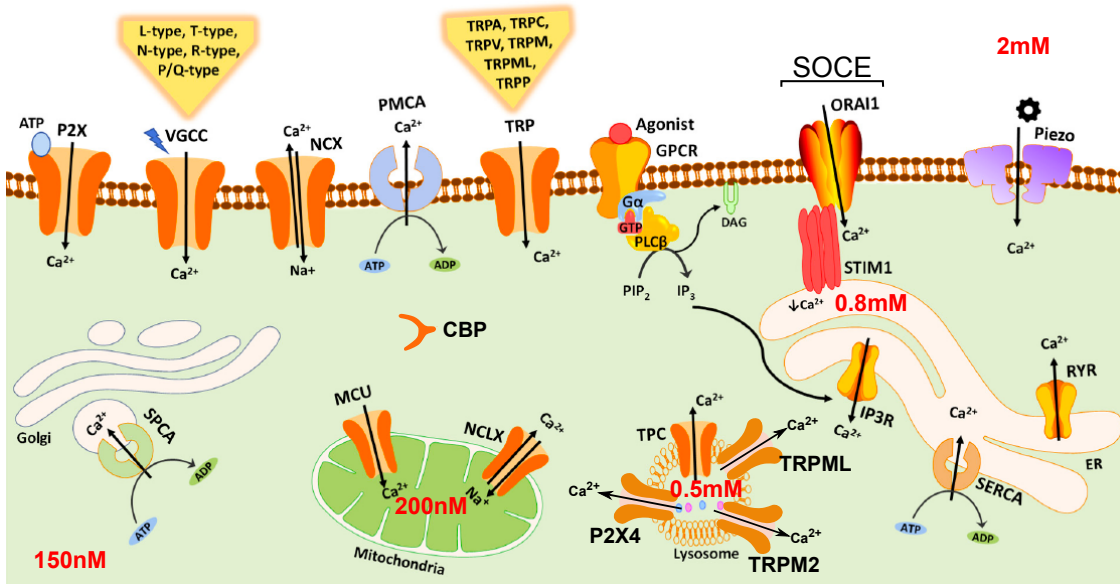
Figure II.8: Schematic representation of the main molecules involved in Ca^{2+} signaling expressed in astrocytes. This schematic presents the main channels, pumps and Ca^{2+} binding proteins (CBP) responsible for the variations of Ca^{2+} concentration in the cytosol of astrocytes. Note that specific sub-cellular distributions, such as molecular co-localizations, can increase the efficiency of those mechanisms. A widely spread mechanism is the store-operated Ca^{2+} entry (SOCE) process. During Ca^{2+} flux from the ER to the cytosol, stromal interaction molecules (STIM) translocate to the plasma membrane at ER/plasma membrane contact sites, where they interact with ORAI channels, which induces Ca^{2+} influx from the extracellular space and then into the ER. GPCR: G-protein coupled receptor, IP_3R: inositol 1,4,5-triphosphate receptor, MCU: mitochondrial uniporter complex, NCLX: mitochondrial Na^+, Ca^{2+} exchanger, NCX: Na^+, Ca^{2+} exchanger, PLC: phosopholipase C, PMCA: plasma membrane Ca^{2+}-ATPase, RyR: ryanodine receptor, SERCA: Sarcoplasmic/endoplasmic reticulum Ca^{2+} -ATPase, SPCA: secretory pathway Ca^{2+}/Mn^{2+}-ATPase, TPC: two-pore channel, TRP: transient potential channels, VGCC: voltage-gated Ca^{2+} channels. Concentrations in the main Ca^{2+} reservoirs and in the cytosol are indicated in bold red. This figure was modified from Maklad et al [148], according to Shigetomi et al [177].

(Fig II.9A), which increases local [Ca^{2+}].

Forms of Ca^{2+} signals

Ca^{2+} signals can be of diverse forms, as illustrated by Fig II.9B, being often divided in 3 different types: blips, puffs and waves. Blips correspond to signals of low amplitude and duration and are associated with the activity of single IP$_3$Rs. Blips are representative of the stochastic binding of Ca^{2+} and IP$_3$ to IP$_3$R channels. The [Ca^{2+}] at the mouth of an open IP$_3$R can reach $\approx$ 10 μM. Puffs correspond to signals of higher amplitude, which can emerge from the simultaneous opening of several IP$_3$R channels. Non-uniform spatial distributions of the channels into clusters, i.e arrangements of several channels close together can favor this process. Such spatial arrangements of IP$_3$R channels into clusters have been reported in SH-SY5Y and COS7 cells [264, 265]. Finally, Ca^{2+} waves and global events (spikes) rely on the propagation of Ca^{2+} puffs from a cluster to neighboring clusters via Ca^{2+}-induced Ca^{2+} release (CICR). The spatial organization of IP$_3$R channels thus dictates the spatial spread of CICR and the resulting variability of Ca^{2+} signals: from blips and puffs to waves and whole-cell signals.

IP$_3$R ultrastructure and kinetics

IP$_3$R is a ubiquitous 25 nm-long Ca^{2+} channel consisting in tetramers of 3 different isoforms in Vertebrates: IP$_3$R1, 2 or 3, with 60-80% homology in their amino acid sequences [269]. IP$_3$R can be composed of either homo- or hetero-tetramers [270]. IP$_3$Rs are involved in cell signaling of various cell types and are impaired in many diseases (see Seo et al [271] for a review). IP$_3$R channels have been first characterized in mice in 1989 [272] and their detailed structure with a 4.7 Å resolution has been uncovered in 2015 [273]. The detailed ultrastructure of IP$_3$Rs, including IP$_3$ binding sites, is presented in Fig II.10A. Note that Ca^{2+} binding sites as well as the precise conformational changes associated to Ca^{2+} binding are still not clear so that current models are based on experimental measurements of IP$_3$R kinetics rather than on structural data. For more details on the ultrastructure of IP$_3$Rs, see Serysheva et al [274].

Most studies on IP$_3$R kinetics are based on IP$_3$R1 isoform. A recent study has demonstrated that all of the 4 subunits must be bound to IP$_3$ to trigger IP$_3$R opening, independent of [Ca^{2+}] or [ATP] [275]. Recent patch clamp measurements from single IP$_3$R channels (Fig II.10C) have refined our understanding of IP$_3$R functioning by revealing their modal gating kinetics [276]. In the study from Ionescu et al, IP$_3$R channels can be in 3 distinct modes, characterized by different IP$_3$R opening probabilities, from low to high. Channels stay in each mode for long periods of time (tens of opening/closing sequences). [Ca^{2+}] and [IP$_3$] do not influence the
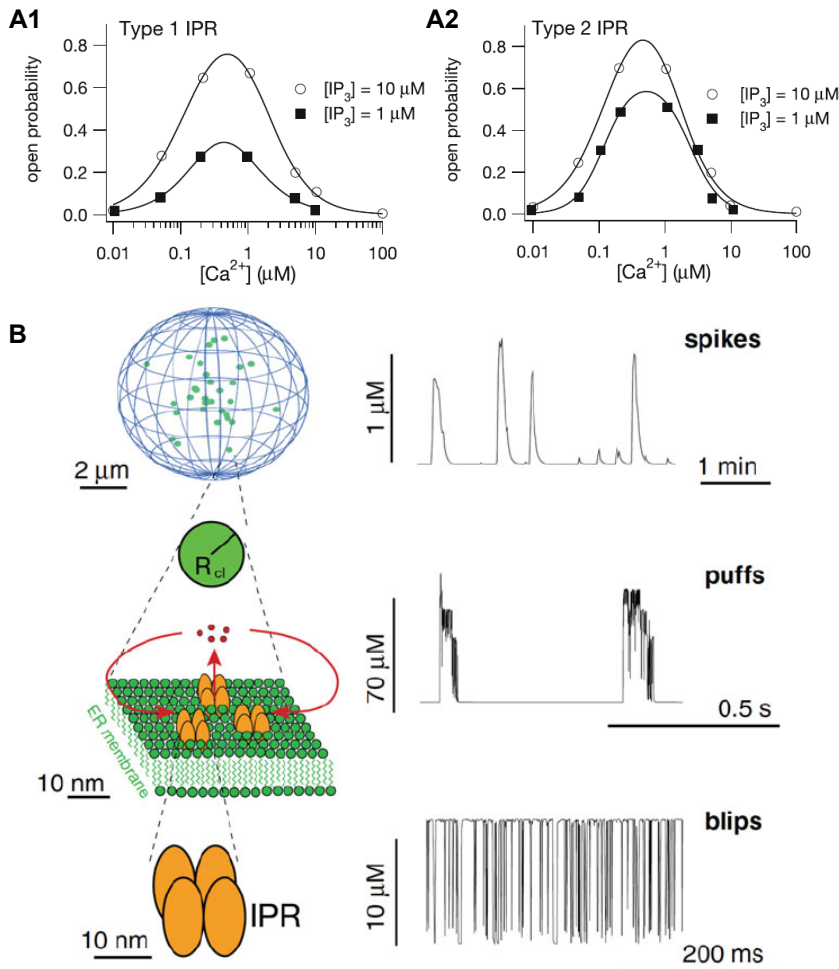
Figure II.9: IP$_3$-**dependent** Ca^{2+}-**induced** Ca^{2+} **release mechanism.** (A) Probability of IP$_3$R opening P_0 as a function of [Ca^{2+}]. Plots display the variability of P_0 depending on [IP$_3$] and on the IP$_3$R subtype: IP$_3$R1 (A1) or IP$_3$R2 (A2). Experimental data (symbols) were measured with on-nucleus patch clamp in DT40-3KO cells [266]. The smooth curves correspond to biphasic curves, commonly referred to as 'bell curves'. (B) Representation of the diversity of IP$_3$-induced Ca^{2+} signals. The right column presents the equivalent Ca^{2+} signals, here corresponding to stochastic simulations. Bottom: signals of low amplitude and duration, called "blips", associated with the activity of single IP$_3$R channels. Middle: IP$_3$R-mediated signals of higher amplitude, referred to as "puffs", which emerge from the simultaneous opening of several IP$_3$R channels. Top: at a higher spatial level, Ca^{2+} waves and global events (spikes) can be observed. They rely on the propagation of Ca^{2+} puffs from a cluster to neighboring clusters via Ca^{2+}-induced Ca^{2+} release (CICR). For more details on blips, puffs and waves, see dedicated paragraph in section II.2.3.2. Panel A was taken from Dupont et al [267] and B from Thurley et al [268].

opening probability within each mode but rather the probability of the channel to transition between modes. Those observations have changed the paradigms of IP$_3$R models (see section III.2), so that the major mechanism for regulating IP$_3$R activity in newly developed models occurs through modal switches of IP$_3$R states.

IP$_3$R channels can interact with various molecules that can modulate their kinetics and activity. Those molecules include IP$_3$ [275], Phosphatidylinositol 4,5-bisphosphate (PIP_2) [277], phosphatases and kinases [278, 279], Adenosine triphosphate (ATP) [266], cyclic adenosine monophosphate (cAMP) [278], calmodulin [280, 278, 281], Homer [282] and BCl-2 [283] (see also Fig II.10B). See dedicated reviews for more details on the modulation of IP$_3$R activity and kinetics [284, 269].
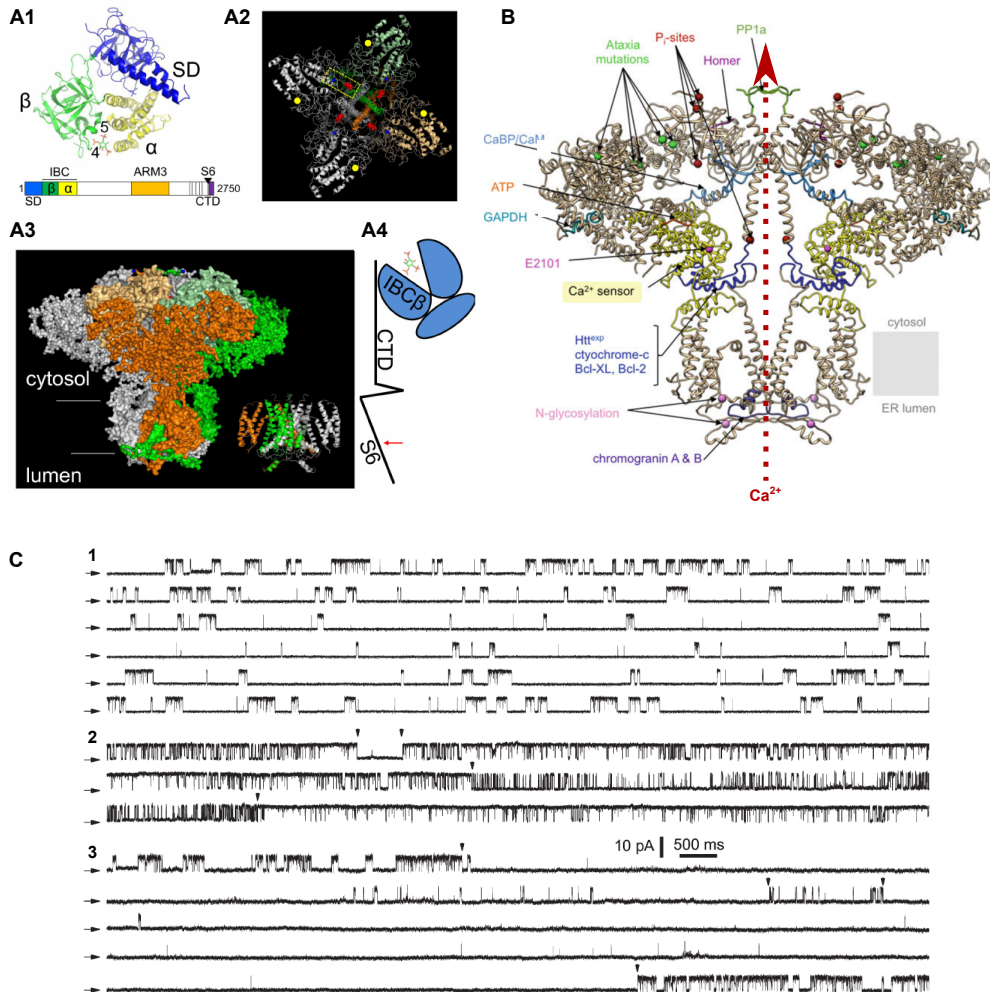
Figure II.10: Structure and kinetics of the IP₃R channel. Panel (*A*) represents the structure of the IP₃R. (*A1*) Key domains of one subunit of IP₃R. When IP₃ binds α and β domains of the IP₃-binding domain (IBC), a conformational change occurs, consisting in a movement of both α and suppressor domains (SD). (*A2*) View from the cytosol of the IP₃R, revealing 4 subunits and their contact sites. Red region corresponds to the C-termini of the 4 subunits, blue to the N-termini, yellow box represents the C- and N- termini of a single subunit and yellow circles to IP₃ binding sites. (*A3*) View across the ER membrane of IP₃R structure (2 subunits visible). (*A4*) Possible mechanism for inter-subunit interactions. When IP₃ binds the IBC, it can induce a conformational change of the C-terminal domain (CTD) from the neighboring subunit, which lines the S6 region (red arrow), which causes hydrophobic constriction that maintains the Ca²⁺ pore closed. IP₃ binding thus contributes to conformational changes in S6 region of the neighboring subunit, enabling the opening of the pore and Ca²⁺ flux from the ER to the cytosol. (*B*) Visualization of the various molecules that can interact with IP₃R channels and the corresponding binding sites. Ca²⁺ pore is schematized by a red dashed arrow. (C) Current traces from single IP₃R recordings from Ionescu et al [276], illustrating modal gating of IP₃R. In those recordings, [IP₃]= 10 μM (saturating) and [Ca²⁺] = 100 nM (1), 1 μM (2) & 89 μM (3). Horizontal arrows on the left indicate the background currents of closed channels. Arrowheads in B and C indicate transitions corresponding to modified gating behavior of the IP₃R. Panel A was taken from Taylor et al [285], B from Serysheva et al [286] and C from Ionescu et al [276].

Chapter III

Modeling astrocytic Ca^{2+} signals

A computational model corresponds to a simplification that describes relevant parameters of a system of interest (its elements, their states and their interactions), allowing for better understanding, quantification and visualization of the system. Modeling is particularly useful to conduct experiments that are time-consuming or even unfeasible experimentally and can be predictive and informative about the system's behavior. For a model to be predictive, it first needs to be validated against experimental data. Molecular reaction kinetics can be simulated with 4 main different strategies, depending on whether they account for the stochasticity arising from discrete molecules and whether they include spatial information.

In this chapter, after presenting the different methods available for simulating the kinetics of molecular reactions, the main generic (i.e not cell type-specific) and astrocytic Ca^{2+} signaling models will be presented. Only IP$_3$-mediated Ca^{2+} signaling models will be described. For information about models of other Ca^{2+} signaling pathways, the reader can refer to [287, 288, 289].

III.1   Deterministic well-mixed models

At the beginning of the XXth century, Michaelis and Menten have described enzymatic reactions with differential equations, which has been one of the first steps towards using modeling as a complementary approach to experimental studies. Modeling chemical reactions with ordinary differential equations (ODEs) has been historically the first modeling approach for biological systems and has contributed to a better understanding of molecular pathways, including Ca^{2+} signaling. Those models are both deterministic, i.e the average behavior of populations of molecules is monitored, and well-mixed, i.e space is considered homogeneous and molecules are assumed to be equally distributed within the system so that spatial effects such as

geometry and diffusion are ignored.

In this section, the methods and computational approaches for deterministic well-mixed models will be introduced before presenting examples of their implementation for simulating Ca^{2+} dynamics.

III.1.1   Methods and computational approaches

Biological processes often display noise. Extrinsic noise corresponds to fluctuations in cellular environment, including temperature, pH, local concentrations as well as cell-to-cell variability [290]. Intrinsic noise (=molecular noise) [291] is expected to vary as $\frac{1}{\sqrt{X}}$ where X is the number of molecules in the system [292] and thus arises from low number of molecules but also from the intrinsic stochastic nature of biochemical reactions [292]. If X is high enough, noise can be averaged and deterministic approximation is valid. If the number of molecules decreases, stochasticity must be taken into account, which is the focus of section III.2.

At any time point, the system is described by a vector containing the concentration of each reactant. The velocity of each reaction assumes mass action kinetics (see Eq III.1) or is based on an enzymatic kinetic law like Michaelis-Menten or Hill kinetics [293] and is specified using a rate equation. Mathematical description of those rates is done through the use of ordinary differential equations (ODEs), called reaction-rate equations, that can be solved analytically or numerically with an ODE solver [294] (see Eq III.4 for examples of rate equations describing IP$_3$R-dependent Ca^{2+} dynamics). ODEs coupled with initial concentrations of all molecular species are enough to predict their concentrations at any time point. Numerical methods for solving ODEs are presented in e.g Butcher et al [294].

A simple example to illustrate the principle of ODEs is to consider the bimolecular reaction in which substrates S_1 and S_2 react to form S_3 and S_4: $S_1 + S_2 \underset{k_b}{\overset{k_f}{\rightleftarrows}} S_3 + S_4$, where k_f is the forward binding rate constant and k_b the backward unbinding rate constant. Then the variation of the concentration of the species S_3 with time can be described by the following deterministic formulation:

$$\frac{d[S_3]}{dt} = k_f[S_1][S_2] - k_b[S_3][S_4] \tag{III.1}$$

Systems of differential equations are often studied two variables at a time with phase plane diagrams, which can help predict the dynamics of the system under study. The nullclines (curves where each derivative is zero) and the values of the
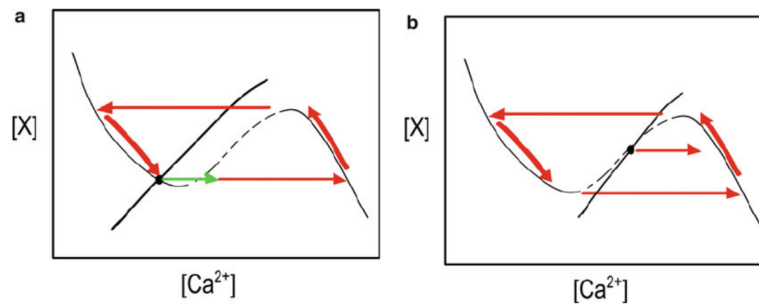
Figure III.1: Phase plane diagrams of excitable and oscillatory systems. (a) An excitable system is characterized by an n-shaped nullcline crossed by a second "straight" nullcline. The intersection of those nullclines forms a steady state (black circle). Enough perturbation from steady state (green arrow) crosses the unstable portion of the n-nullcline and values of $[Ca^{2+}]$ then follow the red arrow, generating a transient rise in $[Ca^{2+}]$. The dashed and solid portions correspond to the unstable and stable portions, respectively. For more details, see Girard et al [297]. (b) When the "straight" nullcline is shifted, the crossing of the nullclines can lead to an unstable steady state (black circle). Then, perturbations off the steady state, even small, lead to oscillations of $[Ca^{2+}]$. The red trajectory will be followed, without returning to the steady state. This figure was taken from Jafri et al [298].

derivatives at other points (vector fields) define the trajectories of possible solutions of the set of ODEs. A steady state is a point where the derivatives all equal zero. Trajectories go away from the unstable portions, towards stable portions. Fig III.1 presents 2 examples of phase plane diagrams of the Ca^{2+}X-plane, one excitable (Fig III.1A) and one oscillatory (Fig III.1B). In models of IP$_3$-induced Ca^{2+} waves and oscillations, changing $[IP_3]$ can shift the "straight nullcline" from a condition similar to Fig III.1A to Fig III.1B, thus triggering oscillations that persist without any perturbation. Those systems are referred to as Hopf bifurcation systems (see Marsden et al [295] for a review). For a detailed review on deterministic modeling principles, see Dupont et al [296].

III.1.2   Deterministic well-mixed models of Ca^{2+} signals

Ca^{2+} oscillations have been first observed in excitable cells such as cardiac myocytes and neurons before being characterized in a variety of other non-excitable cell types such as e.g oocytes, hepatocytes and astrocytes [299]. Their frequency varies from $\approx 10^{-3}$ to 1 Hz. In the next paragraphs, the most influential historical models of IP$_3$Rs (Fig III.2), in which $[IP_3]$ is constant, are presented. In those models, Ca^{2+} oscillations emerge from Hopf bifurcations for a given range of $[IP_3]$ (Fig III.2C1,D1).

One of the first models of Ca^{2+} oscillations has been developed by Meyer & Stryer [305]. They hypothesized that oscillations resulted from Ca^{2+}-dependent IP_3 production by PLCδ and successfully reproduced Ca^{2+} oscillations, coupled with IP_3 oscillations, which have been proven not to exist in several cell types.

The model from Goldbeter, Dupont & Berridge consisted in two Ca^{2+} cellular pools: one that was IP_3-sensitive and one that was Ca^{2+}-sensitive (Fig III.2A1). Ca^{2+} released from the IP_3-sensitive pool activates CICR from the Ca^{2+}-sensitive pool. As experimental work suggested that IP_3-sensitive and Ca^{2+}-sensitive pools consisted in a unique pool, the ER, Dupont et al [301] have developed a one-pool version of this model, presented in Fig III.2A2,A3. This model has been further refined in subsequent studies [306, 307]. Those models have been very influential in the early 1990s but binding models, that take into account conformational states of IP_3R channels, have been preferred in future IP_3R models. The 2 most influential historical binding models of IP_3R are the De Young & Keizer model [8] and the Li-Rinzel model [302].

The bell-shaped relationship of the open probability of IP_3R (P_0) with $[Ca^{2+}]$ [263, 308] (Fig II.9) can be interpreted as a consequence of a slower inactivation of IP_3R by Ca^{2+} than its activation. This can be modeled simply by the existence of activating and inactivating Ca^{2+} binding sites, the latter displaying a smaller affinity for Ca^{2+}. The first binding model of IP_3R that took into account those different kinetics of IP_3R was the model by De Young & Keizer (DYK) [8]. The parameter values of the model were fitted on IP_3R open probability data [308] and IP_3 binding data [309]. Because 4 different conductances were observed for a single IP_3R and that the most commonly open one was 3rd highest conductance [310], DYK assumed that IP_3R opened when 3 subunits were open.

In their model, each IP_3R subunit contains 3 binding sites: two activating sites, for Ca^{2+} and IP_3, and one inactivating site for Ca^{2+}. ijk is the state of an IP_3R subunit, where i, j & k correspond respectively to Ca^{2+}-activating, IP_3 and Ca^{2+}-inactivating sites. Each site can be in two states: 1 = bound or 0 = unbound, so that each subunit has 2^3 possible states which are depicted, along with their transition rates, in Fig III.2B2. For example, 110 represents an IP_3R subunit with Ca^{2+}-activating and IP_3 sites bound and Ca^{2+}-inhibiting site unbound. Open probability P_O of a single IP_3R is thus $P_O = x_{110}^3$, where x_{110} corresponds to the fraction of IP_3R subunits in state 110. The model was then simplified by considering that IP_3 binding is fast compared to the others, thus leaving 4 equations to describe the system: one for Ca^{2+} and 2^2-1 for IP_3R subunits (as $\sum_{ijk} x_{ijk} = 1$), with x_{ijk} the fraction of subunits in state ijk). Ca^{2+} dynamics in the DYK model is characterized by 2 Hopf bifurcations (Fig III.2C1). If $[IP_3]$ (fixed in the DYK model) is chosen
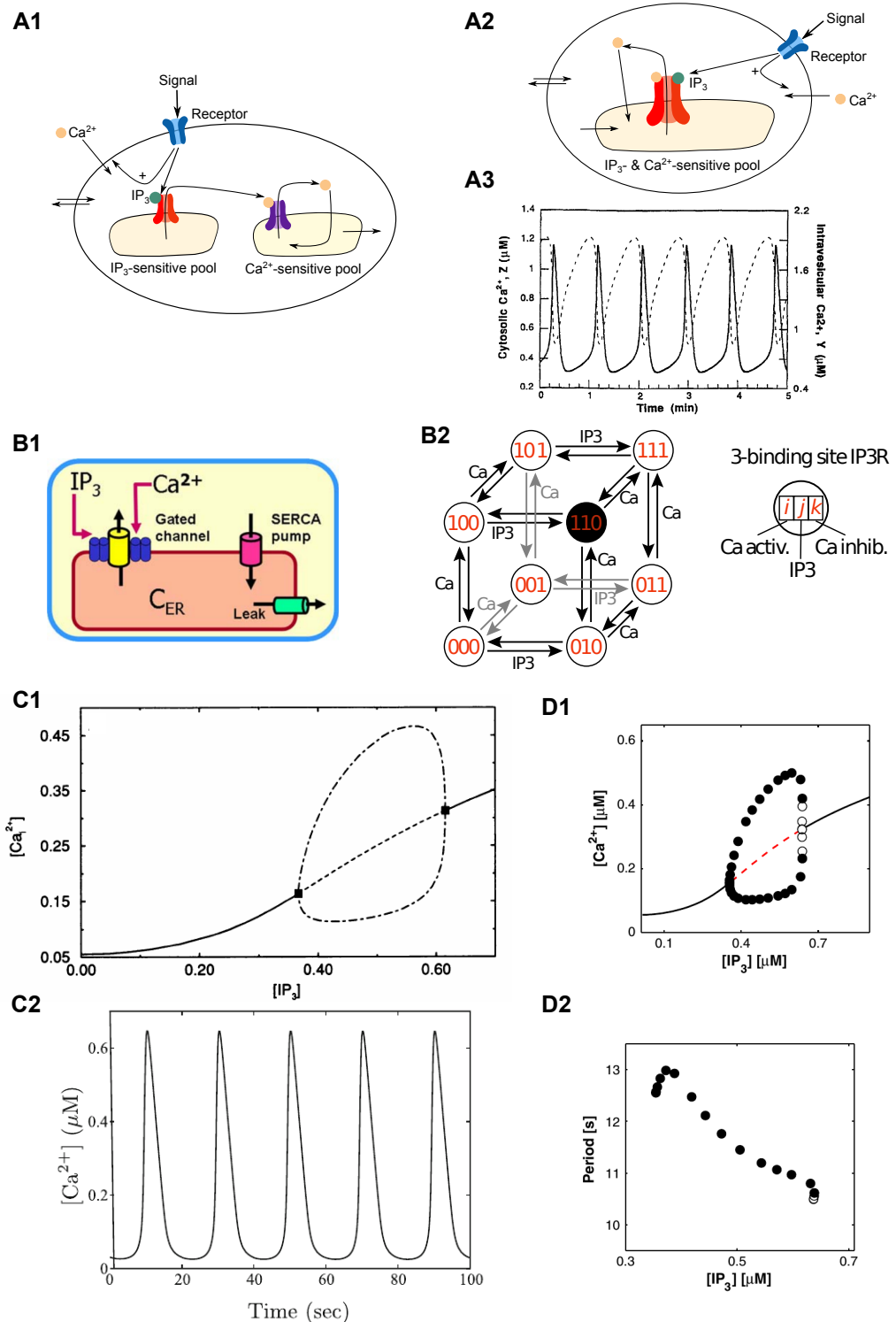
Figure III.2: Historical, deterministic well-mixed, models of IP3R channels. This figure presents the historical models of Ca^{2+} dynamics from Golbeter-Dupont-Berridge [300, 301] (A), De Young-Keizer [8] (B, C) and Li-Rinzel [302] (B, D). (A1) Schematic representation of the two-pools model from Goldbeter-Dupont-Berridge. (A2) Schematic representation of the one-pool model from Dupont et al [301]. (*A3*) Typical oscillations from the one-pool model based on CICR. (*A3*) Ca^{2+} oscillations from the one-pool model are presented for I=0.53 μM. (*B1*) Schematic representation of the kinetic scheme from the De Young-Keizer (DYK) and Li-Rinzel models.

Figure III.2: Historical, deterministic well-mixed, models of IP3R channels (continued).
(*B2*) Schematic representation of the 8 possible states of an IP$_3$R subunit in the DYK and Li-Rinzel models. The corresponding bifurcation diagram and examples of oscillations from DYK model are presented respectively in panels *C1* and *C2*. (*D1*) Bifurcation diagram of the Li-Rinzel model. Ca²⁺ oscillations arise from Hopf bifurcation at [IP$_3$]=0.355 μM and stop at supercritical Hopf bifurcation at [IP$_3$]=0.637 μM. Between those bifurcation points, the amplitude of the oscillations increases with [IP$_3$] while their period remains almost constant (*D2*). Stable and unstable oscillations are represented with filled and open circles respectively, at their maximum and minimum values. Panel A3 was taken from Dupont et al [301], *B1, D1 & D2* from De Pitta et al [303], C1 from DYK [8] and C2 from Timofeeva et al [304].

between those 2 points, then cellular Ca²⁺ oscillates (Fig III.2C2).

Several studies have developed alternative versions of the DYK model, that modeled sequential binding of Ca²⁺ and IP$_3$ [311], conformational transitions [312, 313] or implemented saturated effects at high [Ca²⁺] [314, 315]. See Shuai et al for a review [316]. The DYK model is still influential, even though it is not in accordance with recent data such as the necessity of 4 IP$_3$ to be bound for the channel to open or the modal switching of the receptors (see Fig III.4).

Li & Rinzel have proposed a simplified version of the DYK model by taking into account that binding of activating IP3 and Ca²⁺ is much faster than inactivating Ca²⁺ [302]. They simplified those 2 dynamics in their model so that it consists in 2 equations, describing the evolution of [Ca²⁺] (C) and of the probability h that IP$_3$R is unbound to inactivating Ca²⁺. The open probability of IP$_3$R can be expressed as follows:

$$P_O = x_{110}^3 = (m_\infty h)^3 \tag{III.2}$$

where $h = x_{000} + x_{010} + x_{100} + x_{110}$. m_∞ and $\frac{dh}{dt}$ can be expressed as follows:

$$m_\infty = \frac{[I]}{[I + d_1]} \frac{C}{C + d_5}$$
$$\frac{dh}{dt} = \frac{h_\infty - h}{\tau_h} \tag{III.3}$$

where C, I correspond to [Ca²⁺] and [IP$_3$], respectively, and $d_i = \frac{b_i}{a_i}$ are derived from DYK model.

Similarly to DYK model, [IP$_3$] is not a variable but a parameter of the model. Ca²⁺ oscillations occur only for intermediate values of [IP$_3$] (I) ($\approx 0.3\mu M < I < 0.65\mu M$), associated with Hopf bifurcations (Fig III.2D1,D2). Increased [IP$_3$] is associated with increased amplitudes of Ca²⁺ oscillations. Despite its simplifications,

this model displays a similar behavior than that of the DYK model, notably the bell-shaped relationship between P_O and [Ca^{2+}], and has thus been widely used in the field.

The Li-Rinzel model has been adapted to account for variations of the total $[Ca^{2+}] = [Ca^{2+}]_{\text{cyt}} + [Ca^{2+}]_{\text{ER}}$ [317, 318, 319].

For detailed reviews on deterministic well-mixed models of Ca^{2+} oscillations, see [320, 321].

III.1.3   Deterministic well-mixed models of astrocytic Ca^{2+} signals

Diverse models have used deterministic well-mixed approaches to model Ca^{2+} signals in astrocytes, being in their soma [322, 323, 324], whole-cell intracellular signals[325], their encoding [303], inter-astrocyte signals [326, 327, 328], astrocyte-neuron signals [329, 330] or astrocyte-blood vessels signals [331].

Ca^{2+} oscillations in astrocytes can occur in response to extracellular signals released from neighboring neurons that trigger intracellular IP$_3$ signals. Therefore, models of astrocytic excitability have adapted the historical IP$_3$R models in order to take into account the variations of [IP$_3$] associated with GPCR activation. The typical kinetic scheme of those models is presented in Fig III.3A and its mathematical formulation is as follows (parameters are defined in Fig III.3):

$$
\begin{aligned}
\frac{d[Ca^{2+}]_{\text{cyt}}}{dt} &= J_{\text{IP3R}} + J_{\text{leak}} - J_{\text{SERCA}} + J_{\text{in}} - J_{\text{out}} \\
\frac{d[Ca^{2+}]_{\text{ER}}}{dt} &= \alpha(J_{\text{SERCA}} - J_{\text{leak}} - J_{\text{IP3R}}) \\
\frac{d[IP3]}{dt} &= J_{\text{PLC}} - k_{\text{D}}[IP3]
\end{aligned}
\tag{III.4}
$$

In most models, J_{IP3R} corresponds to the Li-Rinzel model of IP$_3$R [322, 327, 331, 332, 333]. For example, the model from De Pitta et al [333] displays the same equations for [Ca^{2+}] (C) and IP$_3$R closure (h) than the Li-Rinzel model but also contains a third variable corresponding to variations of [IP$_3$]: I, which varies depending on regulatory pathways of IP$_3$ production and degradation. This three-variable model is thus referred to as the ChI model. Typical evolution of C, h and I with time during a Ca^{2+} wave is presented in Fig III.3C. The ChI model has been extended into the G-ChI model, to account for GPCR-dependent IP$_3$ production. Using bifurcation analysis, they predicted that accounting for variations of [IP$_3$] in their model could trigger persistent oscillations, in which [Ca^{2+}] dynamics was encoded in frequency

or frequency & amplitude but not in amplitude alone.

Deterministic models of IP$_3$R channels mainly differ in their mechanism of Ca^{2+} oscillations, which can be either IP$_3$-independent [8, 302, 336, 312], coupled with passive [306] and/or with active IP$_3$ oscillations [305, 333, 337, 338]. Only representative models of IP$_3$R have been presented here. For more information, see dedicated reviews [339, 316, 340, 341, 342].

III.2   Stochastic well-mixed models

As presented in section III.1, deterministic approaches fail to describe molecular interactions at low concentrations [343, 344] so that the discovery of highly localized Ca^{2+} signals occurring in femtoliter volumes encouraged modelers to go from deterministic to stochastic descriptions of Ca^{2+} signals. Stochastic approaches have been essential to grasp intracellular dynamics, such as the switching in bistable systems like the gallactose signalling pathway [345].

In this section, the common methods to model well-mixed stochastic processes will be introduced before presenting their implementation in models of Ca^{2+} dynamics.

III.2.1   Methods and computational approaches

Stochastic formulation of biochemical interactions consists in considering each reaction as a probabilistic event. The state of a given system of N molecular species S_i, with $i \in [1, N]$ is described by a time-dependent state vector $x(t) = [x_1(t), ..., x_N(t)]$, which contains the copy number $x_i(t)$ of each molecular species S_i at time t. $\alpha_j(x)dt$ is the likelihood of reaction j to occur during the time step dt, called propensity. This probability depends on the number of distinct reactants combinations for reaction $j \in [1, R]$ and on the probability that a given combination of reactants interacts. Table III.1 illustrates examples of propensity functions for different types of reactions. v_j corresponds to the jth column of the stoichiometry matrix v, and is the state change vector for reaction R_j, which specifies changes of the system when R_j occurs. Then the entire system of R reactions can be described with a differential equation, the chemical master equation (CME) [346, 347], that describes the temporal evolution of the probability density P(x,t), which results from transitions from
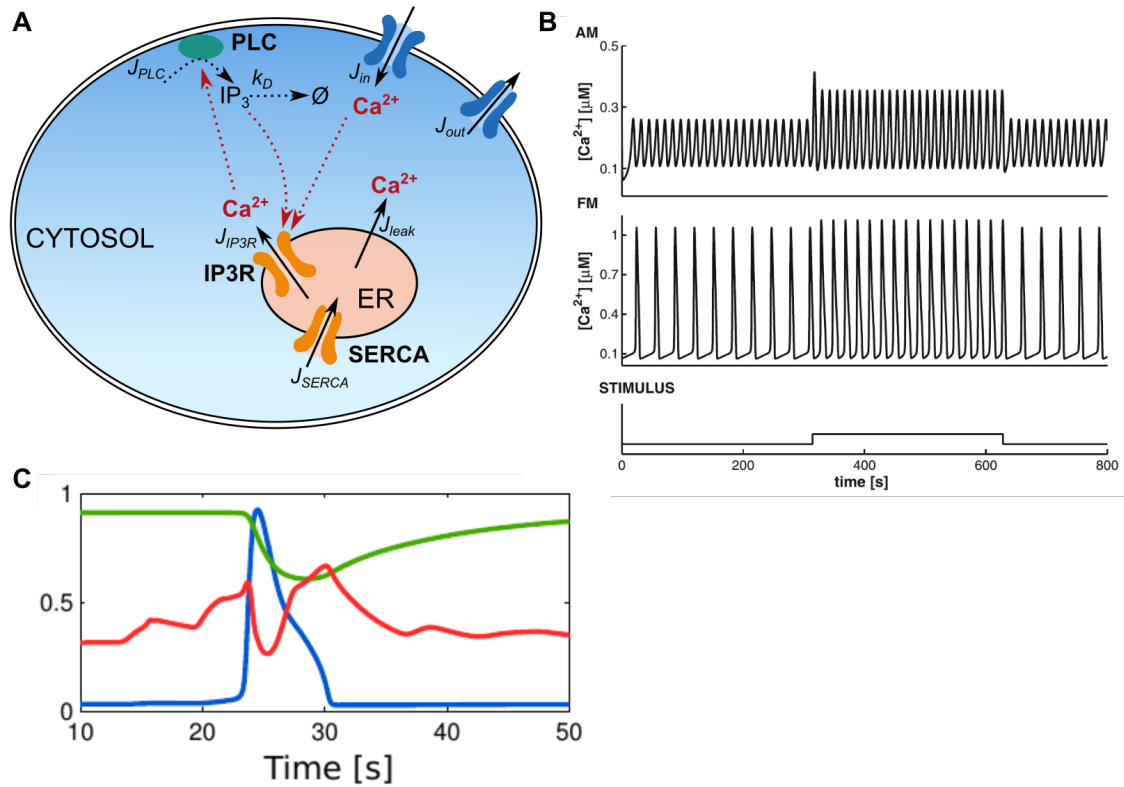
Figure III.3: Typical kinetic scheme of astrocytic Ca^{2+} **oscillations and the associated** Ca^{2+} **dynamics.** (*A*) Schematic representation of the typical kinetic scheme of astrocytic Ca^{2+} models. Plain black arrows correspond to Ca^{2+} fluxes. Dotted black arrows represent IP_3 formation, via Ca^{2+}-dependent PLC activity, and degradation. Red dotted arrows represent the activation of certain molecules by IP_3 and/or Ca^{2+} such as IP_3R and PLC. The common ODE formulation for this system includes three equations that describe Ca^{2+} concentration in the cytosol, $[Ca^{2+}]_{cyt}$, Ca^{2+} concentration in the ER, $[Ca^{2+}]_{ER}$, and IP_3 concentration, $[IP_3]$ (Eq III.4). J_{PLC} corresponds to the formation of IP_3 by PLC, J_{in}, J_{IP3R}, J_{leak} correspond respectively to Ca^{2+} influx through plasma membrane channels, IP_3Rs or via ER leak. J_{out} and J_{SERCA} correspond respectively to Ca^{2+} outflux through plasma membrane pumps or SERCA pumps. k_D corresponds to IP_3 degradation rate constant. $\alpha = \frac{V}{V_{ER}}$, which reflects the different changes of concentration of Ca^{2+} in the cytosol compared to the ER due to their different volumes V and V_{ER}, respectively (see Dupont et al [296]). Note that the pathway presented here is simplified, please refer to De Pitta et al [334] for further details. (*B*) Variations of stimulus intensity (bottom panel) are encoded by modifications of the amplitude of Ca^{2+} oscillations with the initial parameter values of the Li-Rinzel model (top panel), while for $d_5 = 0.2\mu M$, they are rather frequency-encoded (middle panel). (*C*) Typical variations with time of $[Ca^{2+}]$ C (blue curve), $[IP_3]$ I (red curve) and fraction of IP_3R that are unbound to inactivating Ca^{2+} h (green curve). When $[IP_3]$ increases above a given threshold, it triggers the opening of IP_3R and CICR mechanism (Fig II.9). When $[Ca^{2+}]$ increases, both PLCδ and IP_3-3K are activated and IP_3-3K is faster so that the Ca^{2+} spike is associated with a decreasing $[IP_3]$, participating to the ending of CICR. At intermediate $[Ca^{2+}]$, IP_3-3K is no longer active and the activity of PLCδ leads to a transient increase of $[IP_3]$, associated with its propagation through gap junctions. Panel B was taken from De Pitta et al [303], panel C was taken from Lallouette [335].

state x-v_j to x (via reaction R_j) minus the transitions out of state x:

$$\frac{\partial P(x,t)}{\partial t} = \sum_{j=1}^{R}[\alpha_j(x-v_j)P(x-v_j,t) - \alpha_j(x)P(x,t)] \qquad \text{(III.5)}$$

Most of the time, the CME contains too many equations to be solved analytically and can be computationally expensive when increasing the number of molecules or when there are highly non-linear molecular pathways. In order to solve the CME, kinetic Monte Carlo algorithms have been developed [348, 349]. In those algorithms, random numbers are generated with pseudo-random number generators such as the Mersenne Twister algorithm [350]. Because of the stochasticity of the system, each simulation, corresponding to an individual realization of the possible evolution of states of the system, is different. Thus, probability distributions of variables must be calculated by running simulations with different seeds. For more details, see Wilkinson et al [351].

Table III.1: Propensity functions for different reaction types. $x_i(t)$ corresponds to the number of molecules of species S_i at time t. $c_j dt$ is the probability that a particular reactant combination of R_j will actually react during the time step dt. The constant c_j thus depends on the molecular interaction of interest and can be determined experimentally. It is actually proportional to the value of reaction rate from mass action laws (presented in section III.1). This table was reproduced from Singh et al [352].

reaction R_j	Propensity
$\emptyset \rightarrow$ reaction products	$c_j dt$
$S_i \rightarrow$ reaction products	$c_j x_i dt$
$S_i + S_k (i \neq k) \rightarrow$ reaction products	$c_j x_i x_k dt$

Below are presented the most common stochastic well-mixed approaches, divided into continuous and discrete approaches.

III.2.1.1   Continuous stochastic approaches

Continuous stochastic approaches correspond to differential equations which contain an extra term that accounts for (Gaussian) noise [353, 354], referred to as stochastic ordinary differential equations (SDEs).

III.2.1.2   Discrete stochastic approaches

Discrete stochastic approaches consider the number of reactants as opposed to the use of their concentrations in continuous methods. Several discrete algorithms have been developed to solve the CME:

- **Gillespie's SSA algorithm and variants**
  One of the most commonly used stochastic well-mixed approaches is Gillespie's exact Stochastic Simulation Algorithm (SSA) [346, 355], in which time of next reaction as well as the nature of the reaction are chosen randomly, based on the probabilities of the reactions (propensity functions). This method is statistically exact, i.e it samples the exact trajectories from the distribution predicted by the CME. The probability density that next reaction is R_j and occurs between (t+τ,t+τ+dt) can be expressed as:

$$P(\tau, j) = \alpha_j e^{(-\alpha_0 \tau)} \tag{III.6}$$

  where $\alpha_0 = \sum_{j=1}^{R} \alpha_j$ and α_j is the propensity of reaction R_j (j $\in$ [1, R]). For more details on its implementation, see section IV.1 and e.g [355, 356, 351, 346, 357]. Several variants of the SSA algorithm have been developed [358, 359, 360, 361].

- **The τ-leap method**
  The τ-leap method is an approximation of the SSA method that uses larger time steps τ whereas the SSA method proceeds one reaction at a time. The τ-leap method calculates the total number and nature of reactions that happen during a time step τ, deduced from either Poisson [362] or binomial [363] distributions. This method is thus both faster and less accurate than the SSA. In particular, it can lead to negative numbers of reactants. If for example a Poisson distribution defines the number of realizations of reaction R_i during τ, it can be expressed as follows:

$$x_i(t + \tau) = x_i(t) + \sum_{j=1}^{R} v_{ij} \xi_j(\alpha_j) \tag{III.7}$$

  where ξ_j is the expected number of times for the jth reaction to occur during [t, t + τ) and corresponds to a Poissonian random variable of parameter α_j, v_{ij} describes the change in the copy number of species S_i caused by reaction R_j (j $\in$ [1,R]), α_j is the propensity of reaction R_j, x_i(t) corresponds to the copy number of species S_i at time t.

For more details on stochastic modeling and methods, see [351, 292, 355, 364, 356, 365].

III.2.2   Stochastic well-mixed models of Ca^{2+} signals

Recent studies have suggested that Ca^{2+} signals exhibit stochastic behavior, independent from the level of IP_3 stimulation and that it does not obey deterministic dynamics [366, 367, 368, 369, 370, 371]. The observable global Ca^{2+} signals such as microdomain signals, puffs, oscillations or waves are believed to be emergent properties of this stochastic process. Several models have investigated those dynamics and their modulation by stochastic channel activity. Next paragraphs will present the main representative stochastic well-mixed models of Ca^{2+} dynamics. For a review on possible physiological mechanisms responsible for the stochasticity of Ca^{2+} signals, see Dupont et al [372].

The first type of stochastic IP_3R models that have been developed corresponded to Markov processes or Langevin approaches based on the historical IP_3R models presented in section III.1 [373, 374, 375, 376]. The use of new techniques has enabled the recording of single IP_3R channels. Whereas the first models of IP_3R channels were based on mean behavior over time and over populations of IP_3R channels, models based on those single channels recordings are based on the evolution of the conductance of single channels over time. Those models take into account the conformational changes that IP_3Rs encounter after being bound to activating Ca^{2+} and IP_3 and before being actually open [377, 378, 313, 316].

The development of techniques for measuring time-dependent single channel currents [276, 379] has allowed for the development of a new class of stochastic IP_3R models: modal models [380, 381, 382]. Experimental data have indeed revealed the existence of different modes of activity of IP_3R channels, each characterized by a specific open probability, and mode switching phenomena. The number of modes depends on the study, mostly 2 [380, 381] or 3 [382]. Those models are implemented as hierarchical Markov models, in which each mode corresponds to a Markov model of specific topology. Gating models still take into account state transitions within IP_3R channels but also consider that they can be in different conformations, that correspond to different open probabilities called modes. The two main modal gating models of IP_3R from Ullah et al [382] and Siekmann et al [381] are presented in Fig III.4. Because few mode switches occur in data collected, the first modal models of IP_3R modeled separately the different modes [380], which described accurately the dynamics in each mode but failed to represent the dynamics of mode switching. To go further, Siekmann et al [381] have developed a continuous-time Markov chain model that included different modes of IP_3R activity and switching between those modes. This study has resulted in 2 different modal models for type I and type II IP_3R channels and their regulation by IP_3, ATP and Ca^{2+}. They have isolated 2 different modes referred to as 2-states park (inactive) and 4-states drive

(highly active) modes. State transitions within each mode are ligand-independent while mode switching rates are complex non-linear functions of $[Ca^{2+}]$ and $[IP_3]$, reflecting transitions that cannot be modeled by simple binding of IP_3 or Ca^{2+} and might involve multiple additional states, that are not formulated in those models. Time spent in park mode t_{park} and in drive mode t_{drive} can be expressed as follows:

$$t_{park} = (1 + \frac{q_{45}}{q_{54}})\frac{1}{q_{42}}$$
$$t_{drive} = (1 + \frac{q_{21}}{q_{12}} + \frac{q_{23}}{q_{32}} + \frac{q_{26}}{q_{62}})\frac{1}{q_{24}} \quad \text{(III.8)}$$

so that t_{park} can be approximated by $\frac{1}{q_{42}}$ since the ratio $\frac{q_{45}}{q_{54}}$ is low for IP_3R1 and 2 and where q_{ij} represents the transition rate from state i to state j.

Modal models of IP_3R are still limited by current knowledge on the structure of IP_3R, as, for example, the precise Ca^{2+} binding sites and their physiological roles are still poorly understood [274]. A challenge in the field is to be able to build a model of IP_3R dynamics that combines our knowledge of macroscopic Ca^{2+} dynamics and the microscopic behavior of single IP_3Rs that is now available.

Scaling up to models of global Ca^{2+} events, stochastic models have revealed that puffs are strongly stochastic, noise-induced events [383, 384, 385] (see review [386]). Gillespie's SSA triggered Ca^{2+} oscillations associated to stochasticity while the deterministic implementation of the same model yield to steady state [387, 388, 366, 389, 390, 391]. Those observations highlight the different behaviors of deterministic versus stochastic simulators and that stochastic modeling might reveal subtle emergent behaviors of Ca^{2+} dynamics at subcellular locations.
For a recent review on stochastic Ca^{2+} signaling models, see [392].

III.2.3 Stochastic well-mixed models of astrocytic Ca^{2+} signals

Recently, some astrocyte models have started to incorporate noise, especially for modelling intracellular Ca^{2+} dynamics. Riera et al [332] have developed a stochastic model of Ca^{2+} dynamics with stochastic differential equations. By changing the amount of Ca^{2+} influx through passive leakage, they have demonstrated potential mechanisms for the elevated resting $[Ca^{2+}]$ of astrocyte networks in Alzheimer's disease (AD) mouse models reported by Kuchibotla et al [230]. A recent stochastic model has also been developed to study astrocyte-neuron communication [393], by adding an activity-dependent noise term accounting for stochastic neurotransmitter
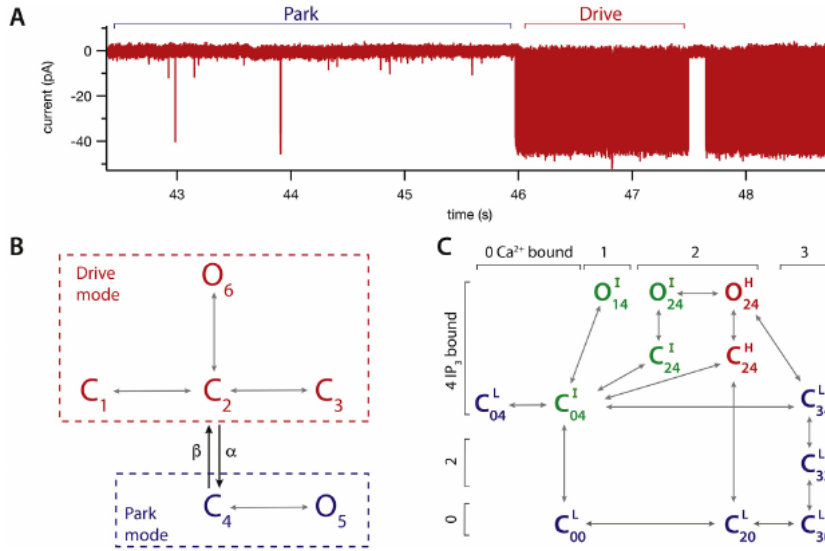
Figure III.4: Example of a modal gating model of IP$_3$R: the Park & Drive model. (*A*) Measurements of single IP$_3$R2 channel currents from Siekmann et al [381], with [Ca^{2+}]=50nM, [IP$_3$]=10 μM and [ATP]=50nM. The recorded IP$_3$R presented here displays for few seconds an activity characterized by a low open probability P_O, referred to as 'Park' mode, before switching to a mode characterized by a higher P_O, the 'Drive' mode. Panel *B* presents the modal model developed by Siekmann et al [381] based on the experimental measurements from panel A. Each mode is described by a Markov model, which different states do not correspond to any physiological observation. Only the inter-mode rates (α & β) depend on [IP$_3$] and [Ca^{2+}]. Subscripts indicate different states. Panel *C* presents the modal model of Ullah et al [382], that accounts for 3 different modes of IP$_3$R activity: low (L), intermediate (I) and high (H) P_O, represented in blue, green and red, respectively. The numbers in the subscripts ij correspond to the number i of Ca^{2+} and j of IP$_3$ bound to the IP$_3$R in the state C_{ij} (or O_{ij} if the receptor is open). Superscripts L, I and H correspond to low, intermediate and high open probabilities respectively. For both models, C refers to close and O to open state. Taken from Dupont & Sneyd [340].

release, stochastic channel opening and diffusive noise.

The models presented in this section have shed light to the stochastic behavior of IP$_3$R channels. As state-based (Markovian) kinetic models are often hard to scale and computationally demanding, those IP$_3$R models are often combined with deterministic descriptions of other cellular processes in so-called multiscale/hybrid models (see section III.5).

As astrocytic Ca^{2+} signals display a striking spatial diversity (see Fig II.7), implementing cellular geometry and Ca^{2+} diffusion in models appears crucial for reproducing and better understanding experimental observations.

III.3 Deterministic spatial models

Robert Brown reported in 1828 that pollen grains displayed constant random movements when suspended in water, which is now referred to as Brownian motion. At the beginning of the XX$^{\text{th}}$ century, Einstein and then Jean Perrin have contributed to a better understanding of those random movements. In parallel to this work, Adolf Fick in 1855 formulated the macroscopic laws of diffusion. Turing has demonstrated that diffusion can spontaneously drive a system to instability, leading to spatial patterns, even if the initial state of the system was uniform [394]. The geometry of the cell, as e.g a large turtuosity (i.e lots of obstacles that impose collisions of molecules onto membranes), can form structures from which the probability of molecules to diffuse outside is low, referred to as molecular traps.

Molecular interactions rely on (1) the probability of encounter of molecules and (2) on the reaction rate of the two molecules once they are close enough to interact. If (2) is great compared to (1), then reactions are diffusion-limited and the system's dynamics cannot be fully grasped by well-mixed models as described in sections III.1 and III.2. In case of diffusion-limited reactions, the spatial character of cellular processes and molecular transport must be taken into account in the model. If reactions are fast enough and if the number of molecular species is high, deterministic spatial approaches can be used to study the system. Those approaches are the least computationally expensive to simulate spatial effects. For heterogeneous space-dependent reaction rates or low-copy numbers of molecules, stochastic spatial approaches should be favored, which are described in section III.4. For more details on the theory of diffusion, see Nicholson et al [395].

III.3.1   Methods and computational approaches

Simulating space with a deterministic model relies on the use of compartmental models. The geometry can be either derived from experiments or analytically constructed in 1D, 2D or 3D. The geometry is then divided into sub-compartments. Each sub-compartment is considered well-mixed and can be described with the tools presented in section III.1.

Incorporating Fick's law of diffusion to the Reaction Rate Equation (RRE) (section III.1) leads to a PDE system, which describes the changes in concentration of a set of species over time and space [396]. Mathematically, a PDE reaction–diffusion system, also referred to as Reaction-diffusion equation (RDE), describes variations of concentrations over time and space and is formulated as follows:

$$\frac{\partial u}{\partial t} = D\nabla^2 u + R(u) \tag{III.9}$$

Or equivalently if the model is in 3 spatial dimensions (x, y & z):

$$\frac{\partial u}{\partial t} = D(\frac{\partial^2 u}{\partial x^2} + \frac{\partial^2 u}{\partial y^2} + \frac{\partial^2 u}{\partial z^2}) + R(u) \tag{III.10}$$

where u is the concentration of the molecular species U of interest $\in \mathbb{R}^\delta$ at time $t \in$ [0,T], δ is the dimension of the space being modeled, D is the diffusion coefficient of U and R is a function representing the reactions involving U, which are described by a set of differential equations. For example, if we come back to the bimolecular reaction presented in section III.1 $S_1 + S_2 \underset{k_b}{\overset{k_f}{\rightleftarrows}} S_3 + S_4$, including diffusion in the model modifies Eq III.1 as follows:

$$\frac{\partial [S_3]}{\partial t} = k_f[S_1][S_2] - k_b[S_3][S_4] + D_{S_3}\nabla^2[S_3] \tag{III.11}$$

where D_{S_3} is the coefficient of diffusion of species S_3.

Theoretical diffusion coefficients of molecular species of interest can be calculated from molecular weights or, more precisely, can be measured by fluorescence recovery experiments in the system of interest. Increasing the number of species and/or of reactions increases computational cost. For techniques to solve numerically PDEs, see e.g Smith et al [397].

Several software tools are available for simulating spatial deterministic molecular interactions:

- Virtual Cell (VCell) [398].

- ReDi-Cell [399], which is a GPGPU solver, so that spatial decomposition of the system occurs over all available GPUs.

- GENESIS [400].

- Chemesis [401].

- MOOSE [402].

- NEURON [403, 404] and the recently derived ASTRO [405]. NEURON enables simulations on 1D branching geometries either described by the modeler or imported from tracing programs. It is one of the most used modeling software in neuroscience, accounting for more than 1900 publications and more than 600 models available on ModelDB, a platform for storing and retrieving neuroscience models [406].

For more details on tools and simulators available for spatially-extended determinisitc models, see the review by Slepchenko et al [407].

III.3.2   Deterministic spatial models of Ca^{2+} signals

As presented in sections III.1 & III.2, the majority of Ca^{2+} models have been developed using rate equations or Markov processes which lack spatiality. When the biological question at stake necessitates to account for Ca^{2+} diffusion and the spatial distributions of Ca^{2+} signals, spatially-explicit models have been used instead. Deterministic spatial models of non-neuronal cell types, such as myocytes [408, 409, 410], have suggested that the positioning of intracellular Ca^{2+} channels affects the characteristics of Ca^{2+} waves. Spatial deterministic models have also provided the first mechanistic insights on Ca^{2+} microdomains [411].

Because of their spatial spread, Ca^{2+} waves are the first type of Ca^{2+} signals that has been investigated with spatially-extended models. Ca^{2+} waves correspond to increases of $[Ca^{2+}]$ that start at a specific location in the cell and then propagate, potentially to the whole-cell. The wave is terminated by re-uptake/buffering mechanisms such as SERCA pump activity and IP_3 degradation (exponential decay). 2 main mechanisms have been proposed to explain wave propagation:

- Passive wave propagation, which relies on Ca^{2+} diffusion within the cytosol.

- Active wave propagation, which relies on an excitable system. An increase of $[Ca^{2+}]$ above a certain threshold triggers additional Ca^{2+} release. Ca^{2+} then diffuses across IP$_3$R-enriched regions, in which the Ca^{2+} wave propagates via Ca^{2+}-induced Ca^{2+} release (CICR) (see Fig II.9) [412, 413].

One of the most used deterministic model of Ca^{2+} waves is the Fire-diffuse-fire (FDF) model [414, 415], which is a threshold model. This model assumes that the wave is driven by passive diffusion of Ca^{2+} between distinct active release sites (IP$_3$R clusters in the case of IP$_3$R-dependent Ca^{2+} signals). Ca^{2+} is released ('fire') at release sites when $[Ca^{2+}]$ is above a given threshold. Those models have been extensively studied mathematically and are computationally inexpensive. FDF models have enabled to study the impact of SERCA pumps on wave propagation [416] and the interactions between the ER and the cytosol [319, 417, 418].

Deterministic spatial models have demonstrated that waves in inhomogeneous medium can display unexpected behaviors [419] and that waves can arise from the interplay between ER distribution within the soma and IP$_3$ generation in the neurite [420].

Only few representative spatially-extended models of Ca^{2+} waves have been presented in this section. For more details on deterministic spatial models of Ca^{2+} waves, see ref [321, 298, 304].

Samanta et al [421] and McIvor et al [422] have developed deterministic spatial models to investigate Ca^{2+} dynamics within Ca^{2+} microdomains and observed that IP$_3$R clustering as well as the spatial distribution of Orai channels influence the amplitude of Ca^{2+} peaks. More spatially-extended models are necessary to investigate microdomains dynamics although stochastic approaches (section III.4) should be preferred because of the small volumes and low copy numbers involved in microdomains.

III.3.3   Deterministic spatial models of astrocytic Ca^{2+} signals

As intra- and inter-cellular Ca^{2+} signals in astrocytes are highly spatialized, from recurrent sites of focal activity (microdomains) to propagating waves (see Fig II.7), spatially-extended models of intracellular Ca^{2+} signals in astrocytes have emerged recently.

A key point for modeling astrocytes with spatially-extended models is to choose the level of details to describe the extremely complex and ramified geometry of astrocytes. Fig III.5 presents the different types of geometries that can be used in spatially-explicit models of astrocytes. Note that apart from 1D that is specific to

deterministic approaches, those geometries can be used in both deterministic and stochastic spatial models. The geometry can either be built from scratch by the modeler, mimicking key geometrical aspects of the system of interest (Fig III.5A2, B2, C2) or directly imported from experiments (Fig III.5A1, B1, C1). If a 3D geometry (Fig III.5A) is not required for investigating the question of interest, the geometry can be projected in 2D ((Fig III.5B) or 1D (Fig III.5C). Discretization should lead to small enough compartments to represent the spatial entities of interest but large enough so that deterministic approximation of the system can hold (i.e high enough copy number of particles in the compartments of interest).

III.3.3.1   Astrocyte models of intercellular Ca^{2+} signals

The first spatial models of astrocytes have mainly focused on intercellular Ca^{2+} waves propagation, in 2D [423, 328] or in 3D [337, 424]. Höfer et al [337] have modified the Li-Rinzel model (Eq III.2 & III.3) to add IP3 dynamics to the model and diffusion of Ca^{2+} and IP_3 in 2 spatial dimensions. The model consists in 4 ODEs for cytosolic $[Ca^{2+}]=$ C, $[Ca^{2+}]$ in the ER=S, $[IP_3]$=I and the active fraction of IP_3R=R:

$$\frac{dC}{dt} = v_{rel} - v_{SERCA} + v_{in} - v_{out} + D_{Ca}(\frac{\partial^2 C}{\partial x^2} + \frac{\partial^2 C}{\partial y^2})$$

$$\frac{dS}{dt} = \beta(v_{SERCA} - v_{rel})$$

$$\frac{dI}{dt} = v_{PLC\beta} + v_{PLC\delta} - v_{deg} + D_{IP_3}(\frac{\partial^2 I}{\partial x^2} + \frac{\partial^2 I}{\partial y^2})$$

$$\frac{dR}{dt} = v_{rec} - v_{inact}$$

$$(III.12)$$

where $v_{PLC\beta}$, $v_{PLC\delta}$, v_{rel}, v_{SERCA}, v_{deg}, v_{in} and v_{out} correspond to the rates of respectively PLCβ, PLCδ, Ca^{2+} release from the ER, Ca^{2+} pumping into the ER by SERCA pumps, IP$_3$ degradation, Ca^{2+} influx to and outflux from the cytosol. v_{inact} and v_{rec} correspond to the rates of IP$_3$R inactivation and recovery, respectively. Note that equations for I and C include the variations of concentration due to IP$_3$ and Ca^{2+} diffusion, with diffusion coefficients D_{IP_3} and D_{Ca}, respectively.

IP$_3$ transport from cell to cell via gap junctions, was derived from Fick's 1st Law of diffusion:

$$J_{net}(i \rightarrow j) = F(IP_3^i - IP_3^j)$$

$$(III.13)$$

where i designates a given compartment(=astrocyte), j a neighboring one, J_{net} the net flux of IP$_3$ from compartment i to j and IP_3^k the concentration of IP$_3$ in compartment k. F represents the coupling strength of the network and depends on the
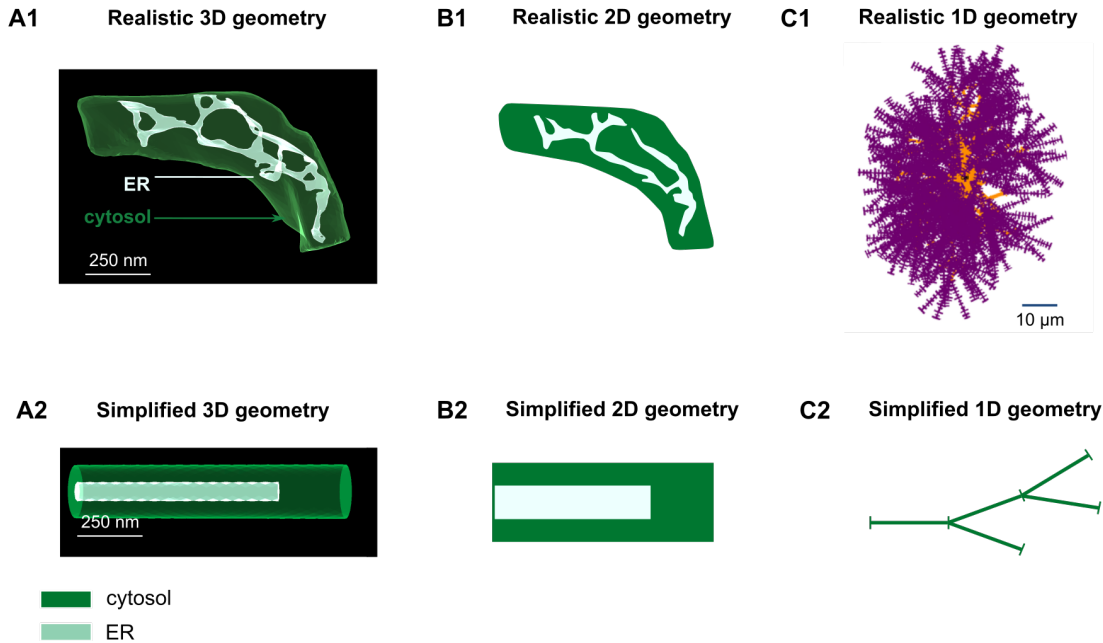
Figure III.5: Examples of geometries for modeling intracellular Ca^{2+} signals in astrocytes. Depending on the biological question, the astrocytic geometry chosen for simulations can be in 3D (A), either realistic, extracted from 3d reconstructions of experimental data (A1), or simplified (A2). The geometry in panel A1 corresponds to a hippocampal astrocytic process ≈ 1 μm long and with a diameter of ≈ 200 nm, extracted and reconstructed from electron microscopy, provided by C. Cali, KAUST University, Saudi Arabia [32]. Cytosolic volume is represented in dark and ER volume in light green. 2D projections of 3D reconstructions (B1) or of simplified geometries (B2) can also be performed for computational efficiency, although it decreases the accuracy of the model. (C) Spatial compartments can even be simplified as 1D segments. They can be derived from experimental data and thus represent a 3D tree composed of 1D segments (C1) or simplified networks of 1D segments representing average network properties (C2). Those 1D networks have been used both for modeling inter-cellular (network of astrocytes) and intra-cellular (network of processes) astrocytic networks. Panel C1 was taken from Savtchenko et al [405]. It presents a complete astrocyte model (z-projection) generated by NEURON software. Main branches are depicted in orange and thin processes in purple.

number of gap junctions in the system and on their permeability.

This model has been used by Goldberg et al [425] in a 1D chain of astrocytes. They have demonstrated that the coupling function of gap junctions must be non-linear and include a threshold of [IP$_3$] for long-distance wave propagation and that this type of propagation is facilitated if internal Ca^{2+} oscillations are in a frequency-modulation mode.

Kang & Othmer [424] have included extracellular ATP signaling in their model of IP$_3$R-mediated inter-cellular Ca^{2+} waves. Geometry of the network was based on *in vitro* and *in vivo* confocal immunofluorescence images. They found that Ca^{2+} waves in astrocytes are probably mediated by a combination of IP$_3$ transport via gap junctions and by ATP signaling via the extracellular space.

Lallouette et al [426] have also used the model from Höfer et al [337] to investigate the impact of astrocytic network topology (i.e gap junction coupling) in 3D on inter-cellular Ca^{2+} waves propagation. Simulations of the model have demonstrated that modifying the topology of the network is sufficient to reproduce diverse forms of waves reported experimentally. Sparse connectivity favored wave propagation while long–distance or dense connectivity impaired it.

Finally, Postnov et al [423] have implemented a model of neuron–astrocytes network and have reproduced typical global and local Ca^{2+} patterns observed in experiments.

III.3.3.2   Models of intracellular Ca^{2+} dynamics in astrocytes

The spatiotemporal complexity of intracellular Ca^{2+} signals in astrocytes presented in section II.2 (Fig II.6B) has given rise to a novel type of models of Ca^{2+} signals in astrocytes, focusing on intracellular Ca^{2+} dynamics rather than intercellular waves propagation. Below are presented the most representative spatially-extended deterministic models that have been developed to study intracellular Ca^{2+} dynamics in astrocytes.

In order to investigate distal Ca^{2+} signals in astrocytes, Brazhe et al [427] (Fig III.6) have developed a model that spatially segregates distal regions from deeper regions of astrocytes. In this model, perimembrane regions (type I) are characterized by metabotropic glutamate receptors (mGluRs)-mediated signals and by the absence of ER. Deeper regions (type II) such as the soma are characterized by IP$_3$R-dependent Ca^{2+} signaling and waves propagation via CICR. The coupling

between those spatially-segregated regions is mediated by the diffusion of Ca^{2+} in the model, J_{diff}. The geometry of the model was extracted from confocal imaging of a rodent hippocampal astrocyte and then mapped in 2D, labeled and discretized (Fig III.6a-d), with a resolution of 0.59 $\mu m/pixel$. The ODEs that describe the 2 distinct Ca^{2+} oscillators and Ca^{2+} diffusion are presented in the bottom panel of Fig III.6. This model offers insights into the interactions between neuronal activity-driven Ca^{2+} signals and somatic global events.

Gordleeva et al [428] have investigated the correlations between local and and global astrocytic Ca^{2+} signals. Similarly to Brazhe et al. 2018 [427], they have used a compartmental approach, in which astrocytic geometry was reconstructed from a cultured astrocyte and was then divided into well-mixed cylinders, coupled with Ca^{2+} and IP_3 diffusion. Their results suggest that Ca^{2+} signals in astrocytes can be triggered by synchronized neuronal signals, suggesting that astrocytes could act as detectors of spatial synchronization of neuronal activity.

A recently published paper by Savtchenko et al [405] has developed a model of Ca^{2+} signaling based on a realistic astrocyte morphology. This study is based on the NEURON software, which enables deterministic simulations within segmented 1D geometries (Fig III.5C1). They modeled Ca^{2+} dynamics based on Fluo4 measurements and investigated the effect of Ca^{2+} buffers and of IP₃R clustering on the propagation of Ca^{2+} signals within the astrocytic intracellular network of processes. Added to those important results, this study has developed a tool derived from NEURON software, called ASTRO, that enables the simulation of macroscopic Ca^{2+} dynamics and of oscillatory Ca^{2+} dynamics at the microscopic scale in small compartments representing PAPs.

As fine processes are the site of neuron-astrocyte communication, modeling studies that investigate Ca^{2+} dynamics in peripheral astrocyte processes (PAPs) have emerged. Some have been developed to study Na^+ [429] or Ca^{2+} [430] dynamics in PAPs. Montes de Oca Balderas et al have investigated Ca^{2+} signaling in PAPs in a spatially-extended model [430]. This study has investigated the impact of the distance of the astrocytic ER from the tip of the astrocytic process that contacts a synapse. They modeled PAPs as 1 μm-long and 100 nm in diameter cylinders and neglected radial diffusion so that the model was in 1 spatial dimension. Their results suggest that IP₃ diffusion on its own is sufficient to trigger Ca^{2+} signals in response to neuronal communication, even if the ER is 1 μm away from the PSD. Note however that no IP₃ degradation term was included in the model so that correct interpretation of simulation results might be tricky.

As PAPs contain low numbers of molecules, deterministic approaches might not
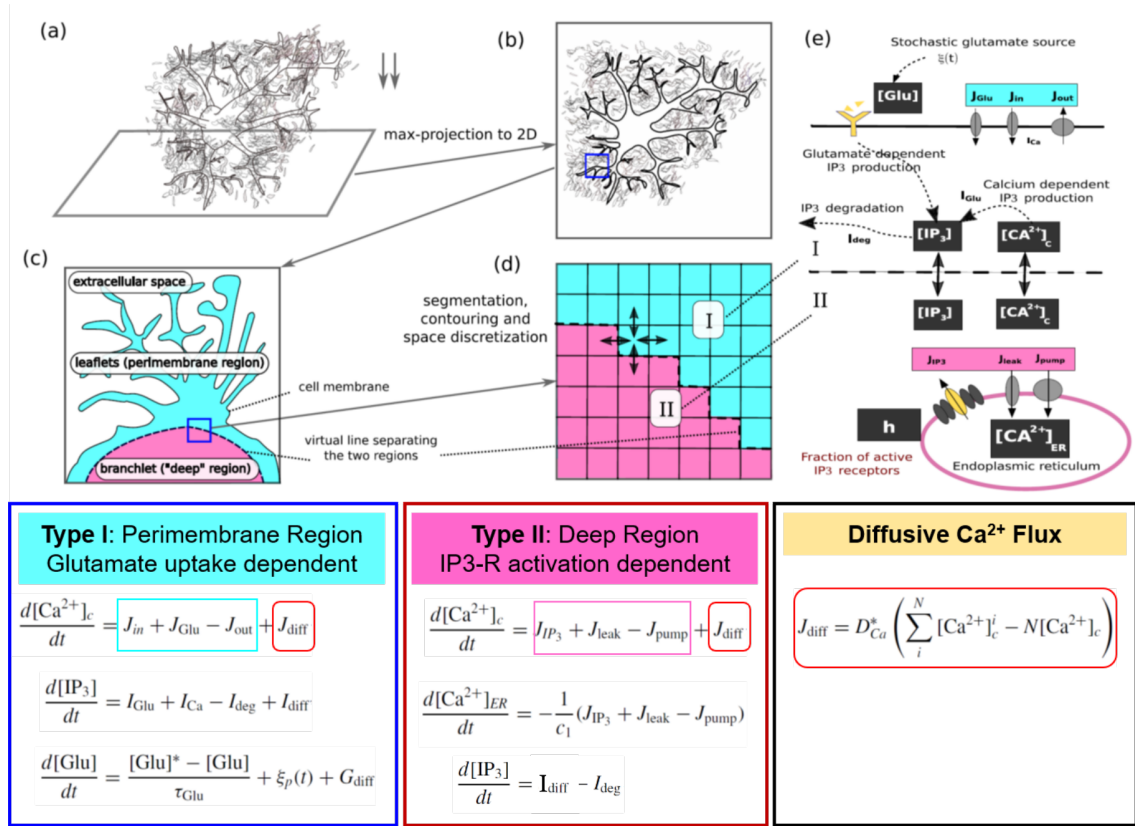
Figure III.6: Example of a spatial oscillator model of intracellular astrocytic Ca²⁺ signals. The top panel of this figure represents the model formulation of Brazhe et al [427]. 3D confocal fluorescent reconstruction (a) was projected in 2D (b). The cellular compartments were then labeled in this 2D geometry as perimembrane and deeper regions (c) before discretizing space in each compartment (d). The kinetic scheme modeled in each compartment is represented in panel (e): IP_3R-independent in leaflets (=perimembrane region, blue) and IP_3R-dependent in deeper regions (pink). Dotted curves indicate a functional dependency between molecular interactions. The Js represent Ca^{2+} fluxes through membranes and the 4 variables are represented in black boxed. The ODEs corresponding to the dynamics in each compartment and their coupling through Ca^{2+} diffusion are presented in the bottom panel of this figure (blue for perimembrane regions and pink for deep regions, yellow for diffusive Ca^{2+} flux). This figure was adapted from Brazhe et al [427].
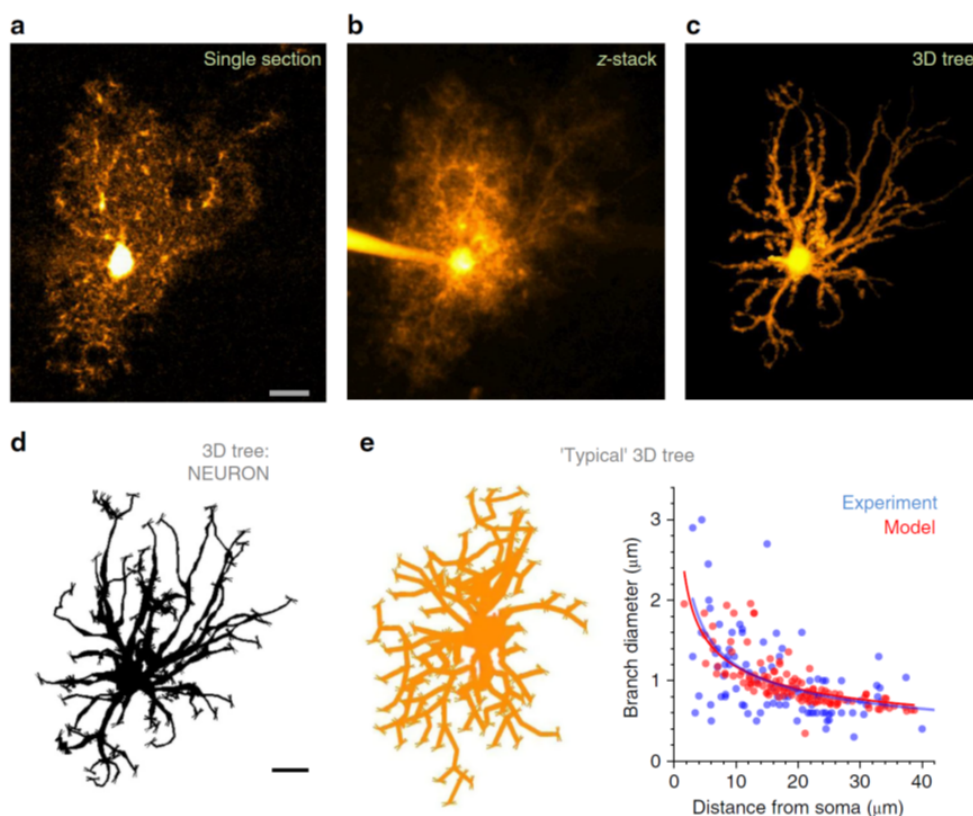
Figure III.7: Towards simulating signal propagation within intracellular astrocytic networks with ASTRO. Single section (a) and full z-stack (b) of a dye-filled astrocyte of the hippocampal CA1 region and its 3D tree reconstruction using NeuroTrace (2D view of the 3D image) (c). Scale bar: 10 μm (d) 2D visualization of the astrocyte stem tree from panel c in NEURON format. Thin 'buds' represent initial regions of nanoscopic protrusions. Scale bar: 10 μm. (e-f) Typical astrocyte stem tree (e), obtained by fitting branch diameters according to available experimental data (f). Data from experiments and the model are presented respectively in blue and red. The solid lines correspond to power law fit of data scatters.

be well-suited to study this system and further investigation using stochastic approaches should be undertaken.

Deterministic spatially-extended models have led to significant advances in our understanding of Ca^{2+} signaling in astrocytes, especially at the whole-cell level. Deterministic spatial methods display however some limitations. For example, the spatial extent of functional compartments is not always well defined and can change over time, which is hard to estimate as some of those functional compartments are smaller than the resolution of conventional light microscopy. Another limitation of this approach is that it ignores low copy number of molecules that are often the hallmark of subcellular processes. Thus, compartmentalized models are well-suited for exploring cellular heterogeneity and the influence of geometry on molecular interactions at the cellular level but stochastic approaches should be favored for modeling local signals involving low copy number of molecules as encountered in PAPs.

III.4   Stochastic spatial models

An increasing number of studies demonstrate important roles of spatial-stochastic effects on cellular processes, from highly heterogeneous intracellular geometry [431], to non-uniform spatial molecular patterns [432] or molecular crowding effects [433]. Spatial-stochastic approaches are essential for modeling systems that display low copy number of molecules as well as diffusive noise. Those models are computationally expensive so that whole-cell simulations have been described as a 'grand challenge of the 21st century' [434]. Those approaches have successfully reproduced dynamics that were not grasped by the corresponding mean-field or non-spatial models for systems such as oscillations of Min proteins in *E. Coli* cell division [435], signal transduction in *E. coli* chemotaxis [436], MAPK pathway [437], morphogen gradients [438] and interactions of DNA-transcription factors [439].

In this section, the main spatial stochastic modeling methods are introduced, before presenting the ones that have been specifically developed for studying Ca^{2+} dynamics. For a detailed review on spatial stochastic simulations of intracellular molecular interactions, see [440, 441, 442, 443, 399, 444].

III.4.1   Methods and computational approaches

Similarly to deterministic spatial models, stochastic spatial approaches rely on geometries that can be either derived from experiments or constructed analytic geometries and can be implemented in 2D or 3D (Fig III.5). When space is discretized, the spatial compartments can be of different forms: from heterogeneous to homogeneous grids in 2D models to voxels of cuboid [445] or tetrahedra [446, 447] shape in 3D models. There are three main approaches for simulating reaction-diffusion systems that are presented in Fig III.8 and in next paragraphs: particle-based, voxel-based and hybrid spatially-extended stochastic approaches. Other spatial stochastic methods exist although out of the scope of this manuscript. Those methods include:

- Molecular dynamics [448], which attributes mass, momentum and energy to individual atoms with an extremely small time step (10^{-15} s) and often very large number of particles ($\approx 10^{10}$).

- Spatial chemical Langevin equation (SCLE) [449], which is a spatialized adaptation of the chemical Langevin equation that incorporates diffusion and consists of a group of stochastic differential equations (SDEs) (see section III.2).

III.4.1.1   Microscopic spatial stochastic approaches

The most straightforward spatially-explicit stochastic approach consists of tracking the diffusive path of each individual molecule/ion (=particle) within the spatial domain. Particles are characterized by their individual spheres of interaction/interaction radii (Fig III.8A1). Second-order reactions occur depending on their rates when the reactants are within their interaction radii. Those approaches, referred to as particle-tracking, particle-based or microscopic approaches, can be implemented with various methods:

- **Brownian dynamics**
  In Brownian dynamics, single molecules are tracked while following Brownian trajectories:
  $$\mathbf{r}(t + \Delta t) = \mathbf{r}(t) + \sqrt{2D_i \Delta t}\xi \qquad (\text{III.14})$$
  where D_i is the diffusion coefficient of molecule i and ξ is a vector of i.i.d. Gaussian-distributed random numbers with zero mean and unit variance. Reactions occur when the molecules are within their interaction radii. The most common methods to implement Brownian dynamics include:
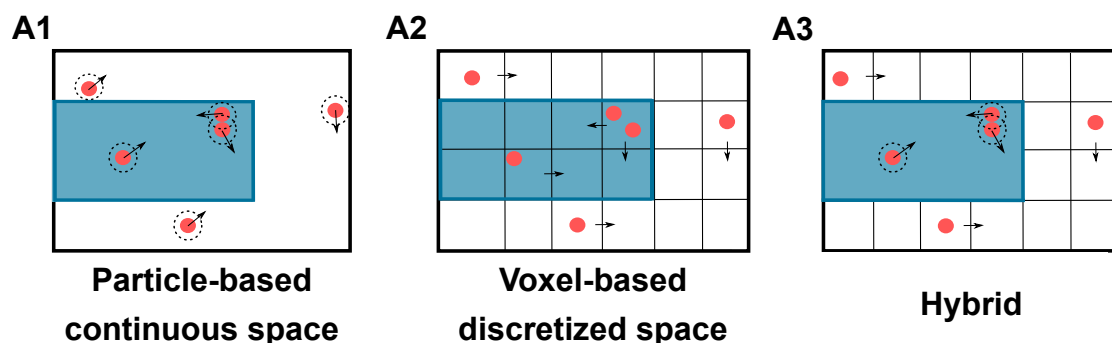
Figure III.8: Spatially-explicit stochastic approaches. This figure represents the main approaches for spatially-explicit stochastic simulations. In particle-based models (A1), particles (red circles) are characterized by their real-valued coordinates in space and by their sphere of interaction (dashed black circles). Second-order reactions occur according to their specific rate when reactants are within their interaction radii. Note that space can be continuous (A1) or discretized (lattice-based method, not represented). In stochastic compartment-based = voxel-based models (A2), space is discretized into voxels that are assumed to be well-mixed. Particles can react with reactants localized in the same voxel. The diffusion of particles is implemented as an additional reaction where single particles can hop from a voxel to a neighboring one. Voxels can be of various shapes, mainly cubes or tetrahedra, the latter leading to higher computational cost but finer description of the membranous contours of the various compartments. In hybrid models (A3), part of the system is implemented with a particle-based approach while the rest of the system is implemented with a voxel-based approach, providing a good compromise between accuracy and computational cost.

– Smoluchowski's model, in which a molecule is characterized by its radius of interaction and 2 reacting particles react immediately if they are within this radius.

– Doi/$\lambda - \rho$ model [450], which is a generalization of Smoluchowski's model [451]. , where a molecule reacts with probability λ per time unit when the distance between its center and another reacting molecule is less than ρ.

– The microscopic lattice method, which discretizes space into subvolumes so that each subvolume can contain at most one molecule. In this method, molecules hop from subvolume to a neighboring one and can react with molecules that are in neighboring subvolumes. The size of the lattice strongly influences reaction rates [452] so that this method has not been used much, except for studies on molecular crowding or on oligomerization [453].

- **Green's function reaction dynamics methods**
  Green's function reaction dynamics (GFRD) is an event-driven method in which reaction step is accurately calculated from propensity functions of individual reactions. Large jumps in time and space can be made if particles are far away from each other, so that this approach is ideal for systems with high time/distance between two reactions. This technique can be up to 5 orders of magnitude faster than Brownian dynamics if the number of molecules is low [454, 455].

III.4.1.2   Mesoscopic spatial stochastic approaches

Mesoscopic approaches are the least computationally expensive stochastic spatially-explicit methods as they track populations of molecules within subvolumes rather than individual molecules. Space is subdivided into non-overlapping voxels in a mesh (Fig III.8A2). Diffusion is modeled as first-order events where a molecule M_l in a voxel v_i diffuses to a neighboring voxel v_j and is treated as a set of reactions in the CME, forming the reaction-diffusion master equation (RDME) [456, 457, 458].

$$M_{li} \xrightarrow{d_{lij}x_{li}} M_{lj}$$
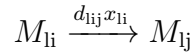
where x_{li} is the number of M_l in v_i and d_{lij} is the diffusion rate constant of M_l from v_i to v_j, that depends on the coefficient of diffusion of M_l, D_l, and on voxel sizes.

Molecules in each voxel are assumed to be well-mixed and can react with other reactants present in the same compartment or diffuse to a neighboring compartment. If space is divided into k voxels/compartments and there are N molecules, then the RDME is an equation for the probability density function (PDF) of kN dimensions and time. This high dimensionality makes RDME hard to be solved directly so that the model is analyzed statistically with Monte Carlo approaches. See Van Kampen's 'Stochastic Processes in Physics and Chemistry' [347] and Hellander et al [459] for more details on RDME.

Voxel size much be chosen carefully as it has to be smaller than the smallest geometrical feature of interest and also smaller than the diffusion length of all the reactants in the timescale chosen [460]. Accuracy and computational cost decrease with increasing sizes of compartments. The main limitations of this approach are the potential errors in capturing the effects at boundaries [450, 461] and decreased accuracy if voxel size is below the well-mixed subvolume condition [444]. Note that if mesh size is chosen carefully, compartment-based models have been shown to provide a very good approximation of molecular trajectories at a much lower computational cost than the corresponding molecular dynamics model [444, 462].

The most common mesoscopic spatial stochastic algorithms are:

- **The next subvolume method**
  In the next subvolume method, the exact Gillespie's SSA (see section III.2) is computed in every voxel independently and diffusion is modeled between neighboring voxels.

- **Spatial τ-leap**
  The spatial τ-leap algorithm is an approximation of the next subvolume method that uses larger time steps τ [463]. It computes the τ-leap method (see section III.2) independently in each voxel and diffusion is modeled between adjacent voxels.

III.4.1.3   Hybrid spatial stochastic methods

In order to optimize both accuracy and computational cost, hybrid (=multiscale) methods describe regions of particular interest such as the vicinity of Ca^{2+} channels with microscopic details while other regions are simulated with a compartment-based approach (Fig III.8A3). Those methods thus decrease the level of details for modeling regions in which accuracy is not necessary, thus optimizing computational cost. Flegg et al [464] have developed such a hybrid spatially-explicit approach, called the two-regime method (TRM).

III.4.1.4   Available stochastic spatial simulators

Currently available software packages for spatially-explicit stochastic models are presented in Table III.2. For more details on the features of the simulators presented here, see dedicated reviews [465, 445, 443, 455, 466, 467, 468, 469].

Note that software tools are also available for smaller spatial scales as e.g SpringSaLaD (vcell.org/ssalad), in which individual molecules are described as collections of spheres that are bound together.

III.4.2   Stochastic spatial models of Ca^{2+} signals

High-resolution Ca^{2+} imaging studies have revealed that puffs occur at fixed cellular sites [480, 481, 265] and involve the simultaneous opening of several channels within a few hundred nm [482]. Those observations motivated the development of stochastic spatially-explicit models of Ca^{2+} signals.

Table III.2: Spatially-extended stochastic simulators. In Method column ('Meth'), 'Vox' refers to voxel-based approaches, 'Part' to particle-based approaches and 'Hyb' to hybrid approaches. 'Det' and 'WM' columns contain 'x' when it is also possible to perform deterministic or well-mixed implementations of the model with the simulator, respectively.

Simulator	Url	Meth	Det	WM	Ref
SmartCell	software.crg.es /smartcell	Vox	x		[470, 456]
MesoRD	mesord.sourceforge.net	Vox			[471]
Gridcell	iml.ece.mcgill.ca /GridCell	Vox			[445]
E-Cell	e-cell.org	Hyb			[472, 473]
VirtualCell (VCell)	vcell.org	Vox		x	[398]
URDME	urdme.org	Vox			[474]
STEPS	steps.sourceforge.net	Vox		x	[475]
Smoldyn	smoldyn.org	Part			[453]
ChemCell	chemcell.sandia.gov	Part			[476]
MCell	MCell.cnl.salk.edu	Part			[477]
eGFRD	gfrd.org	Part			[437]
Cell++	sourceforge.net/projects /cellpp	Hyb			[478]
Spatiocyte	spatiocyte.org	Hyb			[465]
ReaDDy	readdy.github.io	Hyb			[479]

One of the first spatial stochastic model of Ca²⁺ dynamics was based on a 2D lattice and demonstrated the effect of various parameters such as Ca²⁺ diffusion, Ca²⁺ dynamics, the type and dose of agonist and morphological parameters such as size and geometry of the cell and its organelles on the temporal and spatial patterns of Ca²⁺ oscillations [483].

Because of their small volumes and low, highly variable numbers of Ca²⁺ ions (5-6 ions in a half-μm diameter dendritic spine [460]), dendrites have been one of the first systems studied with spatial stochastic approaches. Dendritic morphology, especially dendritic diameter, has been demonstrated to influence the spatio-temporal characteristics of Ca²⁺ signals, molecular diffusion and compartmentalization [484, 485, 486, 487, 488]. Overall, spatial stochastic models have led to significant progress in understanding local Ca²⁺ dynamics in dendrites.

Spatial stochastic models have been used to model Ryanodine receptors (RyRs)-mediated Ca²⁺ signals in microdomains in myocytes [489] and revealed that the intrinsic noise of Ca²⁺ signals is associated with an increased probability of channel

opening. Spatially-explicit stochastic models have also been developed to investigate intracellular IP_3R-mediated Ca^{2+} dynamics. For example, Mazel et al [431] have revealed that IP_3R channels that are located close to mitochondria have a slightly lower probability to open than average, resulting in a lower depletion of the ER in the vicinity of mitochondria. Wieder et al have demonstrated that local fluctuations of the number of Ca^{2+} ions in microdomains due to diffusive noise increases the open probability of a single IP_3R compared to the standard deterministic model [490]. In another model, diffusive noise mixed Ca^{2+} within IP_3R clusters and decreased self-inhibition of IP_3R channels by Ca^{2+}, thus increasing the open time of the channels, resulting in increased durations of Ca^{2+} signals [491].

Beyond the scope of Ca^{2+} signals, those models illustrate the roles of stochasticity, including diffusive noise, in intracellular signaling networks and suggest that they must be taken into account in order to accurately describe intracellular molecular interactions.

As explained in section III.3, waves are modeled as a result of the sequential opening of Ca^{2+} release sites, coupled by diffusion. Experimental studies such as Marchant et al [368] have demonstrated that the frequency of Ca^{2+} waves is influenced by the characteristics of local signals such as puff frequency and amplitude, which are inherently stochastic (see section III.2). Therefore, spatially-explictit stochastic models have been developed to investigate both RyR-mediated [414] and IP_3R-mediated [377] Ca^{2+} waves models. Other models have also implemented stochastic generalizations of the fire-diffuse-fire model (see section III.3) [492, 493] and demonstrated the emergence of coherence resonance of Ca^{2+} stores as well as enhanced transitions from isolated Ca^{2+} releases to steadily propagating Ca^{2+} waves when $[IP_3]$ increases. For reviews on stochastic waves, see [304] but also [392].

III.4.3   Stochastic spatial models of astrocytic Ca^{2+} signals

As described previously, models of Ca^{2+} signals in astrocytes have mostly been performed with spatially-explicit deterministic approaches, which are well-suited to the description of global events but fail to accurately describe the heterogeneous distribution of Ca^{2+} channels and pumps [494, 495, 496, 497, 282] and local variations of the number of Ca^{2+} ions in thin astrocytic processes. For example, a cytosolic Ca^{2+} concentration of 100 nM in the 0.357 μm^3 hippocampal astrocytic volume presented in Fig III.5A1 corresponds to 21 ions.

Recently, some astrocyte models have started to incorporate noise using hybrid

approaches in order to better simulate stochastic components of Ca^{2+} dynamics at the subcellular level. For example, Cresswell-Clay et al [498] have developed a whole-cell model of a single astrocyte consisting in a soma with 5 main branches, all containing ER. Ca^{2+} signals were implemented as a stochastic influx. Their results suggest that both cellular geometry (e.g somatic volume) and the velocity of diffusing molecules influence the coupling and nature of the Ca^{2+} signals in response to neuronal stimulation. Interestingly, simulations also revealed complex spatiotemporal characteristics of Ca^{2+} depletion in the somatic ER in response to Ca^{2+} signals in processes, due to intra-ER Ca^{2+} diffusion.

The model that is presented in this thesis is the first spatially-explicit fully stochastic model of Ca^{2+} signals in astrocytes (see Chapters IV, V, VI).

To conclude, diverse spatially-explicit stochastic approaches can be performed, that display different levels of accuracy. As a general rule, microscopic approaches should only be performed when information about the exact trajectories of single molecules is required. In order to optimize the computational cost associated with spatial stochastic models, another strategy that is very prolific is to combine stochastic and deterministic approaches within the same model, each approach being adapted to reactions/phenomena within the system of interest. Those approaches are called hybrid approaches and are the focus of next section.

III.5   Hybrid models

In most pathways, including Ca^{2+} signaling, some of the molecules involved are in low copy numbers while there are many copies of some others (as e.g the number of IP$_3$ molecules compared to the number of Ca^{2+} buffers in astrocytic processes). Hybrid models, that combine different modelling approaches, can be ideal to model such systems by adding complexity and computational cost only to regions/molecular interactions that need a high level of details. Yet, the coupling of different modeling approaches remains tricky and can introduce errors. In this section, the different techniques that can be used for hybrid simulations as well as examples of hybrid models of Ca^{2+} signaling are briefly presented.

III.5.1 Methods and computational approaches

Next paragraphs present the different combinations of approaches that are commonly performed in hybrid models. Hybrid approaches can be divided into two main categories: well-mixed VS spatially-extended methods. For recent reviews on hybrid methods, see [499, 467, 364].

III.5.1.1 Well-mixed hybrid methods

Well-mixed hybrid methods take into account a separation in timescales in which fast reactions or abundant molecules are described deterministically while slow reactions or scarce molecules are described with a discrete stochastic process [500, 501]. Those deterministic-stochastic models are mathematically defined as Piecewise Deterministic Markov Processes (PDMPs) [502], which combine ODEs (see section III.1) with discrete stochastic processes such as CLE-approximation, Gillespie's SSA or the τ-leap method (see section III.2) or any combination [503]. Those models are simulated with Monte Carlo realizations. The coupling of the two methods can be done with fixed time-steps, associated with time-discretization errors, or with adaptive methods, in which the synchronous treatment of deterministic and stochastic systems should be ensured.

Several studies have developed the theoretical background and algorithms for performing such deterministic-stochastic well-mixed models [361, 504, 505, 506, 500, 507]. Partitioning methods, adaptive or not, have also been developed in order to sort reactions into "fast" and "slow" categories [508, 361, 509]. For examples of implementation of well-mixed hybrid models, see [510, 511]. For rigorous error analysis and identification/partitioning of reactions, see Ganguly et al [508].

III.5.1.2 Spatially-extended hybrid methods

If the system of interest displays heterogeneous distributions of molecular species or if diffusion is heterogeneous or limiting, the modeler can combine different spatially-extended approaches depending on spatial localization. As described previously (section III.3 & III.4), 4 main methods are available for spatially-extended models: macroscopic (well-mixed), mesoscopic, microscopic and molecular dynamics.

Several studies have developed algorithms for spatially-extended hybrid models [512, 513, 456, 514]. For example, Ferm et al [513] propose an adaptive hybrid method that divides the domain into diffusion-limited regions, described with the next subvolume method (see section III.4), and well-mixed regions, described with

PDEs (see section III.3). For detailed and recent reviews on spatially-extended hybrid methods and on the methods used for coupling the different simulators of the model, see [467, 515, 516].

III.5.1.3   Simulators for hybrid approaches

Few simulators allow for multiscale modeling of molecular interactions:

- Multi-scale Object Oriented Simulation Environment (MOOSE, http://moose.ncbs.res.in/) [402, 517] can simulate individual molecules (via an adaptation of the Monte Carlo simulator of Smoldyn [453]) as well as populations of molecules within pathways, entire cells or large networks of cells via a range of numerical engines (deterministc, stochastic, reaction-diffusion with branching or cubic meshes).

- Smoldyn has also recently been adapted to accommodate hybrid stochastic models [518] in which the subsystems with disparate levels of stochasticity are segregated in space but can interact in an interface region [464, 519, 491].

- The GEneral NEural SImulation System simulator (GENESIS, http://genesis-sim.org/GENESIS/genesis.html) [400] has been developed to run hybrid simulations in neural systems but is no longer being actively developed.

- The MUSIC API (http://software.incf.org/software/) is a framework that enables to build multiscale modeling between pre-existing simulators/models, with which promising multi-simulation environment tools have started to be developed [520, 521].

III.5.2   Hybrid models of Ca²⁺ signals

III.5.2.1   Well-mixed hybrid models of Ca²⁺ signals

Well-mixed hybrid approaches have been widely used to model Ca²⁺ signaling. They model whole-cell dynamics (Ca²⁺ influx, removal, binding/unbinding to buffers and diffusion) with deterministic approaches but keep a high level of detail for describing biophysical properties of channel gating and kinetics [384, 340]. Those models have led to significant improvement in our understanding of intracellular

Ca^{2+} signals, as e.g Ca^{2+} microdomains in cardiomyocytes [522, 523].

Hybrid models of IP_3R-dependent Ca^{2+} signaling have investigated the duration of Ca^{2+} signals depending on $[IP_3]$, in a single-cluster study [524] and then extended in a 2D plane with several IP_3R clusters [525]. The amplitude of Ca^{2+} peaks appeared random and only the largest ones could spread to next cluster, contributing to CICR and wave propagation. Another hybrid study on IP_3R clusters also predicted that CICR can be triggered by IP_3R clustering where homogeneous distribution of IP_3Rs didn't display signal propagation [526]. Wieder et al [490] have also proposed a hybrid model of Ca^{2+} microdomain in which IP_3R dynamics was modeled stochastically while diffusion and bulk reactions were modeled deterministically. They have demonstrated the influence of fluctuations in the number of Ca^{2+} ions on the equilibrium behavior of single IP_3Rs by increasing its opening probability compared to the equivalent deterministic implementation.

Those studies demonstrate the influence of discrete Ca^{2+} noise on cellular processes at a higher spatial scale.

III.5.2.2 Spatially-extended hybrid Ca^{2+} models

Consequently to the discovery of the spatial diversity of Ca^{2+} signals, an increasing number of spatially-explicit hybrid approaches have been applied to Ca^{2+} signals. Those models simulate global Ca^{2+} dynamics with PDEs and microdomains surrounding IP_3R channels with spatially-extended stochastic processes. Those models have proven very useful for modeling dendrites in neurons, in which dendritic spines are typically modeled stochastically while bigger cellular subcompartments such as the soma and dendrites are modeled deterministically [460].

Other studies rather focused on Ca^{2+} dynamics at IP_3R clusters and have successfully reproduced puff dynamics measured experimentally [527], investigated the influence of IP_3R clustering on puff dynamics [528], the effect of local signals on signals at the cell level [529, 530], the emergence of Ca^{2+} blips [531], the decrease of intra-cluster coupling of IP_3Rs when inter-channel distance increased [532], predicted that inter-peak-interval (IPI) as well as peak amplitude increase with IP_3R cluster size, even for small amounts of IP_3R within the cluster [533] and suggested optimal cluster sizes for CICR [369].

Other hybrid studies of Ca^{2+} signals have provided plausible mechanisms for the formation of Ca^{2+} waves based on puffs dynamics [534]. Other studies have demonstrated the effect of stochastic IP_3R gating on the propagation of Ca^{2+} waves in 2D [377] and the dependence of the lifetime of Ca^{2+} signals (puffs VS waves) on the inter-cluster distance [535].

Means et al [536] have used a spatially-explicit hybrid approach and modeled

reactions with PDEs except for the stochastic gating of IP$_3$R channels. Simulations were performed in 3D with realistic ER geometry extracted from electron microscopy. They have demonstrated that IP$_3$R clustering might reduce the activity of IP$_3$R channels, which could avoid ER depletion in case of repeated stimulations.

Hybrid computational approaches have promoted the emergence of studies of Ca^{2+} signals in 3D cellular geometries of increasing complexity. Those methods will be essential for understanding the influence of local noisy molecular interactions and diffusion on cellular Ca^{2+} patterns. No spatially-explicit hybrid model has been developed for modeling Ca^{2+} signals in astrocytes yet but should prove most useful for better understanding the diversity of astrocytic Ca^{2+} signals.

III.6   Conclusion

Including more details in a model is associated with higher complexity and longer time to compute so that a compromise must be made between current knowledge of the system and computational cost. The art of modeling thus consists in finding a minimal representation that can capture the system's behavior. The citation from George Box, "All models are wrong but some are useful" [537], illustrates that models are abstract simplifications of a process. Even though those simplifications make the model incomplete to reproduce the system as a whole, they provide new understanding about the system that could not be grasped from a model as complex as the system of interest.

Fig III.9 summarizes the main methods presented in this chapter by order of accuracy/computational cost and sums up the approximations that have to be made for using each method. Models are designed to answer a particular research question and the lowest level of details that is enough to answer the biological question should be chosen. For a detailed list of tools for modeling Ca^{2+} signals, the reader can refer to the Toolbox of Dupont et al [267]. For reviews on Ca^{2+} signaling models developed so far, see [372, 538, 539, 321, 340, 392]. For more details on models of astrocytic excitability, see dedicated reviews [287, 540].

As astrocyte excitability plays key roles in information processing in the brain, better understanding its functioning is crucial in the neuroscience field. The complex spatiotemporal Ca^{2+} code of astrocytes yet remains to be decoded and computational modeling of Ca^{2+} signals in astrocytes is an essential step towards unravelling astrocyte excitability and its involvement in brain function.
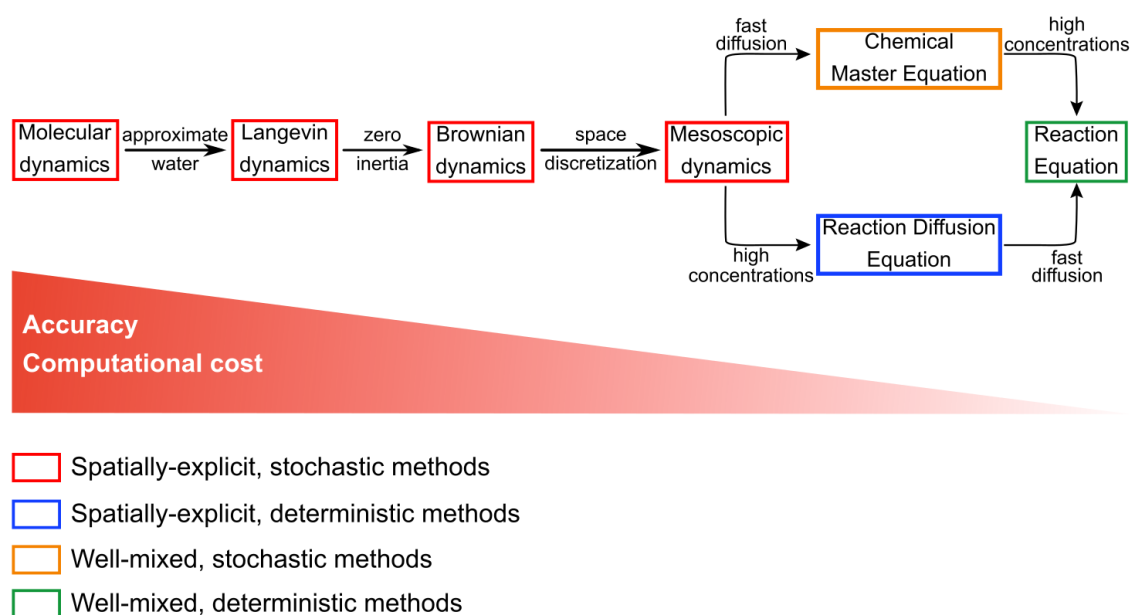
Figure III.9: Overview of the methods for simulating molecular interactions. The different methods presented in chapter III are presented from high accuracy/high computational cost associated with molecular dynamics to less accurate but faster reaction ordinary differential equations.

Part B

Investigating Ca^{2+} dynamics in fine astrocytic processes

Chapter IV

Towards a 2D spatial individual-based model of Ca^{2+} signaling in small volumes

80% of the astrocyte Ca^{2+} activity *in vivo* take place in the gliapil, which is mostly formed by astrocytic ramifications that cannot be spatially resolved by conventional light microscopy [541], yet account for 75% of the astrocytic volume [7] (see Chapter I). At this spatial scale, Ca^{2+} signals are characterized by non-uniform spatial distributions composed of hotspots where Ca^{2+} signals are more likely to occur and repeat [480, 542] (see Chapter II). Those observations suggest the existence of subcellular spatial organizations responsible for the spatial distribution of Ca^{2+} signal patterns. Understanding Ca^{2+} signaling in PAPs, where astrocytes potentially regulate neuronal information processing, is crucial. However, most models of intracellular astrocytic Ca^{2+} have focused on the soma and main processes and did not take into account the stochastic effects associated with the small volumes and the low copy number of molecules involved in fine processes.

This chapter presents the 2D implementation of the model of spontaneous IP_3R-mediated Ca^{2+} signaling that has been developed during this PhD. To account for the stochasticity inherent to small sub-cellular volumes and low copy numbers expected in fine processes, the model is both spatially explicit and particle-based. The kinetics of IP_3R channels is accounted for with a simplified version of the DYK Markov model (see section III.1). This 2D implementation, even though less realistic than the 3D implementations presented in Chapters V and VI, allowed for an exploration of the range of dynamical behaviors that the model can display.

IV.1 Kinetic scheme and modeling approach

IV.1.1 Kinetic scheme

The model considers cytosolic Ca^{2+} and IP$_3$ dynamics in the framework of Ca^{2+}-induced Ca^{2+} release (CICR) signaling. The reaction scheme considered is shown in figure IV.1 A. In short, we consider Ca^{2+} fluxes between the cytosol and the extracellular space or the endoplasmic reticulum (ER), including via IP$_3$R channels. We also take into account the effect of phospholipase C δ (PLCδ), that, when activated by Ca^{2+}, synthesizes IP$_3$. To derive simple models for this scheme, we made the following assumptions:

- We considered that the extracellular and ER Ca^{2+} concentrations are constant during the simulation, as well as the electrical potentials across the plasma and ER membranes. In this case, Ca^{2+} outflow from the cytosol to the ER or to the extracellular medium can be lumped into a single first-order rate α. Likewise, Ca^{2+} entry from the extracellular medium or any IP$_3$R-independent Ca^{2+} influx from the ER can be considered constants, too. We lumped them into a single overall constant flux γ.

- PLCδ enzymes remain located in the cytosol (no translocation) and the amount of their substrate PIP2 is present everywhere in large excess. Under this condition, activated PLCδ produces IP$_3$ with constant rate δ.

IP$_3$R channels are gated both by Ca^{2+} and IP$_3$, with a bell-shaped dependence of the open probability to Ca^{2+} concentration [308] (see Fig II.9). To model their dynamics, we used the classical 8-state Markov model proposed in [308, 8], with two Ca^{2+} binding sites and one IP$_3$ binding site for each IP$_3$R (see figure IV.1B). However we used the following simplifications:

- We considered that the binding or unbinding rate constant of a given binding site is independent from the occupancy state of the other sites (no intra-channel cooperativity). Under this assumption, the rate constant for Ca^{2+} binding at the first Ca^{2+} binding site, a_1, does not depend on whether the other two binding sites are bound or not. Thus, the rate constant for $\{000\}+$Ca $\rightarrow \{100\}$ has the same value as e.g. the reaction $\{011\} +$ Ca $\rightarrow \{111\}$ (where the triplet notation corresponds to the one defined in figure IV.1). Likewise, the rate constants for Ca^{2+} or IP$_3$ binding or unbinding to the three sites were considered independent from the other occupancy states.

- The open state is assumed to be state $\{110\}$ (first Ca site and IP$_3$ bound,

A Kinetic scheme

B IP3R model

C Spatial organization
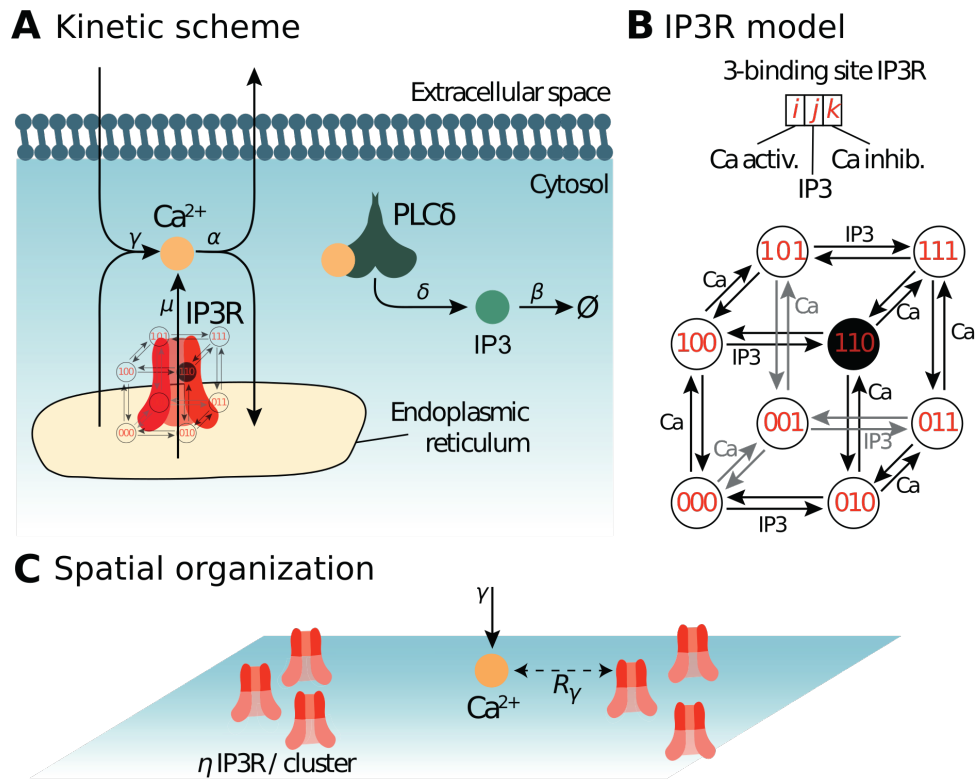
Figure IV.1: Reaction scheme and IP_3R model The biochemical processes included in the model are illustrated in (*A*): Cytosolic Ca^{2+} can exit the cytosol to the extracellular space or the endoplasmic reticulum (ER) at a (total) rate α, lumping together the effects of ER and plasma membrane pumps. Likewise, Ca^{2+} can enter the cytosol from the extracellular space or from the ER via IP_3R-independent flow, with (total) rate γ, emulating Ca^{2+} channels from the plasma membrane. When an IP_3R channel opens, Ca^{2+} enters the cytosol through the channel at rate μ. Phospholipase C δ (PLCδ), once activated by Ca^{2+} binding, produces IP_3 at rate δ. Like Ca^{2+}, IP_3 can bind the IP_3R channel and is removed with rate β. (*B*) Our model of the kinetics of the IP_3R channel is an 8-state Markov model adapted from [8, 308]. Each IP_3R channel monomer is associated with 3 binding sites, two Ca^{2+} binding sites and one IP_3 binding site. Occupancy states are designated by a triplet $\{i, j, k\}$ where i stands for the occupation of the first Ca binding site ($i = 1$ if bound, 0 else), j for that of the IP_3 binding site and k for the second Ca site. The first Ca^{2+} binding site has higher affinity than the second. The open state is state $\{110\}$, where the first Ca and the IP_3 sites are bound but not the second Ca site. (*C*) Spatial parameters for the particle-based model. The N_{IP3R} IP_3R molecules are positioned within uniformly distributed clusters, with η IP_3R in each cluster. Hence $\eta = 1$ corresponds to uniformly distributed IP_3R (no clustering), while the degree of clustering increases with η (for constant total IP_3R number). To account for potential co-localization between IP_3R-dependent and IP_3R-independent Ca^{2+} sources, the influx of IP_3R-independent Ca^{2+} (at rate γ) occurs within distance R_γ of an IP_3R. Thus, low values of R_γ emulate co-localization between IP_3R-dependent and IP_3R-independent Ca^{2+} influx sources.

second Ca site free), as in [308, 8]. These latter models further assume inter-channel cooperativity, where IP$_3$R channels assemble as tetramers of which at least three monomers must be in the open state for Ca^{2+} to be transferred. Here we neglected inter-channel cooperativity and considered that every single channel was open when in the open state i.e., as long as an IP$_3$R channel is open, it is assumed to inject Ca^{2+} in the cytosol at constant rate μ.

IV.1.2   Modeling approach

Monte Carlo simulations of the spatially-explicit stochastic particle-based model

We first modeled the kinetic scheme described in figure IV.1 with a lattice-free spatially-explicit stochastic particle-based model (see section III.4), referred to as "Particle-based" model below, in two spatial dimensions, with reflective boundary conditions. Each molecule of the system was explicitly modeled with its associated position in space. PLCδ and IP$_3$R molecules were considered immobile whereas Ca^{2+} and IP$_3$ molecules were mobile by diffusion. At the beginning of each Monte-Carlo (MC) simulation of this model, the space coordinates for each Ca^{2+}, IP$_3$ and PLCδ molecules were chosen uniformly at random.

To determine the positions of the N_{IP3R} IP$_3$R molecules, we first chose the centers of $N_c = N_{IP3R}/\eta$ IP$_3$R clusters uniformly at random in the reaction space, where η is the number of IP$_3$R channels per cluster (as illustrated in figure IV.1 C). For each cluster, we positioned η IP$_3$R molecules uniformly at random within a distance R_c of the cluster center, with $R_c = d_{IP3R}\sqrt{\eta/0.91}$, where d_{IP3R} is the interaction distance of the IP$_3$R, i.e. the maximal distance between IP$_3$R center and a Ca^{2+} or IP$_3$ molecule below which binding can occur. According to this algorithm, $\eta = 1$ corresponds to randomly distributed independent IP$_3$R molecules (no clustering) whereas IP$_3$R molecules become increasingly clustered when η increases, with constant IP$_3$R density within the clusters and constant total IP$_3$R number in the reaction space.

Each MC stimulation step (of duration Δt) consists in iterating the following steps:

- *Diffusion.* The position of each mobile molecule (Ca^{2+} and IP$_3$) is updated independently according to Brownian motion: $\mathbf{r}(t + \Delta t) = \mathbf{r}(t) + \sqrt{2D_i\Delta t}\xi$, where D_i, $i = \{Ca, IP3\}$ is molecule i diffusion coefficient and ξ is a vector of i.i.d. Gaussian-distributed random numbers with zero mean and unit variance.

In a subset of simulations, the new position of each mobile molecule was chosen at random in the reaction volume, i.e. $\mathbf{r}(t + \Delta t) = \zeta$ were ζ is a vector of i.i.d. random numbers uniformly distributed in $[0, L]$, with L the length of the spatial domain. We refer to this setting as "infinite" diffusion coefficients, $D = \infty$.

- *Binding.* For each Ca^{2+} ion close enough to a PLCδ to react (i.e. when the distance between both is less than the interaction radius of PLCδ), a new IP$_3$ molecule is created with probability $\delta \Delta t$ at the position of the PLCδ molecule. Likewise, each Ca^{2+} or IP$_3$ molecule close enough to an IP$_3$R molecule (i.e. within its interaction radius) can bind it depending on its occupancy state. If the IP$_3$ binding site is free, an IP$_3$ molecule binds with probability $a_2 \Delta t$. If one of the Ca sites is free, a Ca^{2+} ion binds the free site with probability $a_1 \Delta t$ (first Ca site) or $a_3 \Delta t$ (second Ca site). If both Ca sites are free, binding occurs to the first site with probability $a_1 \Delta t$ and to the second one with probability $(1 - a_1 \Delta t) a_3 \Delta t$.

- *Unbinding.* Each IP$_3$R molecule releases its bound Ca^{2+} or IP$_3$ molecules independently, with probability $b_1 \Delta t$ (first Ca site), $b_2 \Delta t$ (IP$_3$ site) and $b_3 \Delta t$ (second Ca site). Ca^{2+} or IP$_3$ molecules that bound the IP$_3$R at the previous (binding) step of the current time step do not unbind.

- *Removal.* Free cytosolic Ca^{2+} and IP$_3$ molecules are removed from the cytosol with probability $\alpha \Delta t$ and $\beta \Delta t$, respectively. Ca^{2+} and IP$_3$ molecules that unbound from IP$_3$R at the previous (unbinding) step of the current time step are not removed.

- *Ca^{2+} Influx.* For each IP$_3$R channel in the open state $\{110\}$, a new Ca^{2+} ion is created in the cytosol at the IP$_3$R position with probability $\mu \Delta t$. A new Ca^{2+} ion can also be created in the cytosol with probability $\gamma \Delta t$, mimicking Ca^{2+} influx from IP$_3$R-independent sources in the ER membrane or through the plasma membrane. Note that the position of this new Ca^{2+} is not uniform over space but depends on parameter R_γ and works as follows: an IP$_3$R molecule is chosen (uniformly) at random and the new Ca^{2+} ion is positioned uniformly at random within distance R_γ of the chosen IP$_3$R. Therefore low values of R_γ emulate co-localization between IP$_3$R-dependent and IP$_3$R-independent Ca^{2+} influx sources, whereas the location of IP$_3$R-independent Ca^{2+} influx is uniform over the reaction volume when R_γ becomes as large as the volume side length.

Table IV.1 gives the parameter values used in our 2D simulations, including the initial numbers of Ca^{2+}, PLCδ, IP$_3$ and IP$_3$R molecules.

Table IV.1: Parameter values and initial conditions of the 2D model. a.u : arbitrary unit. In 2d, by definition, a MC time unit is 100 Δt and one MC space unit is set by the interaction radius of IP$_3$R, i.e. $d_{\text{IP3R}} = 1.0$ MC space unit. δ, β, μ, γ, b_1, b_2 and b_3 are first order constants, in (MC time unit)$^{-1}$. Diffusion coefficients D_{Ca} and D_{IP3} are expressed in (MC space unit)^2.(MC time unit)$^{-1}$ whereas α, a_1, a_2, a_3 are expressed in (MC space unit)^2.(MC time unit)$^{-1}$.

Parameter	Description	Value in 2d model
V	Cell volume	200×200 a.u.
	IP$_3$ dynamics	
IP_0	Initial IP$_3$ number	15 molec.
D_{IP3}	IP$_3$ diffusion	10 a.u
N_{plc}	PLCδ number	1000 molec.
δ	PLCδ max rate	0.1 a.u
β	IP$_3$ decay	0.01 a.u
	Ca^{2+} dynamics	
Ca_0	Initial Ca^{2+} number	50 molec.
D_{Ca}	Ca^{2+} diffusion	varied
μ	Ca^{2+} flux through open IP$_3$R	50 a.u
γ	Cytosolic Ca^{2+} influx	50 a.u
α	Ca^{2+} decay rate	1.0 a.u
	IP$_3$R	
N_{IP3R}	IP$_3$R number	1000 molec.
d_{IP3R}	IP$_3$R interact. distance	1 space unit
	IP$_3$R binding	
a_1	First Ca	1.0 a.u
a_2	IP$_3$	1.0 a.u
a_3	Second Ca	0.1 a.u
	IP$_3$R dissociation	
b_1	First Ca	0.1 a.u
b_2	IP$_3$	0.1 a.u
b_3	Second Ca	0.1 a.u

Mean-field (MF) dynamics of the perfectly stirred model

With infinite diffusion, the dynamics of the system can be assumed to be perfectly stirred. With that mean-field (MF) assumption, the temporal dynamics of reaction scheme figure IV.1 can be modeled using ordinary differential equations based on the mass-action law (see section III.1). IP_3R dynamics in these conditions can be described with seven ODEs that express the temporal dynamics of the concentration of IP_3R in state $\{ijk\}$, $[ijk]$:

$$
\begin{cases}
d[000]/dt = -(a_1[Ca] + a_2[IP3] + a_3[Ca])[000] + b_1[100] + b_2[010] + b_3[001] \\
d[001]/dt = -(a_1[Ca] + a_2[IP3] + b_3)[001] + b_1[101] + b_2[011] + a_3[Ca][000] \\
d[010]/dt = -(a_1[Ca] + b_2 + a_3[Ca])[010] + b_1[110] + a_2[IP3][000] + b_3[011] \\
d[011]/dt = -(a_1[Ca] + b_2 + b_3)[011] + b_1[111] + a_2[IP3][001] + a_3[Ca][010] \\
d[100]/dt = -(b_1 + a_2[IP3] + a_3[Ca])[100] + a_1[Ca][000] + b_2[110] + b_3[101] \\
d[101]/dt = -(b_1 + a_2[IP3] + b_3)[101] + a_1[Ca][001] + b_2[111] + a_3[Ca][100] \\
d[110]/dt = -(b_1 + b_2 + a_3[Ca])[110] + a_1[Ca][010] + a_2[IP3][100] + b_3[111]
\end{cases}
$$
$$\text{(IV.1)}$$

where $[Ca]$ and $[IP_3]$ denote Ca^{2+} and IP_3 concentration, respectively. The concentration of the eighth occupancy state, $\{111\}$ is obtained from conservation of the IP_3R, i.e. $[1111] = N_{IP3R}/V - ([000] + [001] + [010] + [011] + [100] + [101] + [110])$. IP_3 dynamics in the mean-field model is given by :

$$
d[IP3]/dt = -a_2[IP3]\sum_{i=0}^{1}\sum_{k=0}^{1}[i0k] + b_2\sum_{i=0}^{1}\sum_{k=0}^{1}[i1k] + \delta[PLC\delta][Ca] - \beta[IP3] \quad \text{(IV.2)}
$$

where $[PLC\delta] = N_{\text{plc}}/V$. Finally, the mean-field dynamics of the free Ca^{2+} is obtained with:

$$
\begin{aligned}
d[Ca]/dt = &-\left(a_1\sum_{j=0}^{1}\sum_{k=0}^{1}[0jk] + a_3\sum_{i=0}^{1}\sum_{j=0}^{1}[ij0]\right)[Ca] \\
&+ b_1\sum_{j=0}^{1}\sum_{k=0}^{1}[1jk] + b_3\sum_{i=0}^{1}\sum_{j=0}^{1}[ij1] \\
&- \alpha[Ca] + \gamma + \mu[110]
\end{aligned}
\quad \text{(IV.3)}
$$

For comparison with the output of the other models, the concentrations were transformed into numbers of molecules by multiplication by the reaction volume V.

Perfectly-stirred stochastic temporal dynamics (SSA)

For comparison, we also modeled the reaction scheme depicted in Figure IV.1 using Gillespie's exact SSA that accounts for stochasticity due to low copy numbers

and assumes perfect mixing of the reactants [346, 355] (see section III.2). In this
model, the dynamic variables are the number of Ca^{2+} and IP$_3$ molecules in the sys-
tem, N_{Ca} and N_{IP3} and the number of IP$_3$R channels in state $\{ijk\}$, N_{ijk}. The rates
of all the reactions of the scheme of figure IV.1 are then calculated according to
mass-action laws like in the MF model of eq. (IV.1,IV.2,IV.3). For instance, at reac-
tion time t, the rate of reaction $\{001\} + Ca \rightarrow \{101\}$ is given by $a_2/V N_{001}(t) N_{Ca}(t)$.
The next reaction time τ is sampled from an exponential distribution with mean
$1/R_T$, where R_T is the sum of the reaction rates of all reactions. The next re-
action to occur at time $t + \tau$ is chosen as an integer random variable with point
probability given by the ratio of its rate to R_T. For instance, for the reaction illus-
trated above, the probability that this reaction is the one occurring at time $t + \tau$ is
$a_2/V N_{001}(t) N_{Ca}(t)/R_T$. Finally, the variables are updated according to the chosen
reaction. In the data presented below, we have modeled each receptor individu-
ally, i.e. for each receptor $l \in 0 \ldots N_{IP3R}$, $N_{ijk}^l = 1$ if receptor l is in state ijk, 0
else. If the illustration reaction described above on receptor l is chosen, this means
$N_{001}^l(t + \tau) = N_{001}^l(t) - 1$, $N_{Ca}(t + \tau) = N_{Ca}(t) - 1$ and $N_{101}^l(t + \tau) = N_{101}^l(t) + 1$.
The other variables keep their values.

Simulation code

The code of the ODE, Gillespie and Particle-based models is available on Mod-
elDB at http://modeldb.yale.edu/247694.

Peak detection and analysis

In order to characterize Ca^{2+} dynamics, Ca^{2+} peaks were isolated and analyzed.
They correspond to transient increases of the concentration of Ca^{2+}. Automated
peak detection from the model simulations was based on the statistics of baseline
Ca^{2+} trace. A histogram of Ca^{2+} trace was built with a bin size of 0.25 ions and
the mode of this histogram was used to define baseline Ca^{2+}. A peak initiation
corresponded to the time step where Ca^{2+} trace overcame a peak threshold defined
as baseline $+ n\sigma_{Ca}$ where σ_{Ca} is the standard deviation of the above histogram. The
value of n varied between 2 and 4 and was set by hand for each simulation, depending
on its signal/noise ratio. The peak was considered terminated when the Ca^{2+} trace
decreased again below peak threshold. This implies that in case of a second Ca^{2+}
peak starting before the first one terminated, both events were considered as being
part of the same peak. Peak duration was defined as the time between peak initiation
and termination. Peak amplitude was defined as the maximum number of Ca^{2+} ions

reached during the peak duration. The number of IP$_3$R open per peak was defined
as the maximum number of IP$_3$R open simultaneously during peak duration. Puffs
were defined as Ca^{2+} events resulting from the cooperation of more than one IP$_3$R.
In our spatially-explicit simulations, a Ca^{2+} signal was considered to be a puff if
more than one IP$_3$R were open during the peak and if the average distance traveled
by Ca^{2+} within the duration of this peak was larger than the distance between the
simultaneously open IP$_3$R molecules.

IV.2   Results: effect of spatial properties on spontaneous Ca^{2+} activity in the 2D model

IV.2.1   Spontaneous oscillations of the 2D model

We first analyzed our particle-based model for the CICR signaling system of
Fig IV.1. To that end, we compared Monte-Carlo simulations of the particle-based
model in two dimensions with the corresponding Mean-Field and Gillespie's SSA
models (see Methods section). Those three models represent three different levels
of approximation: the Mean-Field model assumes deterministic kinetics and perfect
mixing; the SSA model keeps the perfect mixing hypothesis but assumes stochas-
tic kinetics while the particle-based model assumes stochastic kinetics but accounts
for potential non-perfect mixing, i.e. diffusion effects. For comparison with SSA,
we first considered perfect mixing of Ca^{2+} ions and IP$_3$ molecules in the particle-
based model by setting the diffusion coefficients $D_{Ca} = D_{IP3} = \infty$ (see section IV.1).

Fig IV.2A shows one simulation sample for each model. A first result is that the
stochastic models (SSA and particle-based) do exhibit spontaneous Ca^{2+} peaks with
the parameters of this figure. On top of a background level of roughly 50 Ca^{2+} ions,
with fluctuations of roughly ± 20 ions, large and fast peaks arise spontaneously with
a total amplitude between 20 and 120 ions above the baseline. In strong opposition,
the (deterministic) mean-field model does not show these oscillations: one gets a sta-
tionary trace, that systematically coincides with the baseline level of the stochastic
traces (Fig IV.2B). Comparing the two stochastic models (SSA and particle-based)
indicates that both display the same basal Ca^{2+} level (Fig IV.2B) and the same fre-
quency, mean peak amplitude and duration (Fig IV.2C). Altogether, this suggests
that stochasticity is necessary for spontaneous Ca^{2+} signals to occur in this model.

We next searched for the dynamical mechanism that gives rise to those sponta-
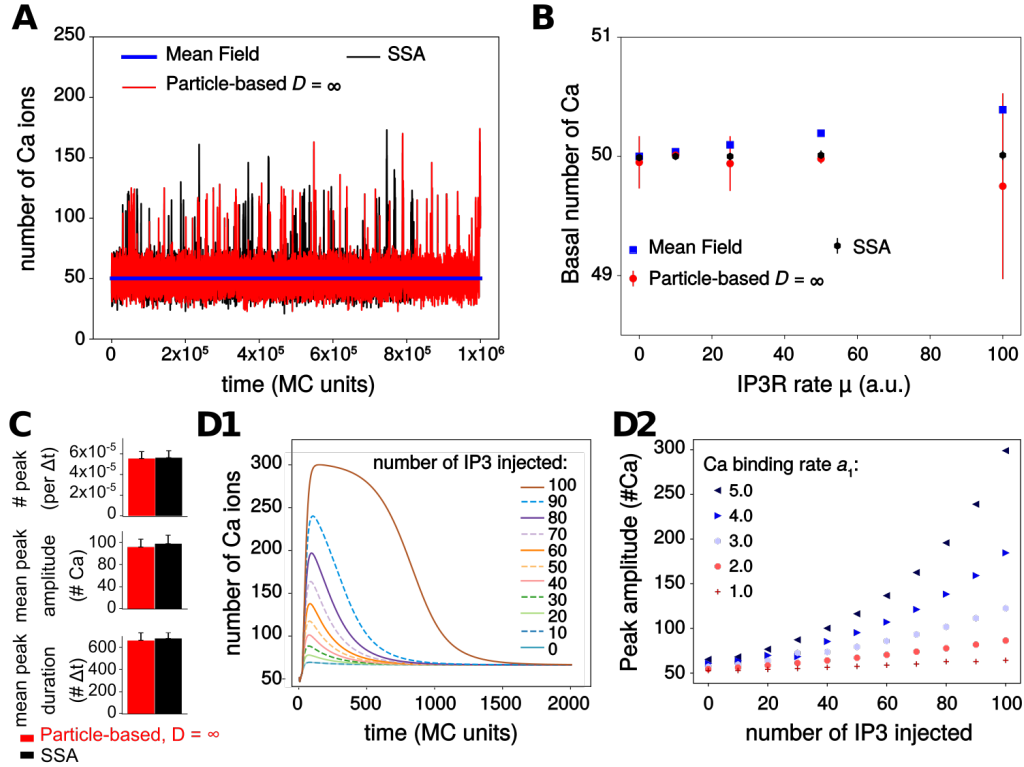
Figure IV.2: 2D model exploration. (*A*) Spontaneous transients are observed in simulations of the particle-based and the Gillespie's SSA model but not in the Mean Field model. (*B*) The three models display the same basal Ca^{2+} level when μ, the Ca^{2+} influx rate through open IP_3R channels, increases. The higher variability in the stochastic models reflects the integer value of basal Ca^{2+} (either 49 or 50, depending on simulations). (*C*) Quantification of Ca^{2+} transients in the stochastic models (Ca^{2+} peak frequency, mean peak amplitude and mean peak duration). No significant difference between the two models was observed. (*D*) Excitability of the Mean-Field model: increasing quantities of exogenous IP_3 molecules were injected at time $t = 20\Delta t$, after model equilibration. The amplitude of the resulting Ca^{2+} response (*D1*) was quantified depending on the amount of IP_3 injected and the value of the binding rate constant to the first Ca^{2+} IP_3R site, a_1 (*D2*). Parameter values for the particle-based model: $D_{Ca} = D_{IP3} = \infty$ (perfect mixing) and $\eta = 1$, $R_\gamma = 200$, i.e. no IP_3R channels clustering, and no co-localization of IP_3R with IP_3R-independent Ca^{2+} sources. For SSA and particle-based models, the figure shows the average $\pm$ standard deviation over 20 simulations.

neous peaks. A thorough numerical parameter exploration of the mean-field model failed to demonstrate the existence of Hopf bifurcations or of any other bifurcation that would generate limit-cycle oscillations in the model. This is a distinctive feature of our model, since spontaneous oscillations in the vast majority of IP_3R-mediated Ca^{2+} signaling models arise from limit-cycle generating bifurcations [8, 300, 302]. This is however not unexpected since the simplifications made to derive our model significantly reduced its nonlinearity compared to these models, and the emergence of limit-cycle bifurcations demands strong nonlinearity. For instance, limit-cycle oscillations in the classical Li-Rinzel model [302] disappear when IP_3R opening needs less than three open monomers . However, our model retains enough nonlinearity to exhibit excitability. To evidence this, we used the mean-field model, waited until all concentrations reached their stationary state, and injected an increasing amount of exogenous IP_3 molecules. In response to this IP_3 injection, a Ca^{2+} transient was obtained, before relaxation to the stationary state (Fig IV.2D). Fig IV.2D2 shows how the resulting transient amplitude depends on the amount of injected IP_3. For low values of IP_3R Ca^{2+} binding rate (first site), a_1, the Ca^{2+} response is basically linear with the number of injected IP_3: doubling the amount of IP_3 injected only doubles the amplitude of the Ca^{2+} response. However, as a_1 increases, peak amplitude becomes a strongly nonlinear function of the number of IP_3 injected. With $a_1 = 5$ a.u. for instance, doubling the number of injected IP_3 from 50 to 100, results in an almost threefold increase of the Ca^{2+} response. Therefore the mean-field model with large values of a_1 is an excitable system that amplifies the fluctuations of IP_3 in its Ca^{2+} responses. We conclude that spontaneous Ca^{2+} transients occur in the system of Fig IV.1 through the interplay of the stochasticity of the SSA or particle-based models and the underlying excitability of the system.

IV.2.2 Transitions between Ca^{2+} activity regimes

The experimental and modeling literature on intracellular Ca^{2+} signals distinguishes two classes of localized Ca^{2+} peaks: puffs and blips [532] (see Fig II.9). Blips refer to brief and weak peaks that correspond to the opening of a single IP_3R channel (or a single IP_3R channel tetramer), whereas puffs are peaks of larger duration and amplitude, resulting from the concerted opening of a group of nearby IP_3R channels (or tetramers thereof), via the Ca^{2+}-induced Ca^{2+}-release principle. We next examined whether our model was able to reproduce these observations.

We carried out parameter exploration of the particle-based model in conditions of perfect mixing for mobile molecules (Ca and IP_3) and uniform spatial distribu-

tion of the immobile ones (PLCδ, IP$_3$R). As expected, we found that Ca^{2+} peaks frequency depends on parameter values (Fig IV.3A). When the rate of Ca^{2+} influx through open IP$_3$R channels μ or the binding rate constant to the first Ca IP$_3$R site a_1 are too small, the model does not exhibit Ca^{2+} peaks at all, only fluctuations around a stationary state (Fig IV.3C★). This is in agreement with our analysis of the systems excitability above, that demonstrated excitability only for large enough values of a_1 (Figure IV.2D2). Note however that in the model, IP$_3$R openings do not necessarily lead to a Ca^{2+} peak, especially for low values of both μ and a_1 (Fig IV.3C★). Spontaneous Ca^{2+} transients are obtained in the particle-based model beyond threshold of (μ, a_1) values, with a peak frequency that increases with parameters values (Fig IV.3A). Inspection of the maximal number of open IP$_3$R per peak, defined as the average over 20 simulations of the maximum number of open IP$_3$R per peak per simulation, reveals that not only the frequency, but also the type of these transient signals changes with parameters values (Fig IV.3A): the less frequent signals are generally associated with a single open IP$_3$R per peak (Fig IV.3C■), corresponding to blips, whereas the high-frequency spontaneous signals rely on the opening of $2 - 12$ IP$_3$R in a peak (Fig IV.3C●), corresponding to puffs. In agreement with experimental observations[265, 264], Ca^{2+} puffs in the particle-based model are characterized by higher peak amplitude and peak duration compared to blips.

Taken together, these results show that our particle-based model not only reproduces the existence of spontaneous Ca^{2+} peaks in conditions of low copy numbers, but is also able to reproduce the existence of different types of localized Ca^{2+} transients, in agreement with experimental measurements.

IV.2.3 Impact of Ca^{2+} diffusion coefficient on Ca^{2+} signals

Flegg et al [543] have demonstrated the necessity to account for the stochasticity inherent to Ca^{2+} diffusion when modeling Ca^{2+} signaling in small volumes. We next investigated the impact of Ca^{2+} diffusion on Ca^{2+} dynamics in the particle-based model. In neurons or astrocytes, the amount of endogenous Ca^{2+} buffers is large so that the diffusion distance of free Ca^{2+} is believed to be very small. Many of the endogenous buffers are however mobile. Buffers can have a very significant effect on Ca^{2+} dynamics because they decrease the diffusion distance and the effective diffusion coefficient of Ca^{2+} ions [544, 530, 545, 546, 547, 548]. Here, we have chosen not to include buffers explicitly in the model for the sake of model simplicity, but to account for their presence by decreasing the diffusion coefficient for Ca^{2+}. Therefore, the latter is to be interpreted as an effective diffusion coefficient lumping together Ca^{2+} buffering by mobile endogenous buffer and diffusion of these buffers.
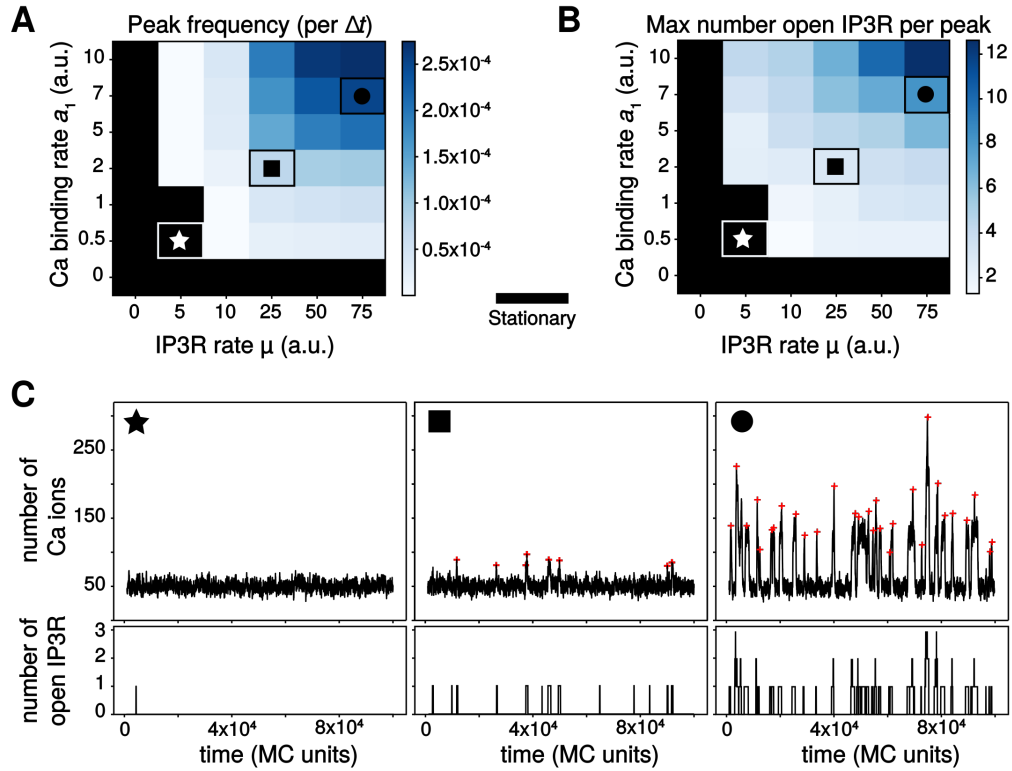
Figure IV.3: The particle-based model produces different Ca^{2+} activity regimes depending on parameter values. Color-coded map of variation of the peak frequency, expressed as the number of Ca^{2+} peaks per MC time step (*A*) and as the maximal number of IP_3R channel open per peak (*B*). The color scale is given for each map. The black area corresponds to the stationary regime. Note that the x and y-axis scales in (*A*) and (*B*) are not regularly spaced. The symbols ★, ■ and ● locate parameter pairs that are illustrative of the three dynamical regimes shown in (*C*): stationary (★, $\mu = 5, a_1 = 0.5$), blips (■, $\mu = 25, a_1 = 2$) and puffs (●, $\mu = 75, a_1 = 7$). Red crosses show the locations of peaks from automatic detection. $D_{Ca} = D_{IP3} = \infty$, $\eta = 1$, $R_\gamma = 200$.

To confirm that explicit addition of buffers yields effects similar to a decrease of the Ca^{2+} diffusion coefficient, we have both developed a mean field model of Ca^{2+} buffering (see Appendix A.2.1.1) and a version of the 2D model described here in which endogenous buffer molecules where explicitly added and in which the coefficient of diffusion was low for buffers and high for free Ca^{2+} ions (see Appendix A.2.1.2). These simulations confirm the absence of significant difference between simulations obtained using fast Ca^{2+} diffusion and slow explicit buffers on the one hand, and our reference model without buffers but with an effective lower D_{Ca} on the other hand (see Appendix A.2.1.2).

Moreover, several plasma membrane proteins, in particular the Na^+-Ca^{2+} exchanger (NCX) have been observed to co-localize with ER proteins in neurons and astrocytes [495]. Such a co-localization of Ca^{2+} signaling molecules might imply spatial organizations including raft-like micro-domains. This organization seems essential for Ca^{2+} wave propagation in astrocytes [496]. mGluR5-ER proteins co-clusters have also been revealed in astrocytic processes and are mediated by an interaction with Homer1 scaffold protein [497]. Homer1 is also known for increasing Ca^{2+} activity in neurons by increasing IP_3R-mGluR5 proximity [282]. Those experimental studies suggest that several Ca^{2+} sources are co-localized with ER proteins in astrocytes and that it might alter Ca^{2+} dynamics. Such a co-localization could be crucial for Ca^{2+} signaling, in particular in small volumes. We thus placed our study of the influence of Ca^{2+} mobility on Ca^{2+} signaling in a framework where Ca^{2+} sources (IP_3R-dependent and IP_3R-independent) can co-localize.

To this end, the IP_3R-independent Ca^{2+} influx in the cytosol (from e.g. plasma membrane transporters or channels) was made dependent on parameter R_γ, that sets the distance from IP_3R receptors within which new Ca^{2+} ions are injected in the cytosol when they originate from IP_3R-independent fluxes (see Methods section). When $R_\gamma = 0$, the initial location of the new Ca^{2+} ion is shared with an IP_3R channel whereas when R_γ increases, the injection positions of new Ca^{2+} ions are increasingly uncorrelated from those of the IP_3R channels. When R_γ becomes as large as the size of the reaction surface (i.e. for $R_\gamma = 100$), the injection position of the new Ca^{2+} ion is effectively independent of the positions of the IP_3R channels.

Our simulations show that the impact of the Ca^{2+} diffusion coefficient is mainly visible when Ca^{2+} sources are co-localized, i.e. for small values of R_γ. Figures IV.4A-B compare a representative simulation obtained when Ca^{2+} diffuses slowly (A) with a simulation obtained with perfectly-mixed Ca^{2+} (B), in a case where the IP_3R receptors are not clustered ($\eta = 1$). Those representative simulations hint that the peak frequency is much larger with slow Ca^{2+}, and suggests that slow Ca^{2+} diffusion slightly favors the puff regime compared to perfect mixing. The systematic quantifi-
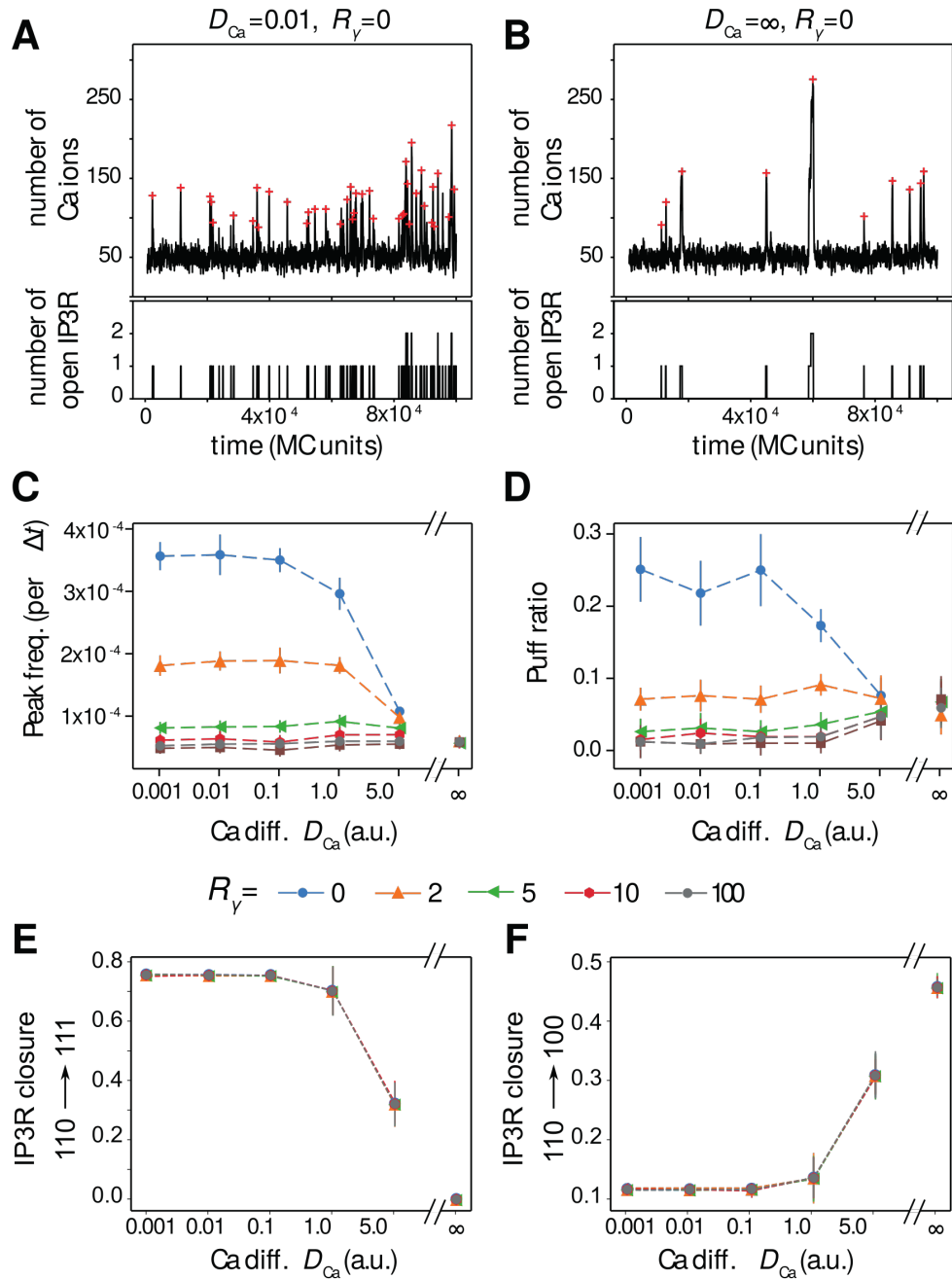
Figure IV.4: Ca^{2+}**diffusion modulates the temporal characteristics of the signals upon
co-localization.** Representative simulations of the particle-based model showing both Ca^{2+}
trace and number of open IP_3R for co-localized Ca^{2+} sources ($R_\gamma = 0$) in the case of slow
Ca^{2+} diffusion (A) or perfect-mixing of Ca^{2+} (B). The red crosses show peak locations from
automatic detection. The impact of Ca^{2+} diffusion coefficient D_{Ca} on peak frequency (C)
and the amount of puff (D) are shown for different values of the co-localization parameter R_γ:
from $R_\gamma = 0$ (IP_3R are not clustered but co-localized with other Ca^{2+} sources) to $R_\gamma = 100$
(IP_3R are neither clustered nor co-localized). The puff ratio quantifies the fraction of peaks
that are puffs. (E) and (F) respectively present the probabilities that IP_3R closure results from
binding of a Ca^{2+} to the inactivating site (probability to switch to state $\{111\}$, $P_{110->111}$) or
unbinding of an IP_3 (probability to switch to state $\{100\}$, $P_{110->100}$) depending on D_{Ca} and
on R_γ. Probability of closure due to Ca^{2+} unbinding from activating site, $P_{110->010}$ can be
deduced from $1 = P_{110->010} + P_{110->100} + P_{110->111}$. Data are presented as mean $\pm$ standard
deviation over 20 simulations. Lines are guide for the eyes. Note that the x-axis scales in (C),
(D), (E) and (F) are not regularly spaced. Other parameters: $\eta = 1$ (no clustering), $a_1 = 1$,

cation of figure IV.4C-D confirms these interpretations: when IP_3R-dependent and IP_3R-independent Ca^{2+} sources are co-localized, i.e. for $R_\gamma < 5$, the value of D_{Ca} controls Ca^{2+} transient frequency, as well as the probability to observe a puff. The effects are strong: for instance for $R_\gamma = 0$, decreasing D_{Ca} from 5 to 0.1 increases the frequency roughly threefold. However, when the IP_3R-independent influx was not co-localized with IP_3R channels (i.e. for $R_\gamma \geq 5$), both the peak frequency and the type of signal were found not to depend on the Ca^{2+} diffusion coefficient anymore. Those results suggest that Ca^{2+} diffusivity could control the frequency and type of Ca^{2+} signals within astrocytes when IP_3R channels are co-localized with IP_3R-independent Ca^{2+} sources.

Once open, i.e in state $\{110\}$, the IP_3R can switch to state $\{111\}$ with probability $P_{110->111}$, due to binding of Ca^{2+} to the inactivating site. Open receptors can also switch to state $\{100\}$ (or $\{010\}$) with probability $P_{110->100}$ (or $P_{110->010}$, respectively), due to the unbinding of IP_3 (or of Ca^{2+}, respectively) from the activating site. Fig IV.4E-F shows how the probabilities $P_{110->111}$ and $P_{110->100}$ vary with D_{Ca} and R_γ ($P_{110->010}$ can be deduced from $1 = P_{110->010} + P_{110->100} + P_{110->111}$). In contrast, R_γ has no significant effect on $P_{110->111}$, $P_{110->100}$ and $P_{110->010}$ probabilities. The effect of the effective diffusion coefficient D_{Ca} is strong: when low, most of IP_3R closure is due to the binding of Ca^{2+} to the inhibiting site. As D_{Ca} increases, $P_{110->111}$ decreases and in well-mixed conditions ($D_{Ca} = \infty$), IP_3R closure is always due to the stochastic unbinding of IP_3 and Ca^{2+}. So, receptor closure is strongly dominated by binding of Ca^{2+} to the inactivating site when Ca^{2+} effective diffusion is slow, but mostly relies on unbinding from the activating sites for fast Ca^{2+} effective diffusion. This result illustrates that well-mixed simulations are not well-suited to study the self-inhibiting behaviour of IP_3R, i.e the fact that the Ca^{2+} influx resulting from the opening of a given IP_3R can subsequently shut down this very receptor. Therefore accounting for diffusion with spatial models appears necessary to the study of the dynamics of IP_3R at the single-receptor scale.

IV.2.4 IP_3R clustering controls Ca^{2+} signals when co-localized

Experimental data demonstrate that IP_3R in SH-SY5Y and COS7 cells are not uniformly distributed on the ER membrane but form clusters [264, 265]. We next investigated the impact of IP_3R clustering on Ca^{2+} signal dynamics in our particle-based model. Simulations were performed with $D_{ca}=0.1$ and various amounts of co-localization between IP_3R channels and other Ca^{2+} sources (parameter R_γ). Representative simulations for uniformly-distributed IP_3R channels ($\eta = 1$) and strongly clustered IP_3R ($\eta = 50$) are presented in figure IV.5A-B. In these two examples, the IP_3R were weakly co-localized with the IP_3-independent Ca^{2+} sources

(i.e. $R_\gamma = 10$). These traces indicate that the frequency and type of Ca^{2+} signal in this case is heavily dependent on the spatial distribution of IP$_3$R channels: clustered IP$_3$R seem to exhibit much larger peak frequency and slightly more frequent puffs. However, here again this effect is quite mitigated by the amount of co-localization between IP$_3$R channels and the IP$_3$R-independent Ca^{2+} sources. In particular, the dynamical range of the modulation by IP$_3$R cluster size η (i.e. the ratio between the frequency at $\eta = 50$ and $\eta = 1$) is maximal for intermediate co-localizations ($2 \leq R_\gamma \leq 10$) but the Ca^{2+} peak frequency is hardly dependent on η when co-localization is either very strong ($R_\gamma < 2$) or very weak ($R_\gamma \geq 50$). Increasing clustering also tends to improve the emergence of puffs, although the effect is significant only for strong co-localization ($R_\gamma \leq 2$, Fig IV.5D). We emphasize that in such cases of strong co-localization, the regime of Ca^{2+} activity (puffs *vs* blips) changes by simply rearranging the spatial distribution of the IP$_3$Rs, without changing any of the kinetics parameters of the model.

Taken together, those simulation results pinpoint the interplay between Ca^{2+} source co-localization and the degree of IP$_3$R clustering as a crucial modulator of temporal characteristics of the Ca^{2+} signals and of the signaling regime. In particular, they suggest that in the presence of certain amount of co-localization between IP$_3$R channels and other sources of Ca^{2+} influx in the cytosol the spontaneous Ca^{2+} peak frequency can have a large amplitude variation. Within this range of parameters, Ca^{2+} peak frequency can be finely tuned by the geometry of the colocalization.

IV.3   Discussion

IP$_3$R subunits cooperativity and spontaneous signals

IP$_3$R channels assemble as tetramers and a recent experimental study suggested that the four subunits of the tetramer must be simultaneously bound to IP$_3$ for the tetramer to allow Ca^{2+} influx, independently of cytosolic Ca^{2+} or ATP concentrations [275] (see section II.2). Actually, the original IP$_3$R models predicted that subunit cooperativity for Ca^{2+} binding is also necessary to fit experimental data of IP$_3$R dynamics [8, 302]. Even though the IP$_3$R binding sites for Ca^{2+} have been characterized, their roles in IP$_3$R dynamics are still poorly understood [274]. The requirement for inter-subunit cooperativity, in which the 4 IP$_3$ binding sites should simultaneously be bound for the tetramer to open, is expected to hinder the emergence of spontaneous Ca^{2+} events. In a subset of simulations, we have replaced our non-cooperative IP$_3$R model, in which the binding of a single IP$_3$ site is enough to open the monomer channel, with the cooperative model proposed by Bicknell and
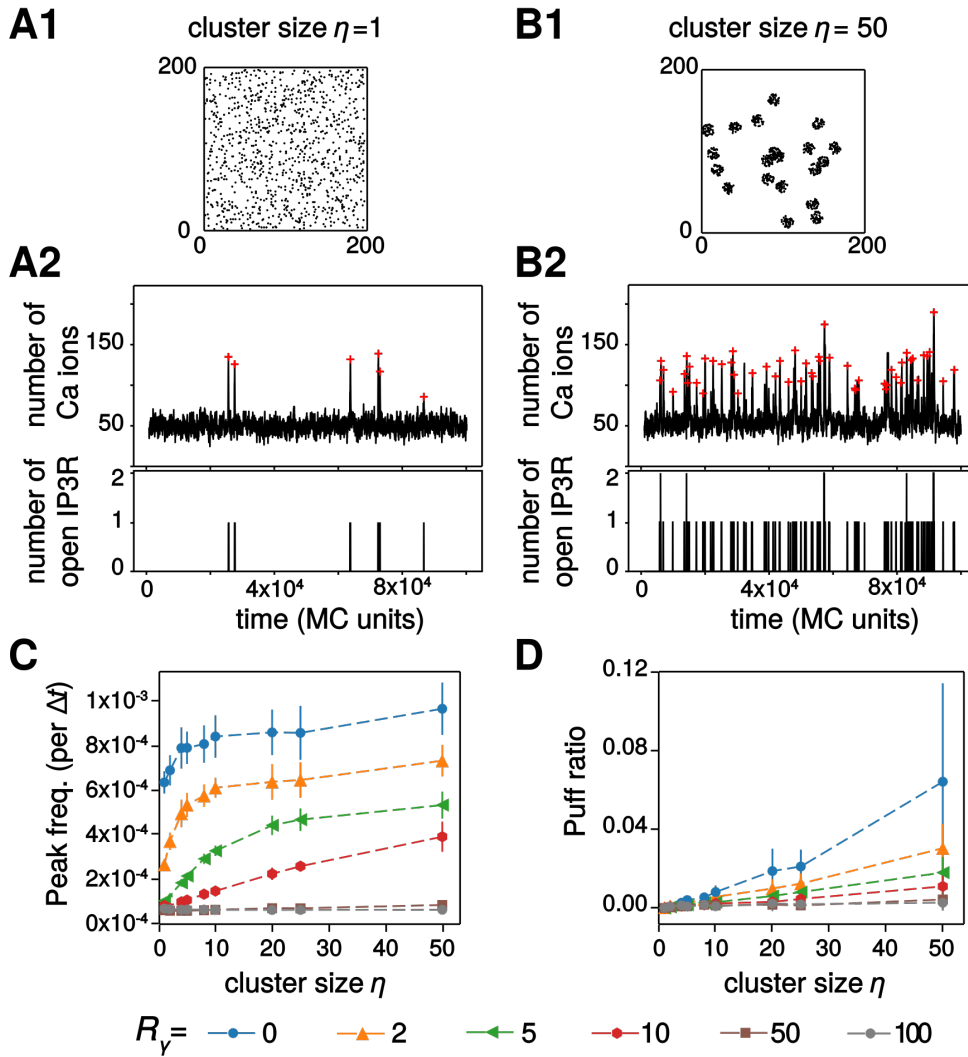
Figure IV.5: IP_3R clustering modulates Ca^{2+} signals when co-localized. Representative simulations of the particle-based model with the corresponding IP_3R distribution over space, the Ca^{2+} trace and number of open IP_3R for weakly co-localized Ca^{2+} sources ($R_\gamma = 10$) in the case of uniform distribution of the IP_3R (*A*) or strongly clustered IP_3R (*B*) are illustrated. The red crosses show peak locations from automatic detection. The impact of IP_3R cluster size η on Ca^{2+} peak frequency (*C*) and on the amount of puffs (*D*) are shown for different values of the cluster size: from $\eta = 1$ (IP_3R are not clustered) to $\eta = 50$ (strong clustering). Data are presented as mean $\pm$ standard deviation over 20 simulations. Lines are guide for the eyes. Other parameters : $D_{Ca} = 0.1$, $a_1 = 1$, $\mu = 50$.

collaborators [549]. With 100 nM basal IP_3 and Ca^{2+} [550, 551], we could not produce spontaneous Ca^{2+} signals, even after a search of the parameter space to locate parameters allowing spontaneous activity with this cooperative model. This issue might reflect a general problem of the De Young Keizer model in discrete particle-based models with low copy number of particles. The De Young-Keizer model is based on steady-state experimental data representing averages over time and over channel populations, which proved sufficient to reproduce experimental statistics such as the average open time or the steady-state open probability. However, this model might not be suited to describe behaviors at the level of individual channels and low copy number of particles. More recent models have been proposed that successfully reproduce the evolution with time of the open/close dynamics of a single IP_3R [380, 381]. In those models, the transition rates between different states of the IP_3R are not triggered by Ca^{2+} or IP_3 binding events but by complex continuous functions of their concentrations (see section III.2). We could not implement such complicated functions with a pure particle-based modeling strategy such as used here. Therefore, further investigation is needed to clarify the suitability of the De Young-Keizer model in the context of particle-based spatially-explicit stochastic models. Alternatively, our results may be interpreted as casting doubts on the existence of spontaneous Ca^{2+} signals in astrocytes when the basal IP_3 and Ca^{2+} concentrations are of the order of 100 nM (see also section V.3).

Varying IP_3R affinity for Ca^{2+} and the effective D_{Ca} as a mechanism for Ca^{2+} signals diversity

In our model, the value of the rate constant for Ca^{2+} binding to IP_3R changes the type of spontaneous dynamics (e.g. blips vs puffs) in addition to its characteristics (frequency, amplitude). Experimentally, several post-transcriptional mechanisms can modulate IP_3R affinity. For instance, phosphorylation of type-1 and -2 IP_3R by cAMP-activated PKA increases the affinity of IP_3R to Ca^{2+} and IP_3 [278]. At a larger time scale, the sensitivity of IP_3R to Ca^{2+} is encoded in a sequence of Ca^{2+} sensor (Cas) region that differs depending on the IP_3R isoform [552, 553, 266]. Since multiple IP_3R isoforms seem to be involved in Ca^{2+} signaling within astrocytic processes [260], they could assemble into a variety of homo- or hetero- IP_3R tetramers that would exhibit a range of Ca^{2+} and IP_3 affinity.

In addition, immobile or weakly mobile endogenous Ca^{2+} buffers are responsible for an effective intracellular Ca^{2+} diffusion that is an order of magnitude slower than free Ca^{2+} ions [554]. The variability of these endogenous Ca^{2+} buffers, with various kinetics and various diffusion coefficients, is large [555]. Some of them are overexpressed in hippocampal and striatal astrocytes, possibly in a region-specific

pattern [28]. Our simulation results indicate that the value of the effective Ca^{2+}
mobility also participates in the determination of the type and characteristics of
the spontaneous events, thus confirming previous modeling approaches [543]. Such
a regional differential expression of the genes coding for endogenous Ca^{2+} buffers
could thus be involved in the regional variability of astrocytic Ca^{2+} signaling [64].

Therefore, the IP_3R repertoire, the post-transcriptional regulation of IP_3R affin-
ity and the differential expression of endogenous Ca^{2+} buffers could also be potential
determinants allowing a range of responsiveness and spatio-temporal characteristics
of Ca^{2+} signals in astrocyte processes.

IP_3R clustering as a potential mechanism for plastic information process-ing in astrocytes

For simplicity, IP_3R clustering in our model was considered static during sim-
ulation time. Experimentally, though, IP_3R clustering might be highly dynamic
[556, 557] even if reported not dynamic over minutes in HelA cells [480]. Several
molecules can trigger IP_3R clustering, including IP_3 and Ca^{2+} themselves [557, 556],
through a mechanism that may include the lateral diffusion of IP_3R on the ER sur-
face [557] or be independent from it [558]. Beyond this IP_3R classification into
clustered and un-clustered populations, another approach is to quantify single IP_3R
channels based on their mobility. A recent study on HeLa cells [480] indicates that
Ca^{2+} signals emerge most of the time from immobile IP_3R channels, which are found
in apposition to ER-plasma membrane junctions, whereas the mobile IP_3R fraction
would not be involved in Ca^{2+} influx. Our simulation results, in agreement with pre-
vious IP_3R-mediated Ca^{2+} models [369, 533], indicate that IP_3R clustering can lead
to an increase of the frequency and amplitude of their Ca^{2+} signals. This result is in
contradiction with a previous modeling study that concluded in favor of a reduction
of IP_3R channel activity upon IP_3R clustering [536]. This discrepancy might rely
on the different modeling choices. In particular, the model in [536] incorporates a
5-state IP_3R model derived from [552, 559]. All of those modeling studies however
agree that dynamical IP_3R clustering could be a mechanism used by astrocyte pro-
cesses to modulate their Ca^{2+} signals. This could provide astrocyte processes with
a capacity for information processing plasticity.

Conclusion

In this chapter, a 2D individual-based model has been presented to investigate
intracellular Ca^{2+} signaling based on CICR in small sub-cellular volumes. Simula-

tions of the model show that spontaneous Ca^{2+} signals arise in the model via the interplay between the excitability of the system and its stochasticity. The model accounts for both types of Ca^{2+} signals in astrocytic ramifications ("blip" or "puff") and their frequencies depend on the spatial organization of the signaling molecules. Therefore, two ramifications expressing exactly the same Ca^{2+} channels can display different types of Ca^{2+} signals depending on the spatial organization of their channels. Moreover, we found that co-localization of sources of Ca^{2+} influx in the cytosol is paramount to the diversity of the signals. It would thus be interesting to investigate whether those co-localizations can be observed at specific locations, such as at neuron-astrocyte contact sites. This model therefore represents a validated spatially-extended stochastic tool to investigate Ca^{2+} signals and constitutes a significant advance in intracellular signaling in general because it presents the first fully stochastic model suited to investigate Ca^{2+} dynamics in small compartments.

Chapter V

Modeling spontaneous Ca^{2+} signals in realistic 3D geometries

The 2D simulations of the particle-based model presented in Chapter IV have the advantage of a good computational efficiency, which makes them suitable for parametric studies with averaging over a number of Monte-Carlo simulations. However, the 2D setting does not facilitate the comparison of the copy number of molecules in the simulations with molecular concentrations as measured experimentally. Moreover, it is difficult to investigate the impact of the localization of IP_3R channels at the surface of the ER membrane (rather than freely diffusing in the cytosol) with a 2D setting. To address those questions, we have extended the model for simulations in three-dimensional geometries, which will be presented in this chapter. In this implementation, molecular concentrations and volumes can be precisely adjusted to experimental data from astrocytic processes.

The experimental work presented in this chapter has been performed by our collaborators: U. V. Nägerl's team, Interdisciplinary Institute for Neuroscience, Université de Bordeaux, France and C. Calì, BESE Division, King Abdullah University of Science and Technology, Thuwal, Saudi Arabia. They have conducted Ca^{2+} imaging experiments (see Arizono et al [9] for methods) and electron microscopy (see Calì et al [32] for methods), respectively.

V.1   Simulating Ca^{2+} signals in a simplified 3D PAP geometry

As 80% of Ca^{2+} activity occurs in astrocytic ramifications that cannot be resolved by optical microscopy [7], astrocytic Ca^{2+} signaling models must take into account

small volumes associated to it. This section presents simulations performed in a simplified 3D geometry that is suited for reproducing concentrations and volumes encountered in PAPs. After validating the model against experimental data, we have investigated its behavior depending on spatial distributions of molecules and on cellular geometry.

V.1.1   Experimental measurements of Ca^{2+} signals

Experimental measurements of Ca^{2+} dynamics in microdomains in mice hippocampal organotypic culture have been performed by our collaborators (see Fig V.2A for data and Arizono et al [9] for methods). Organotypic slices were used as they provide better optical access and sample stability, which, combined with confocal microscopy, enabled to distinguish individual processes (resolution $\approx$ 200 nm VS $\approx$ 500 nm with two-photon microscopy *in vivo*). While this resolution was not enough to resolve the exact sizes of PAPs, it provided the most realistic Ca^{2+} dynamics experimentally available for Ca^{2+} transients occurring at fine astrocytic processes. Their data reveal the sponge-like structure of processes (Fig V.2A1), with localized submicron Ca^{2+} microdomains (regions of interest (ROI) in Fig V.2A2) of size that can be less than $0.5\mu m^2$. The corresponding Ca^{2+} traces display infrequent (a few hundredths of Hz) peaks with average amplitude $\approx$ 2.5 ($\Delta F/F$) and typical duration of $\approx$ 2.7 seconds at FWHM (Fig V.2A3 and D). Notice that these experimental traces correspond to spontaneous signals to the extent that they were measured in the absence of any neuronal or astrocytic stimulation. In particular, TTX application in this preparation did not alter peak frequency [9]. Ca^{2+} traces are available at https://figshare.com/articles/Astrocytic_calcium_traces_from_-organotypic_hippocampal_slices/8951006.

V.1.2   Modeling approach

In order to simulate Ca^{2+} dynamics within a 3D geometry with realistic volumes and concentrations, we have built a model in STEPS (http://steps.sourceforge.net/). STEPS is a software for voxel-based stochastic reaction-diffusion simulations within complex 3D geometries that simulates stochastic chemical reaction-diffusion with a spatialized version of Gillespie's SSA, usually referred to as the reaction-diffusion master equation (RDME) [475] (see section III.4). STEPS uses a derivative of the SSA in tetrahedral voxels that allows for a better resolution than the cubic voxels mostly used in voxel-based models [475].

Geometry

The main advantage of STEPS in the context of this study is its automatic handling of external and internal membranes [446]. Moreover, STEPS simulations can easily be parallelized [560], a crucial property given the computational burden of such compartmentalized 3D simulations. This allowed us to explicitly describe the presence of the ER membrane inside the 3D cell cytoplasm and the fact that IP$_3$R channels are located on the ER membrane. The geometry of the reaction volume consisted in a cylinder of length L_{astro}=1 μm and radius R_{astro}=0.1 μm. The ER was modeled as a second cylinder, internal, with length L_{ER}=0.75 μm and radius R_{ER}=0.03 μm. The resulting cytosolic volume (2.81×10^{-17} L) was meshed with 11345 tetrahedra of individual volume $2.48 \times 10^{-21} L$, thus ensuring the well-mixed subvolume condition [475]. The geometry is presented in Fig V.2B.

Reactions

In this spatial configuration, we modeled the IP$_3$R-mediated Ca^{2+} signaling kinetic scheme of Fig IV.1. Ca^{2+} ions and IP$_3$ molecules diffuse in the bulk 3D space located between the plasma membrane and that of the ER, while IP$_3$R molecules are distributed uniformly at random over ER membrane surface. Three model variants were implemented:

- A first variant, referred to as the "No-GCaMP" model, did not include fluorescent Ca^{2+} indicators. In this 3D model, parameter values were taken, whenever possible, from the literature (Table A.1). γ and α values were adjusted to yield basal Ca^{2+} concentration 83 $\pm$ 29 nM [551, 177]. Likewise, β and μ were adjusted for a basal IP$_3$ concentration of 120nM [550]. Note that this value is based on recent, precise measurements of IP$_3$ concentration and differs by an order of magnitude from IP$_3$ concentration values routinely used in IP$_3$R-mediated Ca^{2+} models [264, 561, 342]. IP$_3$R density on the ER surface has been measured by Wiltgen et al with TIRF-microscopy on cell cultures [481], reporting IP$_3$R cluster diameters of 0.3 μm at most, with up to 10 IP$_3$R per cluster. The ER surface area in our model is 0.69 μm^2. Ignoring the potential unclustered IP$_3$R channels [558], this represents a maximum of 4 clusters, thus at most 40 IP$_3$R channels. We thus set the number of IP$_3$R in our model to 50 channels on the ER surface. Finally, Ca^{2+} and IP$_3$ binding and dissociation constants to IP$_3$R were adjusted to fit the experimental data from our collaborators of Ca^{2+} microdomains in organotypic cultures of hippocampal astrocytes.

- A second variant of the 3D model, referred to as the "GCaMP"(="GCaMP6s") model, was obtained by adding GCaMP6s Ca^{2+} indicators in the cytosol.
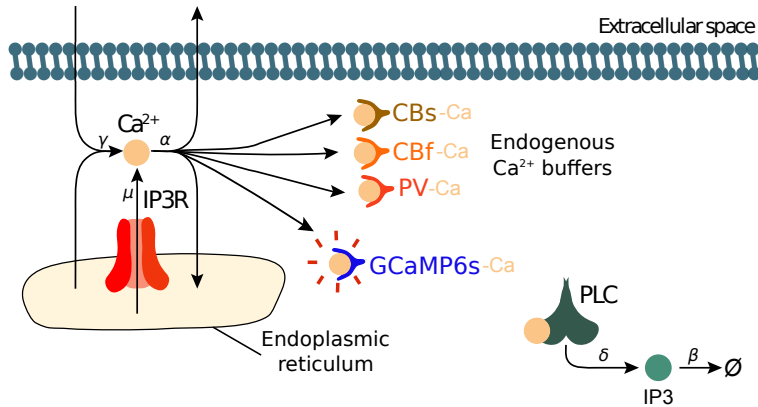
Figure V.1: Reaction scheme of the 3D "GC+Buf" model. This figure presents the biochemical reactions and regulatory interactions modeled in the endogenous buffers model, "GC+Buf", in 3D. Reactions are the same as the ones described in Fig IV.1, except that new particles have been added: slow (CBs) and fast (CBf) calbindin as well as parvalbumin (PV), that can bind Ca^{2+} ions and diffuse, whether bound or not. Parameter values associated with this model are presented in Table A.2.

GCaMP6s are ultrasensitive Ca^{2+} indicators that fluoresce when bound to Ca^{2+}. The fluorescence signal from experimental data indeed corresponds to the concentration of Ca^{2+}-bound GCaMP6s, which can be quite different from free cytosolic Ca^{2+} trace. The same GCaMP-independent parameter values as the "No-GCaMP" model have been used. The parameters related to GCaMP were taken from the available experimental literature and are shown in Table A.1. Some variations of this model with GCaMP6f indicator have been developed: "GCaMP6f" and "Lck-GCaMP6f", referring respectively to models with GCaMP6f that is cytosolic or anchored to the plasma membrane. GCaMP6f kinetics was taken from Chen et al [186].

- A third variant of the 3D model, referred to as the "GC+Buf" model, was obtained by adding endogenous buffers to the "GCaMP" model. The kinetic scheme is presented in Fig V.1. Briefly, 3 different endogenous buffers were modeled: slow and fast calbindin (CBs and CBf, respectively) and parvalbumin (PV). Parameter values for Ca^{2+}, IP_3, IP_3R and GCaMP dynamics were the same as the "GCaMP" model. Parameter values for endogenous buffers dynamics were taken from the literature [484] and are presented in Table A.2.

Clustering

In order to investigate the effect of IP_3R clustering in the 3D implementation of the model, the same parameters as the "GCaMP" model were used, except IP_3R-

independent cytosolic Ca^{2+} influx, γ. Indeed, in order to facilitate the control of the localization of Ca^{2+} sources in STEPS, IP$_3$R-independent cytosolic Ca^{2+} influx has been implemented as channel-dependent Ca^{2+} fluxes. To do so, Ca^{2+} channels, $\gamma_{\text{ch}_{\text{PM}}}$, were added to the model, located at the plasma membrane. There were as many $\gamma_{\text{ch}_{\text{PM}}}$ on the plasma membrane as IP$_3$R channels on the ER membrane: 50. γ in those simulations is $15 \times 10^{-8} s^{-1}$.

- *Clustering algorithm*
  ER surface was divided in triangles. As ER is cylindrical and in order to facilitate the implementation of co-clustering, we have omitted the circles as potential surface for IP$_3$R clustering. Triangles that belong to the surface of interest were stored in a list. For each cluster, a triangle was chosen randomly within the list. If no cluster center existed yet, then cluster center was defined in this triangle. If some cluster centers already existed, then for each cluster center, inter-cluster center distance had to be greater than 20nm. Then each cluster center and its neighboring triangles formed the surface of an IP$_3$R cluster. Please note that this approach is simplistic and does not account for IP$_3$R size (25nm [274]) or for inter-IP$_3$R and inter-clusters distances found in the literature [481]. Each cluster surface was then defined as a region of interest (ROI) as defined in STEPS. The given number of IP$_3$R per cluster was then added to this ROI.

- *Co-clustering algorithm*
  If cocl=0, $\gamma_{\text{ch}_{\text{PM}}}$ Ca^{2+} channels were randomly distributed on the plasma membrane. If cocl=1, $\gamma_{\text{ch}_{\text{PM}}}$ channels were co-clustered with IP$_3$Rs. Similarly to IP$_3$R clustering algorithm, pumps were distributed into cluster patches on the plasma membrane. For each IP$_3$R cluster center previously described, the closest triangle on plasma membrane was defined as the center for $\gamma_{\text{ch}_{\text{PM}}}$ cluster. Each $\gamma_{\text{ch}_{\text{PM}}}$ cluster patch was then defined as a ROI consisting in this center triangle and its neighboring triangles. For simplicity, $\gamma_{\text{ch}_{\text{PM}}}$ cluster size was identical to IP$_3$R cluster size.

Note that in order to avoid spatial overlapping of both IP$_3$R and $\gamma_{\text{ch}_{\text{PM}}}$ clusters, the list of potential membranous triangles for positioning a new cluster center was deprived of the triangles that belonged to previously created clusters. Because of this implementation, clusters did not always consist in the same number of triangles. Indeed, most clusters contained the central triangle and its 3 neighbors but few contained only 3 triangles as one of the neighbors already belonged to another cluster. This effect occurred in simulations with a high number of clusters (i.e small cluster size η).

Simulation code

The code of the "GCaMP" variant of the model is available on ModelDB [562] at http://modeldb.yale.edu/247694.

Peak detection and analysis

Peak detection was performed with the same strategy as presented in section IV.1. Peak amplitude A was however rescaled to facilitate comparison with experimental data, using $\Delta F/F = (A - Ca_{\text{baseline}})/Ca_{\text{baseline}}$, where Ca_{baseline} is the basal [Ca^{2+}] and peak duration was expressed as full width at half maximum (FWHM).

V.1.3   Results

Simulations in a compartmentalized 3D geometry reproduce spontaneous Ca^{2+} microdomains signals

Our first noticeable result is that the model is able to reproduce the emergence of spontaneous Ca^{2+} peaks of comparable frequency, duration and signal-to-noise ratio (Fig V.2C) to those measured experimentally. This result therefore indicates that spontaneous Ca^{2+} signals can emerge in fine processes even with a realistic basal Ca^{2+} concentration of 83 ± 29 nM, which corresponds to only one to two Ca^{2+} ions in the whole cylinder. Quantification of free Ca^{2+} signal properties (Fig V.2D) shows that signals are quantitatively and qualitatively different from experimental signals (Fig V.2C, D, "No-GCaMP" simulations). Adding GCaMP6s to the model, and thus measuring GCaMP-Ca=Ca-GCaMP signals, improved drastically both qualitatively and quantitatively the match between simulations and experimental data (Fig V.2C, D, "GCaMP" and "GC+Buf" simulations), with no apparent difference between the "GCaMP" and the "GC+Buf" simulations. Note that our experimental statistics are tightly associated with the temporal sampling frequency used in the experiments (2 Hz) since very fast Ca^{2+} events may be accessible only to higher sampling frequencies [7]. In particular, the experimental peak frequency measured might have been higher with better temporal resolution. The spontaneous signals measured in organotypic hippocampal cultures by our collaborators are of the same order of magnitude than the ones measured *in vivo* [563, 7]. In any case, our results show that genetically encoded Ca^{2+} indicators (GECIs), such as GCaMP6s, may change local Ca^{2+} concentration, in particular close to open IP$_3$R channels, leading to an increased peak duration. Those results are in accordance with previous studies that demonstrate that Ca^{2+} buffers, such as GECIs, modulate signal readout [366, 545].

Together those results demonstrate that our model, without any endogenous
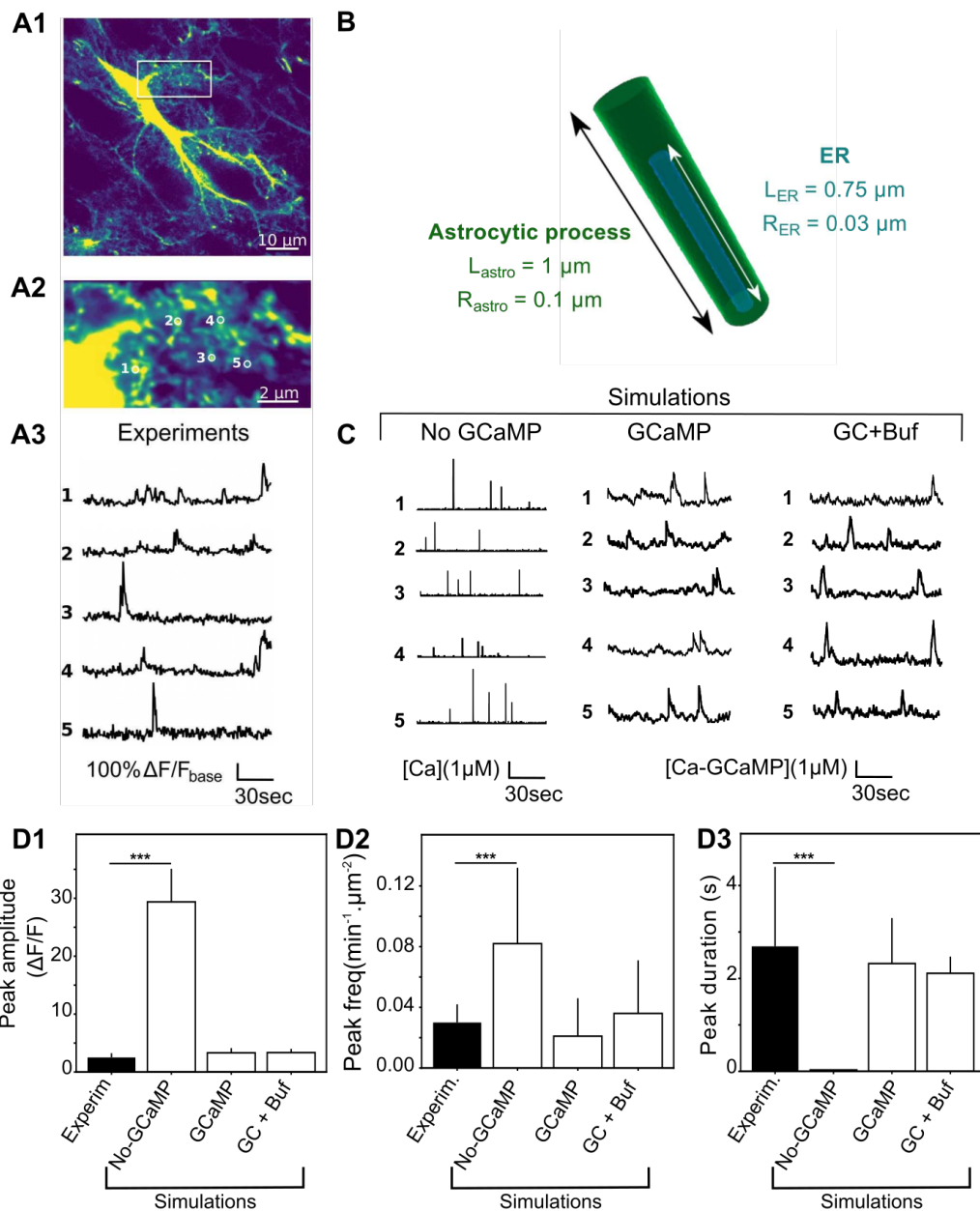
Figure V.2: 3D model simulations in fine astrocyte processes successfully reproduce Ca^{2+} **microdomains signals.** (*A*) Experimental monitoring of the spontaneous local Ca^{2+} signals in astrocytic sponge-like processes. Panel *A1* shows a 'summed projection' of a confocal time lapse image stack of a GCaMP6s-expressing astrocyte. Panel *A2* illustrates magnification of the boxed region of panel *A1*. Panel *A3* displays spontaneous Ca^{2+} traces from the regions of interest shown in (*A2*). (*B*) The 3D geometry used for the 3D model is a cylinder of length L_{astro}=1 μm and radius R_{astro}=0.1 μm, with ER as a thinner cylinder inside. The interior volume is roughly 0.03 fL. (*C*) Representative simulations of Ca^{2+} dynamics within the above cylinder with the "No-GCaMP", "GCaMP" and "GC+Buf" simulations. The raw signal corresponds to cytosolic free Ca^{2+} concentration for the "No-GCaMP" model and to Ca^{2+}-bound GCaMP concentration for "GCaMP" and "GC+Buf" models. For all simulation types, parameter values were partly taken from the literature and partly adjusted for fitting Ca^{2+} traces shown in *A* (see Table A.1). (*D*) Quantitative comparisons of the spontaneous Ca^{2+} signals measured experimentally (black bars) or simulated with the "No-GCaMP", "GCaMP" or "GC+Buf" models (white bars). The compared quantities are peaks amplitude in terms of $\Delta F/F$ ratio (D1), their frequency (measured in min^{-1} for each μm^2 area, D2) and duration (expressed as full width at half maximum, FWHM, in s, D3). Significance is assigned by * for

buffers, is enough to reproduce Ca^{2+} signals within fine astrocytic processes in a quantitative way, making it a powerful tool to investigate Ca^{2+} dynamics in the small volumes associated with PAPs.

Effect of GCaMP properties on Ca^{2+} dynamics

Because "GCaMP" simulations revealed that the use of GECIs may change local Ca^{2+} concentration and thus impact peak duration, we have next investigated the effect on Ca^{2+} dynamics of several parameters defining GCaMP molecules: their kinetics and their concentration. We tested to what extent using different GECIs in our simulations impacted Ca^{2+} dynamics. We compared the dynamics of [GCaMP6s-Ca] with those of cytosolic [GCaMP6f-Ca] and membrane-anchored, immobile, [Lck-GCaMP6f-Ca]. Although the total concentration of GECIs in those three models was identical, GCaMP6f-Ca signals displayed higher amplitude and smaller duration than GCaMP6s-Ca signals (Fig V.3A1,3). No significant difference between GCaMP6f-Ca and Lck-GCaMP6f-Ca was observed (Fig V.3A1-3). Those results are partially in agreement with experimental measurements [186] that have reported a similar decrease of peak duration when using GCaMP6f compared to GCaMP6s. However, experimental observations also included a decrease of the peak amplitude with GCaMP6f, that we do not observe. This discrepancy could be due to a higher fluorescence baseline of GCaMP6f-Ca in those experiments, leading to decreased $\Delta F/F$ ratio.

As the concentration of GECIs cannot be controlled experimentally and is often not reported in Ca^{2+} imaging studies, we have next investigated its effect on Ca^{2+} signals (Fig V.3B). Our simulations demonstrate that an increased GCaMP concentration in the cell results in a linear increase of basal GCaMP-Ca levels (Fig V.3B1), with an unchanged basal concentration of free Ca^{2+}. This result is consistent with simulations of our ODE model of Ca^{2+} buffering (see section A.2.1.1). Increased [GCaMP] is associated with a decrease of GCaMP-Ca peak amplitude expressed in terms of $\Delta F/F$ ratio (Fig V.3B2) and an increase of peak duration (Fig V.3B4). Interestingly, varying [GCaMP] does not seem to have an impact on peak frequency (Fig V.3B3), which is contradictory to Skupin et al's results [530] that have demonstrated a non-linear increase of the average signal period with the concentration of exogenous buffers. However, Skupin et al studied whole-cell EGTA or BAPTA dynamics, which is fundamentally different from the local spontaneous GCaMP-Ca signals in the fine processes that we are modelling here. The fact that we measure no significant difference between membrane-anchored and cytosolic GCaMP concentration is against experimental observations [255] and, according to our sim-
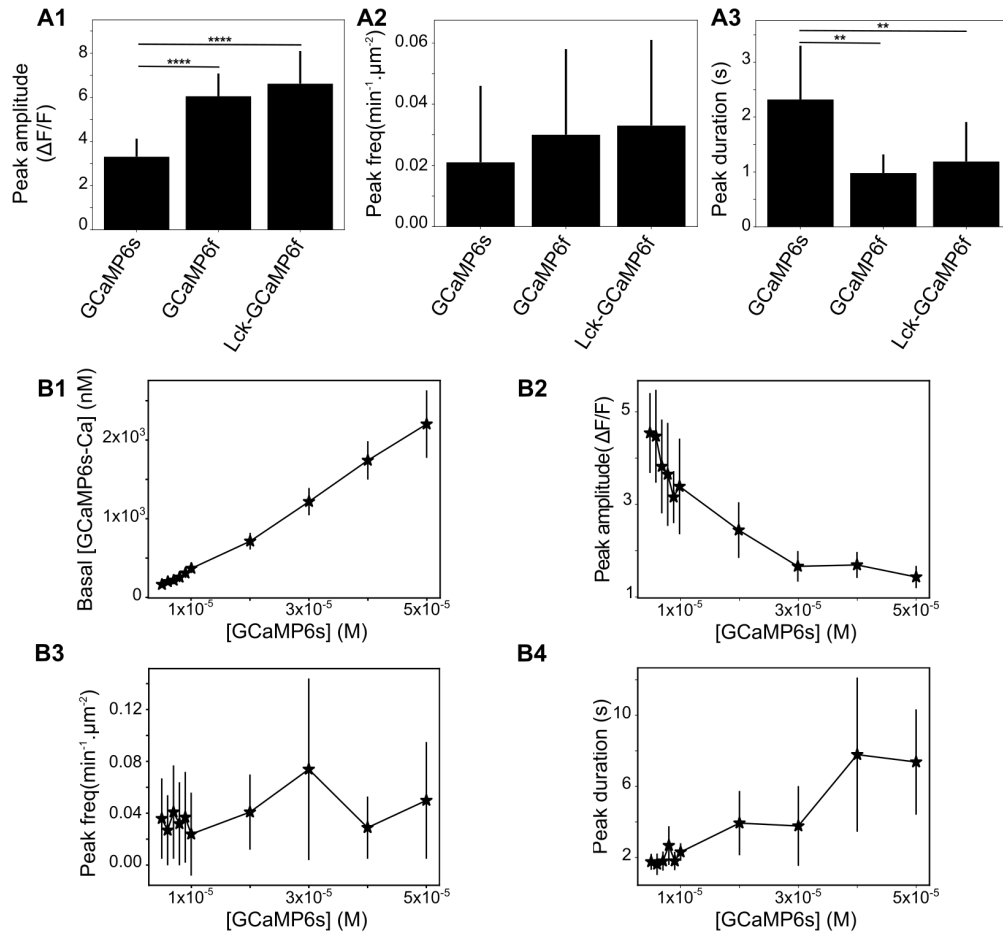
Figure V.3: The kinetics and concentration of GECIs strongly influence Ca^{2+} **dynamics.** (*A*) Quantitative comparisons of the spontaneous Ca^{2+} signals measured with "GCaMP6s", "GCaMP6f" or "Lck-GCaMP6f" as fluorescent reporters. The compared quantities are peaks amplitude in terms of $\Delta F/F$ ratio (A1), their frequency (measured in min^{-1} for each μm^2 area, A2) and duration (expressed as full width at half maximum, FWHM, in s, A3). Significance is assigned by * for $p \leq 0.05$, ** for $p \leq 0.01$, *** for $p \leq 0.001$. (*B*) Impact of the concentration of GCaMP6s on basal concentration of GCaMP-Ca (B1, ANOVA, p-value<0.0001 ***), on the GCaMP-Ca peak amplitude (B2, ANOVA, p-value<0.0001 ***), frequency (B3, ANOVA, p-value=0.0013 **) and duration (B4, ANOVA, p-value=0.049 *). Data are presented as mean ± standard deviation over 20 simulations. Lines are guide for the eyes.

ulations, might reflect different levels of expression of Lck-GCaMP compared to cytosolic GCaMP. Local variations of GCaMP concentration might thus yield variations of peak duration and amplitude, so that measuring GCaMP concentration and its variations along cellular compartments appears crucial to analyze Ca^{2+} signals more accurately.

Effect of IP$_3$R clustering and of cellular geometry on spontaneous Ca^{2+} signals

As simulations in 2D suggested a role of IP$_3$R clustering on Ca^{2+} dynamics (see Fig IV.5), we have investigated whether this effect could still be observed in the low copy number 3D voxel-based implementation of the model. Since a recent EM study has detected contact sites between ER and plasma membrane (PM) in endfeet [30], we have investigated the effect of the juxtaposition of the endoplasmic (ER) and plasma (PM) membranes on Ca^{2+} dynamics. To do so, we have performed simulations with 2 different ER cylinder radii, R_{ER}=30nm and 80nm and constant ER surface (Fig V.4A), with different IP$_3$R cluster sizes (η=1, 2, 5, 10, 25, 50) and constant total number of IP$_3$R=50, with or without co-clustering of Ca^{2+} sources (cocl=1 or 0, respectively) (Fig V.4B).

Ca^{2+} signals in geometries with an ER-PM distance at cluster sites that was 20nm (R_{ER}=80nm) was associated with higher peak amplitude, frequency and duration compared to geometries with an ER-PM distance of 70 nm (R_{ER}=30nm) (Fig V.4C). Moreover, similarly to the 2D model, IP$_3$R cluster size η had a low impact on Ca^{2+} signals when Ca^{2+} sources were not co-localized (cocl=0, mild increase of peak frequency with η, no impact of η on peak duration and amplitude). As observed in the 2D version of the model (see Fig IV.5), IP$_3$R cluster size η influences peak amplitude and frequency in 3D but not its duration when Ca^{2+} sources are co-clustered (cocl=1), for R_{ER} = 80 (see Fig V.4D) and R_{ER} = 30 (not shown).

Overall, our results confirm the results from the 2D implementation of the model (see Chapter IV) that increased IP$_3$R cluster size, when associated with the co-clustering of IP$_3$R channels with other Ca^{2+} sources, results in an increase of both peak frequency and amplitude. Ca^{2+} peak amplitude and frequency are furthermore increased at ER-PM contact sites. This suggests that ER-PM contact sites could constitute preferential sites of Ca^{2+} signaling in the cell, favoring the existence of local 'hotspots' of Ca^{2+} activity.

To conclude, we show that the spontaneous Ca^{2+} signals generated by the 3D implementation of the model with realistic process volume and astrocytic Ca^{2+} concentrations successfully reproduce the spontaneous Ca^{2+} transients measured in Ca^{2+}
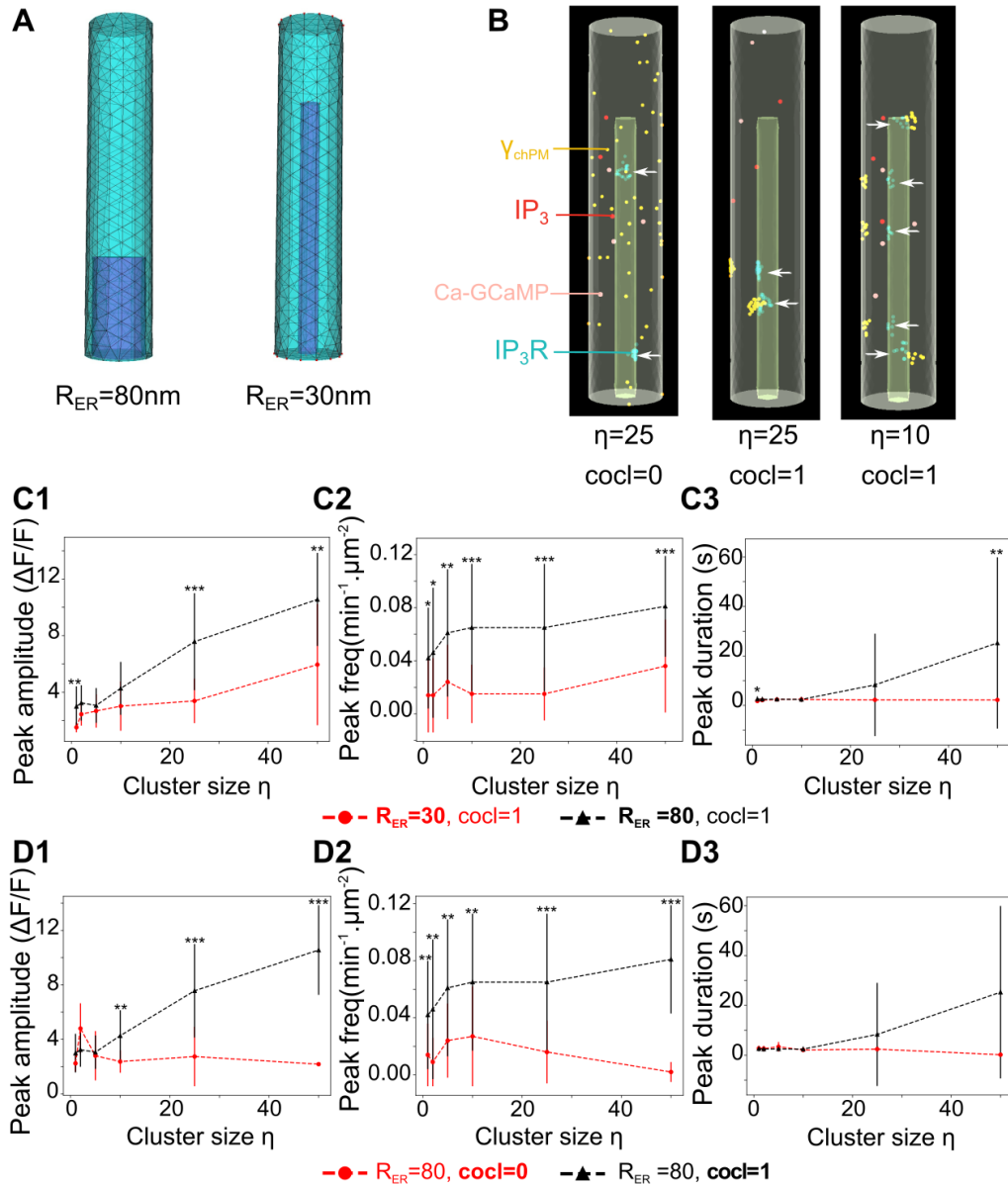
Figure V.4: IP$_3$R **clustering and ER-PM distance influence** Ca^{2+} **dynamics in 3D.** (*A*) In order to test the impact of ER-plasma membrane (PM) distance on the effect of the co-clustering of Ca^{2+} sources, geometries with different ER radii (R_{ER}) have been designed. R_{ER}=30nm corresponds to the geometry used in previous simulations (see Fig V.2). R_{ER}=80nm, corresponds to an ER-PM distance of 20nm, mimicking ER-PM contact sites. The height of ER cylinders has been adapted so that varying R_{ER} does not affect total ER surface and IP$_3$R density. Screenshots of simulations (*B*) reveal the distribution of molecules in reaction space with varying cluster sizes (η=10 or 25) and the presence or absence of co-clustering of γ_{chPM} with IP$_3$R (respectively cocl=1 or 0, see section V.1.2). White arrows: IP$_3$R clusters. The influence of IP$_3$R cluster size η on Ca^{2+} peak amplitude (*C1*, ANOVA, p-value<0.0001 *** for both R_{ER}=30 and 80), peak frequency (*C2*, ANOVA, p-value=0.0084 ** for R_{ER}=30 and p-value=0.0092 ** for R_{ER}=80) and on peak duration (*C3*, ANOVA, p-value=0.81 for R_{ER}=30 and p-value<0.0001 *** for R_{ER}=80) is shown for different values of cluster size: from $\eta = 1$ (IP$_3$R channels are not clustered) to $\eta = 50$ (strong clustering), with co-clustering, cocl=1 and with R_{ER}= 30nm (red) or 80nm (black), D_{Ca}=13$\mu m^2.s^{-1}$.

Figure V.4: IP$_3$R clustering and ER-PM distance influence Ca^{2+} dynamics in 3D (continued). (*D*) Quantification of the effect of cluster size on Ca^{2+} signals peak amplitude (D1, ANOVA, p-value=0.50 for cocl=0), frequency (D2, ANOVA, p-value=0.031 * for cocl=0) and duration (D3, ANOVA, p-value=0.091 for cocl=0), for cocl=0 (black) and cocl=1 (red), D_{Ca}=13$\mu m^2.s^{-1}$. Data are presented as mean $\pm$ standard deviation over 20 simulations. Lines are guide for the eyes. Significance of the difference between simulations with $R_{\mathrm{ER}} = 30$ and $R_{\mathrm{ER}} = 80$ (C) or cocl=0 and cocl=1 (D) is assigned by * for $p \leq 0.05$, ** for $p \leq 0.01$, *** for $p \leq 0.001$.

micro-domains with confocal microscopy in organotypic culture of hippocampal astrocytes. Our simulations predict that local variations of the concentration of Ca^{2+} indicators such as GECIs might contribute to the diversity of Ca^{2+} signals observed in astrocytes so that precise monitoring of their concentration should be performed. Finally, simulations in the 3D geometry confirm the results from the 2D implementation of the model (see Fig IV.5) that increased IP$_3$R cluster size, when associated with the co-clustering of IP$_3$R channels with other Ca^{2+} sources, results in an increase of both peak frequency and amplitude. Furthermore, the 3D implementation of the model suggests that, in 3 spatial dimensions, those effects are particularly enhanced at ER-PM contact sites.

V.1.4   Discussion

Ca^{2+} buffering in astrocytes is currently not well described. Ca^{2+} buffering could differ depending on sub-cellular localization as some recent papers revealed the existence of local translation in radial glia [564], in processes compared to soma [565] and in endfeet [30]. This could potentially allow for local sets of proteins to be expressed in different concentrations than in the soma. Immobile or weakly mobile endogenous Ca^{2+} buffers are responsible for an effective intracellular Ca^{2+} diffusion that is an order of magnitude slower than free Ca^{2+} ions [554]. Our simulation results indicate that the value of the effective Ca^{2+} mobility participates in the determination of the characteristics of the spontaneous events, thus confirming previous experimental [566] and modeling studies [545, 567, 546, 490, 543]. Although our simulations with both GCaMP and endogenous buffers,"GC+Buf", overall displayed similar dynamics to the simulations without endogenous buffers ("GCaMP"), we note that, similarly to the effect of GCaMP concentration, increasing the concentration of endogenous buffers led to longer duration of the Ca^{2+} signals. Those results are consistent with previous studies that have demonstrated significant effects of buffers [544] or of intra-cluster channel communication and coupling [545] on Ca^{2+} dynam-

ics. Endogenous Ca^{2+} buffers display various kinetics and diffusion coefficients in astrocytes [555] and some of them are overexpressed in hippocampal and striatal astrocytes, possibly in a region-specific pattern [28], which could be involved in the regional variability of astrocytic Ca^{2+} signals [64]. Our study shows that precisely accounting for the effects of GECIs and endogenous Ca^{2+} buffers on Ca^{2+} dynamics is crucial for better interpreting Ca^{2+} signals in PAPs. Particular care should be taken when interpreting GCaMP-Ca signals as GCaMP concentration is rarely monitored although it could be partly responsible for the diversity of Ca^{2+} signals observed in PAPs.

V.2 Simulating Ca^{2+} signals in a 3D geometry extracted from EM

Computational studies of fine astrocytic processes typically consider that their geometry can be simplified as being a cylinder of length $\approx 1\mu$m and of radius $\approx$ 50-100 nm [429, 430], similar to the mesh that we have used in section V.1. In order to investigate whether the cylinder geometry presented in Fig V.2 is a good approximation of a fine astrocytic process, we have performed similar simulations within a realistic PAP geometry. This geometry, referred to as 'Real' or 'Realistic', was extracted from electron microscopy (EM) by our collaborator, C. Calì, KAUST University, Saudi Arabia. We have first compared Ca^{2+} dynamics in the 'Real' geometry to the dynamics in the simplified PAP geometry presented in section V.1, referred to as 'Cyl' or 'Cylinder'. Next, we have investigated the impact of the geometrical parameters that were isolated by our previous studies (see section IV.2 and V.1) on Ca^{2+} dynamics in the realistic geometry.

V.2.1 Modeling approach

The realistic 3D mesh used in this study corresponds to a 220 μm^3 hippocampal astrocyte extracted from electron microscopy by C. Calì, presented in Fig V.5A. From this mesh, we have extracted, in collaboration with Erik De Schutter's team, Okinawa Institute for Science and Technology (OIST), Japan, a process that contains ER. A screenshot of a simulation in the resulting realistic PAP geometry is presented in Fig V.5B. Cytosolic volume of the PAP mesh is $0.357\mu m^3$ and ER sur-
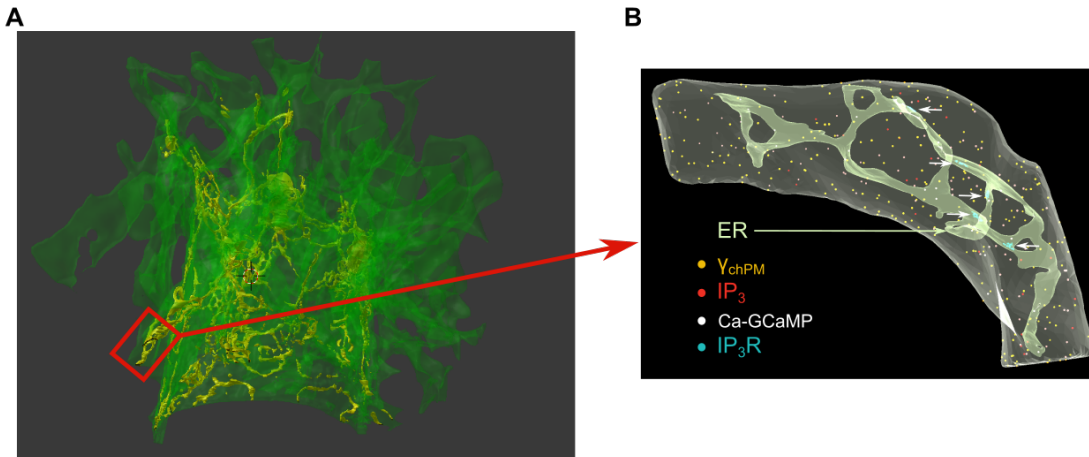
Figure V.5: Realistic astrocytic mesh extracted from EM. This figure presents the 3D mesh that has been provided by C. Calì, which allowed us to perform simulations within a realistic PAP geometry. Panel *A* presents the mesh of the 220 μm^3 hippocampal astrocytic volume extracted and reconstructed from EM. Cytosol is in green and endoplasmic reticulum (ER) in yellow. One process from the reconstructed astrocyte that contains ER has been isolated (*B*). The simulation screenshot presented in panel *B* displays 250 IP$_3$R channels that are organized in clusters of size $\eta = 50$ (white arrows) and 250 $\gamma_{ch_{PM}}$ channels that are randomly distributed on the plasma membrane (yellow) (cocl = 0). ER is represented in light green and plasma membrane is transparent.

face is $0.891 \mu m^2$ so that 250 IP$_3$R channels must be placed on the membrane of the ER in order to keep the same IP$_3$R density as in the cylinder mesh (see section V.1).

Simulations were performed for different cluster sizes η, with and without co-clustering (cocl= 1 or 0, respectively) with the "GCaMP" model from section V.1 within the realistic PAP mesh presented in FigV.5B. Clustering and co-clustering algorithms were identical to the ones described in section V.1. In a subset of simulations, referred to as 'ER-PM cl' (see Fig V.8A2), IP$_3$R clusters were positioned at ER sites that were the closest to the plasma membrane in the mesh. To do so, ER triangles were sorted according to their distance to the closest plasma membrane triangle. Then, depending on the number of clusters in the simulation ($250/\eta$), the ER triangle corresponding to the shortest ER-PM distance was selected as an IP$_3$R cluster site. Cluster area then consisted in this triangle and its 3 neighbors. Those 4 triangles were then removed from the list of available ER triangles for placing IP$_3$R channels. Thus, if a new cluster had to be placed, it would not be placed onto those triangles, avoiding cluster overlapping.

Parameter values were the same as in the simulations in the simplified geometry (see Table A.1), except γ. Indeed, as IP$_3$R-independent Ca^{2+} influx γ occurs at

individual channels $\gamma_{\mathrm{ch_{PM}}}$, as the number of pumps is that of IP$_3$R channels and as the ER surface and cytosolic volume in the realistic mesh are roughly 5 and 12 times larger than in the cylinder mesh, respectively, the value of γ had to be adjusted for this model and is $3 \times 10^{-2} s^{-1}$.

V.2.2   Results

Simulations in realistic geometry reproduce spontaneous Ca^{2+} signals measured experimentally

The simulations presented in section V.1 have the advantage of being performed in a simplified mesh, which results in a decreased computational cost of simulations. Moreover, the simplified mesh allows the study of the effect of geometrical parameters, which can be easily modified in the simple mesh, as e.g decreasing the distance between the ER and PM membranes (see e.g R_{ER}=30 VS 80 in Fig V.4). However, it is not clear to what extent the symmetries inherent to the geometry of the cylinder by itself can influence Ca^{2+} dynamics, in particular in simulations with co-clustering of Ca^{2+} channels of the ER and of the plasma membranes. To address those questions, we have carried out simulations in the realistic PAP mesh presented in Fig V.5B. Ca^{2+} peak duration and frequency are both qualitatively (Fig V.6A3, B2, C2) and quantitatively (Fig V.6D) similar to experimental measurements of Ca^{2+} dynamics in mice hippocampal organotypic culture (Fig V.6A) and to simulations in the simplified cylinder ('Cyl.') geometry (Fig V.6B). Peak amplitude, expressed as ΔF/F, is lower in the realistic mesh than in the "GCaMP" simulations in the cylinder mesh ('Cyl.', p-value=0.002 **) and than experimental traces ('Expe.', black bar, p-value=0.012 *). This difference might be due to the lower basal [Ca-GCaMP] in 'Real' compared to 'Cyl' simulations. This hypothesis could be tested by modifying the value of γ in 'Real' simulations in order to reach the same basal [Ca-GCaMP] in 'Real' than in 'Cyl' simulations.

Our first result is that, with no IP$_3$R clustering (η=1) and with no co-clustering of Ca^{2+} sources (cocl=0), simulations in the realistic PAP mesh are similar to simulations in the simplified cylinder mesh.

A1

A2

A3   Experiments

1

2

3

B1

Astrocytic process
L_{astro} = 1 µm
R_{astro} = 0.1 µm

ER
L_{ER} = 0.75 µm
R_{ER} = 0.03 µm

B2   'Cyl.' simulations

1

2

3

100% $\Delta F/F_{base}$ |___|
                            30sec

C1   ER   Plasma membrane

1µm

C2   'Real.' simulations

1

2

3

D1

D2

D3
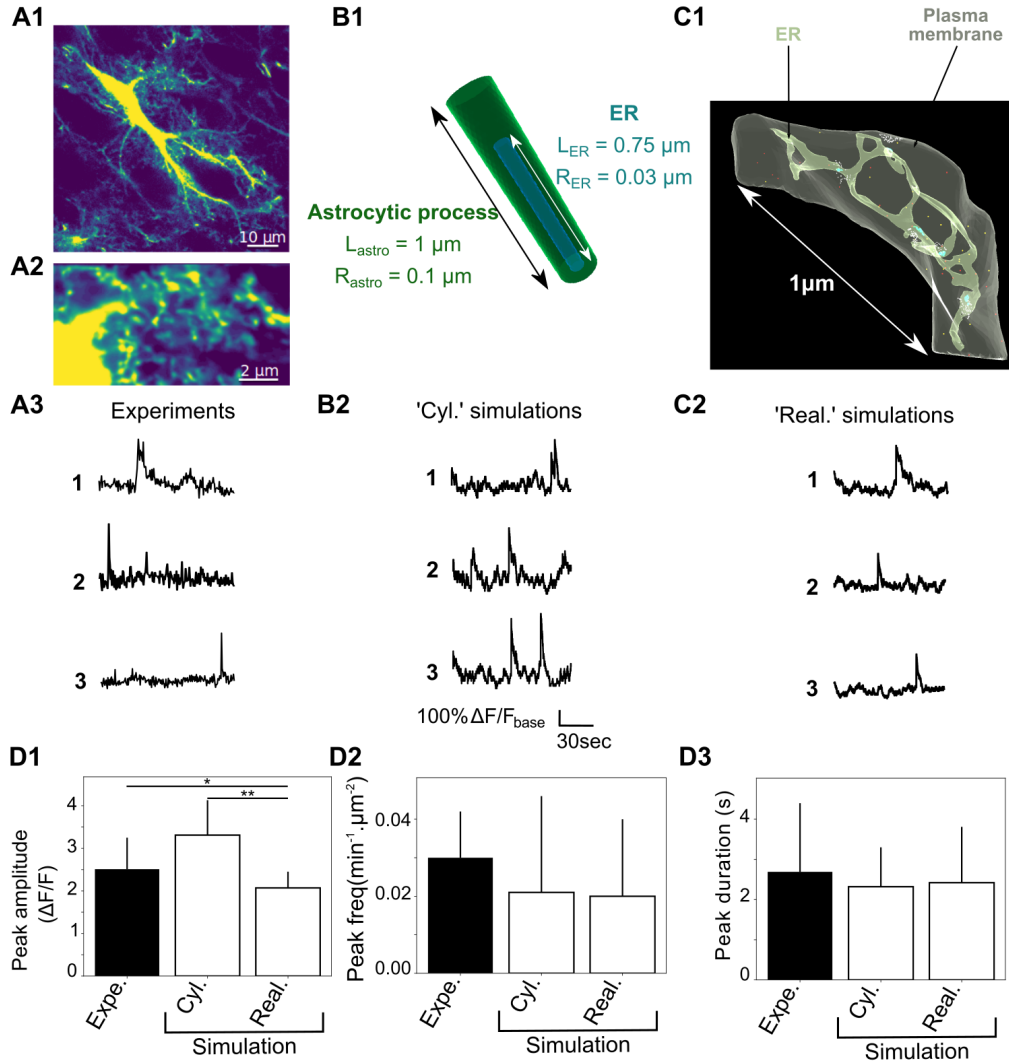
Figure V.6: Simulations in a realistic 3D PAP geometry reproduce experimental astrocytic Ca^{2+} traces. (*A*) Experimental monitoring of the spontaneous local Ca^{2+} signals in astrocytic sponge-like processes. Panel *A1* shows a 'summed projection' of a confocal time lapse image stack of a GCaMP6s-expressing astrocyte. Panel *A2* illustrates magnification of the boxed region of panel *A1*. Panel *A3* displays spontaneous Ca^{2+} traces from the regions of interest shown in (*A2*). (*B*) The 3d simplified geometry used in section V.1 (*B1*) and representative spontaneous Ca^{2+} traces from simulations of the "GCaMP" model (*B2*). (*C*) Screenshot of the 3d mesh extracted from electron microscopy, of similar length than the simplified PAP geometry from Panel (*B*) and representative Ca^{2+} traces from simulations of the model (*C2*). (*D*) Quantitative comparisons of the spontaneous Ca^{2+} signals measured experimentally (black bars) with simulations in the cylinder ('Cyl.') or realistic ('Real.') PAP meshes (white bars). In those simulations, η=1 and cocl=0, i.e IP$_3$R and $\gamma_{ch_{PM}}$ channels are randomly distributed on the ER and plasma membrane, respectively. Data are presented as mean $\pm$ standard deviation over 20 simulations. Significance is assigned by * for $p \leq 0.05$, ** for $p \leq 0.01$, *** for $p \leq 0.001$.

Effect of IP$_3$R (co-)clustering on spontaneous Ca^{2+} signals in a realistic PAP mesh

As 'Cyl' simulations revealed that increased IP$_3$R cluster size, when associated with the co-clustering of IP$_3$R channels with other Ca^{2+} sources, results in an increase of both peak frequency and amplitude (Fig V.7D), we have investigated whether this effect could still be observed in 'Real' simulations. The first noticeable result is that the effect of cluster size η when cocl=1 observed in 'Cyl' simulations is not observed in 'Real' simulations (see Fig V.7B). Note that, similarly to 'Cyl' simulations where $R_{\text{ER}} = 30$, no effect of IP$_3$R cluster size was observed in 'Real' simulations when cocl=0 (not shown). Furthermore, even when Ca^{2+} sources were co-clustered (cocl=1), contrary to the results in the cylinder mesh (see Fig V.4) η had no significant impact on peak amplitude (Fig V.7C1), frequency (Fig V.7C2) or duration (Fig V.7C3).

Overall, our simulations reveal that the effects of molecular distributions and co-clustering that were observed in the cylinder mesh no longer hold in a more realistic geometry. This could be due to the more complex geometry of the ER in the realistic mesh, which results in smaller areas of ER that are close to the plasma membrane compared to the cylinder mesh (see Fig V.4). Those results shed light to the importance of the mesh that is chosen to perform simulations to investigate Ca^{2+} dynamics in PAPs.

As 'Cyl' simulations revealed that a decreased ER-PM distance at cluster sites (R_{ER}=80 VS 30) was associated with higher peak amplitude and frequency (see Fig V.4C), we have investigated whether those effects could be observed in 'Real' simulations. To do so, the closest ER sites to plasma membrane in the realistic mesh were selected (see section V.2.1). IP$_3$R clusters were positioned at those sites, thus decreasing ER-PM distance at cluster (and co-cluster) sites (see Fig V.8A, 'ER-PM cl' VS 'random cl'), approximating the $R_{\text{ER}} = 80$ geometry in the cylinder mesh (see section V.1). No significant difference was observed between 'ER-PM cl' and 'random cl' conditions, suggesting that, in the realistic mesh, the ER-PM contact sites are not large enough to impact Ca^{2+} peak amplitude and frequency.

Here again, our simulations demonstrate that the geometrical effects, here of ER-PM distance at cluster site, observed in 'Cyl' simulations are no longer observed in 'Real' simulations. Particular care should be taken when choosing a simplified geometry in order to limit or at least be aware of the potential effects of its inherent geometry on the dynamics of the system.

Overall, simulations in a realistic mesh extracted from electron microscopy displayed similar Ca^{2+} dynamics to experimental data as well as to simulations in the cylinder mesh from section V.1 (Fig V.6). However, simulations did not reproduce
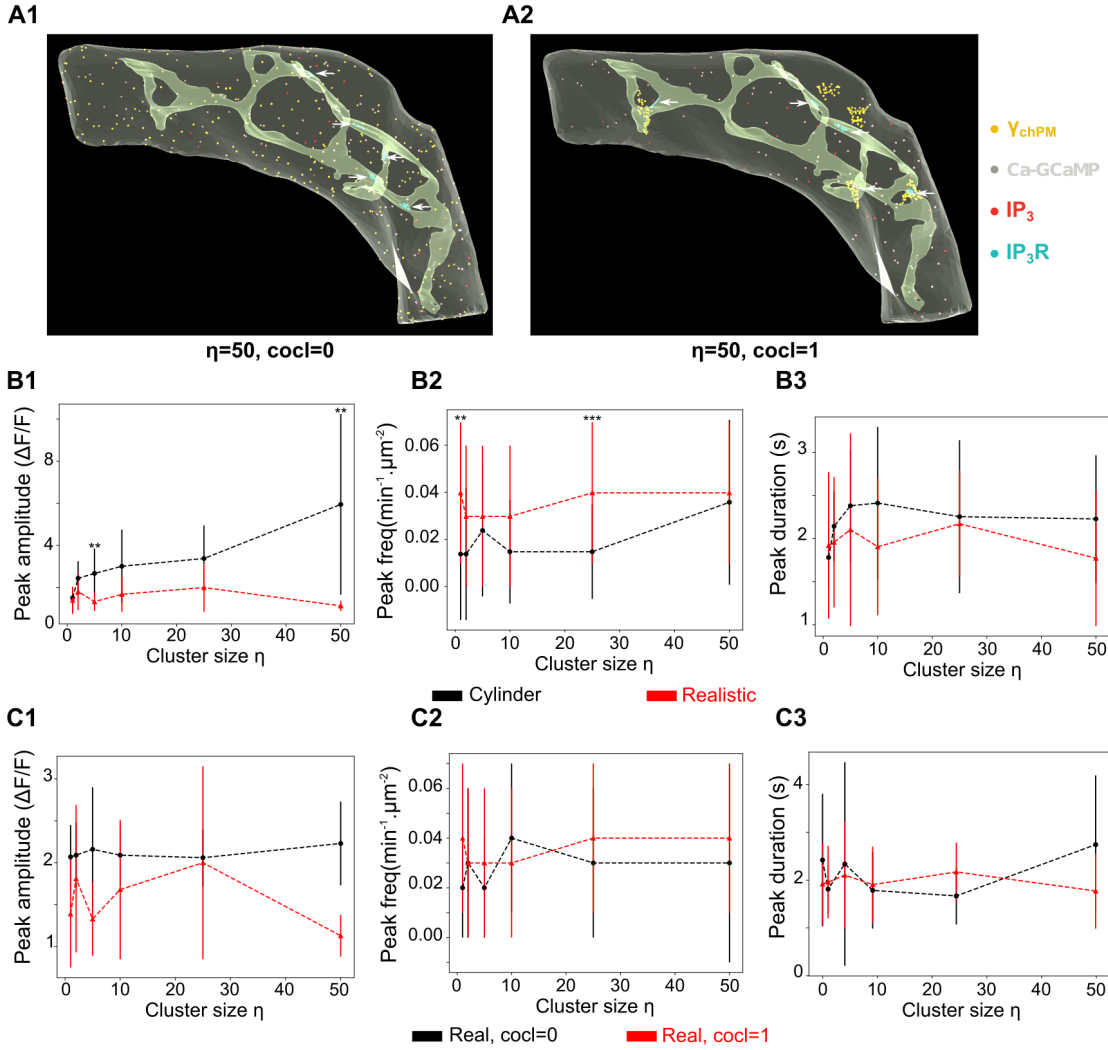
Figure V.7: Effect of IP_3R clustering on spontaneous Ca^{2+} dynamics in a realistic PAP geometry. (*A*) Screenshots displaying simulations with 5 clusters of size 50 ($\eta = 50$), with (A2) and without (A1) co-clustering of Ca^{2+} sources (cocl=1 or 0, respectively). When cocl=1, each cluster of IP_3R-independent Ca^{2+} sources, $\gamma_{ch_{PM}}$, is placed on the plasma membrane area that is the closest to the IP_3R cluster (white arrow) to which it is co-localized. Note that the size of molecular species has been increased in those screenshots for a better visualization of their localization. (*B*) Quantification of the effect of IP_3R cluster size η on Ca^{2+} peak amplitude (B1), frequency (B2) and duration (B3) in the cylinder (black, $R_{ER}=30$, see section V.1) and realistic (red, see Fig V.5) meshes, cocl=1, $D_{Ca}=13\mu m^2.s^{-1}$. (*C*) Comparison of Ca^{2+} peak amplitude (C1), frequency (C2) and duration (C3) with or without co-clustering of Ca^{2+} sources (cocl=1 or 0, respectively). Data are presented as mean $\pm$ standard deviation over 20 simulations. Significance is assigned by * for $p \leq 0.05$, ** for $p \leq 0.01$, *** for $p \leq 0.001$.
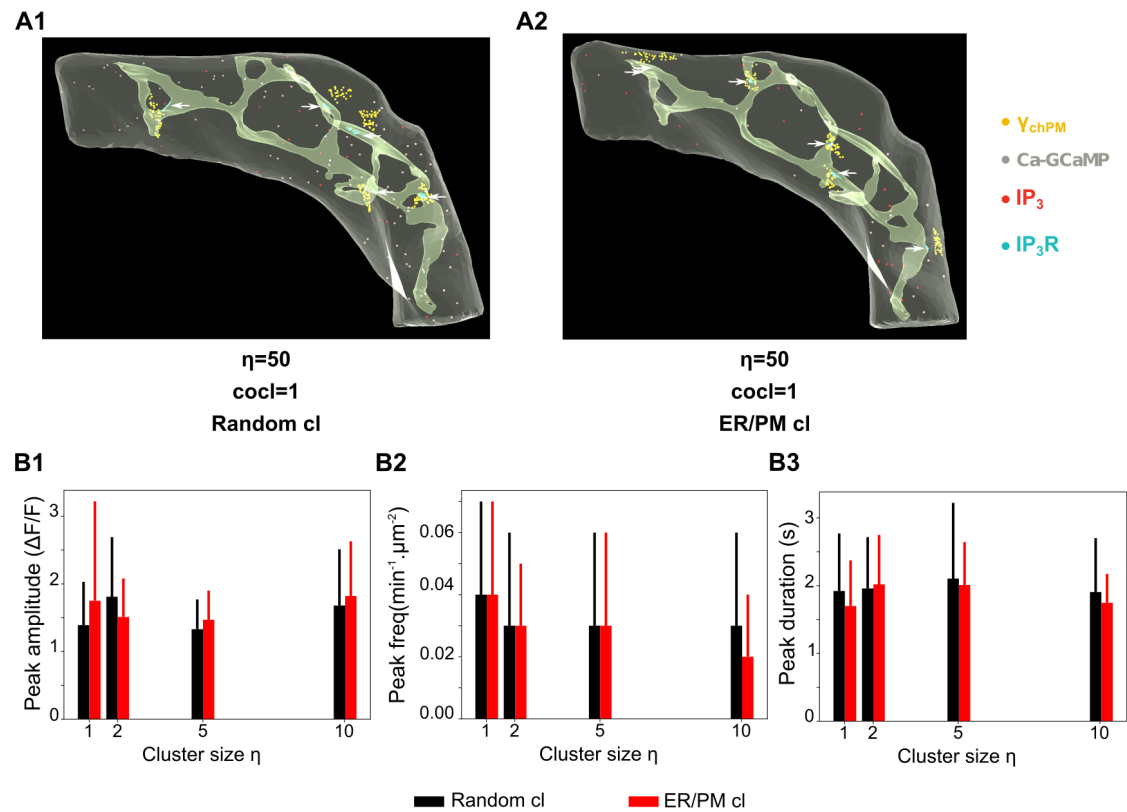
Figure V.8: Clustering at ER-PM contact sites does not impact spontaneous Ca^{2+} **signals.** (*A*) Screenshots displaying simulations with 5 clusters of size 50 ($\eta = 50$, white arrows), with co-clustering of Ca^{2+} sources (cocl=1), i.e each cluster of IP$_3$R-independent Ca^{2+} sources, $\gamma_{\text{ch}_{\text{PM}}}$, is placed on the plasma membrane area that is the closest to the IP$_3$R cluster to which it is co-localized. 'Random cl' (A1) corresponds to random distribution of IP$_3$R clusters onto the ER membrane. 'ER/PM cl' (A2) corresponds to the positioning of IP$_3$R clusters at the closest ER-PM contact sites. Note that the size of molecular species has been increased in those screenshots for a better visualization of their localization. (*B*) Quantification of Ca^{2+} signal amplitude (B1), frequency (B2) and duration (B3) for 'Random cl' (black) and 'ER/PM cl' (red) conditions. Data are presented as mean $\pm$ standard deviation over 20 simulations. Significance is assigned by * for $p \leq 0.05$, ** for $p \leq 0.01$, *** for $p \leq 0.001$.

the effect of spatial parameters that were observed in the cylinder mesh. More specifically, no effect of IP$_3$R clustering was observed, even when co-clustered with other Ca^{2+} sources and when IP$_3$R channels were clustered at the closest ER-PM contact sites in the realistic mesh. Those results underline the importance of the geometry chosen to investigate the phenomenon of interest.

V.2.3   Discussion

The differences observed between the cylinder VS realistic meshes regarding the effect of ER-PM contact sites on Ca^{2+} signals may be due to the different ER geometries in those two meshes. Indeed, the average distance of ER triangles to the closest plasma membrane triangle is 168 ± 88 nm in the realistic mesh while it is 70nm and 20 nm in cylinder meshes with R_{ER}=30 and 80, respectively (when only considering the surface on which IP$_3$R clusters were positioned). Thus, the distance that separates co-clusters of IP$_3$R and $\gamma_{\text{ch}_{\text{PM}}}$ channels in the realistic mesh is 2 times larger than in the cylinder mesh, which increases the probability of Ca^{2+} to diffuse away from the co-cluster site. Moreover, when IP$_3$R clusters are positioned at the closest ER-PM contact sites in the realistic mesh, the average distance of ER triangles to the closest plasma membrane goes from 19 nm (η=1) to 35.8 ± 7.6 nm (η=50). Those distances are closer to those observed in the cylinder mesh. However, the cylinder geometry potentially allowed to create more efficient molecular traps than the ER geometry of the realistic mesh, because of the larger area of ER being in close contact with the PM. Overall, the results presented in this section demonstrate that a small ER-PM distance (e.g 19nm here) by itself is not enough to generate Ca^{2+} hotspots and that further parameters might be at stake to enhance local Ca^{2+} activity. Those parameters could involve an increased surface of ER close to plasma membrane at the contact site, increased local Ca^{2+} buffering or any other parameter that could result in a decreased effective D_{Ca} at cluster site. Preliminary simulations were thus performed with an effective Ca^{2+} coefficient of diffusion D_{Ca} decreased by an order of magnitude ($1.3\mu m^2.s^{-1}$ instead of $13\ \mu m^2.s^{-1}$), which mimics the effect of Ca^{2+} buffering (see section IV.2.3 for further discussion). Ca^{2+} peaks in those simulations were characterized by increased peak amplitude (ANOVA, p-value=0.024 *) and frequency (ANOVA, 0.0099 **) with cluster size η with both cocl=0 and cocl=1 (ANOVA, p-value=0.0008 *** and p-value<0.0001 *** for peak amplitude and frequency, respectively). Those results suggest that Ca^{2+} buffering, in particular when associated with the co-clustering of Ca^{2+} sources, influences Ca^{2+} dynamics, thus confirming the results from the 2D simulations (see Fig IV.4).

In order to get a better approximation of molecular localization and interactions

in the 'Real' simulations, quantified data on the size of IP$_3$R channels as well as the spacing within and between IP$_3$R clusters are necessary. For example, as IP$_3$R channels are $\approx$ 25 nm long, the minimal distance between the barycenters of two adjacent IP$_3$R channels would be at the very least 25nm, most probably higher. Furthermore, IP$_3$R inter-cluster distance is thought to be $\approx$ 200nm on average [480] or even $>$ 300-400nm [481]. Wiltgen et al [481] further reported that intra-cluster distance between adjacent IP$_3$R was $>$ 100nm. The total area of ER in our 3D mesh (Fig V.5) does not allow to both comply with those geometrical rules and with the supposed IP$_3$R density proposed by Wiltgen et al. For example, the total ER area should be larger than $2.1 \times 10^5 nm^2$ for having only 4 clusters of size 2, while the current area of the ER in the mesh is $1.76 \times 10^5 nm^2$ in our the cylinder geometry, on which 50 IP$_3$R channels must be positioned. This is also incompatible with having 250 IP$_3$R channels on the ER membrane of $8.91 \times 10^5 nm^2$ of the realistic mesh. The predictions from Wiltgen et al might be wrong and over-estimate inter- and intra-cluster distances as they were based on 2D images. This nevertheless points out that further experimental investigation is needed to get a better approximation of both the density and intracellular distribution of IP$_3$R channels in fine processes.

A straightforward extension of this work would be to investigate Ca^{2+} dynamics upon neuronal stimulation, depending on neuron-astrocyte geometrical interaction. We have started to investigate the encoding of IP$_3$ infusion at the tip of the process, emulating neuronal stimulation (Fig V.9A). For both cocl=0 and 1, increasing neuronal stimulation results in mild increase of Ca^{2+} peak amplitude (Fig V.9B1) and strong increase of peak frequency (Fig V.9B3). Overall, our simulations predict that neuronal stimulation of astrocytes is mostly encoded in frequency modulation (FM) of Ca^{2+} signals, although further investigation is necessary to confirm this preliminary result.

To go further, C. Calì [32] has provided us with a mesh that includes markers of individual PSDs at the vicinity of processes (see Fig V.10A). The mesh reveals that peri-synaptic processes are extremely diverse regarding their intracellular content: some contain ER only, mitochondria only, both or are devoid of intracellular stores (Fig V.10B). This diversity could be responsible for part of the diversity of Ca^{2+} signals in PAPs. Simulations within those different types of processes upon neuronal stimulation will help investigate this hypothesis.
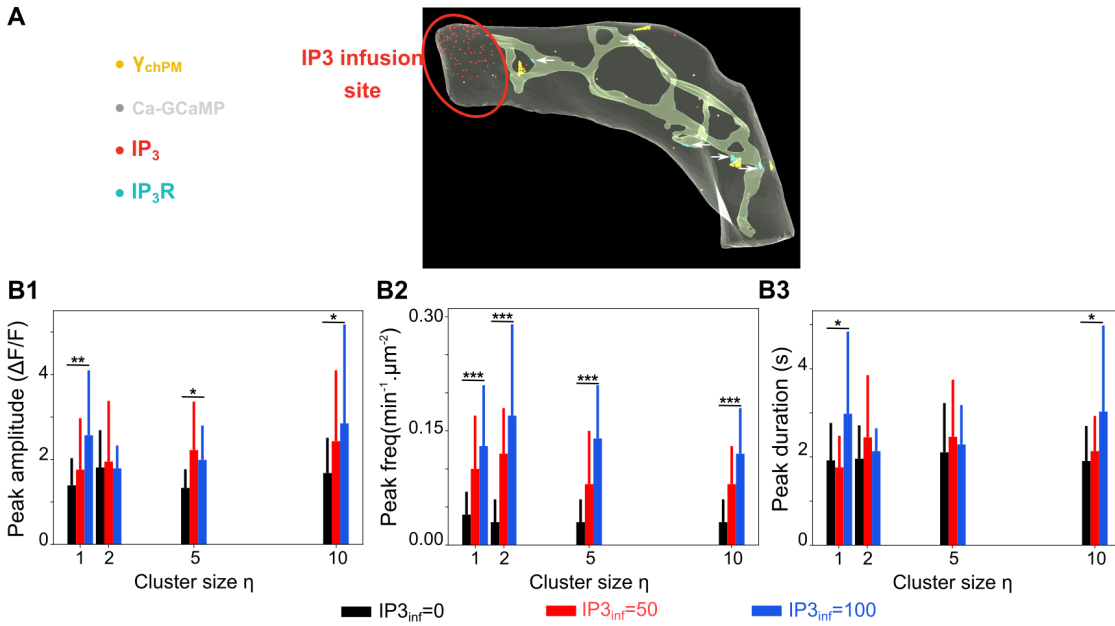
Figure V.9: Neuronal stimulation is encoded in amplitude and frequency of Ca^{2+} signals in PAPs. (*A*) Schematic representation of simulations of neuronal-induced Ca^{2+} signals in the realistic mesh. At time t=t_0=1s, IP_{3inf} molecules of IP_3 (the number varies upon simulation) are injected at the tip of the astrocytic process, which models the effect of neuronal stimulation. IP_3R clusters are indicated with white arrows. (*B*) Quantification of peak amplitude ($\Delta F/F$, B1), frequency ($\mu m^2.s^{-1}$, B2) and duration (s, B3), for different cluster sizes η, with co-clustering (cocl=1), with IP_{3inf}=0 (black), 50 (red) or 100 (blue) IP_3 molecules infused at t=1s. One-way ANOVA was performed to investigate the effect of the number of IP_3 molecules infused (i.e the intensity of neuronal stimulation) on peak amplitude, duration and frequency. Significance is assigned by * for $p \leq 0.05$, ** for $p \leq 0.01$, *** for $p \leq 0.001$.

V.3   Discussion

Controversies regarding the presence of ER in PAPs

Both meshes used in this study (Fig V.2B and Fig V.5B) correspond to geometries of an astrocytic process that contains ER. However, during the past few years, fine astrocytic processes have been regarded as devoid of ER [33, 430]. Thus, the mesh extracted from electron microscopy used in section V.2 on its own (Fig V.5B) contradicts this strong belief in the field. Moreover, a recent EM study has also observed that ER dynamically ramifies in astrocyte perivascular processes *in vivo*
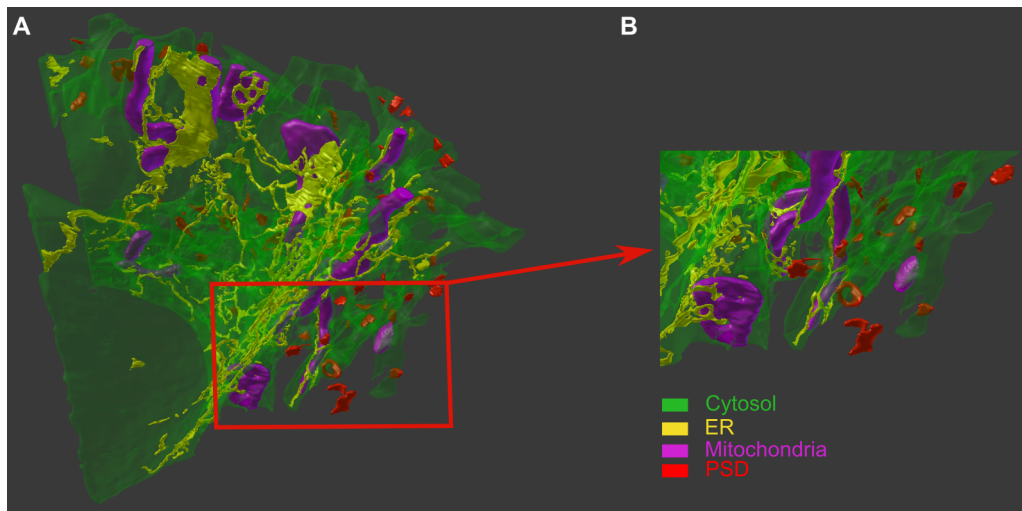
Figure V.10: Mesh extracted from electron microscopy revealing PSDs at the vicinity of PAPs. (*A*) Screenshot revealing the same 3D mesh extracted from electron microscopy that was presented in Fig V.5 but with further information on mitochondria localization (purple) and on the presence and size of neighboring neuronal PSDs (red). (*B*) Zoom on some peri-synaptic processes, illustrating their diversity in terms of intracellular stores.

and detected contact sites between ER processes and plasma membrane [30]. Such contiguous membranous juxtapositions would definitely validate the presence of ER in PAPs.

Although dynamical ER remodeling has been reported in dissociated astrocyte culture [568], technical limitations have prevented direct investigation of ER localization within PAPs *in vivo* or in slices. Super-resolution microscopy of cellular ER and mitochondrial dynamics and structure (resolution $\approx$ 100nm) has recently been developed and could help answer those questions [569, 570]. Correlative super-resolution fluorescence imaging and electron microscopy approaches can yield a resolution of less than 50 nm (down to 10nm) [571], which is very promising avenue to PAPs ultrastructure investigation. ER-bound GECIs, OER-GCaMP6f, have been recently developed and, combined with the use of ER luminal Ca^{2+} indicators such as G-CEPIA1^{er} [175], could help investigate the involvement of Ca^{2+} channels on the ER membrane in Ca^{2+} dynamics depending on subcellular localization in astrocytes [168]. Further investigation regarding ER sub-cellular localization, its sub-compartmentalization and dynamics *in vivo* are crucial for better understanding astrocyte information processing.

Controversies regarding the existence of spontaneous Ca^{2+} signals in astrocytes

The simulations presented in Chapters IV and V aim at better understanding spontaneous Ca^{2+} activity in small volumes such as PAPs. The existence of spontaneous Ca^{2+} signals in astrocytes is actually by itself a matter of debate. Even in the absence of presynaptic neural activity, presynaptic axon terminals do probabilistically release neurotransmitter vesicles, generating so-called miniature EPSCs. Bafilomycin application has been used in several experimental studies to investigate the dependence of astrocytic Ca^{2+} signals on EPSCs, because this inhibitor of V-ATPases inhibits miniature EPSCs by blocking the refill of presynaptic vesicles. However, the impact of bafilomycin bath application on the frequency of spontaneous Ca^{2+} signals in astrocytes has proven variable (compare e.g. Sun et al [572], Arizono et al [9] and Agarwal et al [573]). As bafilomycin has a wide range of effects on Ca^{2+} signaling that is independent of its effect on the refill of presynaptic neurotransmitter vesicles [574, 575], we cannot conclude whether those signals are triggered by EPSCs. Further investigation is needed to decipher whether the "spontaneous" Ca^{2+} signals reported in astrocyte processes are due to spontaneous release of presynaptic vesicles or rely on a synapse-independent mechanism inherent to the CICR system.

ER-PM contact sites, privileged sites of Ca^{2+} signaling

A decade ago, Marchaland et al [576] proposed that localized Ca^{2+} signals in astrocytes could be mediated by contact sites between ER and plasma membranes (ER-PM contact sites). A more recent EM study from Boulay et al [30] has revealed the presence of ER-PM contact sites in perivascular astrocytic processes. Actually, ER-PM contact sites can be observed in all cell types and represent 2-5% of the PM surface [577] (for reviews, see e.g [578, 579]). $\approx$ 1000 ER-PM contact sites of various geometries can exist per cell. Moreover, a recent study on HeLA cells has reported that most Ca^{2+} signals occured at ER-PM contact sites [480], which were populated with immobile IP$_3$R clusters of size 2-9. Whether such an organization exists in astrocytes is still to be uncovered. Finally, TIRF microscopy experiments have revealed that ER-PM contact sites often form at the same location in a given cell, suggesting that they constitute stable structures [580]. Those observations, added to the diversity of Ca^{2+} dynamics observed in our model depending on the geometry of their ER-PM contact sites, suggest that ER-PM contact sites are privileged sites of Ca^{2+} dynamics so that it is crucial to better estimate their localization in astrocytes.

The presence of ER-PM contact sites in the gliapil near synapses could enhance local Ca^{2+} activity and thus influence neuron-astrocyte communication.

Conclusion

In this chapter, a 3D voxel-based implementation of the 2D particle-based model presented in Chapter IV has been presented. Simulations of the model, both in a simplified and in a realistic mesh of a fine astrocytic process, were able to reproduce spontaneous astrocytic Ca^{2+} transients measured in Ca^{2+} micro-domains. Furthermore, our simulations predict that local variations of the concentration of Ca^{2+} buffers might contribute to the diversity of Ca^{2+} signals observed in astrocytes. Simulations in the simplified 3D geometry confirmed the results from the 2D implementation of the model (see Fig IV.5) that increased IP$_3$R cluster size, when associated with their co-clustering with other Ca^{2+} sources, results in an increase of both Ca^{2+} peak frequency and amplitude. Furthermore, the model suggests that, in 3 spatial dimensions, those effects are particularly enhanced at ER-PM contact sites. However, neither the effect of IP$_3$R clustering nor that of ER-PM contact sites were observed in the realistic mesh. As most models of astrocytic processes use cylinder geometries, our results suggest that the characteristics of their Ca^{2+} dynamics might strongly rely on the geometry of their mesh.

Chapter VI

Modeling the onset and propagation of neuronal activity-induced Ca^{2+} signals in processes

Our collaborators [9] (Fig VI.1) as well as other studies [7, 581] have observed Ca^{2+} waves that propagate along astrocytic processes. Those waves can be triggered by increased neuronal firing and are associated with mouse movements *in vivo* [7]. The concomitant existence of both focal and spreading Ca^{2+} signals in astrocytes in response to neuronal activity rises questions on the mechanisms that trigger wave propagation. In small volumes such as PAPs, cellular geometry could be a factor influencing the isolation and/or the propagation of Ca^{2+} events.

In this chapter, we investigate the effect of cellular and ER geometry on the onset and propagation of neuronal-induced Ca^{2+} signals, contrary to Chapters IV and V, that focused on spontaneous Ca^{2+} activity. This work has been performed in collaboration with U. V. Nägerl's team from the Interdisciplinary Institute for Neuroscience, Université de Bordeaux, France. They have provided us with *in vitro* structural data and Ca^{2+} imaging. Furthermore, C. Calì, KAUST University, Saudi Arabia, has provided us with quantified structural data from electron miscroscopy, notably on the intracellular localization of Ca^{2+} stores in a hippocampal astrocyte. They have conducted all the experimental work presented in this chapter.
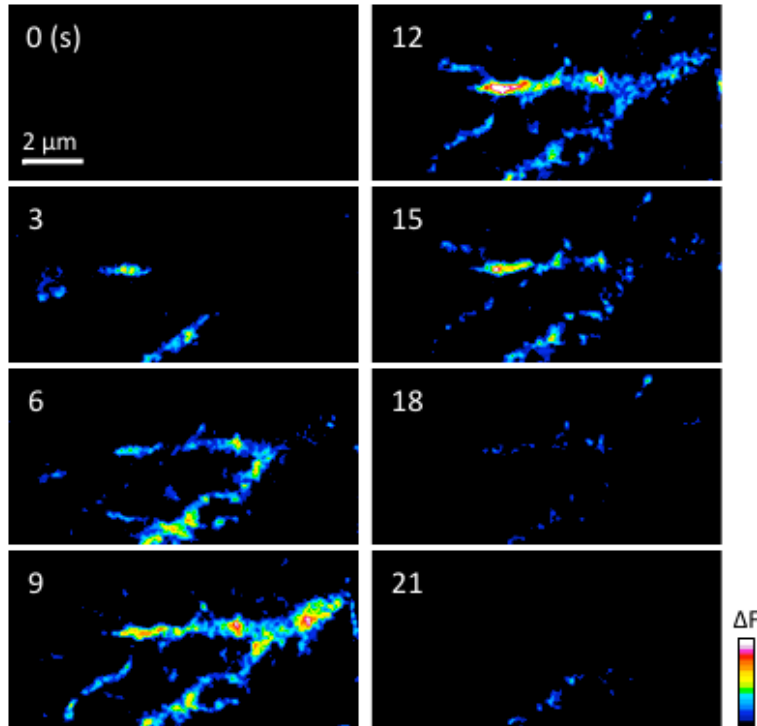
Figure VI.1: Spontaneous Ca^{2+} **waves propagate along astrocytic processes in the gliapil.** This figure, taken from Arizono et al [9], presents time-lapse images of a Ca^{2+} wave propagating in an astrocytic process located in the gliapil. Ca^{2+} signals are expressed as $\Delta F/F_0$, as shown by the color scale bar.

VI.1 Simulating the propagation of Ca^{2+} signals in processes displaying node/shaft geometries

VI.1.1 Experimental background

A recent experimental study from our collaborators [9] has revealed new aspects of the morphological architecture of the astrocytic spongiform domain. The gliapil appears as a succession of bulbous structures, referred to as nodes, that are connected with thinner structures, referred to as shafts (Fig VI.2A). Quantification of the widths of shafts and nodes as well as inter-node distance based on STED microscopy are presented in Fig VI.2B. $\approx 70\%$ of Ca^{2+} signals stayed localized in one node and did not propagate.
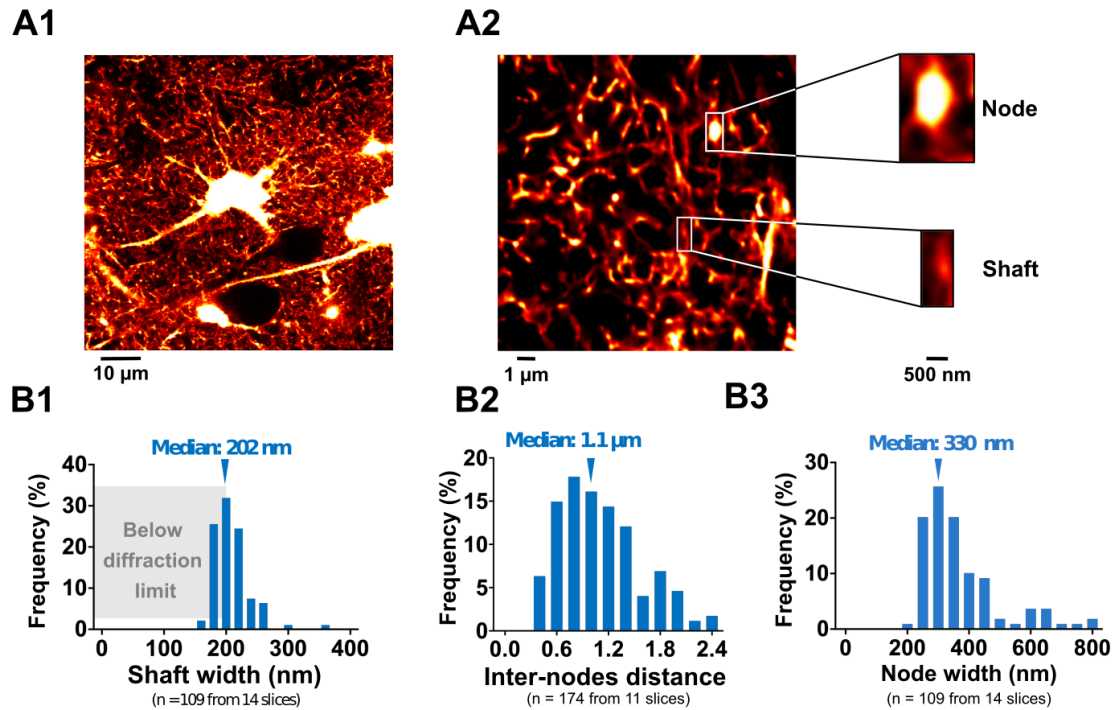
Figure VI.2: Super-resolution microscopy reveals node/shaft structures in the gliapil. Confocal (A1) and STED (A2) microscopy images revealing the geometry of the spongiform domain of astrocytes consisting in successions of nodes and shafts. Quantification of the distribution of shaft width (B1), inter-node distance (B2) and node width (B3). Note that shaft width is often below the diffraction limit of conventional light microscopy ($\approx$ 250 nm, gray rectangle) so that super-resolution microscopy is mandatory for resolving those ultrastructures. This figure was adapted from Arizono et al [9].

In this section, we investigate the influence of such a node/shaft geometry on spatiotemporal characteristics of Ca^{2+} signals. Notably, we look for parameters that could prevent the propagation of Ca^{2+} signals.

VI.1.2 Modeling approach and geometry

In order to investigate the effect of node/shaft geometries on signal propagation, we have built geometries with different node/shaft width ratios δ using Trelis software (https://www.csimsoft.com/trelis), with constant node width (see Fig VI.3). The geometry of a node was approximated as being a sphere of diameter 380 nm. Shaft geometry consisted in a 1μm long cylinder. Shaft diameter was defined rela-
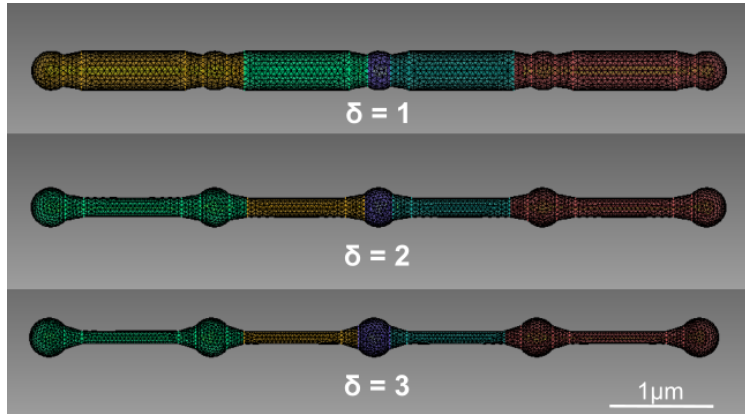
Figure VI.3: Geometries designed for investigating node/shaft structures of the gliapil. Geometries constructed with Trelis software (https://www.csimsoft.com/trelis) to simulate node/shaft geometries of the gliapil for different width ratios δ between nodes and shafts (from $\delta = 1$ to 3). Nodes are represented as spheres and shafts as cylinders. Conic geometries were fused to connect spheres and cylinders in order to get smoother and a bit more realistic geometries. The geometries presented here contain 5 identical nodes and 4 identical shafts.

tive to node width. Indeed, if node/shaft width ratio, δ, was 1, then shaft diameter was the same as node diameter, i.e 380 nm. Similarly, shaft diameter was 190 nm for δ=2 and 127 nm for δ=3. Cones were added between spheres and cylinders to create a smoother transition between nodes and shafts. Note that the values used here for node diameter and shaft length are not the exact median values presented in Fig VI.2 as they correspond to the first values that were provided by our collaborators. They are however of the same order of magnitude so that the geometries presented in Fig VI.3 constitute a reasonable approximation of the observed gliapil ultrastructure presented in Fig VI.5. The ER geometry was considered to be identical to the geometry of the process: node/shaft successions. ER nodes were aligned with cytosolic nodes and ER volume was 10% of total process volume (see Fig VI.4C). While creating the geometry, different sub-regions were defined so that they could later be monitored independently using STEPS.

VI.1.3   Simulations reproduce bleaching experiments

Experimental results

In order to investigate whether nodes, depending on node/shaft width ratio δ, could function as diffusionally isolated compartments such as demonstrated in

mushroom-like spines [582, 488], our collaborators have performed photobleaching experiments (FRAP). Briefly, they applied 2-photon laser pulses on a region of interest (node or shaft) and recorded the fluorescence recovery with confocal imaging. After bleaching, the fluorescence level in the region of interest decreases to I_0. Then, fluorescence increases, because of the diffusion of fluorescent molecules that were not bleached into the region of interest, until it reaches a new steady state, I_{inf}. We characterize node isolation by measuring the time taken by molecules to diffuse into the node, τ, which depends on the diffusion of fluorescent molecules. In other words, a high node isolation will be associated with a high value of τ. Thus, 3 main parameters characterize bleaching traces: I_0, τ and I_{inf} (see also Fig VI.4E). The results from Arizono et al [9] are presented in Fig VI.4A,B and indicate that a high node/shaft width ratio δ can result in an increased recovery time τ and thus in an increased isolation of nodes.

Modeling approach

To test whether node/shaft geometry by itself can reproduce the results from bleaching experiments presented in Fig VI.4A,B, we have simulated bleaching experiments within the geometries presented in Fig VI.3. As experiments measured fluorescence mediated by ZSGreen molecules, ZSGreen molecules were added to simulation space. After 2 seconds of simulation, providing basal level of fluorescence, 60% of ZSGreen molecules were bleached. As our collaborators have bleached a node during 10 ms, the volume that was impacted by the bleaching, because of molecular diffusion, was larger than the bleached region. Thus, in order to fit I_0 and I_{inf} that were measured experimentally, bleached volume in simulations was adjusted depending on the geometry (see Fig VI.4C). Bleaching was simulated as the transition from ZSGreen to ZSGreen-bleached, the latter being accounted as non-fluorescing molecules. The number of ZSGreen molecules was recorded over simulation time and a fit was performed following equation VI.1 to determine the values of I_0, I_{inf} and τ (see Fig VI.4E).

$$I(t) = I_0 - (I_0 - I_{inf})e^{-t/\tau} \tag{VI.1}$$

Parameters that were adjusted to fit experimental data were the coefficient of diffusion of ZSGreen and its concentration. In the simulations presented here, the coefficient of diffusion of ZSGreen, $D_{ZSGreen}$, is 90 $\mu m^2.s^{-1}$ and [ZSGreen]=10 μM.
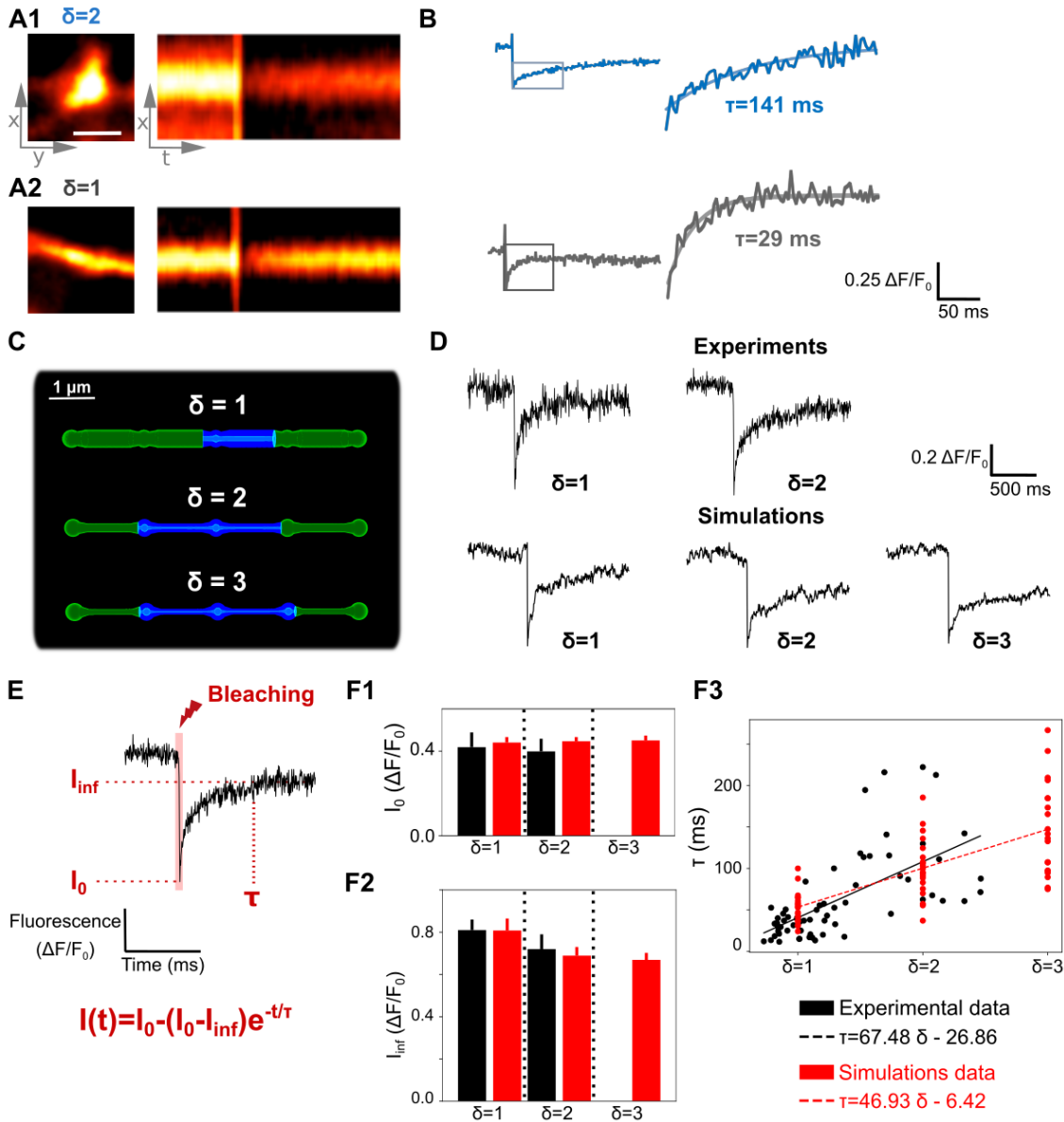
Figure VI.4: Simulations confirm that node/shaft width ratio is a good predictor of the diffusional isolation of nodes. (*A*) Left: Representative astrocytic processes with $\delta=2$ (A1, node) and $\delta=1$ (A2, shaft). (*B*) Fluorescence recovery after photobleaching (FRAP) traces obtained from A1 and A2, respectively, illustrating fluorescence recovery normalized to basal fluorescence before bleaching. (*C*) Geometries of different node/shaft ratios ($\delta = 1$, 2 or 3) used in our simulations. Blue color represents the bleached volume (adapted to fit experimental values of I_0 and I_{inf}) and green the remaining parts of the geometry. Note that blue volume is transparent, revealing the geometry of the ER. (*D*) Representative experimental and simulation traces for different node/shaft width ratios δ. (*E*) Example trace presenting the evolution of the number of fluorescing ZSGreen molecules over time. Vertical red line presents bleaching time. The parameters that characterize a bleaching experiment and the equation that fits bleaching recovery are presented in red. (*F*) Quantification of I_0 (F1), I_{inf} (F2) and τ (F3) values in simulations compared to experiments. Note that we were not provided with experimental data for $\delta = 3$. In F1 and F2, n=5×2 and 20×3 for experiments and simulations respectively. Data are presented as mean ± STD. In F3, n=66 and n=20×3 for experiments and simulations, respectively. τ is positively correlated to δ in experiments (n=66 from 7 slices; Spearman r=0.7179, p<0.0001) and simulations (n=60; Spearman r=0.7520, p<0.0001). Black and red lines represent linear regressions of τ as a function of δ for experiments and simulations,

Results

In order to test the influence of the diverse node/shaft width ratios δ observed experimentally on the isolation of nodes and in order to test whether the geometries presented in Fig VI.3 are a good approximation of the spongiform ultrastructure observed by our collaborators (Fig VI.2), we have simulated a protocol of photobleaching (see section VI.1.3 for details). The major result of our simulations is that bleaching traces in simulations are both qualitatively (Fig VI.4D) and quantitatively (Fig VI.4F) similar to experimental bleaching traces, for node/shaft width ratios δ=1 and 2. Indeed, no significant difference of I_0 (Fig VI.4F1), I_{inf} (Fig VI.4F2) and τ (Fig VI.4F3) was observed between simulations and experimental traces for δ=1 and 2. Simulations were also performed with δ=3 in order to investigate the correlation between bleaching recovery time τ and node/shaft width ratio δ (Fig VI.4F3). Note that in order to verify that the geometries presented in Fig VI.4C are a reasonable approximation of node/shafts geometries observed experimentally (Fig VI.4A,B), we have also verified that the model reproduced the basal noise amplitude of [ZSGreen] and its auto-correlation (not shown). Overall, simulation results suggest that τ, and thus node isolation, increases linearly with node/shaft width ratio, which confirms experimental results.

To conclude, our model successfully reproduces FRAP experiments and predicts that geometries of high node/shaft width ratio δ by themselves can result in an increased node isolation. As those geometries successfully reproduce experimental results, they can reasonably be considered as a good approximation of the ultrastructure of the gliapil observed with STED microscopy by our collaborators (see Fig VI.2).

VI.1.4 Investigating signal propagation in node/shaft geometries

Experimental results

Arizono et al [9] have further demonstrated that 90% of dendritic spines were in contact with nodes and shafts (see Fig VI.5). $\approx$ 70% of Ca^{2+} signals occurred and stayed localized in one node and did not propagate to the neighboring one (see Fig VI.5A, B), suggesting that node/shaft geometries insulate Ca^{2+} hotspots within nodes that are in the vicinity of synapses. Furthermore, they have reported a huge

variety of spine coverage by astrocytic processes (see Fig VI.5C). Contacts were
stable with time and 88% of contact sites were specific (only one node contacted
a given spine). Overall, their results suggest that nodes are preferential sites of
neuron-astrocyte communication at synapses.

Modeling approach

In order to investigate the propagation of Ca^{2+} signals from nodes that contact
neuronal spines, we have developed 2 different protocols:

- In the first protocol, 100 IP_3 molecules were infused in Node 1 at the end of
  the node/shaft geometry, at t=t_0, while the activity in the neighboring node
  (Node 2) was recorded(see Fig VI.6A). Simulations were performed in geome-
  tries with varying node/shaft width ratio δ (see Fig VI.3).

- In the second protocol, we have investigated signal propagation in the node/shaft
  geometry depending on δ when several nodes were successively stimulated (see
  Fig VI.7A). At t=t_0=5s, 50 molecules of IP_3 were infused in Node 1, mimick-
  ing neuronal activation of the astrocytic node. After a time period τ_{IP3}, the
  same amount of IP_3 was then infused in Node 2, at $t_0 + 2\tau_{IP3}$ in Node 3 and
  $t_0 + 3\tau_{IP3}$ in Node 4. During the whole simulation time, Ca^{2+} activity was
  recorded in Node 5.

In both protocols, the kinetic scheme of the model and the corresponding param-
eter values were the same as the 3D "GCaMP" model, presented in section V.1. The
geometries correspond to those presented in Fig VI.3. Nodes and shafts were di-
vided into separate regions of interest so that they could be stimulated and analyzed
separately.

Results

Investigating node to node signal propagation

As the experimental results presented in Fig VI.5 suggest that nodes are preferen-
tial sites of neuron-astrocyte communication, we have next investigated the influence
of node/shaft width ratio δ on wave propagation in the context of neuronal-induced
astrocytic Ca^{2+} activity. To do so, we have first investigated the propagation of a
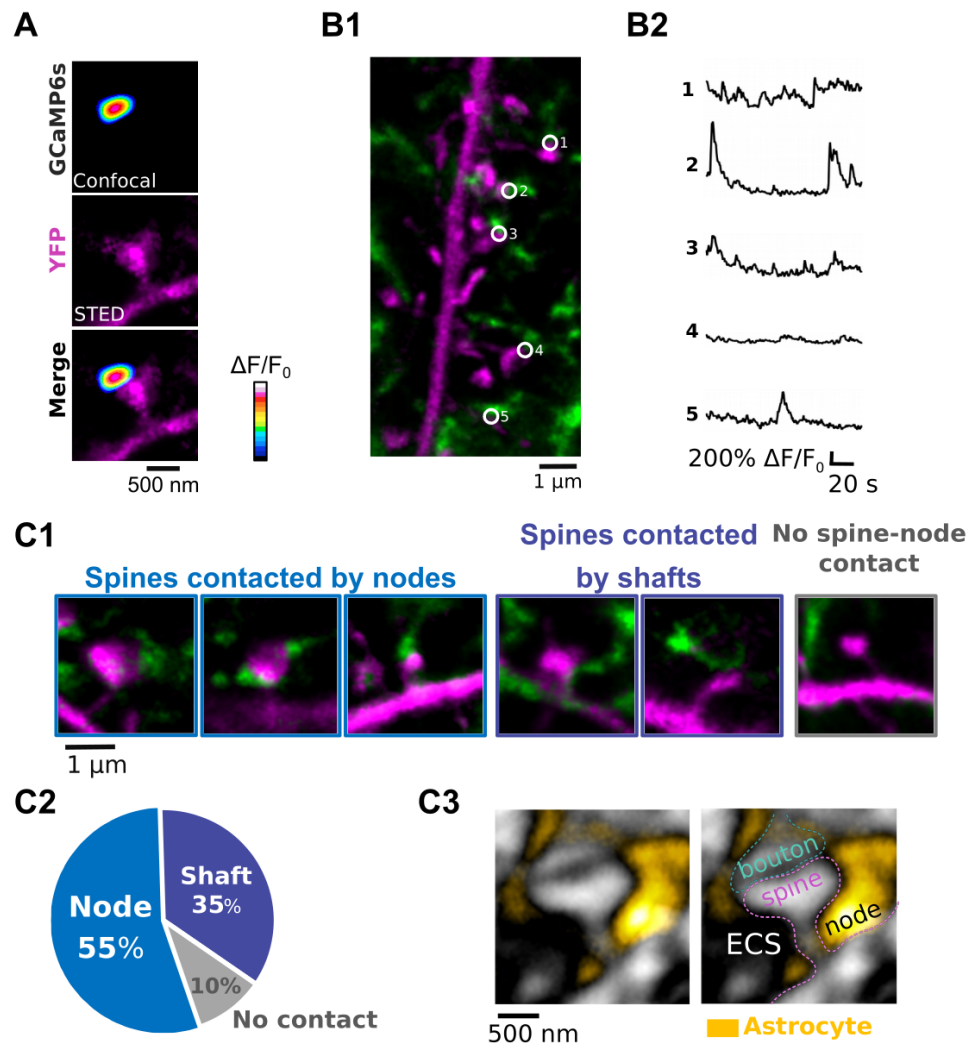
Figure VI.5: Nodes of the gliapil often interact with dendritic spines. Figure adapted from Arizono et al [9]. (*A*) Confocal astrocytic Ca^{2+} signal mapped onto a dendritic spine morphology, visualized with STED. (*B1*) Representative STED image of the morphological interactions between a GCaMP6s-expressing astrocyte (green) and a neighboring YFP-expressing neuron (magenta). (*B2*) Representative spontaneous Ca^{2+} traces from the 5 ROIs shown in panel B1 (white circles). (*C1*) Representative images of spine/node (left), spine/shaft contacts (middle) and spines that do not contact any astrocytic structure (right). (*C2*) Distribution of spines that contact nodes, shafts or no astrocytic structure (n = 188 from 21 slices). (*C3*) Representative image of extracellular space (black) surrounding a synapse (grey) and a neighboring astrocyte (yellow).

signal from one node (Node 1) to the neighboring node (Node 2) (see the proto-col described in Fig VI.6A). Representative Ca^{2+} traces in Node 2 are displayed in Fig VI.6B, which illustrate the variability of Ca^{2+} signals depending on node/shaft width ratio δ=1, 2 and 3. Our first noticeable result is that the delay between the stimulation of Node 1 and peak onset in Node 2 decreases with δ (Fig VI.6C), which suggests that signals propagate faster in geometries of increased node/shaft width ratio. Moreover, the probability of signal propagation to Node 2 increases with δ, which suggests that signal propagation is facilitated in geometries with high node/shaft width ratio δ.

As IP_3R molecules in this model were uniformly distributed onto the ER membrane and as the area of the ER varied between the geometries δ=1, 2 and 3, the total number of IP_3R molecules varied depending on δ. The total number of IP_3R molecules thus equaled 620, 363 and 283, for δ=1, 2 and 3, respectively, although the IP_3R density remained the same in the geometry. To verify whether our results are a consequence of the total number of IP_3R molecules rather than of the geometries, we have performed additional simulations in which IP_3R molecules were located on the ER surface within nodes only. As nodes display exactly the same area in all geometries δ=1, 2 and 3, the total number of IP_3R molecules was identical regardless of the geometry. Results were not significantly different from results presented in Fig VI.6, confirming that the node/shaft width ratio δ influences the speed and probability of signal propagation.

Overall, our results suggest that an increased node/shaft width ratio, although it diffusionally isolates nodes, favors higher probability and speed of Ca^{2+} signal propagation.

Investigating signal propagation resulting from successive node stimulations

Our collaborators have observed that 55% of spines were connected to nodes (Fig VI.5) and that when Ca^{2+} signals propagated in several nodes, those nodes were often associated with spines that belonged to the same dendrite. The frequency of node stimulation is believed to vary drastically depending on whether nodes are contacted by spines from the same dendrite or by spines that belong to different dendrites or even different neurons. In order to test the impact of such a variability of the frequency of the stimulation of neighboring nodes, we have performed simulations in which neighboring nodes were successively stimulated after a time period τ_{IP3} that varied from 50 ms to 5s (see protocol in Fig VI.7A). Representative Ca^{2+} traces in Node 5 are presented in Fig VI.7B and illustrate their variability depending on node/shaft width ratio δ. Our first result in that, similarly to results presented in Fig VI.6, the time to 1st peak in Node 5 significantly decreases when δ increases, whatever the value of τ_{IP3} (Fig VI.7C). More specifically,
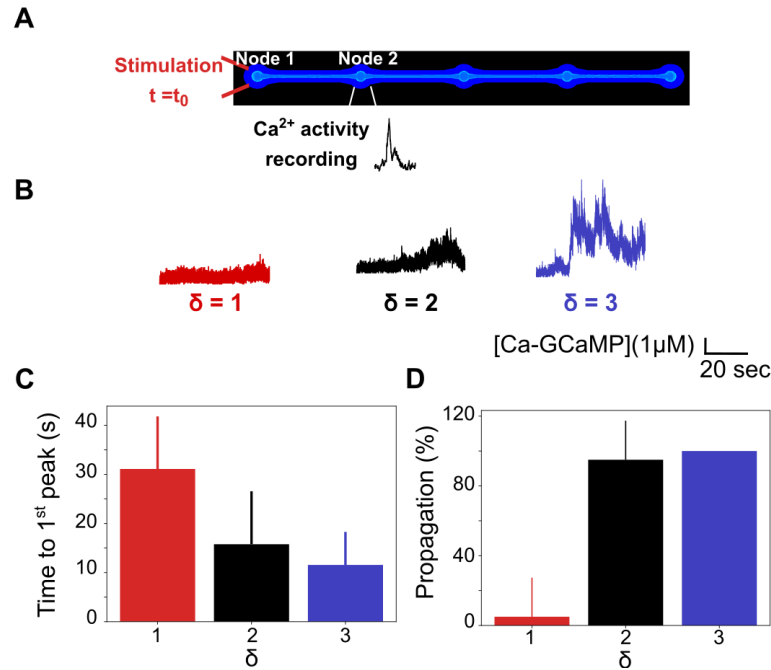
Figure VI.6: Study of the effect of node/shaft width ratio on signal propagation from one node to a neighboring node. (*A1*) Schematic representing the approach that has been developed for investigating the propagation of a neuronal-induced Ca^{2+} signal from node 1 to node 2. Node 1 was stimulated (IP_3 molecules infusion in node 1) at t=t_0 while Ca^{2+} activity was recorded in Node 2. (*B*) Representative Ca^{2+} traces in Node 2 for δ= 1 (red), 2 (black) and 3 (blue). (*C*) Time to 1st peak in Node 2 after stimulation time of Node 1, t_0, significantly decreases with δ (ANOVA, p-value=0.005 **). (*D*) The percentage of signals that propagate to Node 2 significantly increases with δ (ANOVA, p-value < 0.0001 ***).

time to 1st peak is significantly higher for δ=1 compared to both δ=2 and δ=3, while differences between δ=2 and 3 are not as striking (see Fig VI.7C). Note that the difference between δ=1 and δ=2 or 3 increases with the delay between successive node stimulation, τ_{IP3}. This suggests that geometries with δ=1 better discriminate slow from fast frequency of node stimulation compared to geometries with δ=2 or 3. Note that Ca^{2+} signals were often saturated (Fig VI.7B), potentially displaying a non-physiological behavior. Indeed, Ca^{2+} signals lasted more than 15-20s and peaks were not terminating at the end of simulation time. This effect could be due to our boundary conditions (reflective), which do not replicate the potential diffusion of molecules away from the process.

As simulations from Fig VI.6 suggested that the probability of signal propagation from one node to the neighboring one is lower in geometries with δ=1 compared to δ=2 or 3, we have investigated whether this effect is still visible when neighboring nodes are successively stimulated. Similarly to the results from Fig VI.6, geometries

with δ=1 are characterized by a lower probability of signal propagation. Moreover, the probability of signal propagation decreases as τ_{IP3} increases for δ=1 (Fig VI.7D). This suggests that geometries with δ=1 can prevent the propagation of signals in case of successive node stimulation when the frequency of stimulation is low ($\tau_{\text{IP3}} >$ 2s).

In accordance with results presented in Fig VI.6, those results suggest that increased node/shaft width ratio δ is associated with both an increased probability of signal propagation as well as an increased propagation speed.

Together, our results suggest that geometries with δ=1 can prevent or at least decrease the probability of signal propagation in case of single node stimulation or if the frequency of stimulation of successive nodes is low (time period > 2s). As low τ_{IP3} might reflect neuronal stimulation from the same dendritic tree while high τ_{IP3} would characterize signals from different neuronal populations, our results suggest that geometries with low node/shaft width ratio (δ=1) might decrease both the probability and speed of signal propagation when neighboring nodes are stimulated by different neuronal populations.

VI.1.5   Investigating the influence of node branching on the propagation of Ca^{2+} signals

Experimental background

Rather than presenting an aligned geometry in which one node connects 2 neighboring ones like the geometries that were used so far in this study (see Fig VI.3), nodes in the gliapil often consisted in branching points or even formed rings (see Fig VI.8 A, B, respectively). Arizono et al [9] indeed revealed that 75% of nodes consist in branching points (Fig VI.8A3).

In the study presented in this section, we have investigated the effect of such branching points or ring geometries on Ca^{2+} signal propagation.

Modeling approach

In order to investigate the effect of branching at nodes, geometries with the same number of shafts and nodes (4 each) but with different branching properties were designed. Some geometries consisted in linear nodes, without any branching points (Fig VI.8C1), referred to as 'Align', others possessed one branching point at node
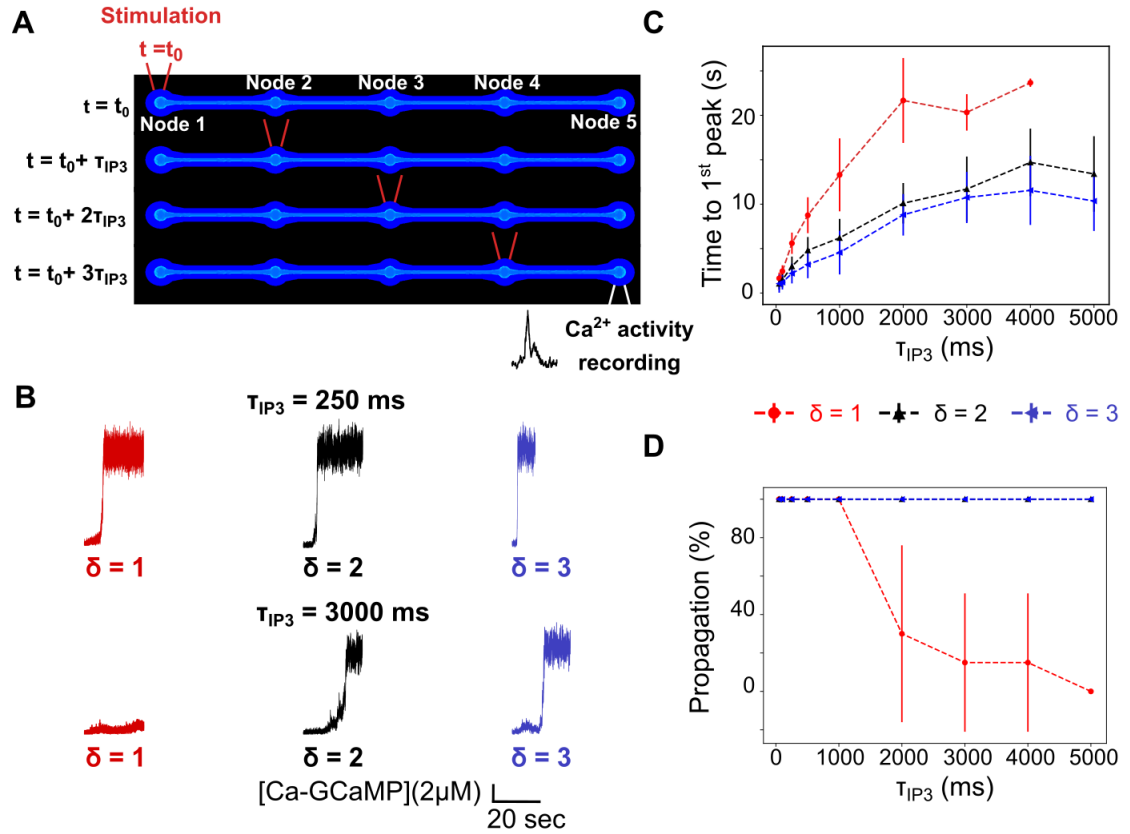
Figure VI.7: Study of the effect of node/shaft width ratio on signal propagation upon successive neuronal stimuli. (*A*) At t=t_0, Node 1 was stimulated. Then, τ_{IP3} defines the frequency at which a new node stimulation occurs so that node 2 is stimulated at time $t_0 + \tau_{IP3}$, node 3 at $t_0 + 2\tau_{IP3}$ and node 4 at $t_0 + 3\tau_{IP3}$. Ca^{2+} activity is recorded in node 5. (*B*) Representative Ca^{2+} traces for $\delta=1$ (red), 2 (black) and 3 (blue), with τ_{IP3}=250ms and 3000ms. (*C*) Time to 1st peak significantly increases with τ_{IP3} for $\delta=1$ (ANOVA, p-value=0.00016 ***, red), $\delta=2$ (ANOVA, p-value < 0.0001 ***, black) and $\delta=3$ (ANOVA, p-value < 0.0001 ***, blue). T-tests revealed that for any value of τ_{IP3}, time to 1st peak is significantly higher for $\delta=1$ compared to both $\delta=2$ and $\delta=3$. Time to 1st peak is not significantly different for $\delta=2$ compared to $\delta=3$, except for τ_{IP3}=250 (p=0.032 *), 500 (p=0.0025 **), 1000 (p=0.034 *), 4000 (p=0.016 *) and 5000 (p=0.019 *) ms. (*D*) The probability of signal propagation, expressed as the percentage of signals that propagated to Node 5, is significantly lower for $\delta = 1$ compared to $\delta=2$ and 3. The probability of signal propagation decreases as τ_{IP3} increases for $\delta = 1$ (ANOVA, p-value < 0.0001 ***).
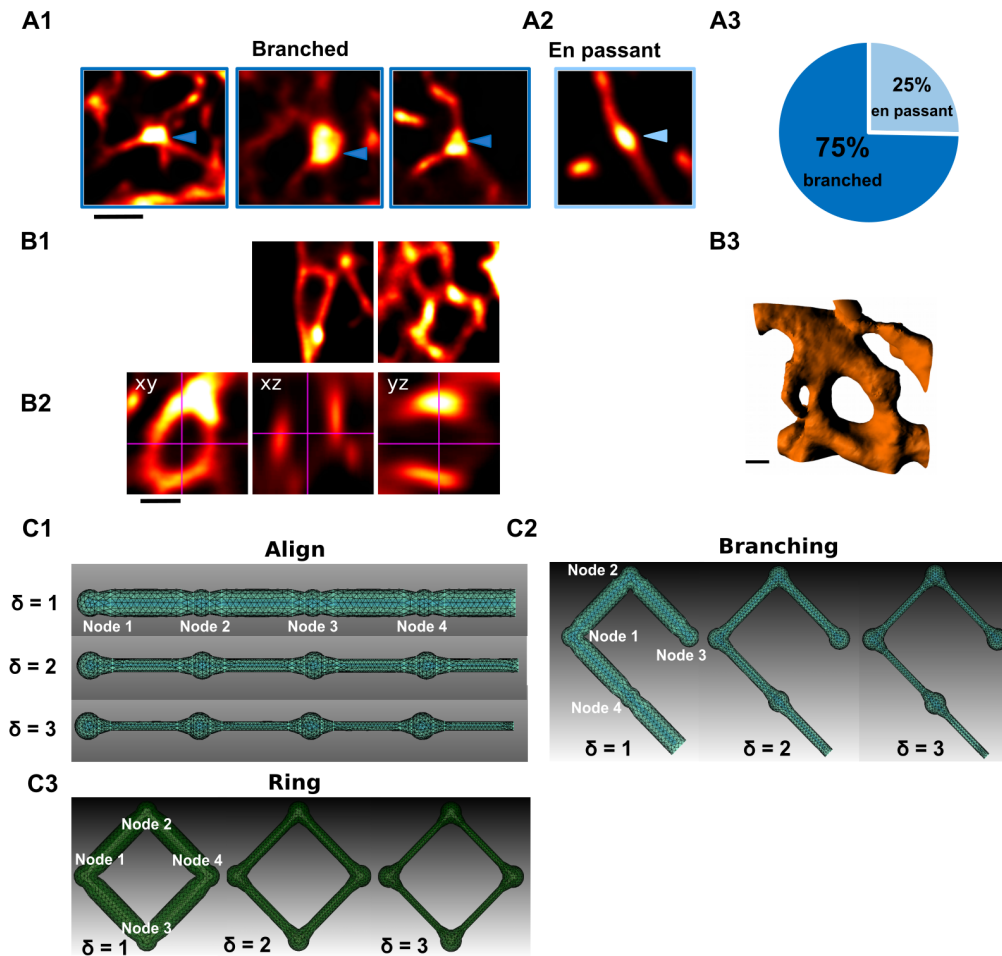
Figure VI.8: Experimental analysis of node branching and designed geometries. (*A, B*) Experimental data. (*A*) Several shafts often branch from a single node. (*A1*) Representative STED images revealing branching at nodes ('Branched'). (*A2*) Representative node without branching points ('En passant'). (*A3*) Quantification of the proportion of 'Branched' VS 'En passant' nodes (n = 261 from 14 slices). (*B*) STED images revealing ring-like geometries in the gliapil. (*B1*) Representative ring structures observed in the gliapil. (*B2*) Orthogonal views of a representative ring structure, demonstrating a ring shape rather than a cup shape. Scale bar: 500 nm. (*B3*) 3D reconstruction of the ring presented in panel B2. (*C*) Geometries with 4 nodes and 4 shafts of the same size were built with linear nodes (C1, 'Align'), branched (C2, 'Branching') or forming a ring (C3, 'Ring'). Each geometry was built for node/shaft widths ratios δ=1, 2 and 3.

1 (Fig VI.8C2), referred to as 'Branching' and some formed rings (Fig VI.8C3), referred to as 'Ring'. All geometries were built for node/shaft width ratios δ=1, 2 or 3.

At t=t_0=5s, 25 IP$_3$ molecules were infused in Node 1, mimicking neuronal stimulation. Similarly to the previous study (section VI.1.4), after a time period τ_{IP3}=100ms, the same amount of IP$_3$ was then infused in Node 2 and then at t_0+2τ_{IP3} in Node 3. During the whole simulation time, Ca^{2+} activity was recorded in Node 4. The kinetic scheme of the model and the corresponding parameter values were the same as the 3D "GCaMP" model, presented in section V.1.

Results

As $\approx$ 75% of nodes of the gliapil consist in branching points (Fig VI.8), we have investigated the propagation and characteristics of Ca^{2+} signals in structures with different levels of branching: 'Align', 'Branching' and 'Ring' (see section VI.1.5 for more details). Fig VI.9A presents representative Ca^{2+} traces in Node 4 for δ=1, 2 and 3 in 'Align' (Fig VI.9A1, black), 'Branching' (Fig VI.9A2, red) and 'Ring' (Fig VI.9A3, blue) geometries, which suggest that 'Align', 'Branching' and 'Ring' geometries are associated with different Ca^{2+} dynamics. Here again, simulations reveal that the time to 1$^{\text{st}}$ Ca^{2+} peak in Node 4 after the stimulation of Node 1, at t_0, decreases with node/shaft width ratio δ (Fig VI.9B1). Interestingly, time to 1$^{\text{st}}$ peak is increased in 'Ring' simulations compared to 'Align' and 'Branching', i.e the speed of signal propagation is significantly decreased in 'Ring' geometries, especially for δ=2 and 3 (Fig VI.9B1).

As the probability of signal propagation in Fig VI.6 increased with δ in aligned geometries, we have investigated whether this phenomenon could still be observed in branched and ring-like geometries and if branching was somehow impacting signal propagation. Similarly to the results presented in Fig VI.6 and Fig VI.7, an increased δ is also associated with a higher probability of signal propagation to Node 4, for 'Align', 'Branching' as well as 'Ring' geometries (Fig VI.9B2). Note that in addition to a decreased propagation speed, 'Ring' geometries are also associated with a lower probability of signal propagation to Node 4 compared to 'Align' and 'Branching' geometries (Fig VI.9B2).

As Ca^{2+} traces presented in Fig VI.9A displayed diverse Ca^{2+} peak characteristics depending on the geometry, we have next investigated the effect of node branching and of ring-like structures on peak amplitude and duration. Our results suggest that both peak amplitude (Fig VI.9B3) and duration (Fig VI.9B4) increase with δ, for 'Ring', 'Align' and 'Branching geometries. Interestingly, peak amplitude and duration are significantly lower in 'Ring' compared to 'Align' or 'Branching'

geometries, whatever the value of δ. Moreover, peak amplitude and duration is significantly higher in 'Branching' geometries compared to 'Align', whatever the value of δ.

Overall, node branching seems to increase local Ca²⁺ peak duration and amplitude while its 'fusion' into ring-like structures is associated with decreased peak amplitude and duration. Moreover, ring-like structures are characterized by both lower probability and speed of signal propagation. Ring-like structures might thus be associated with highly localized puncta of Ca²⁺ activity, potentially favoring neuron-astrocyte communication at the single-synapse level.

Conclusion

The geometries developed in this study, presented in Fig VI.4C and VI.8, emerge as interesting tools to investigate the influence of cellular geometry on Ca²⁺ dynamics in the gliapil. Our results suggest that high node/shaft ratios are associated with an increased diffusional isolation of nodes while favoring the propagation of signals, which is the opposite of the suggestions from Arizono et al[9]. Indeed, our collaborators suggested that the higher diffusional isolation of nodes for high δ could 'trap' Ca²⁺ signals in nodes and thus be responsible for the $\approx 70\%$ of signals that stayed localized in nodes. Our simulations however predict that the greater δ, the higher the probability and speed of signal propagation. This suggests that geometries with $\delta=1$ might favor the existence of local communication at the node-spine level, i.e at the single-synapse level. Finally, our results suggest that the formation of ring-like structures might decrease both the probability and speed of signal propagation and that signals in ring-like structures are characterized by decreased peak amplitude and duration compared to the equivalent 'align' or 'branching' geometries. Ring-like structures might thus favor local signaling rather than Ca²⁺ waves, which might have strong implications on neuron-astrocyte communication at the sub-cellular level.

Together, our results suggest that the $\approx 70\%$ of signals that stayed localized in one node [9] might result from a high density of ring-like structures and/or from the presence of processes with low node/shaft ratios. The remaining 30% of signals that propagated might result from aligned/branched geometries, potentially with higher node/shaft width ratio. In any case, our results reveal potential geometrical properties that can at least partially explain the variety of signal propagation cues observed experimentally.
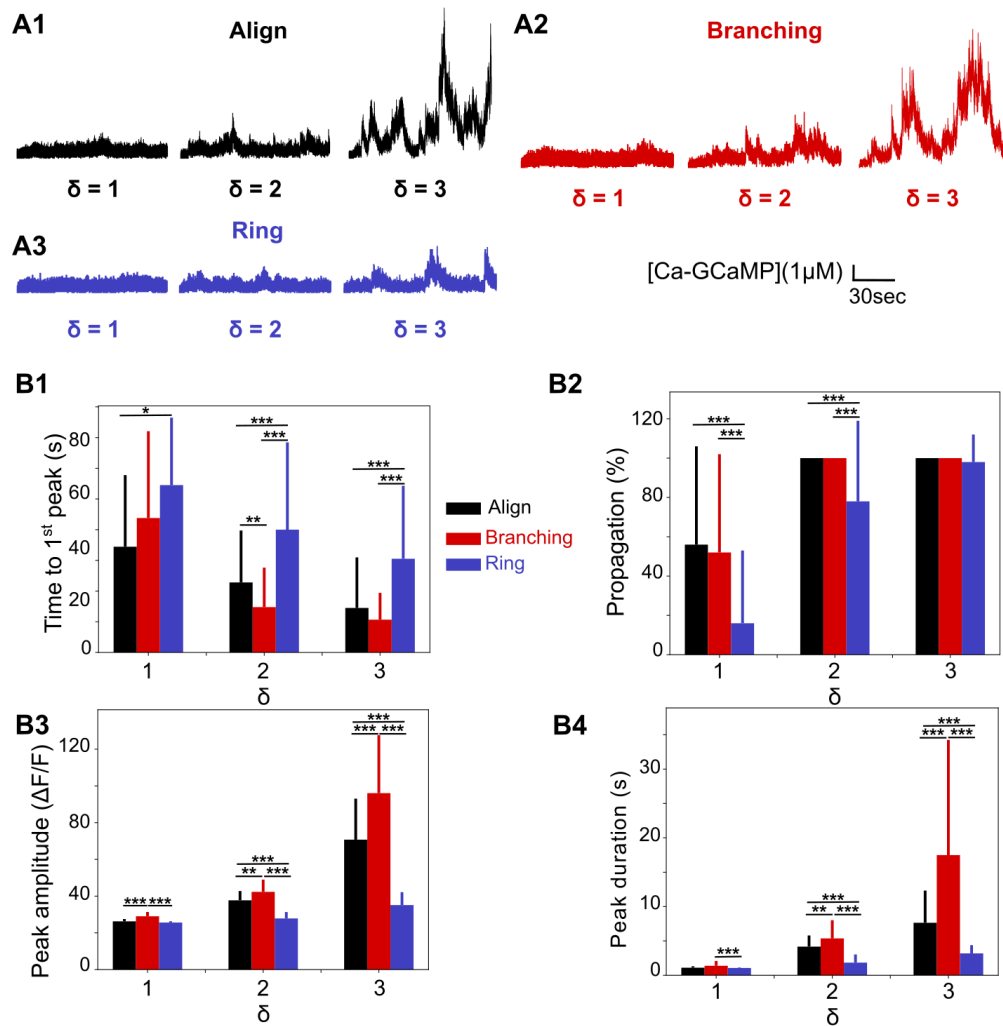
Figure VI.9: Effect of node branching and of ring-like structures on signal propagation.
(*A*) Representative [Ca-GCaMP] traces for δ=1, 2 and 3 and for 'Align' (A1, black), 'Branching'
(A2, red) and 'Ring' (A3, blue) geometries. Panel *B* presents the quantification of the delay
between stimulation time of Node 1 and peak onset in Node 4 (B1, ANOVA, p-values<0.0001
*** for 'Align' and 'Branching' and p-value=0.0066 ** for 'Ring'), the percentage of simulations
in which signal propagated to Node 4 (B2, ANOVA, p-values<0.0001 ***), peak amplitude (B3,
ANOVA, p-values<0.0001 ***) and peak duration (B4, ANOVA, p-values<0.0001 ***) in Node
4, for δ=1, 2 and 3 and for 'Align', 'Branching' and 'Ring' geometries, respectively. Data are
represented as mean $\pm$ STD, n=50 for each condition. Significance of the difference between
'Align', 'Branching' and 'Ring' geometries is assigned by * for $p \leq 0.05$, ** for $p \leq 0.01$, ***
for $p \leq 0.001$.

VI.1.6   Discussion

For τ_{IP3}=4s and 5s and for δ=2 or 3, signals were detected in Node 5 $\approx$ 10s after the stimulation of Node 1 (at t_0), which means that they occurred before the stimulation of Node 4 (t=t_0 + 12s and t=t_0 + 15s for τ_{IP3}=4s and 5s, respectively). This phenomenon was not observed in geometries with δ=1, for which time to 1st peak when τ_{IP3}=4s was 23.67 $\pm$ 0.47 s, which is larger than stimulation time of Node 4 (t=t_0 + 12s). This suggests that for δ=2 and 3, contrary to δ=1, one node stimulation can be omitted without having any consequence on signal propagation. Large node/shaft width ratio would thus result in a more robust signal propagation. In order to test this hypothesis, we plan to perform simulations of the protocol presented in Fig VI.7 in which, for each node stimulation, IP_3 infusion occurs with a given probability of failure. The percentage of signals that propagate to Node 5, depending on the value of the probability of failure, reflects the robustness of signal propagation and can be tested depending on δ.

As described above, our collaborators [9] have observed different fractions of spines covered by astrocytes (Fig VI.5). The physiological implications of such a variability is however not understood yet. Simulations with varying astrocytic plasma membrane areas contacted by the spine could help investigate this question. More particularly, those simulations would allow to study the influence of the surface of astrocytic processes that is contacted by a spine on the onset and probability of Ca^{2+} wave propagation.

The presence of "Rings" in the gliapil by itself is striking and requires further investigation. Indeed, even if reported previously [541], those structures have not been observed using electron microscopy. This discrepancy could be due to possible tissue distortions associated to the chemical fixation of samples in electron microscopy [583] or to the poor resolution of STED in z (200nm), which might result in wrong reconstructions of the 3D structure. Combining those fluorescent techniques with expansion microscopy [584, 585, 586, 587, 588] might increase the resolution of the images and help better characterize those apparent "Rings". Indeed, for the moment we cannot rule out whether those structures result from the fusion of membranes of neighboring astrocytic processes or from the formation of inter-processes gap junctions. Better understanding the exact geometry of this structure and its formation as well as its potential dynamical restructuration is crucial for better understanding its impact on Ca^{2+} signaling in the gliapil. How do those structures form? When does the formation of ring-like structures occur? Is this phenomenon plastic and related to neuronal activity? Many questions arise from this study, which could help better understand neuron-astrocyte communication and information processing in astrocytes. In any case, the formation of ring-like structures might, according to our simulations, result in a decrease of the local speed and probability of signal

propagation, probably favoring local signaling between astrocytes and neurons.

VI.2 Simulating the effect of ER-PSD distance on neuronal activity-induced Ca^{2+} signals in astrocytic processes

VI.2.1 Experimental background

During the past few years, fine astrocytic processes have been regarded as devoid of ER [33, 430]. As presented in section V.2, our collaborator C. Calì, KAUST, Saudi Arabia, has detected ER in some PAPs using electron microscopy (see Fig V.5). Fig VI.10A presents different images from electron microscopy of a representative tripartite synapse, displaying a PAP that contains ER, with an ER-PSD (post-synaptic density) distance of $\approx$ 68nm. Fig VI.10B presents quantification of the distance between the closest ER to PSD. According to those results, the closest astrocytic ER is at an average distance of 776 nm $\pm$ 567 nm from PSD and can be < 100 nm (see Fig VI.10B). Those results are very important as they contradict the strong belief in the field that no ER is present in perisynaptic processes [33, 430]. Minimal ER-synapse distance turns out to be extremely variable. In this study, we have thus investigated the influence of such diverse ER-PSD distance on neuronal-induced Ca^{2+} signals (see Fig VI.11A).

VI.2.2 Modeling approach and geometry

Fig VI.11 presents the modeling approach developed in this study (Fig VI.11A) as well as the 3D geometries that were created to investigate the impact of the distance between the ER and the tip of the process on Ca^{2+} signaling (Fig VI.11B). Similarly to simulations from section VI.1, neuronal stimulation was modeled as an infusion of 25 IP$_3$ molecules (i.e 460 nM for λ=0 nm and $\approx$ 200 nM for λ=1000 nm) at the tip of the process, at time t=2s. In order to get the same density of IP$_3$R channels among simulations, the length and diameter of the ER was conserved (1 μm long, 160nm in diameter), whatever the distance from the tip of the process λ, so that the total number of IP$_3$R molecules was constant: 160. Therefore, changes of λ were obtained by varying the total process length, which was associated with modifications of total cytosolic volume (see Fig VI.11B).
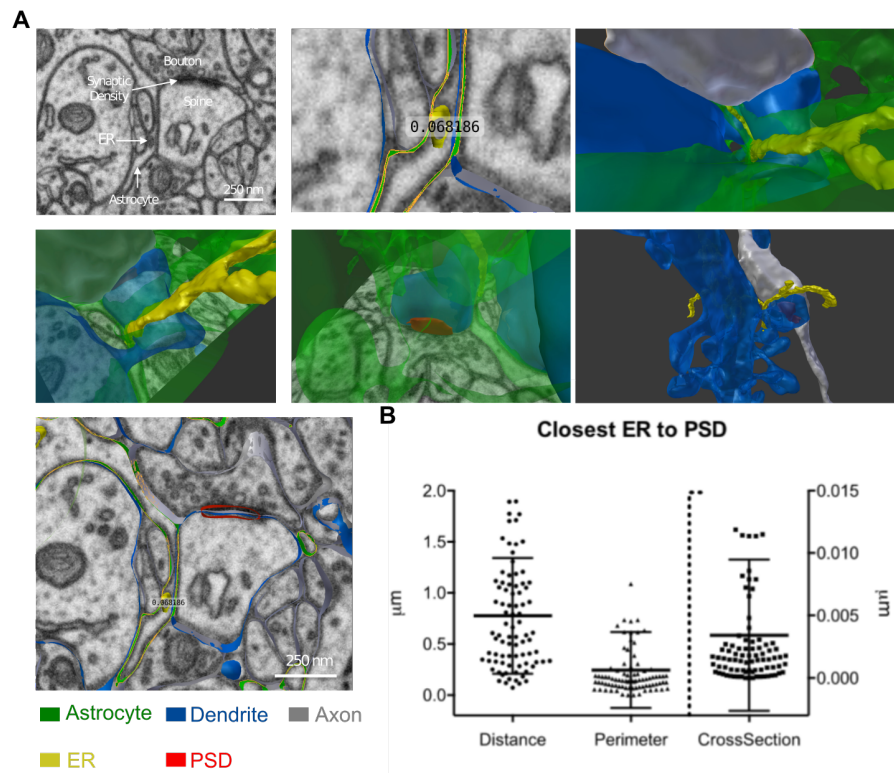
Figure VI.10: Electron microscopy reveals the presence of ER in PAPS and its vicinity to synapses. (*A*) Electron microscopy images revealing a representative example of an astrocytic (green) process containing ER (yellow) that is in the vicinity of synaptic PSD(post-synaptic density, red). Axons are represented in grey. In this example, the ER is at a distance of 68nm from the PSD. (*B*) Quantitative analysis of the distance of ER to PSD, of the perimeter and cross-section of the ER (in μm). The closest astrocytic ER is at an average distance of 776 nm $\pm$ 567 nm from PSD, with some PSDs that are at $<$ 100nm away from a PSD.

VI.2.3   Results: Effect of ER-PSD distance on the onset and characteristics of astrocytic Ca^{2+} signals

As our collaborator has reported diverse distances between synapses and the closest astrocytic ER (ER-PSD distance, λ), we have investigated the effect of the variability of this distance on Ca^{2+} signals in fine astrocytic processes. To do so, we have performed simulations within simplified cylinder geometries in which the ER was positioned at various distances from IP_3 infusion site, which reflects PSD location: from $\lambda=0$ to 1 μm. In order to visualize the propagation of Ca^{2+} signals within the process, space was discretized into 100 nm-long bins, so that the geometry with $\lambda=0$nm ($l_{\text{astro}}=1\mu$m) was discretized into 10 bins while the geometry with
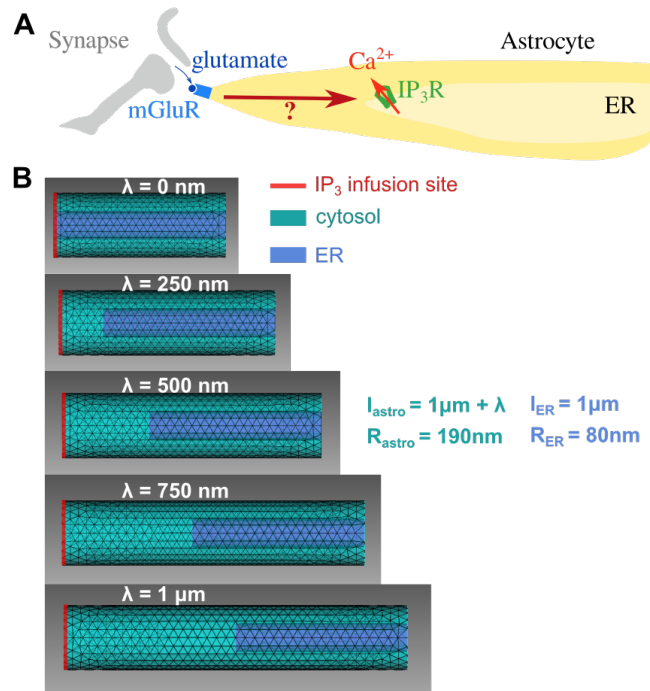
Figure VI.11: Modeling approach for investigating the effect of ER-PSD distance on
Ca^{2+} **signaling.** (*A*) Schematic representation of the biological question. This study aims at
investigating the effect of the distance between a synapse (PSD) and the closest astrocytic
endoplasmic reticulum (ER) to PSD, λ, on the onset and characteristics of Ca^{2+} signals. (*B*)
3D geometries that were designed for investigating the effect of λ on Ca^{2+} dynamics. ER
surface was constant across those geometries to ensure constant IP$_3$R density.

$\lambda=1\mu$m ($l_{\text{astro}}=2\mu$m) was discretized into 20 bins (see Fig VI.12A1). The resulting
plots of Ca^{2+} dynamics in each bin from t=0 to t=50s reveal striking differences of
Ca^{2+} dynamics depending on λ (Fig VI.12A2). Interestingly, [Ca-GCaMP] peaks
plotted as a function of time and space consist in horizontal lines (Fig VI.12A2).
This suggests that signals propagate very fast so that [Ca-GCaMP] in a PAP is soon
homogenized, preventing the observation and quantification of wave propagation at
this spatial scale. Ca^{2+} activity in the whole process qualitatively varied depend-
ing on ER-PSD distance λ for a given neuronal stimulus (here 25 IP$_3$ molecules)
(Fig VI.12A3). Quantitative analysis of Ca^{2+} signals depending on λ are presented in
Fig VI.12B. Peak amplitude (Fig VI.12B1) and frequency (Fig VI.12B3) significantly
decreased when λ increased while time to 1$^{\text{st}}$ peak increased with λ (Fig VI.12B4).
However, λ did not seem to impact peak duration (Fig VI.12B2). Note that we have
checked that spontaneous Ca^{2+} signals (number of IP$_3$ infused=0) did not vary in
amplitude, frequency and duration depending on λ (not shown, ANOVA, p-value=
0.31, 0.18 and 0.63, respectively). Our results thus reveal a strong effect of ER-PSD

distance on peak amplitude and frequency.

Overall, our results suggest that the variety of PSD-ER distances that are observed experimentally might partly be responsible for the diversity of both amplitude and frequency of Ca²⁺ signals observed in fine processes. Please note that the geometry used in this study is characterized by a slightly larger volume than that is believed to represent PAPs. In order to confirm whether our predictions are still valid for thinner processes of the gliapil, we plan to perform those simulations again within meshes of thinner processes (R_astro=100nm rather than 190nm).

VI.2.4   Discussion

The study presented in this section is similar to a previous dimensionless mass diffusion model from Montes de Oca Balderas [430], although their model was devoid of a degradation term for IP₃, thus compromising interpretation of their simulation results. Our predictions are in accordance with their finding: even if the ER is located 1 μm away from the PSD, IP₃R-dependent Ca²⁺ transients can be triggered in the astrocyte. Our study however goes further in studying the effect of ER-PSD distance on astrocytic Ca²⁺ signals. We show that peak amplitude and frequency strongly decrease with ER-PSD distance, so that for a similar neuronal input and cellular location, varying ER-PSD distances can result in diverse Ca²⁺ signals.

Our results suggest that signals propagate very fast so that the concentration of IP₃ is soon homogenized within a fine process, resulting in the absence of a detectable Ca²⁺ wave at this spatial scale. In fact, the coefficient of diffusion of IP₃ molecules in the model is D_IP3=280 μm².s⁻¹, and that of GCaMP molecules is D_GCaMP=50 μm².s⁻¹ so that IP₃ and Ca-GCaMP molecules can diffuse along the entire geometry within few ms. Overall, our results suggest that the increase of IP₃ concentration rather than its diffusion is critical for the onset of Ca²⁺ peaks in a PAP with the parameter values used in this model. Note that the coefficient of diffusion of IP₃ available in the literature was measured in Xenopus laevis oocytes cytosolic extracts in the 1990s [554], which might not reflect its dynamics in astrocytes. Further experimental investigation on the coefficient of diffusion of molecules of the Ca²⁺ pathway in astrocytes is crucial in order to better understand signal propagation in the small volumes that characterize processes of the gliapil.

As simulations in section V.2 have revealed that Ca²⁺ dynamics can vary drastically depending on the mesh in which simulations are performed, it would be interesting to test the predictions of the simulations presented in this section in a more realistic PAP geometry. To do so, we plan to perform simulations with varying
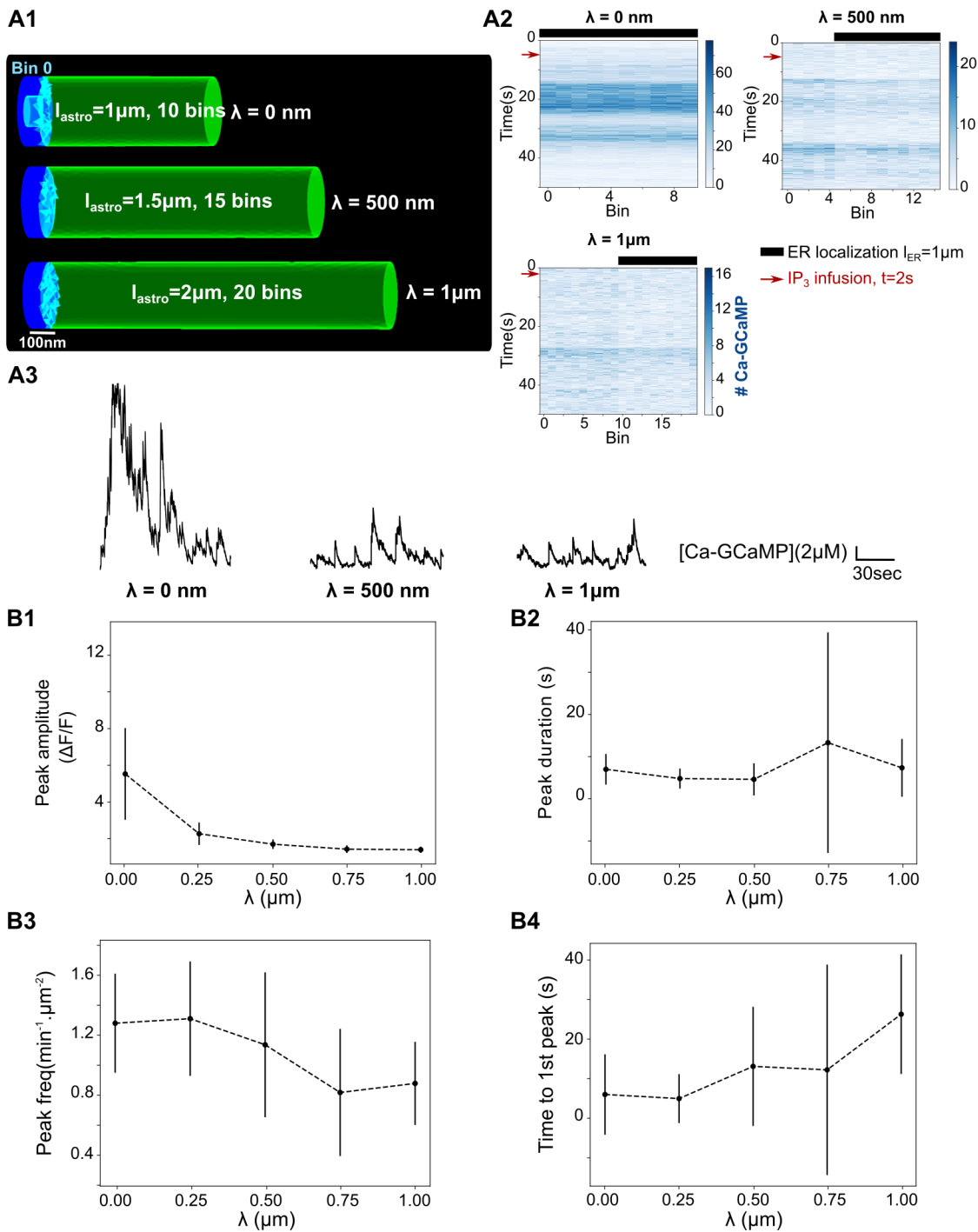
Figure VI.12: ER-PSD distance influences Ca^{2+} peak duration and amplitude. (*A1*) Screenshots revealing the spatial discretization of processes into 100nm-long bins, for ER-PSD distance λ=0, 500 and 1000 nm. One bin is highlighted in blue while the rest of the volume is in green. (*A2*) Representative plots illustrating the number of Ca^{2+} ions in each bin as a function of time for geometries with λ=0, 500 and 1000nm, from t=0 to t=50s. (*A3*) Representative simulations with ER-PSD distances λ=0nm, 500nm and 1 μm (see geometries in Fig VI.11B). (*B*) Quantification of peak amplitude (*B1*, ANOVA, p-value $\leq$ 0.0001 ***), frequency (*B2*, ANOVA, p-value $\leq$ 0.0001 ***), duration (*B3*, ANOVA, p-value= 0.16) and time to 1st peak (*B4*, ANOVA, p-value= 0.05 *) as a function of λ. Data are expressed as mean $\pm$ standard deviation, n=20. Dashed lines are guides for the eye.

ER-PSD distances in the realistic mesh presented in Fig V.5B. In order to investigate the effect of ER-PSD distance in this mesh, we will perform simulations in which IP$_3$ infusion will occur at different locations in the cell, associated with varying distances to the closest ER. Simulations in larger volumes of the mesh presented in Fig V.5A could also enable the investigation of signal propagation within a realistic network of astrocytic processes. Such a larger volume would probably be more suited to the study of signal propagation depending on ER-PSD distance and would help better understand signal integration in the gliapil, which might be important for neuron-astrocyte communication.

VI.3 Conclusion

In this chapter, we have used the 3D voxel-based implementation of our model presented in Chapter V in order to investigate the onset and propagation of neuronal-induced Ca^{2+} signals in astrocytes. More particularly, we have investigated the effect of cellular and of ER geometry on the characteristics of induced Ca^{2+} signals. The geometries tested in this chapter were based on experimental data from our collaborators. Overall, our simulations suggest that the geometry of fine processes by itself can be responsible for various properties of signal propagation. Furthermore, dynamical remodeling of the geometry of processes, as e.g the formation of ring-like structures observed by Arizono et al [9], can result in a striking modification of the probability and speed of signal propagation in the structure. Finally, simulations in a simplified cylinder mesh have enabled us to study the effect of the varying ER-PSD distances that were observed by our collaborator on local peak amplitude and frequency in a fine astrocytic process. Cellular and ER geometries are thus important parameters that can influence focal VS spread Ca^{2+} activity in the gliapil. A thorough characterization of the ultrastructure of the gliapil should thus provide a better understanding of information processing in astrocytes.

Chapter VII

Conclusion and perspectives

Conclusion

As all studies from Chapters IV, V and VI were presented together with discussions on their results, limitations and perspectives, broader conclusion and perspectives are presented here.

The small size of astrocytic processes that interact with neurons (< 200nm in diameter), associated to the low concentrations of molecular species such as Ca^{2+} ions (≈ 100 nM), implies that reactions that result in Ca^{2+} signals occur stochastically. Mathematical models of CICR-based signaling date back to the beginning of the 1990s (for recent reviews see e.g. [540, 287, 288]) and most assumed perfect mixing of the molecules and deterministic kinetics (ODEs, see section III.1) [8, 300, 302]. Stochastic models of IP_3R-mediated Ca^{2+} signaling have also been proposed, that take into account the stochasticity associated with molecular interactions [377, 531, 545, 530]. Yet, none of those studies accounts both for the diffusion of molecular species and the stochasticity of the reactions taking place inside astrocytes. Recently, individual-based modeling has been introduced to evaluate the impact of diffusive noise on IP_3R opening dynamics [491], but this simplified model disregarded IP_3 dynamics and restricted stochasticity to the vicinity of the IP_3R channels. To our knowledge, our model is the first fully stochastic individual-based model that is suited to reproduce spontaneous Ca^{2+} signals in the finest astrocyte processes, where low copy number and spatial localization effects are expected to be more prominent than in larger volumes.

Simulations in the 2D version of the model allowed for a better understanding of its dynamics and of the basic spatial parameters that could influence the regime and temporal characteristics of Ca^{2+} signals (Chapter IV). Simulations in 3D geometries representing PAP volumes and realistic molecular concentrations allowed us to

further investigate the impact of cellular geometry on spontaneous Ca^{2+} dynamics, notably the interplay between molecular clustering and the distance between plasma membrane and intracellular Ca^{2+} stores (Chapter V). The last part of this thesis consisted in investigating the impact of astrocytic geometry at the nanoscale on the onset and propagation of neuronal-induced Ca^{2+} signals (Chapter VI). Overall, simulations of the model suggest that (1) molecular diffusion, strongly influenced by the concentration and kinetics of endogenous and exogenous buffers, (2) intracellular spatial organization of molecules, notably Ca^{2+} channels co-clustering, (3) ER geometry and localization within the cell, (4) cellular geometry strongly influence Ca^{2+} dynamics and can be responsible for the striking diversity of astrocytic Ca^{2+} signals.

All of the studies presented in this manuscript rely on IP_3R-dependent Ca^{2+} signals. As the ER is most probably absent from some processes (see e.g Fig V.10), the model developed in this thesis cannot fully represent the diversity of Ca^{2+} signals encountered in astrocytes. For more details on the controversies and perspectives on the presence of ER in processes and on the dependence of local Ca^{2+} signals on the ER, see dedicated discussion in section V.3. Similarly, experimental reports suggest that the complete dependence of cytosolic Ca^{2+} transients on IP_3R2 channels is only observed in the astrocytic soma whereas Ca^{2+} signals measured within astrocytic processes are a mix of IP_3R2-dependent and IP_3R2-independent Ca^{2+} signals [6, 254]. The identity, subtype and localization of the channels responsible for IP_3R2-independent Ca^{2+} signals in astrocytes are still to be uncovered. Our study sheds light on the importance of the localization of these various Ca^{2+} sources, whatever their specific subtypes.

Overall, simulations of the model demonstrate that low copy number of molecules can display dynamics that cannot be predicted by deterministic approaches and that spatial modeling is crucial to better understand the effect of molecular distributions and of cellular geometry on Ca^{2+} dynamics in astrocytes. Recent studies have proposed models for the simulation of astrocytic Na^+ [429] and Ca^{2+} signals [589, 430, 405] in 3D with deterministic differential equation models that correspond to cellular volumes large enough to validate a law of large numbers. Since fine processes are thought to be the place of neuron-astrocyte interactions, we believe that this model, combined with models of signal propagation between astrocytic compartments such as Savtchenko et al [405], might be useful to investigate the spatiotemporal integration of Ca^{2+} signals in the spongiform network of astrocyte processes.

Towards replicable and reproducible models

Several meta studies have put forward the different behaviors that models of the same biological system can display [590, 540]. Actually, reproducing the results from computational models, even though they do not suffer from experimental measurement errors, is not straightforward, which has been pointed out in several fields, including in models of astrocytes [591, 540]. One of the big challenges in the modeling community is to develop reproducible models. Models should be replicable, cross-replicable and reproducible (see [592] for details). Basically, the simulation results should not depend on the code and tools used for implementing the model.

In order to improve the reproducibility of computational models, it is recommended to systematically share the code (with e.g ModelDB [593], see Crook et al [592] for other available model databases). Guidelines for sharing models have been suggested in the form of Minimum Information Required in the Annotation of Models (MIRIAM, http://co.mbine.org/standards/miriam) [594]. Those studies suggest that all modeling studies should include model description, hypothesis, implementation (providing the code is best), analysis, validation against experimental data and justification. Using common languages for describing molecular interactions independently of the simulator can also promote cross-replicability of models. The most popular of those languages is the Systems Biology Markup Language (SBML) [595] (but see Crook et al [592] for an overview of other markup languages). Finally, some platforms have started to build tools that allow for inter-operability of different simulators, as e.g the interface MUSIC [520].

Such initiatives have also emerged in the field of computational neuroscience. For example, PyNN and NeuroML provide simulation tools for standardized formats of neuroscience models. PyNN [596] is a programming interface using Python programming language, in which a growing toolbox is available for simulation and data analysis. NeuroML is an XML-based programming interface, which enables the description of model components at various scales of the nervous system [597].

Overall, producing models that are better documented, easily reproducible and replicable should help improve knowledge and collaborative work in the field of computational neuroscience.

Perspectives

Since contact sites have been detected in perivascular astrocytic processes between ER and plasma membrane (PM) [30] and as simulations of the model in Chapter V suggested an effect of ER-PM distance on Ca^{2+} signals (see section V.3

for further discussion), we would like to investigate the impact of ER-PM contact sites on Ca^{2+} signals at the sub-cellular scale. To do so, we have started to develop a mesh in which the main geometrical parameters of ER-PM contact sites can be modified. Simulations in this mesh are characterized by the existence of a Ca^{2+} gradient from the contact site. To our knowledge, this is the first fully stochastic spatially-explicit model of Ca^{2+} nanodomains. Meanwhile, our collaborator is investigating the number and distribution of ER-PM contact sites in astrocytes. This study might be helpful to better understand the influence of ER-PM geometry on Ca^{2+} signaling.

IP_3R-dependent Ca^{2+} signals can involve a substantial transient decrease of $[Ca^{2+}]$ within the ER. For simplicity, those variations have not been taken into account in the models that have been presented in this manuscript. Local Ca^{2+} depletion in the ER could however strongly influence cytosolic Ca^{2+} signals, especially in small volumes such as encountered within microdomains. In order to test this hypothesis, we have adapted the "GCaMP" model presented in section V.1 in order to account for Ca^{2+} dynamics within the ER. This model is interesting for investigating local depletion of Ca^{2+} in the ER following Ca^{2+} activity, which has not been investigated so far to our knowledge in systems with low copy number of molecules.

One astrocyte can be viewed as the summation of units of signal integration, its processes. However, whether processes consist in independent, heterogeneous units still remains to be uncovered. More particularly, it is not known under which conditions signals emerging from independent processes can interact. A perspective of the work presented in this manuscript would be to simulate signals emerging from different processes and to investigate the integration of Ca^{2+} signals in this intracellular network. As astrocytes in the rat hippocampus can contact simultaneously ≈ 100 000 synapses [27] and human astrocytes could contact up to 2 000 000 synapses [37], this question is fundamental to understand the potential role that single astrocytes could play in connecting different neuronal networks. To model signal integration and propagation within networks of astrocytic processes, we could create geometries in which several processes are connected, each of them being stimulated by different neuronal sources, at different timing. We could also simulate signal integration directly in our mesh of a realistic 3D astrocyte, with neuronal PSDs, extracted from electron microscopy (see Fig V.5A), although simulations in this geometry with STEPS would probably take years to compute. Using hybrid approaches for modeling the integration of stochastic local signals and the subsequent global activity thus emerges as the best compromise to simulate signal integration within whole astrocytes. Those multiscale modeling studies will be of high importance for understanding the influence of information processing at the (sub-)cellular level on

higher-level brain functions.

Bibliography

[1] R. Ventura and K. M. Harris, "Three-Dimensional Relationships between Hippocampal Synapses and Astrocytes," *The Journal of Neuroscience*, vol. 19, pp. 6897–6906, Aug. 1999.

[2] M. R. Witcher, S. A. Kirov, and K. M. Harris, "Plasticity of perisynaptic astroglia during synaptogenesis in the mature rat hippocampus," *Glia*, vol. 55, pp. 13–23, Jan. 2007.

[3] N. Bazargani and D. Attwell, "Astrocyte calcium signaling: the third wave," *Nature Neuroscience*, vol. 19, pp. 182–189, Feb. 2016.

[4] J. P. Heller and D. A. Rusakov, "The Nanoworld of the Tripartite Synapse: Insights from Super-Resolution Microscopy," *Frontiers in Cellular Neuroscience*, vol. 11, 2017.

[5] S. Berlin, E. C. Carroll, Z. L. Newman, H. O. Okada, C. M. Quinn, B. Kallman, N. C. Rockwell, S. S. Martin, J. C. Lagarias, and E. Y. Isacoff, "Photoactivatable genetically encoded calcium indicators for targeted neuronal imaging," *Nature Methods*, vol. 12, pp. 852–858, Sept. 2015.

[6] R. Srinivasan, B. S. Huang, S. Venugopal, A. D. Johnston, H. Chai, H. Zeng, P. Golshani, and B. S. Khakh, "Ca(2+) signaling in astrocytes from Ip3r2(-/-) mice in brain slices and during startle responses in vivo," *Nature Neuroscience*, vol. 18, pp. 708–717, May 2015.

[7] E. Bindocci, I. Savtchouk, N. Liaudet, D. Becker, G. Carriero, and A. Volterra, "Three-dimensional Ca^{2+} imaging advances understanding of astrocyte biology," *Science*, vol. 356, p. eaai8185, May 2017.

[8] G. W. De Young and J. Keizer, "A single-pool inositol 1,4,5-trisphosphate-receptor-based model for agonist-stimulated oscillations in Ca2+ concentration.," *Proceedings of the National Academy of Sciences*, vol. 89, pp. 9895–9899, Oct. 1992.

[9] M. Arizono, A. Panatier, V. V. G. K. Inavalli, T. Pfeiffer, J. Angibaud, J. Stobart, L. Bellocchio, G. Marsicano, K. Mikoshiba, S. H. R. Oliet, B. Weber, and U. V. Nägerl, "Structural Basis of Astrocytic Ca ^{2} Signals at Tripartite Synapses," SSRN Scholarly Paper ID 3287791, Social Science Research Network, Rochester, NY, Nov. 2018.

[10] R. Virchow, "Die Cellularpathologie in ihrer Begr{\"u}ndung auf physiologische und pathologische Gewebelehre," *A. Hirschwald*, vol. 1, 1862.

[11] C. Golgi, "Sulla sostanza connettiva del cervello (nevroglia)," *Rendiconti del R Instituto Lombardo di Scienze e Lettere*, vol. 3, pp. 275–277, 1870.

[12] C. Golgi, "Opera Omnia, Vol. 1," *Milano: U. Hoepli*, p. 40, 1903.

[13] M. v Lenhossek, "Der feinere Bau des Nervensystems im Lichte neuester Forschung," *Fischer's Medicinische Buchhandlung H. Kornfield*, 1893.

[14] V. García-Marín, P. García-López, and M. Freire, "Cajal's contributions to glia research," *Trends in Neurosciences*, vol. 30, pp. 479–487, Sept. 2007.

[15] S. R. y Cajal, *Algunas conjeturas sobre el mecanismo anatómico de la ideación, asociación y atención.* 1895.

[16] F. De Castro, "The anatomical aspects of the ganglionic synaptic transmission in mammals," *Archives internationales de physiologie*, vol. 59, no. 4, p. 479, 1951.

[17] R. Galambos, "A GLIA-NEURAL THEORY OF BRAIN FUNCTION," *Proceedings of the National Academy of Sciences of the United States of America*, vol. 47, pp. 129–136, Jan. 1961.

[18] A. Verkhratsky and M. Nedergaard, "Physiology of Astroglia," *Physiological Reviews*, vol. 98, pp. 239–389, Jan. 2018.

[19] A. Chvátal, M. Anderová, M. Hock, I. Prajerová, H. Neprasová, V. Chvátal, F. Kirchhoff, and E. Syková, "Three-dimensional confocal morphometry reveals structural changes in astrocyte morphology in situ," *Journal of Neuroscience Research*, vol. 85, pp. 260–271, Feb. 2007.

[20] M. M. Boisvert, G. A. Erikson, M. N. Shokhirev, and N. J. Allen, "The Aging Astrocyte Transcriptome from Multiple Regions of the Mouse Brain," *Cell Reports*, vol. 22, pp. 269–285, Jan. 2018.

[21] Y. Zhang, K. Chen, S. A. Sloan, M. L. Bennett, A. R. Scholze, S. O'Keeffe, H. P. Phatnani, P. Guarnieri, C. Caneda, N. Ruderisch, S. Deng, S. A. Liddelow, C. Zhang, R. Daneman, T. Maniatis, B. A. Barres, and J. Q. Wu, "An RNA-sequencing transcriptome and splicing database of glia, neurons, and vascular cells of the cerebral cortex," *The Journal of Neuroscience: The Official Journal of the Society for Neuroscience*, vol. 34, pp. 11929–11947, Sept. 2014.

[22] Y. Zhang, S. A. Sloan, L. E. Clarke, C. Caneda, C. A. Plaza, P. D. Blumenthal, H. Vogel, G. K. Steinberg, M. S. B. Edwards, G. Li, J. A. Duncan, S. H. Cheshier, L. M. Shuer, E. F. Chang, G. A. Grant, M. G. H. Gephart, and B. A. Barres, "Purification and Characterization of Progenitor and Mature Human Astrocytes Reveals Transcriptional and Functional Differences with Mouse," *Neuron*, vol. 89, pp. 37–53, Jan. 2016.

[23] W. Schulze, A. Hayata-Takano, T. Kamo, T. Nakazawa, K. Nagayasu, A. Kasai, K. Seiriki, N. Shintani, Y. Ago, C. Farfan, R. Hashimoto, A. Baba, and H. Hashimoto, "Simultaneous neuron- and astrocyte-specific fluorescent marking," *Biochemical and Biophysical Research Communications*, vol. 459, pp. 81–86, Mar. 2015.

[24] L. Zhuo, B. Sun, C.-L. Zhang, A. Fine, S.-Y. Chiu, and A. Messing, "Live Astrocytes Visualized by Green Fluorescent Protein in Transgenic Mice," *Developmental Biology*, vol. 187, pp. 36–42, July 1997.

[25] Y. Zuo, J. L. Lubischer, H. Kang, L. Tian, M. Mikesh, A. Marks, V. L. Scofield, S. Maika, C. Newman, P. Krieg, and W. J. Thompson, "Fluorescent Proteins Expressed in Mouse Transgenic Lines Mark Subsets of Glia, Neurons, Macrophages, and Dendritic Cells for Vital Examination," *Journal of Neuroscience*, vol. 24, pp. 10999–11009, Dec. 2004.

[26] E. Shigetomi, E. A. Bushong, M. D. Haustein, X. Tong, O. Jackson-Weaver, S. Kracun, J. Xu, M. V. Sofroniew, M. H. Ellisman, and B. S. Khakh, "Imaging calcium microdomains within entire astrocyte territories and endfeet with GCaMPs expressed using adeno-associated viruses," *The Journal of General Physiology*, vol. 141, pp. 633–647, May 2013.

[27] E. A. Bushong, M. E. Martone, Y. Z. Jones, and M. H. Ellisman, "Protoplasmic astrocytes in CA1 stratum radiatum occupy separate anatomical domains," *The Journal of Neuroscience: The Official Journal of the Society for Neuroscience*, vol. 22, pp. 183–192, Jan. 2002.

[28] H. Chai, B. Diaz-Castro, E. Shigetomi, E. Monte, J. C. Octeau, X. Yu, W. Cohn, P. S. Rajendran, T. M. Vondriska, J. P. Whitelegge, G. Coppola, and B. S. Khakh, "Neural Circuit-Specialized Astrocytes: Transcriptomic, Proteomic, Morphological, and Functional Evidence," *Neuron*, vol. 95, pp. 531–549.e9, Aug. 2017.

[29] A. Reichenbach, A. Derouiche, and F. Kirchhoff, "Morphology and dynamics of perisynaptic glia," *Brain Research Reviews*, vol. 63, pp. 11–25, May 2010.

[30] A.-C. Boulay, B. Saubaméa, N. Adam, S. Chasseigneaux, N. Mazaré, A. Gilbert, M. Bahin, L. Bastianelli, C. Blugeon, S. Perrin, J. Pouch, B. Ducos, S. Le Crom, A. Genovesio, F. Chrétien, X. Declèves, J.-L. Laplanche, and M. Cohen-Salmon, "Translation in astrocyte distal processes sets molecular heterogeneity at the gliovascular interface," *Cell Discovery*, vol. 3, p. 17005, Mar. 2017.

[31] N. Medvedev, V. Popov, C. Henneberger, I. Kraev, D. A. Rusakov, and M. G. Stewart, "Glia selectively approach synapses on thin dendritic spines," *Phil. Trans. R. Soc. B*, vol. 369, p. 20140047, Oct. 2014.

[32] C. Calì, J. Baghabra, D. J. Boges, G. R. Holst, A. Kreshuk, F. A. Hamprecht, M. Srinivasan, H. Lehväslaiho, and P. J. Magistretti, "Three-dimensional immersive virtual reality for studying cellular compartments in 3d models from EM preparations of neural tissues," *Journal of Comparative Neurology*, vol. 524, pp. 23–38, Jan. 2016.

[33] I. Patrushev, N. Gavrilov, V. Turlapov, and A. Semyanov, "Subcellular location of astrocytic calcium stores favors extrasynaptic neuron-astrocyte communication," *Cell Calcium*, vol. 54, pp. 343–349, Nov. 2013.

[34] M. Pekny and M. Pekna, "Astrocyte Reactivity and Reactive Astrogliosis: Costs and Benefits," *Physiological Reviews*, vol. 94, pp. 1077–1098, Oct. 2014.

[35] M. M. Halassa, T. Fellin, H. Takano, J.-H. Dong, and P. G. Haydon, "Synaptic islands defined by the territory of a single astrocyte," *The Journal of Neuroscience: The Official Journal of the Society for Neuroscience*, vol. 27, pp. 6473–6477, June 2007.

[36] K. Ogata and T. Kosaka, "Structural and quantitative analysis of astrocytes in the mouse hippocampus," *Neuroscience*, vol. 113, pp. 221–233, Aug. 2002.

[37] N. A. Oberheim, X. Wang, S. Goldman, and M. Nedergaard, "Astrocytic complexity distinguishes the human brain," *Trends in Neurosciences*, vol. 29, pp. 547–553, Oct. 2006.

[38] C. S. von Bartheld, J. Bahney, and S. Herculano-Houzel, "The search for true numbers of neurons and glial cells in the human brain: A review of 150 years of cell counting," *The Journal of Comparative Neurology*, vol. 524, no. 18, pp. 3865–3895, 2016.

[39] J. Bahney and C. S. von Bartheld, "Validation of the isotropic fractionator: Comparison with unbiased stereology and DNA extraction for quantification of glial cells," *Journal of Neuroscience Methods*, vol. 222, pp. 165–174, Jan. 2014.

[40] R. Lent, F. A. C. Azevedo, C. H. Andrade-Moraes, and A. V. O. Pinto, "How many neurons do you have? Some dogmas of quantitative neuroscience under revision," *The European Journal of Neuroscience*, vol. 35, pp. 1–9, Jan. 2012.

[41] A. V. Molofsky, R. Krenick, E. Ullian, H.-h. Tsai, B. Deneen, W. D. Richardson, B. A. Barres, and D. H. Rowitch, "Astrocytes and disease: a neurodevelopmental perspective," *Genes & Development*, vol. 26, pp. 891–907, May 2012.

[42] J. D. Cahoy, B. Emery, A. Kaushal, L. C. Foo, J. L. Zamanian, K. S. Christopherson, Y. Xing, J. L. Lubischer, P. A. Krieg, S. A. Krupenko, W. J. Thompson, and B. A. Barres, "A Transcriptome Database for Astrocytes, Neurons, and Oligodendrocytes: A New Resource for Understanding Brain Development and Function," *Journal of Neuroscience*, vol. 28, pp. 264–278, Jan. 2008.

[43] J. P. Doyle, J. D. Dougherty, M. Heiman, E. F. Schmidt, T. R. Stevens, G. Ma, S. Bupp, P. Shrestha, R. D. Shah, M. L. Doughty, S. Gong, P. Greengard, and N. Heintz, "Application of a Translational Profiling Approach for the Comparative Analysis of CNS Cell Types," *Cell*, vol. 135, pp. 749–762, Nov. 2008.

[44] W. H. Evans and P. E. M. Martin, "Gap junctions: structure and function (Review)," *Molecular Membrane Biology*, vol. 19, pp. 121–136, Jan. 2002.

[45] A. Nimmerjahn, E. A. Mukamel, and M. J. Schnitzer, "Motor Behavior Activates Bergmann Glial Networks," *Neuron*, vol. 62, p. 400, May 2009.

[46] N. Kuga, T. Sasaki, Y. Takahara, N. Matsuki, and Y. Ikegaya, "Large-Scale Calcium Waves Traveling through Astrocytic Networks In Vivo," *Journal of Neuroscience*, vol. 31, pp. 2607–2614, Feb. 2011.

[47] H. Hirase, L. Qian, P. Bartho, and G. Buzsáki, "Calcium Dynamics of Cortical Astrocytic Networks In Vivo," *PLoS biology*, vol. 2, p. E96, May 2004.

[48] T. Sasaki, N. Kuga, S. Namiki, N. Matsuki, and Y. Ikegaya, "Locally Synchronized Astrocytes," *Cerebral Cortex*, p. bhq256, Jan. 2011.

[49] V. Houades, N. Rouach, P. Ezan, F. Kirchhoff, A. Koulakoff, and C. Giaume, "Shapes of astrocyte networks in the juvenile brain," *Neuron Glia Biology*, vol. 2, pp. 3–14, Feb. 2006.

[50] W. Meme, M. Vandecasteele, C. Giaume, and L. Venance, "Electrical coupling between hippocampal astrocytes in rat brain slices," *Neuroscience Research*, vol. 63, pp. 236–243, Apr. 2009.

[51] C. Giaume, A. Koulakoff, L. Roux, D. Holcman, and N. Rouach, "Astroglial networks: a step further in neuroglial and gliovascular interactions," *Nature Reviews Neuroscience*, vol. 11, pp. 87–99, Feb. 2010.

[52] A. Rohlmann and J. R. Wolff, "Subcellular Topography and Plasticity of Gap Junction Distribution on Astrocytes," *SpringerLink*, pp. 175–192, 1996.

[53] T. Mishima and H. Hirase, "In vivo intracellular recording suggests that gray matter astrocytes in mature cerebral cortex and hippocampus are electrophysiologically homogeneous," *The Journal of Neuroscience: The Official Journal of the Society for Neuroscience*, vol. 30, pp. 3093–3100, Feb. 2010.

[54] A. Louise and D. M. Lovinger, "Electrophysiological properties and gap junction coupling of striatal astrocytes," *Neurochemistry international*, vol. 52, pp. 1365–1372, June 2008.

[55] V. Parpura and P. G. Haydon, eds., *Astrocytes in (Patho)Physiology of the Nervous System.* Springer US, 2009.

[56] J. Emsley and J. Macklis, "Astroglial heterogeneity closely reflects the neuronal-defined anatomy of the adult murine CNS.," *Neuron Glia Biol*, vol. 2, no. 3, 2006.

[57] N. A. Oberheim, S. A. Goldman, and M. Nedergaard, "Heterogeneity of astrocytic form and function," *Methods in Molecular Biology (Clifton, N.J.)*, vol. 814, pp. 23–45, 2012.

[58] A. V. Molofsky, K. W. Kelley, H.-H. Tsai, S. A. Redmond, S. M. Chang, L. Madireddy, J. R. Chan, S. E. Baranzini, E. M. Ullian, and D. H. Rowitch, "Astrocyte-encoded positional cues maintain sensorimotor circuit integrity," *Nature*, vol. 509, pp. 189–194, May 2014.

[59] S. Shah, E. Lubeck, W. Zhou, and L. Cai, "In Situ Transcription Profiling of Single Cells Reveals Spatial Organization of Cells in the Mouse Hippocampus," *Neuron*, vol. 92, pp. 342–357, Oct. 2016.

[60] N. Takata and H. Hirase, "Cortical Layer 1 and Layer 2/3 Astrocytes Exhibit Distinct Calcium Dynamics In Vivo," *PLOS ONE*, vol. 3, p. e2525, June 2008.

[61] R. D'Ambrosio, J. Wenzel, P. A. Schwartzkroin, G. M. McKhann, and D. Janigro, "Functional specialization and topographic segregation of hippocampal astrocytes," *The Journal of Neuroscience: The Official Journal of the Society for Neuroscience*, vol. 18, pp. 4425–4438, June 1998.

[62] E. W. Kostuk, J. Cai, and L. Iacovitti, "Subregional differences in astrocytes underlie selective neurodegeneration or protection in Parkinson's disease models in culture," *Glia*, vol. 0, no. 0, 2019.

[63] O. A. Bayraktar, L. C. Fuentealba, A. Alvarez-Buylla, and D. H. Rowitch, "Astrocyte Development and Heterogeneity," *Cold Spring Harbor Perspectives in Biology*, vol. 7, p. a020362, Jan. 2015.

[64] L. B. Haim and D. H. Rowitch, "Functional diversity of astrocytes in neural circuit regulation," *Nature Reviews Neuroscience*, vol. 18, pp. 31–41, Jan. 2017.

[65] B. Zhou, Y.-X. Zuo, and R.-T. Jiang, "Astrocyte morphology: Diversity, plasticity, and role in neurological diseases," *CNS neuroscience & therapeutics*, Mar. 2019.

[66] F. W. Pfrieger and B. A. Barres, "Synaptic Efficacy Enhanced by Glial Cells in Vitro," *Science*, vol. 277, pp. 1684–1687, Sept. 1997.

[67] M. R. Freeman, "Specification and morphogenesis of astrocytes," *Science (New York, N.Y.)*, vol. 330, pp. 774–778, Nov. 2010.

[68] E. Blanco-Suarez, T.-F. Liu, A. Kopelevich, and N. J. Allen, "Astrocyte-Secreted Chordin-like 1 Drives Synapse Maturation and Limits Plasticity by Increasing Synaptic GluA2 AMPA Receptors," *Neuron*, vol. 100, pp. 1116–1132.e13, Dec. 2018.

[69] K. K. Murai, L. N. Nguyen, F. Irie, Y. Yamaguchi, and E. B. Pasquale, "Control of hippocampal dendritic spine morphology through ephrin-A3/EphA4 signaling," *Nature Neuroscience*, vol. 6, pp. 153–160, Feb. 2003.

[70] H. Nishida and S. Okabe, "Direct Astrocytic Contacts Regulate Local Maturation of Dendritic Spines," *Journal of Neuroscience*, vol. 27, pp. 331–340, Jan. 2007.

[71] M. R. Regan, Y. H. Huang, Y. S. Kim, M. I. Dykes-Hoberg, L. Jin, A. M. Watkins, D. E. Bergles, and J. D. Rothstein, "Variations in Promoter Activity Reveal a Differential Expression and Physiology of Glutamate Transporters by Glia in the Developing and Mature CNS," *Journal of Neuroscience*, vol. 27, pp. 6607–6619, June 2007.

[72] M. Nedergaard and A. Verkhratsky, "Artifact versus reality–how astrocytes contribute to synaptic events," *Glia*, vol. 60, pp. 1013–1023, July 2012.

[73] A. Verkhratsky and M. Nedergaard, "Astroglial cradle in the life of the synapse," *Philosophical Transactions of the Royal Society B: Biological Sciences*, vol. 369, Oct. 2014.

[74] G. Dallérac, J. Zapata, and N. Rouach, "Versatile control of synaptic circuits by astrocytes: where, when and how?," *Nature reviews. Neuroscience*, Nov. 2018.

[75] T. Ishibashi, K. A. Dakin, B. Stevens, P. R. Lee, S. V. Kozlov, C. L. Stewart, and R. D. Fields, "Astrocytes promote myelination in response to electrical impulses," *Neuron*, vol. 49, pp. 823–832, Mar. 2006.

[76] L. E. Clarke and B. A. Barres, "Emerging roles of astrocytes in neural circuit development," *Nature reviews. Neuroscience*, vol. 14, pp. 311–321, May 2013.

[77] J. Schiweck, B. J. Eickholt, and K. Murk, "Important Shapeshifter: Mechanisms Allowing Astrocytes to Respond to the Changing Nervous System During Development, Injury and Disease," *Frontiers in Cellular Neuroscience*, vol. 12, 2018.

[78] A. I. Amaral, T. W. Meisingset, M. R. Kotter, and U. Sonnewald, "Metabolic Aspects of Neuron-Oligodendrocyte-Astrocyte Interactions," *Frontiers in Endocrinology*, vol. 4, 2013.

[79] E. R. Kandel, T. M. Jessell, J. H. Schwartz, S. A. Siegelbaum, and A. J. Hudspeth, *Principles of Neural Science, Fifth Edition*. McGraw Hill Professional, 2013.

[80] D. Lee-Liu, G. Edwards Faret, V. S. Tapia, and J. Larraín, "Spinal cord regeneration: Lessons for mammals from non mammalian vertebrates," *genesis*, vol. 51, no. 8, pp. 529–544, 2013.

[81] W. Walz, "Role of glial cells in the regulation of the brain ion microenvironment," *Progress in Neurobiology*, vol. 33, pp. 309–333, Jan. 1989.

[82] N. C. Danbolt, "Glutamate uptake," *Progress in Neurobiology*, vol. 65, pp. 1–105, Sept. 2001.

[83] F. A. Chaudhry, K. P. Lehre, M. v. L. Campagne, O. P. Ottersen, N. C. Danbolt, and J. Storm-Mathisen, "Glutamate transporters in glial plasma membranes: Highly differentiated localizations revealed by quantitative ultrastructural immunocytochemistry," *Neuron*, vol. 15, pp. 711–720, Sept. 1995.

[84] M. Bélanger, I. Allaman, and P. Magistretti, "Brain Energy Metabolism: Focus on Astrocyte-Neuron Metabolic Cooperation," *Cell Metabolism*, vol. 14, pp. 724–738, Dec. 2011.

[85] L. Pellerin and P. J. Magistretti, "Glutamate uptake into astrocytes stimulates aerobic glycolysis: a mechanism coupling neuronal activity to glucose utilization," *Proceedings of the National Academy of Sciences*, vol. 91, pp. 10625–10629, Oct. 1994.

[86] G. K. Gandhi, N. F. Cruz, K. K. Ball, and G. A. Dienel, "Astrocytes are poised for lactate trafficking and release from activated brain and for supply of glucose to neurons," *Journal of Neurochemistry*, vol. 111, no. 2, pp. 522–536, 2009.

[87] P. Ballabh, A. Braun, and M. Nedergaard, "The blood–brain barrier: an overview: Structure, regulation, and clinical implications," *Neurobiology of Disease*, vol. 16, pp. 1–13, June 2004.

[88] M. R. Metea and E. A. Newman, "Glial Cells Dilate and Constrict Blood Vessels: A Mechanism of Neurovascular Coupling," *Journal of Neuroscience*, vol. 26, pp. 2862–2870, Mar. 2006.

[89] S. Mulligan and B. A MacVicar, "Calcium transients in astrocyte endfeet cause cerebrovascular constrictions.," *Nature*, vol. 431, pp. 195–9, Oct. 2004.

[90] T. Takano, G.-F. Tian, W. Peng, N. Lou, W. Libionka, X. Han, and M. Nedergaard, "Astrocyte-mediated control of cerebral blood flow," *Nature Neuroscience*, vol. 9, pp. 260–267, Feb. 2006.

[91] E. Dossi, F. Vasile, and N. Rouach, "Human astrocytes in the diseased brain," *Brain Research Bulletin*, vol. 136, pp. 139–156, Jan. 2018.

[92] L. Ben Haim, M.-A. Carrillo-de Sauvage, K. CeyzÃ©riat, and C. Escartin, "Elusive roles for reactive astrocytes in neurodegenerative diseases," *Frontiers in Cellular Neuroscience*, vol. 9, Aug. 2015.

[93] G. O. Mizuno, Y. Wang, G. Shi, Y. Wang, J. Sun, S. Papadopoulos, G. J. Broussard, E. K. Unger, W. Deng, J. Weick, A. Bhattacharyya, C.-Y. Chen, G. Yu, L. L. Looger, and L. Tian, "Aberrant Calcium Signaling in Astrocytes Inhibits Neuronal Excitability in a Human Down Syndrome Stem Cell Model," *Cell Reports*, vol. 24, pp. 355–365, July 2018.

[94] G. Dallérac and N. Rouach, "Astrocytes as new targets to improve cognitive functions," *Progress in Neurobiology*, vol. 144, pp. 48–67, 2016.

[95] H. Wang, G. Song, H. Chuang, C. Chiu, A. Abdelmaksoud, Y. Ye, and L. Zhao, "Portrait of glial scar in neurological diseases," *International Journal of Immunopathology and Pharmacology*, vol. 31, p. 2058738418801406, Dec. 2018.

[96] K. L. Adams and V. Gallo, "The diversity and disparity of the glial scar," *Nature Neuroscience*, vol. 21, pp. 9–15, Jan. 2018.

[97] M. V. Sofroniew, "Molecular dissection of reactive astrogliosis and glial scar formation," *Trends in neurosciences*, vol. 32, pp. 638–647, Dec. 2009.

[98] R. Brambilla, "Neuroinflammation, the thread connecting neurological disease," *Acta Neuropathologica*, Apr. 2019.

[99] M. A. Anderson, J. E. Burda, Y. Ren, Y. Ao, T. M. O'Shea, R. Kawaguchi, G. Coppola, B. S. Khakh, T. J. Deming, and M. V. Sofroniew, "Astrocyte scar formation aids central nervous system axon regeneration," *Nature*, vol. 532, pp. 195–200, Apr. 2016.

[100] A. R. Filous and J. Silver, ""Targeting astrocytes in CNS injury and disease: A translational research approach"," *Progress in Neurobiology*, vol. 144, pp. 173–187, 2016.

[101] K. Ceyzériat, L. Ben Haim, A. Denizot, D. Pommier, M. Matos, O. Guillemaud, M.-A. Palomares, L. Abjean, F. Petit, P. Gipchtein, M.-C. Gaillard, M. Guillermier, S. Bernier, M. Gaudin, G. Aurégan, C. Joséphine, N. Déchamps, J. Veran, V. Langlais, K. Cambon, A. P. Bemelmans, J. Baijer, G. Bonvento, M. Dhenain, J.-F. Deleuze, S. H. R. Oliet, E. Brouillet, P. Hantraye, M.-A. Carrillo-de Sauvage, R. Olaso, A. Panatier, and C. Escartin, "Modulation of astrocyte reactivity improves functional deficits in mouse models of Alzheimer's disease," *Acta Neuropathologica Communications*, vol. 6, p. 104, Oct. 2018.

[102] J. E. Burda and M. V. Sofroniew, "Reactive gliosis and the multicellular response to CNS damage and disease," *Neuron*, vol. 81, pp. 229–248, Jan. 2014.

[103] J. E. Burda, A. M. Bernstein, and M. V. Sofroniew, "Astrocyte roles in traumatic brain injury," *Experimental Neurology*, vol. 275 Pt 3, pp. 305–315, Jan. 2016.

[104] S. A. Liddelow and B. A. Barres, "Reactive Astrocytes: Production, Function, and Therapeutic Potential," *Immunity*, vol. 46, pp. 957–967, June 2017.

[105] W.-S. Chung, C. A. Welsh, B. A. Barres, and B. Stevens, "Do glia drive synaptic and cognitive impairment in disease?," *Nature Neuroscience*, vol. 18, pp. 1539–1545, Nov. 2015.

[106] S. A. Liddelow and M. V. Sofroniew, "Astrocytes usurp neurons as a disease focus," *Nature Neuroscience*, p. 1, Mar. 2019.

[107] A. Soung and R. S. Klein, "Viral Encephalitis and Neurologic Diseases: Focus on Astrocytes," *Trends in Molecular Medicine*, Oct. 2018.

[108] R. K. Orkand, J. G. Nicholls, and S. W. Kuffler, "Effect of nerve impulses on the membrane potential of glial cells in the central nervous system of amphibia," *Journal of Neurophysiology*, vol. 29, pp. 788–806, July 1966.

[109] H. Sontheimer, "Voltage-dependent ion channels in glial cells," *Glia*, vol. 11, pp. 156–172, June 1994.

[110] A. Cornell-Bell, S. Finkbeiner, M. Cooper, and S. Smith, "Glutamate induces calcium waves in cultured astrocytes: long-range glial signaling," *Science*, vol. 247, pp. 470–473, Jan. 1990.

[111] M. A. Di Castro, J. Chuquet, N. Liaudet, K. Bhaukaurally, M. Santello, D. Bouvier, P. Tiret, and A. Volterra, "Local Ca2+ detection and modulation of synaptic release by astrocytes," *Nature Neuroscience*, vol. 14, pp. 1276–1284, Oct. 2011.

[112] M. Gómez-Gonzalo, M. Navarrete, G. Perea, A. Covelo, M. Martín-Fernández, R. Shigemoto, R. Luján, and A. Araque, "Endocannabinoids Induce Lateral Long-Term Potentiation of Transmitter Release by Stimulation of Gliotransmission," *Cerebral Cortex (New York, N.Y.: 1991)*, vol. 25, pp. 3699–3712, Oct. 2015.

[113] A. Panatier, D. T. Theodosis, J.-P. Mothet, B. Touquet, L. Pollegioni, D. A. Poulain, and S. H. R. Oliet, "Glia-Derived d-Serine Controls NMDA Receptor Activity and Synaptic Memory," *Cell*, vol. 125, pp. 775–784, May 2006.

[114] N. Takata, T. Mishima, C. Hisatsune, T. Nagai, E. Ebisui, K. Mikoshiba, and H. Hirase, "Astrocyte calcium signaling transforms cholinergic modulation to cortical plasticity in vivo," *The Journal of Neuroscience: The Official Journal of the Society for Neuroscience*, vol. 31, pp. 18155–18165, Dec. 2011.

[115] Y. Bernardinelli, D. Muller, and I. Nikonenko, "Astrocyte-Synapse Structural Plasticity," *Neural Plasticity*, vol. 2014, 2014.

[116] J. Grosche, V. Matyash, T. Möller, A. Verkhratsky, A. Reichenbach, and H. Kettenmann, "Microdomains for neuron–glia interaction: parallel fiber signaling to Bergmann glial cells," *Nature Neuroscience*, vol. 2, pp. 139–143, Feb. 1999.

[117] M. A. Xu-Friedman, K. M. Harris, and W. G. Regehr, "Three-Dimensional Comparison of Ultrastructural Characteristics at Depressing and Facilitating Synapses onto Cerebellar Purkinje Cells," *Journal of Neuroscience*, vol. 21, pp. 6666–6672, Sept. 2001.

[118] J. Grosche, H. Kettenmann, and A. Reichenbach, "Bergmann glial cells form distinct morphological structures to interact with cerebellar neurons," *Journal of Neuroscience Research*, vol. 68, pp. 138–149, Apr. 2002.

[119] L. Pasti, A. Volterra, T. Pozzan, and G. Carmignoto, "Intracellular calcium oscillations in astrocytes: a highly plastic, bidirectional form of communication between neurons and astrocytes in situ," *The Journal of Neuroscience: The Official Journal of the Society for Neuroscience*, vol. 17, pp. 7817–7830, Oct. 1997.

[120] J. Kang, L. Jiang, S. A. Goldman, and M. Nedergaard, "Astrocyte-mediated potentiation of inhibitory synaptic transmission," *Nature Neuroscience*, vol. 1, pp. 683–692, Dec. 1998.

[121] M. Navarrete, G. Perea, D. Fernandez de Sevilla, M. Gómez-Gonzalo, A. Núñez, E. D. Martín, and A. Araque, "Astrocytes mediate in vivo cholinergic-induced synaptic plasticity," *PLoS biology*, vol. 10, p. e1001259, Feb. 2012.

[122] Z. U. Khan, P. Koulen, M. Rubinstein, D. K. Grandy, and P. S. Goldman-Rakic, "An astroglia-linked dopamine D2-receptor action in prefrontal cortex," *Proceedings of the National Academy of Sciences of the United States of America*, vol. 98, pp. 1964–1969, Feb. 2001.

[123] P. Jourdain, L. H. Bergersen, K. Bhaukaurally, P. Bezzi, M. Santello, M. Domercq, C. Matute, F. Tonello, V. Gundersen, and A. Volterra, "Glutamate exocytosis from astrocytes controls synaptic strength," *Nature Neuroscience*, vol. 10, pp. 331–339, Mar. 2007.

[124] M. Santello, P. Bezzi, and A. Volterra, "TNFα Controls Glutamatergic Gliotransmission in the Hippocampal Dentate Gyrus," *Neuron*, vol. 69, pp. 988–1001, Mar. 2011.

[125] Y. Bernardinelli, C. Salmon, E. V. Jones, W. T. Farmer, D. Stellwagen, and K. K. Murai, "Astrocytes Display Complex and Localized Calcium Responses to Single-Neuron Stimulation in the Hippocampus," *Journal of Neuroscience*, vol. 31, pp. 8905–8919, June 2011.

[126] M. Navarrete and A. Araque, "Endocannabinoids Mediate Neuron-Astrocyte Communication," *Neuron*, vol. 57, pp. 883–893, Mar. 2008.

[127] M. Navarrete and A. Araque, "Endocannabinoids Potentiate Synaptic Transmission through Stimulation of Astrocytes," *Neuron*, vol. 68, pp. 113–126, Oct. 2010.

[128] R. Min and T. Nevian, "Astrocyte signaling controls spike timing–dependent depression at neocortical synapses," *Nature Neuroscience*, vol. 15, pp. 746–753, May 2012.

[129] K. Matsui and C. E. Jahr, "Differential Control of Synaptic and Ectopic Vesicular Release of Glutamate," *Journal of Neuroscience*, vol. 24, pp. 8932–8939, Oct. 2004.

[130] V. Parpura and R. Zorec, "Gliotransmission: Exocytotic release from astrocytes," *Brain Research Reviews*, vol. 63, pp. 83–92, May 2010.

[131] M. Zonta, A. Sebelin, S. Gobbo, T. Fellin, T. Pozzan, and G. Carmignoto, "Glutamate-mediated cytosolic calcium oscillations regulate a pulsatile prostaglandin release from cultured rat astrocytes," *The Journal of Physiology*, vol. 553, pp. 407–414, Dec. 2003.

[132] G. Perea, M. Navarrete, and A. Araque, "Tripartite synapses: astrocytes process and control synaptic information," *Trends in Neurosciences*, vol. 32, pp. 421–431, Aug. 2009.

[133] A. Araque, G. Carmignoto, P. G. Haydon, S. H. R. Oliet, R. Robitaille, and A. Volterra, "Gliotransmitters travel in time and space," *Neuron*, vol. 81, pp. 728–739, Feb. 2014.

[134] N. B. Hamilton and D. Attwell, "Do astrocytes really exocytose neurotransmitters?," *Nature Reviews. Neuroscience*, vol. 11, pp. 227–238, Apr. 2010.

[135] I. Savtchouk and A. Volterra, "Gliotransmission: Beyond Black-and-White," *Journal of Neuroscience*, vol. 38, pp. 14–25, Jan. 2018.

[136] T. A. Fiacco and K. D. McCarthy, "Multiple Lines of Evidence Indicate That Gliotransmission Does Not Occur under Physiological Conditions," *Journal of Neuroscience*, vol. 38, pp. 3–13, Jan. 2018.

[137] S. Guerra-Gomes, N. Sousa, L. Pinto, and J. F. Oliveira, "Functional Roles of Astrocyte Calcium Elevations: From Synapses to Behavior," *Frontiers in Cellular Neuroscience*, vol. 11, 2018.

[138] A. Perez-Alvarez, M. Navarrete, A. Covelo, E. D. Martin, and A. Araque, "Structural and functional plasticity of astrocyte processes and dendritic spine interactions," *The Journal of Neuroscience: The Official Journal of the Society for Neuroscience*, vol. 34, pp. 12738–12744, Sept. 2014.

[139] D. T. Theodosis, D. A. Poulain, and S. H. R. Oliet, "Activity-dependent structural and functional plasticity of astrocyte-neuron interactions," *Physiological Reviews*, vol. 88, pp. 983–1008, July 2008.

[140] J. P. Heller and D. A. Rusakov, "Morphological plasticity of astroglia: Understanding synaptic microenvironment," *Glia*, vol. 63, pp. 2133–2151, Dec. 2015.

[141] V. Dave, G. W. Gordon, and K. D. McCarthy, "Cerebral type 2 astroglia are heterogeneous with respect to their ability to respond to neuroligands linked to calcium mobilization," *Glia*, vol. 4, no. 5, pp. 440–447, 1991.

[142] M. O. K. Enkvist, I. Holopainen, and K. E. O. Åkerman, "Glutamate receptor-linked changes in membrane potential and intracellular Ca2+ in primary rat astrocytes," *Glia*, vol. 2, no. 6, pp. 397–402, 1989.

[143] C. H. Kastritsis, A. K. Salm, and K. McCarthy, "Stimulation of the P2y purinergic receptor on type 1 astroglia results in inositol phosphate formation and calcium mobilization," *Journal of Neurochemistry*, vol. 58, pp. 1277–1284, Apr. 1992.

[144] W. T. Kim, M. G. Rioult, and A. H. Cornell-Bell, "Glutamate-induced calcium signaling in astrocytes," *Glia*, vol. 11, pp. 173–184, June 1994.

[145] K. D. McCarthy and A. K. Salm, "Pharmacologically-distinct subsets of astroglia can be identified by their calcium response to neuroligands," *Neuroscience*, vol. 41, pp. 325–333, Jan. 1991.

[146] M. J. Berridge, M. D. Bootman, and H. L. Roderick, "Calcium signalling: dynamics, homeostasis and remodelling," *Nature Reviews. Molecular Cell Biology*, vol. 4, pp. 517–529, July 2003.

[147] M. Glitsch, "Mechano- and pH-sensing convergence on Ca2+-mobilising proteins – a recipe for cancer?," *Cell Calcium*, Mar. 2019.

[148] A. Maklad, A. Sharma, and I. Azimi, "Calcium Signaling in Brain Cancers: Roles and Therapeutic Targeting," *Cancers*, vol. 11, p. 145, Feb. 2019.

[149] R. Rizzuto and T. Pozzan, "Microdomains of Intracellular Ca2+: Molecular Determinants and Functional Consequences," *Physiological Reviews*, vol. 86, pp. 369–408, Jan. 2006.

[150] G. Dupont, M. Falcke, V. Kirk, and J. Sneyd, "Some Background Physiology," in *Models of Calcium Signalling* (G. Dupont, M. Falcke, V. Kirk, and J. Sneyd, eds.), Interdisciplinary Applied Mathematics, pp. 3–27, Cham: Springer International Publishing, 2016.

[151] H. Plattner and A. Verkhratsky, "The ancient roots of calcium signalling evolutionary tree," *Cell Calcium*, vol. 57, pp. 123–132, Mar. 2015.

[152] K. K. Baskin, C. A. Makarewich, S. M. DeLeon, W. Ye, B. Chen, N. Beetz, H. Schrewe, R. Bassel-Duby, and E. N. Olson, "MED12 regulates a transcriptional network of calcium-handling genes in the heart," *JCI Insight*, vol. 2, July 2017.

[153] B. N. Armbruster, X. Li, M. H. Pausch, S. Herlitze, and B. L. Roth, "Evolving the lock to fit the key to create a family of G protein-coupled receptors potently activated by an inert ligand," *Proceedings of the National Academy of Sciences of the United States of America*, vol. 104, pp. 5163–5168, Mar. 2007.

[154] G. Ma, S. Wen, L. He, Y. Huang, Y. Wang, and Y. Zhou, "Optogenetic toolkit for precise control of calcium signaling," *Cell Calcium*, vol. 64, pp. 36–46, 2017.

[155] Z.-G. Ji and H. Wang, "Optogenetic control of astrocytes: Is it possible to treat astrocyte-related epilepsy?," *Brain Research Bulletin*, vol. 110, pp. 20–25, Jan. 2015.

[156] A. X. Xie, J. Petravicz, and K. D. McCarthy, "Molecular approaches for manipulating astrocytic signaling in vivo," *Frontiers in Cellular Neuroscience*, vol. 9, p. 144, 2015.

[157] G. Losi, L. Mariotti, M. Sessolo, and G. Carmignoto, "New Tools to Study Astrocyte Ca2+ Signal Dynamics in Brain Networks In Vivo," *Frontiers in Cellular Neuroscience*, vol. 11, p. 134, 2017.

[158] D. A. Rusakov, "Disentangling calcium-driven astrocyte physiology," *Nature Reviews Neuroscience*, vol. 16, pp. 226–233, Apr. 2015.

[159] A. Volterra, N. Liaudet, and I. Savtchouk, "Astrocyte Ca2+ signalling: an unexpected complexity," *Nature Reviews Neuroscience*, vol. 15, pp. 327–335, Apr. 2014.

[160] A. Panatier, J. Vallée, M. Haber, K. K. Murai, J.-C. Lacaille, and R. Robitaille, "Astrocytes are endogenous regulators of basal transmission at central synapses," *Cell*, vol. 146, pp. 785–798, Sept. 2011.

[161] X. Tong, E. Shigetomi, L. L. Looger, and B. S. Khakh, "Genetically encoded calcium indicators and astrocyte calcium microdomains," *The Neuroscientist: A Review Journal Bringing Neurobiology, Neurology and Psychiatry*, vol. 19, pp. 274–291, June 2013.

[162] N. A. Smith, B. T. Kress, Y. Lu, D. Chandler-Militello, A. Benraiss, and M. Nedergaard, "Fluorescent Ca2+ indicators directly inhibit the Na,K-ATPase and disrupt cellular functions," *Sci. Signal.*, vol. 11, p. eaal2039, Jan. 2018.

[163] S. A. Hires, L. Tian, and L. L. Looger, "Reporting neural activity with genetically encoded calcium indicators," *Brain Cell Biology*, vol. 36, p. 69, Aug. 2008.

[164] L. Tian, S. A. Hires, and L. L. Looger, "Imaging Neuronal Activity with Genetically Encoded Calcium Indicators," *Cold Spring Harbor Protocols*, vol. 2012, p. pdb.top069609, June 2012.

[165] L. Ye, M. A. Haroon, A. Salinas, and M. Paukert, "Comparison of GCaMP3 and GCaMP6f for studying astrocyte Ca2+ dynamics in the awake mouse brain," *PLOS ONE*, vol. 12, p. e0181113, July 2017.

[166] R. Srinivasan, T. Y. Lu, H. Chai, J. Xu, B. S. Huang, P. Golshani, G. Coppola, and B. S. Khakh, "New Transgenic Mouse Lines for Selectively Targeting Astrocytes and Studying Calcium Signals in Astrocyte Processes In Situ and In Vivo," *Neuron*, vol. 92, no. 6, pp. 1181–1195, 2016.

[167] F. Niwa, S. Sakuragi, A. Kobayashi, S. Takagi, Y. Oda, H. Bannai, and K. Mikoshiba, "Dissection of local Ca(2+) signals inside cytosol by ER-targeted Ca(2+) indicator," *Biochemical and Biophysical Research Communications*, vol. 479, no. 1, pp. 67–73, 2016.

[168] H. Bannai, M. Hirose, F. Niwa, and K. Mikoshiba, "Dissection of Local Ca2+ Signals in Cultured Cells by Membrane-targeted Ca2+ Indicators," *JoVE (Journal of Visualized Experiments)*, p. e59246, Mar. 2019.

[169] E. Shigetomi, S. Kracun, M. V. Sofroniew, and B. S. Khakh, "A genetically targeted optical sensor to monitor calcium signals in astrocyte processes," *Nature Neuroscience*, vol. 13, pp. 759–766, June 2010.

[170] Y. Zhao, S. Araki, J. Wu, T. Teramoto, Y.-F. Chang, M. Nakano, A. S. Abdelfattah, M. Fujiwara, T. Ishihara, T. Nagai, and R. E. Campbell, "An Expanded Palette of Genetically Encoded Ca2+ Indicators," *Science*, vol. 333, pp. 1888–1891, Sept. 2011.

[171] M. J. Henderson, H. A. Baldwin, C. A. Werley, S. Boccardo, L. R. Whitaker, X. Yan, G. T. Holt, E. R. Schreiter, L. L. Looger, A. E. Cohen, D. S. Kim, and B. K. Harvey, "A Low Affinity GCaMP3 Variant (GCaMPer) for Imaging the Endoplasmic Reticulum Calcium Store," *PLOS ONE*, vol. 10, p. e0139273, Oct. 2015.

[172] J. Suzuki, K. Kanemaru, K. Ishii, M. Ohkura, Y. Okubo, and M. Iino, "Imaging intraorganellar Ca^{2+} at subcellular resolution using CEPIA," *Nature Communications*, vol. 5, p. 4153, June 2014.

[173] J. Suzuki, K. Kanemaru, and M. Iino, "Genetically Encoded Fluorescent Indicators for Organellar Calcium Imaging," *Biophysical Journal*, vol. 111, pp. 1119–1131, Sept. 2016.

[174] H. Li, X. Wang, N. Zhang, M. K. Gottipati, V. Parpura, and S. Ding, "Imaging of mitochondrial Ca2+ dynamics in astrocytes using cell-specific mitochondria-targeted GCaMP5g/6s: Mitochondrial Ca2+ uptake and cytosolic Ca2+ availability via the endoplasmic reticulum store," *Cell calcium*, vol. 56, pp. 457–466, Dec. 2014.

[175] Y. Okubo, K. Kanemaru, J. Suzuki, K. Kobayashi, K. Hirose, and M. Iino, "Inositol 1,4,5-trisphosphate receptor type 2-independent Ca2+ release from the endoplasmic reticulum in astrocytes," *Glia*, vol. 67, no. 1, pp. 113–124, 2019.

[176] H. A. Zariwala, B. G. Borghuis, T. M. Hoogland, L. Madisen, L. Tian, C. I. D. Zeeuw, H. Zeng, L. L. Looger, K. Svoboda, and T.-W. Chen, "A Cre-Dependent GCaMP3 Reporter Mouse for Neuronal Imaging In Vivo," *Journal of Neuroscience*, vol. 32, pp. 3131–3141, Feb. 2012.

[177] E. Shigetomi, S. Patel, and B. S. Khakh, "Probing the Complexities of Astrocyte Calcium Signaling," *Trends in Cell Biology*, vol. 26, pp. 300–312, Apr. 2016.

[178] B. R. Conway and K. T. Demarest, "The Use of Biosensors to Study GPCR Function: Applications for High-Content Screening," *Receptors and Channels*, vol. 8, pp. 331–341, Jan. 2002.

[179] F. Ataei, M. Torkzadeh-Mahani, and S. Hosseinkhani, "A novel luminescent biosensor for rapid monitoring of IP3 by split-luciferase complementary assay," *Biosensors and Bioelectronics*, vol. 41, pp. 642–648, Mar. 2013.

[180] A. Tanimura, T. Mochizuki, T. Morita, A. Nezu, Y. Tojyo, M. Arisawa, and S. Shuto, "A fluorescence-based method for evaluating inositol 1,4,5-trisphosphate receptor ligands: Determination of subtype selectivity and partial agonist effects," *Journal of Biotechnology*, vol. 167, pp. 248–254, Sept. 2013.

[181] A. Miyamoto and K. Mikoshiba, "Probes for manipulating and monitoring IP3," *Cell Calcium*, vol. 64, pp. 57–64, June 2017.

[182] F. Barbagallo, B. Xu, G. R. Reddy, T. West, Q. Wang, Q. Fu, M. Li, Q. Shi, K. S. Ginsburg, W. Ferrier, A. M. Isidori, F. Naro, H. H. Patel, J. Bossuyt, D. Bers, and Y. K. Xiang, "Genetically Encoded Biosensors Reveal PKA Hyperphosphorylation on the Myofilaments in Rabbit Heart Failure," *Circulation research*, vol. 119, pp. 931–943, Sept. 2016.

[183] N. C. Surdo, M. Berrera, A. Koschinski, M. Brescia, M. R. Machado, C. Carr, P. Wright, J. Gorelik, S. Morotti, E. Grandi, D. M. Bers, S. Pantano, and M. Zaccolo, "FRET biosensor uncovers cAMP nano-domains at β-adrenergic targets that dictate precise tuning of cardiac contractility," *Nature Communications*, vol. 8, p. 15031, Apr. 2017.

[184] D. L. Prole and C. W. Taylor, "A genetically-encoded toolkit of functionalized nanobodies against fluorescent proteins for visualizing and manipulating intracellular signalling," *bioRxiv*, p. 544700, Feb. 2019.

[185] H. Dana, Y. Sun, B. Mohar, B. Hulse, J. P. Hasseman, G. Tsegaye, A. Tsang, A. Wong, R. Patel, J. J. Macklin, Y. Chen, A. Konnerth, V. Jayaraman,

L. L. Looger, E. R. Schreiter, K. Svoboda, and D. S. Kim, "High-performance GFP-based calcium indicators for imaging activity in neuronal populations and microcompartments," *bioRxiv*, p. 434589, Oct. 2018.

[186] T.-W. Chen, T. J. Wardill, Y. Sun, S. R. Pulver, S. L. Renninger, A. Baohan, E. R. Schreiter, R. A. Kerr, M. B. Orger, V. Jayaraman, L. L. Looger, K. Svoboda, and D. S. Kim, "Ultrasensitive fluorescent proteins for imaging neuronal activity," *Nature*, vol. 499, pp. 295–300, July 2013.

[187] S. Tang, F. Reddish, Y. Zhuo, and J. J. Yang, "Fast kinetics of calcium signaling and sensor design," *Current Opinion in Chemical Biology*, vol. 27, pp. 90–97, Aug. 2015.

[188] L. Lindenburg and M. Merkx, "Engineering Genetically Encoded FRET Sensors," *Sensors*, vol. 14, pp. 11691–11713, July 2014.

[189] T. A. Weissman, P. A. Riquelme, L. Ivic, A. C. Flint, and A. R. Kriegstein, "Calcium Waves Propagate through Radial Glial Cells and Modulate Proliferation in the Developing Neocortex," *Neuron*, vol. 43, pp. 647–661, Sept. 2004.

[190] M. R. Metea and E. A. Newman, "Calcium Signaling in Specialized Glial Cells," *Glia*, vol. 54, pp. 650–655, Nov. 2006.

[191] J. Yang, H. Yang, Y. Liu, X. Li, L. Qin, H. Lou, S. Duan, and H. Wang, "Astrocytes contribute to synapse elimination Via type 2 inositol 1,4,5-trisphosphate receptor-dependent release of ATP," *eLife*, vol. 5, no. APRIL2016, 2016.

[192] S. Sultan, L. Li, J. Moss, F. Petrelli, F. Cassé, E. Gebara, J. Lopatar, F. Pfrieger, P. Bezzi, J. Bischofberger, and N. Toni, "Synaptic Integration of Adult-Born Hippocampal Neurons Is Locally Controlled by Astrocytes," *Neuron*, vol. 88, pp. 957–972, Dec. 2015.

[193] S. A. Hill, A. Blaeser, A. Coley, Y. Xie, K. A. Shepard, C. Harwell, W.-J. Gao, and A. D. R. Garcia, "Sonic hedgehog signaling in astrocytes mediates cell-type-specific synaptic organization," *bioRxiv*, p. 537860, Feb. 2019.

[194] M. Nedergaard, "Direct signaling from astrocytes to neurons in cultures of mammalian brain cells," *Science*, vol. 263, pp. 1768–1771, Mar. 1994.

[195] V. Parpura, T. A. Basarsky, F. Liu, K. Jeftinija, S. Jeftinija, and P. G. Haydon, "Glutamate-mediated astrocyte–neuron signalling," *Nature*, vol. 369, p. 744, June 1994.

[196] I. R. Winship, N. Plaa, and T. H. Murphy, "Rapid astrocyte calcium signals correlate with neuronal activity and onset of the hemodynamic response in vivo," *The Journal of Neuroscience: The Official Journal of the Society for Neuroscience*, vol. 27, pp. 6268–6272, June 2007.

[197] E. Shigetomi, X. Tong, K. Y. Kwan, D. P. Corey, and B. S. Khakh, "TRPA1 channels regulate astrocyte resting calcium and inhibitory synapse efficacy through GAT-3," *Nature Neuroscience*, vol. 15, pp. 70–80, Jan. 2012.

[198] J. A. Filosa, A. D. Bonev, S. V. Straub, A. L. Meredith, M. K. Wilkerson, R. W. Aldrich, and M. T. Nelson, "Local potassium signaling couples neuronal activity to vasodilation in the brain," *Nature Neuroscience*, vol. 9, pp. 1397–1403, Nov. 2006.

[199] D. Attwell, A. M. Buchan, S. Charpak, M. Lauritzen, B. A. MacVicar, and E. A. Newman, "Glial and neuronal control of brain blood flow," *Nature*, vol. 468, pp. 232–243, Nov. 2010.

[200] Y. Bernardinelli, J. Randall, E. Janett, I. Nikonenko, S. König, E. V. Jones, C. E. Flores, K. K. Murai, C. G. Bochet, A. Holtmaat, and D. Muller, "Activity-dependent structural plasticity of perisynaptic astrocytic domains promotes excitatory synapse stability," *Current biology: CB*, vol. 24, pp. 1679–1688, Aug. 2014.

[201] D. Molotkov, S. Zobova, J. M. Arcas, and L. Khiroug, "Calcium-induced outgrowth of astrocytic peripheral processes requires actin binding by Profilin-1," *Cell Calcium*, vol. 53, pp. 338–348, May 2013.

[202] M. Tanaka, P.-Y. Shih, H. Gomi, T. Yoshida, J. Nakai, R. Ando, T. Furuichi, K. Mikoshiba, A. Semyanov, and S. Itohara, "Astrocytic Ca2+ signals are required for the functional integrity of tripartite synapses," *Molecular Brain*, vol. 6, p. 6, 2013.

[203] T. Sasaki, N. Matsuki, and Y. Ikegaya, "Action-Potential Modulation During Axonal Conduction," *Science*, vol. 331, pp. 599–601, Feb. 2011.

[204] M. C. Angulo, A. S. Kozlov, S. Charpak, and E. Audinat, "Glutamate Released from Glial Cells Synchronizes Neuronal Activity in the Hippocampus," *Journal of Neuroscience*, vol. 24, pp. 6920–6927, Aug. 2004.

[205] T. Fellin, O. Pascual, S. Gobbo, T. Pozzan, P. G. Haydon, and G. Carmignoto, "Neuronal Synchrony Mediated by Astrocytic Glutamate through Activation of Extrasynaptic NMDA Receptors," *Neuron*, vol. 43, pp. 729–743, Sept. 2004.

[206] P. Morquette, D. Verdier, A. Kadala, J. Féthière, A. G. Philippe, R. Robitaille, and A. Kolta, "An astrocyte-dependent mechanism for neuronal rhythmogenesis," *Nature Neuroscience*, vol. 18, no. 6, pp. 844–854, 2015.

[207] K. E. Poskanzer and R. Yuste, "Astrocytic regulation of cortical UP states," *Proceedings of the National Academy of Sciences*, vol. 108, pp. 18453–18458, Nov. 2011.

[208] T. Sasaki, T. Ishikawa, R. Abe, R. Nakayama, A. Asada, N. Matsuki, and Y. Ikegaya, "Astrocyte calcium signalling orchestrates neuronal synchronization in organotypic hippocampal slices," *The Journal of Physiology*, vol. 592, pp. 2771–2783, July 2014.

[209] K. E. Poskanzer and R. Yuste, "Astrocytes regulate cortical state switching in vivo," *Proceedings of the National Academy of Sciences of the United States of America*, vol. 113, pp. E2675–2684, May 2016.

[210] J. F. Oliveira, V. M. Sardinha, S. Guerra-Gomes, A. Araque, and N. Sousa, "Do stars govern our actions? Astrocyte involvement in rodent behavior," *Trends in Neurosciences*, vol. 38, pp. 535–549, Sept. 2015.

[211] M. Tanaka, X. Wang, K. Mikoshiba, H. Hirase, and Y. Shinohara, "Rearing-environment-dependent hippocampal local field potential differences in wild-type and inositol trisphosphate receptor type 2 knockout mice," *The Journal of Physiology*, vol. 595, pp. 6557–6568, Oct. 2017.

[212] J. Petravicz, K. M. Boyt, and K. D. McCarthy, "Astrocyte IP3r2-dependent Ca2+ signaling is not a major modulator of neuronal pathways governing behavior," *Frontiers in Behavioral Neuroscience*, vol. 8, Nov. 2014.

[213] V. M. Sardinha, S. Guerra-Gomes, I. Caetano, G. Tavares, M. Martins, J. S. Reis, J. S. Correia, A. Teixeira-Castro, L. Pinto, N. Sousa, and J. F. Oliveira, "Astrocytic signaling supports hippocampal–prefrontal theta synchronization and cognitive function," *Glia*, vol. 65, pp. 1944–1960, Dec. 2017.

[214] A. Adamsky, A. Kol, T. Kreisel, A. Doron, N. Ozeri-Engelhard, T. Melcer, R. Refaeli, H. Horn, L. Regev, M. Groysman, M. London, and I. Goshen, "Astrocytic Activation Generates De Novo Neuronal Potentiation and Memory Enhancement," *Cell*, vol. 174, pp. 59–71.e14, June 2018.

[215] X. Han, M. Chen, F. Wang, M. Windrem, S. Wang, S. Shanz, Q. Xu, N. A. Oberheim, L. Bekar, S. Betstadt, A. J. Silva, T. Takano, S. A. Goldman, and

M. Nedergaard, "Forebrain engraftment by human glial progenitor cells enhances synaptic plasticity and learning in adult mice," *Cell Stem Cell*, vol. 12, pp. 342–353, Mar. 2013.

[216] M. Santello, N. Toni, and A. Volterra, "Astrocyte function from information processing to cognition and cognitive impairment," *Nature Neuroscience*, p. 1, Jan. 2019.

[217] X. Wang, N. Lou, Q. Xu, G.-F. Tian, W. G. Peng, X. Han, J. Kang, T. Takano, and M. Nedergaard, "Astrocytic Ca2+ signaling evoked by sensory stimulation in vivo," *Nature Neuroscience*, vol. 9, pp. 816–823, June 2006.

[218] K. Kanemaru, H. Sekiya, M. Xu, K. Satoh, N. Kitajima, K. Yoshida, Y. Okubo, T. Sasaki, S. Moritoh, H. Hasuwa, M. Mimura, K. Horikawa, K. Matsui, T. Nagai, M. Iino, and K. Tanaka, "In Vivo Visualization of Subtle, Transient, and Local Activity of Astrocytes Using an Ultrasensitive Ca2+ Indicator," *Cell Reports*, vol. 8, pp. 311–318, July 2014.

[219] Y. Otsu, K. Couchman, D. G. Lyons, M. Collot, A. Agarwal, J.-M. Mallet, F. W. Pfrieger, D. E. Bergles, and S. Charpak, "Calcium dynamics in astrocyte processes during neurovascular coupling," *Nature Neuroscience*, vol. 18, pp. 210–218, Feb. 2015.

[220] J. Schummers, H. Yu, and M. Sur, "Tuned responses of astrocytes and their influence on hemodynamic signals in the visual cortex," *Science (New York, N.Y.)*, vol. 320, pp. 1638–1643, June 2008.

[221] N. Chen, H. Sugihara, J. Sharma, G. Perea, J. Petravicz, C. Le, and M. Sur, "Nucleus basalis-enabled stimulus-specific plasticity in the visual cortex is mediated by astrocytes," *Proceedings of the National Academy of Sciences*, vol. 109, pp. E2832–E2841, Oct. 2012.

[222] H. Monai, M. Ohkura, M. Tanaka, Y. Oe, A. Konno, H. Hirai, K. Mikoshiba, S. Itohara, J. Nakai, Y. Iwai, and H. Hirase, "Calcium imaging reveals glial involvement in transcranial direct current stimulation-induced plasticity in mouse brain," *Nature Communications*, vol. 7, p. 11100, Mar. 2016.

[223] P. Cao, G. Donovan, M. Falcke, and J. Sneyd, "A stochastic model of calcium puffs based on single-channel data," *Biophysical Journal*, vol. 105, pp. 1133–1142, Sept. 2013.

[224] X. Cao, L.-P. Li, Q. Wang, Q. Wu, H.-H. Hu, M. Zhang, Y.-Y. Fang, J. Zhang, S.-J. Li, W.-C. Xiong, H.-C. Yan, Y.-B. Gao, J.-H. Liu, X.-W. Li, L.-R. Sun,

Y.-N. Zeng, X.-H. Zhu, and T.-M. Gao, "Astrocyte-derived ATP modulates depressive-like behaviors," *Nature Medicine*, vol. 19, pp. 773–777, June 2013.

[225] M. Martin-Fernandez, S. Jamison, L. M. Robin, Z. Zhao, E. D. Martin, J. Aguilar, M. A. Benneyworth, G. Marsicano, and A. Araque, "Synapse-specific astrocyte gating of amygdala-related behavior," *Nature Neuroscience*, vol. 20, pp. 1540–1548, Nov. 2017.

[226] C. Agulhon, K. M. Boyt, A. X. Xie, F. Friocourt, B. L. Roth, and K. D. McCarthy, "Modulation of the autonomic nervous system and behaviour by acute glial cell Gq protein-coupled receptor activation in vivo," *The Journal of Physiology*, vol. 591, pp. 5599–5609, Nov. 2013.

[227] C. H. T. Tran, G. Peringod, and G. R. Gordon, "Astrocytes Integrate Behavioral State and Vascular Signals during Functional Hyperemia," *Neuron*, Oct. 2018.

[228] X. Yu, A. M. W. Taylor, J. Nagai, P. Golshani, C. J. Evans, G. Coppola, and B. S. Khakh, "Reducing Astrocyte Calcium Signaling In Vivo Alters Striatal Microcircuits and Causes Repetitive Behavior," *Neuron*, vol. 99, pp. 1170–1187.e9, Sept. 2018.

[229] M. P. Mattson and S. L. Chan, "Neuronal and glial calcium signaling in Alzheimer's disease," *Cell Calcium*, vol. 34, pp. 385–397, Nov. 2003.

[230] K. V. Kuchibhotla, C. R. Lattarulo, B. T. Hyman, and B. J. Bacskai, "Synchronous Hyperactivity and Intercellular Calcium Waves in Astrocytes in Alzheimer Mice," *Science*, vol. 323, pp. 1211–1215, Feb. 2009.

[231] D. Lim, J. J. Rodríguez-Arellano, V. Parpura, R. Zorec, F. Zeidán-Chuliá, A. A. Genazzani, and A. Verkhratsky, "Calcium signalling toolkits in astrocytes and spatio-temporal progression of Alzheimer's disease," *Current Alzheimer Research*, vol. 13, no. 4, pp. 359–369, 2016.

[232] N. Vardjan, A. Verkhratsky, and R. Zorec, "Astrocytic Pathological Calcium Homeostasis and Impaired Vesicle Trafficking in Neurodegeneration," *International Journal of Molecular Sciences*, vol. 18, Feb. 2017.

[233] J. J. Rodríguez-Arellano, V. Parpura, R. Zorec, and A. Verkhratsky, "Astrocytes in physiological aging and Alzheimer's disease," *Neuroscience*, vol. 323, pp. 170–182, May 2016.

[234] H. D. Booth, W. D. Hirst, and R. Wade-Martins, "The Role of Astrocyte Dysfunction in Parkinson's Disease Pathogenesis," *Trends in Neurosciences*, vol. 40, pp. 358–370, June 2017.

[235] P. Bedner, A. Dupper, K. Hüttmann, J. Müller, M. K. Herde, P. Dublin, T. Deshpande, J. Schramm, U. Häussler, C. A. Haas, C. Henneberger, M. Theis, and C. Steinhäuser, "Astrocyte uncoupling as a cause of human temporal lobe epilepsy," *Brain*, vol. 138, pp. 1208–1222, May 2015.

[236] G. Seifert, G. Carmignoto, and C. Steinhäuser, "Astrocyte dysfunction in epilepsy," *Brain Research Reviews*, vol. 63, pp. 212–221, May 2010.

[237] A. Goudriaan, C. de Leeuw, S. Ripke, C. M. Hultman, P. Sklar, P. F. Sullivan, A. B. Smit, D. Posthuma, and M. H. G. Verheijen, "Specific Glial Functions Contribute to Schizophrenia Susceptibility," *Schizophrenia Bulletin*, vol. 40, pp. 925–935, July 2014.

[238] J. Nagai, A. K. Rajbhandari, M. R. Gangwani, A. Hachisuka, G. Coppola, S. C. Masmanidis, M. S. Fanselow, and B. S. Khakh, "Hyperactivity with Disrupted Attention by Activation of an Astrocyte Synaptogenic Cue," *Cell*, Apr. 2019.

[239] G. Schmunk, R. L. Nguyen, D. L. Ferguson, K. Kumar, I. Parker, and J. J. Gargus, "High-throughput screen detects calcium signaling dysfunction in typical sporadic autism spectrum disorder," *Scientific Reports*, vol. 7, p. 40740, Feb. 2017.

[240] R. Moraga-Amaro, J. M. Jerez-Baraona, F. Simon, and J. Stehberg, "Role of astrocytes in memory and psychiatric disorders," *Journal of Physiology-Paris*, vol. 108, pp. 240–251, Sept. 2014.

[241] E. Shigetomi, K. Saito, F. Sano, and S. Koizumi, "Aberrant Calcium Signals in Reactive Astrocytes: A Key Process in Neurological Disorders," *International Journal of Molecular Sciences*, vol. 20, p. 996, Jan. 2019.

[242] M. Nedergaard, J. J. Rodríguez, and A. Verkhratsky, "Glial calcium and diseases of the nervous system," *Cell Calcium*, vol. 47, pp. 140–149, Feb. 2010.

[243] M. Pekny, M. Pekna, A. Messing, C. Steinhäuser, J.-M. Lee, V. Parpura, E. M. Hol, M. V. Sofroniew, and A. Verkhratsky, "Astrocytes: a central element in neurological diseases," *Acta Neuropathologica*, vol. 131, pp. 323–345, Mar. 2016.

[244] J. R. Jones, L. Kong, M. G. Hanna, B. Hoffman, R. Krencik, R. Bradley, T. Hagemann, J. Choi, M. Doers, M. Dubovis, M. A. Sherafat, A. Bhattacharyya, C. Kendziorski, A. Audhya, A. Messing, and S.-C. Zhang, "Mutations in GFAP Disrupt the Distribution and Function of Organelles in Human Astrocytes," *Cell Reports*, vol. 25, pp. 947–958.e4, Oct. 2018.

[245] J. W. Dani, A. Chernjavsky, and S. J. Smith, "Neuronal activity triggers calcium waves in hippocampal astrocyte networks," *Neuron*, vol. 8, pp. 429–440, Mar. 1992.

[246] E. A. Newman and K. R. Zahs, "Calcium waves in retinal glial cells," *Science (New York, N.Y.)*, vol. 275, pp. 844–847, Feb. 1997.

[247] C. G. Schipke, C. Boucsein, C. Ohlemeyer, F. Kirchhoff, and H. Kettenmann, "Astrocyte Ca2+ waves trigger responses in microglial cells in brain slices," *FASEB journal: official publication of the Federation of American Societies for Experimental Biology*, vol. 16, pp. 255–257, Feb. 2002.

[248] M. Paukert, A. Agarwal, J. Cha, V. A. Doze, J. U. Kang, and D. E. Bergles, "Norepinephrine controls astroglial responsiveness to local circuit activity," *Neuron*, vol. 82, pp. 1263–1270, June 2014.

[249] F. Ding, J. O'Donnell, A. S. Thrane, D. Zeppenfeld, H. Kang, L. Xie, F. Wang, and M. Nedergaard, "α1-Adrenergic receptors mediate coordinated Ca2+ signaling of cortical astrocytes in awake, behaving mice," *Cell Calcium*, vol. 54, pp. 387–394, Dec. 2013.

[250] P. B. Guthrie, J. Knappenberger, M. Segal, M. V. Bennett, A. C. Charles, and S. B. Kater, "ATP released from astrocytes mediates glial calcium waves," *The Journal of Neuroscience: The Official Journal of the Society for Neuroscience*, vol. 19, pp. 520–528, Jan. 1999.

[251] M. L. Cotrina, J. H. Lin, J. C. López-García, C. C. Naus, and M. Nedergaard, "ATP-mediated glia signaling," *The Journal of Neuroscience: The Official Journal of the Society for Neuroscience*, vol. 20, pp. 2835–2844, Apr. 2000.

[252] C. E. Stout, J. L. Costantin, C. C. G. Naus, and A. C. Charles, "Intercellular calcium signaling in astrocytes via ATP release through connexin hemichannels," *The Journal of Biological Chemistry*, vol. 277, pp. 10482–10488, Mar. 2002.

[253] C. Giaume and L. Venance, "Intercellular calcium signaling and gap junctional communication in astrocytes," *Glia*, vol. 24, pp. 50–64, Sept. 1998.

[254] M. D. Haustein, S. Kracun, X.-H. Lu, T. Shih, O. Jackson-Weaver, X. Tong, J. Xu, X. W. Yang, T. J. O'Dell, J. S. Marvin, M. H. Ellisman, E. A. Bushong, L. L. Looger, and B. S. Khakh, "Conditions and constraints for astrocyte calcium signaling in the hippocampal mossy fiber pathway," *Neuron*, vol. 82, pp. 413–429, Apr. 2014.

[255] E. Shigetomi, S. Kracun, and B. S. Khakh, "Monitoring astrocyte calcium microdomains with improved membrane targeted GCaMP reporters," *Neuron Glia Biology*, vol. 6, pp. 183–191, Aug. 2010.

[256] S. V. Straub, A. D. Bonev, M. K. Wilkerson, and M. T. Nelson, "Dynamic inositol trisphosphate-mediated calcium signals within astrocytic endfeet underlie vasodilation of cerebral arterioles," *The Journal of General Physiology*, vol. 128, pp. 659–669, Dec. 2006.

[257] K. M. Dunn, D. C. Hill-Eubanks, W. B. Liedtke, and M. T. Nelson, "TRPV4 channels stimulate Ca2+-induced Ca2+ release in astrocytic endfeet and amplify neurovascular coupling responses," *Proceedings of the National Academy of Sciences of the United States of America*, vol. 110, pp. 6157–6162, Apr. 2013.

[258] R. Zorec, A. Araque, G. Carmignoto, P. G. Haydon, A. Verkhratsky, and V. Parpura, "Astroglial excitability and gliotransmission: an appraisal of Ca2+ as a signalling route," *ASN NEURO*, vol. 4, Mar. 2012.

[259] D. A. Rusakov, L. Bard, M. G. Stewart, and C. Henneberger, "Diversity of astroglial functions alludes to subcellular specialisation," *Trends in Neurosciences*, vol. 37, pp. 228–242, Apr. 2014.

[260] M. W. Sherwood, M. Arizono, C. Hisatsune, H. Bannai, E. Ebisui, J. L. Sherwood, A. Panatier, S. H. R. Oliet, and K. Mikoshiba, "Astrocytic IP3rs: Contribution to Ca2+ signalling and hippocampal LTP," *Glia*, vol. 65, pp. 502–513, Mar. 2017.

[261] I. Bosanac, J.-R. Alattia, T. K. Mal, J. Chan, S. Talarico, F. K. Tong, K. I. Tong, F. Yoshikawa, T. Furuichi, M. Iwai, T. Michikawa, K. Mikoshiba, and M. Ikura, "Structure of the inositol 1,4,5-trisphosphate receptor binding core in complex with its ligand," *Nature*, vol. 420, pp. 696–700, Dec. 2002.

[262] M. J. Berridge, "Inositol trisphosphate and calcium signalling," *Nature*, vol. 361, pp. 315–325, Jan. 1993.

[263] I. Parker and I. Ivorra, "Inhibition by Ca2+ of Inositol Trisphosphate-Mediated Ca2+ Liberation: A Possible Mechanism for Oscillatory Release of Ca2+," *Proceedings of the National Academy of Science*, vol. 87, pp. 260–264, Jan. 1990.

[264] G. Dickinson, D. Swaminathan, and I. Parker, "The Probability of Triggering Calcium Puffs Is Linearly Related to the Number of Inositol Trisphosphate

Receptors in a Cluster," *Biophysical Journal*, vol. 102, pp. 1826–1836, Apr. 2012.

[265] I. F. Smith, S. M. Wiltgen, J. Shuai, and I. Parker, "Ca2+ Puffs Originate from Preestablished Stable Clusters of Inositol Trisphosphate Receptors," *Sci. Signal.*, vol. 2, pp. ra77–ra77, Nov. 2009.

[266] L. E. Wagner and D. I. Yule, "Differential regulation of the $InsP_3$ receptor type-1 and -2 single channel properties by $InsP_3$, Ca^{2+} and ATP," *The Journal of Physiology*, vol. 590, pp. 3245–3259, July 2012.

[267] G. Dupont, M. Falcke, V. Kirk, and J. Sneyd, "The Calcium Toolbox," in *Models of Calcium Signalling* (G. Dupont, M. Falcke, V. Kirk, and J. Sneyd, eds.), Interdisciplinary Applied Mathematics, pp. 29–96, Cham: Springer International Publishing, 2016.

[268] K. Thurley, A. Skupin, R. Thul, and M. Falcke, "Fundamental properties of Ca2 + signals," *Biochimica et Biophysica Acta (BBA) - General Subjects*, vol. 1820, pp. 1185–1194, Aug. 2012.

[269] H. Ivanova, T. Vervliet, L. Missiaen, J. B. Parys, H. De Smedt, and G. Bultynck, "Inositol 1,4,5-trisphosphate receptor-isoform diversity in cell death and survival," *Biochimica et Biophysica Acta (BBA) - Molecular Cell Research*, vol. 1843, pp. 2164–2183, Oct. 2014.

[270] C. W. Taylor and S. C. Tovey, "IP3 Receptors: Toward Understanding Their Activation," *Cold Spring Harbor Perspectives in Biology*, vol. 2, p. a004010, Dec. 2010.

[271] M.-D. Seo, M. Enomoto, N. Ishiyama, P. B. Stathopulos, and M. Ikura, "Structural insights into endoplasmic reticulum stored calcium regulation by inositol 1,4,5-trisphosphate and ryanodine receptors," *Biochimica Et Biophysica Acta*, vol. 1853, pp. 1980–1991, Sept. 2015.

[272] T. Furuichi, S. Yoshikawa, A. Miyawaki, K. Wada, N. Maeda, and K. Mikoshiba, "Primary structure and functional expression of the inositol 1,4,5-trisphosphate-binding protein P400," *Nature*, vol. 342, pp. 32–38, Nov. 1989.

[273] G. Fan, M. L. Baker, Z. Wang, M. R. Baker, P. A. Sinyagovskiy, W. Chiu, S. J. Ludtke, and I. I. Serysheva, "Gating machinery of $InsP_3R$ channels revealed by electron cryomicroscopy," *Nature*, vol. 527, pp. 336–341, Nov. 2015.

[274] I. I. Serysheva, M. R. Baker, and G. Fan, "Structural Insights into IP<Subscript>3</Subscript>R Function," in *Membrane Dynamics and Calcium Signaling*, Advances in Experimental Medicine and Biology, pp. 121–147, Springer, Cham, 2017.

[275] K. J. Alzayady, A. Sebé-Pedrós, R. Chandrasekhar, L. Wang, I. Ruiz-Trillo, and D. I. Yule, "Tracing the Evolutionary History of Inositol, 1, 4, 5-Trisphosphate Receptor: Insights from Analyses of Capsaspora owczarzaki Ca2+ Release Channel Orthologs," *Molecular Biology and Evolution*, vol. 32, pp. 2236–2253, Sept. 2015.

[276] L. Ionescu, C. White, K.-H. Cheung, J. Shuai, I. Parker, J. E. Pearson, J. K. Foskett, and D.-O. D. Mak, "Mode Switching Is the Major Mechanism of Ligand Regulation of InsP3 Receptor Calcium Release Channels," *The Journal of General Physiology*, vol. 130, pp. 631–645, Dec. 2007.

[277] V. D. Lupu, E. Kaznacheyeva, U. M. Krishna, J. R. Falck, and I. Bezprozvanny, "Functional coupling of phosphatidylinositol 4,5-bisphosphate to inositol 1,4,5-trisphosphate receptor," *The Journal of Biological Chemistry*, vol. 273, pp. 14067–14070, June 1998.

[278] C. W. Taylor, "Regulation of IP3 receptors by cyclic AMP," *Cell Calcium*, vol. 63, pp. 48–52, May 2017.

[279] T.-S. Tang, H. Tu, Z. Wang, and I. Bezprozvanny, "Modulation of Type 1 Inositol (1,4,5)-Trisphosphate Receptor Function by Protein Kinase A and Protein Phosphatase 1α," *Journal of Neuroscience*, vol. 23, pp. 403–415, Jan. 2003.

[280] H. Sipma, P. De Smet, I. Sienaert, S. Vanlingen, L. Missiaen, J. B. Parys, and H. De Smedt, "Modulation of inositol 1,4,5-trisphosphate binding to the recombinant ligand-binding site of the type-1 inositol 1,4, 5-trisphosphate receptor by Ca2+ and calmodulin," *The Journal of Biological Chemistry*, vol. 274, pp. 12157–12162, Apr. 1999.

[281] N. Nadif Kasri, G. Bultynck, I. Sienaert, G. Callewaert, C. Erneux, L. Missiaen, J. B. Parys, and H. De Smedt, "The role of calmodulin for inositol 1,4,5-trisphosphate receptor function," *Biochimica et Biophysica Acta (BBA) - Proteins and Proteomics*, vol. 1600, pp. 19–31, Nov. 2002.

[282] B. Xiao, J. C. Tu, and P. F. Worley, "Homer: a link between neural activity and glutamate receptor function," *Current Opinion in Neurobiology*, vol. 10, pp. 370–374, June 2000.

[283] H. Ivanova, L. E. Wagner, A. Tanimura, E. Vandermarliere, T. Luyten, K. Welkenhuyzen, K. J. Alzayady, L. Wang, K. Hamada, K. Mikoshiba, H. De Smedt, L. Martens, D. I. Yule, J. B. Parys, and G. Bultynck, "Bcl-2 and IP3 compete for the ligand-binding domain of IP3rs modulating Ca2+ signaling output," *Cellular and Molecular Life Sciences*, Apr. 2019.

[284] I. Bosanac, T. Michikawa, K. Mikoshiba, and M. Ikura, "Structural insights into the regulatory mechanism of IP3 receptor," *Biochimica et Biophysica Acta (BBA) - Molecular Cell Research*, vol. 1742, pp. 89–102, Dec. 2004.

[285] C. W. Taylor and V. Konieczny, "IP3 receptors: take four IP3 to open," *Science signaling*, vol. 9, p. pe1, Apr. 2016.

[286] I. I. Serysheva and S. J. Ludtke, "Chapter 8 - 3d Structure of IP3 Receptor," in *Current Topics in Membranes* (I. I. Serysheva, ed.), vol. 66 of *Structure and Function of Calcium Release Channels*, pp. 171–189, Academic Press, Jan. 2010.

[287] F. Oschmann, H. Berry, K. Obermayer, and K. Lenk, "From in silico astrocyte cell models to neuron-astrocyte network models: A review," *Brain Research Bulletin*, Feb. 2017.

[288] T. Manninen, R. Havela, and M.-L. Linne, "Computational Models for Calcium-Mediated Astrocyte Functions," *Frontiers in Computational Neuroscience*, vol. 12, Apr. 2018.

[289] M. D. Pittà and H. Berry, *Computational Glioscience.* Springer, Jan. 2019. Google-Books-ID: LcKEDwAAQBAJ.

[290] D. Gonze, C. Gérard, B. Wacquier, A. Woller, A. Tosenberger, A. Goldbeter, and G. Dupont, "Modeling Based Investigation of the Effect of Noise in Cellular Systems," *Frontiers in Molecular Biosciences*, vol. 5, Apr. 2018.

[291] M. B. Elowitz, A. J. Levine, E. D. Siggia, and P. S. Swain, "Stochastic gene expression in a single cell," *Science (New York, N.Y.)*, vol. 297, pp. 1183–1186, Aug. 2002.

[292] T. Székely and K. Burrage, "Stochastic simulation in systems biology," *Computational and Structural Biotechnology Journal*, vol. 12, pp. 14–25, Nov. 2014.

[293] Cornish-Bowden, *Fundamentals of Enzyme Kinetics.* Portland Press, cornish-3rd ednma, l. e ed., 2004.

[294] J. C. Butcher, *Numerical Methods for Ordinary Differential Equations.* John Wiley & Sons, Aug. 2016. Google-Books-ID: JlSvDAAAQBAJ.

[295] J. E. Marsden and M. McCracken, *The Hopf Bifurcation and Its Applications*. Springer Science & Business Media, Dec. 2012. Google-Books-ID: FTv0BwAAQBAJ.

[296] G. Dupont, M. Falcke, V. Kirk, and J. Sneyd, "Basic Modelling Principles: Deterministic Models," in *Models of Calcium Signalling* (G. Dupont, M. Falcke, V. Kirk, and J. Sneyd, eds.), Interdisciplinary Applied Mathematics, pp. 97–161, Cham: Springer International Publishing, 2016.

[297] S. Girard, A. Lückhoff, J. Lechleiter, J. Sneyd, and D. Clapham, "Two-dimensional model of calcium waves reproduces the patterns observed in Xenopus oocytes," *Biophysical Journal*, vol. 61, pp. 509–517, Feb. 1992.

[298] M. S. Jafri and A. Ullah, "Calcium Waves," in *Encyclopedia of Computational Neuroscience* (D. Jaeger and R. Jung, eds.), pp. 1–11, New York, NY: Springer New York, 2013.

[299] A. Goldbeter, *Biochemical Oscillations and Cellular Rhythms: The Molecular Bases of Periodic and Chaotic Behaviour*. Cambridge University Press, Jan. 1996. Google-Books-ID: 6stfQgAACAAJ.

[300] A. Goldbeter, G. Dupont, and M. J. Berridge, "Minimal Model for Signal-Induced Ca2+ Oscillations and for Their Frequency Encoding Through Protein Phosphorylation," *Proceedings of the National Academy of Science*, vol. 87, pp. 1461–1465, Feb. 1990.

[301] G. Dupont and A. Goldbeter, "One-pool model for Ca2+ oscillations involving Ca2+ and inositol 1,4,5-trisphosphate as co-agonists for Ca2+ release," *Cell Calcium*, vol. 14, pp. 311–322, Apr. 1993.

[302] Y.-X. Li and J. Rinzel, "Equations for InsP3 Receptor-mediated [Ca2+]i Oscillations Derived from a Detailed Kinetic Model: A Hodgkin-Huxley Like Formalism," *Journal of Theoretical Biology*, vol. 166, pp. 461–473, Feb. 1994.

[303] M. De Pittà, V. Volman, H. Levine, and E. Ben-Jacob, "Multimodal encoding in a simplified model of intracellular calcium signaling," *Cognitive Processing*, vol. 10 Suppl 1, pp. S55–70, Feb. 2009.

[304] Y. Timofeeva, "Intracellular Calcium Dynamics: Biophysical and Simplified Models," in *Computational Glioscience* (M. De Pittà and H. Berry, eds.), Springer Series in Computational Neuroscience, pp. 69–90, Cham: Springer International Publishing, 2019.

[305] T. Meyer and L. Stryer, "Molecular model for receptor-stimulated calcium spiking," *Proceedings of the National Academy of Sciences*, vol. 85, pp. 5051–5055, July 1988.

[306] G. Dupont and C. Erneux, "Simulations of the effects of inositol 1,4,5-trisphosphate 3-kinase and 5-phosphatase activities on Ca2+ oscillations," *Cell Calcium*, vol. 22, pp. 321–331, Nov. 1997.

[307] G. Dupont, O. Koukoui, C. Clair, C. Erneux, S. Swillens, and L. Combettes, "Ca2+ oscillations in hepatocytes do not require the modulation of InsP3 3-kinase activity by Ca2+," *FEBS Letters*, vol. 534, no. 1-3, pp. 101–105, 2003.

[308] I. Bezprozvanny, J. Watras, and B. E. Ehrlich, "Bell-shaped calcium-response curves of Ins(1,4,5)P3- and calcium-gated channels from endoplasmic reticulum of cerebellum," *Nature*, vol. 351, pp. 751–754, June 1991.

[309] S. K. Joseph, H. L. Rice, and J. R. Williamson, "The effect of external calcium and pH on inositol trisphosphate-mediated calcium release from cerebellum microsomal fractions," *Biochemical Journal*, vol. 258, pp. 261–265, Feb. 1989.

[310] J. Watras, I. Bezprozvanny, and B. E. Ehrlich, "Inositol 1,4,5-trisphosphate-gated channels in cerebellum: presence of multiple conductance states," *Journal of Neuroscience*, vol. 11, pp. 3239–3245, Oct. 1991.

[311] H. G. Othmer and Y. Tang, "Oscillations and Waves in a Model of InsP3-Controlled Calcium Dynamics," in *Experimental and Theoretical Advances in Biological Pattern Formation* (H. G. Othmer, P. K. Maini, and J. D. Murray, eds.), pp. 277–300, Boston, MA: Springer US, 1993.

[312] I. Bezprozvanny, "Theoretical analysis of calcium wave propagation based on inositol (1,4,5)-trisphosphate (InsP3) receptor functional properties," *Cell Calcium*, vol. 16, pp. 151–166, Sept. 1994.

[313] J. Shuai, J. E. Pearson, J. K. Foskett, D.-O. D. Mak, and I. Parker, "A kinetic model of single and clustered IP3 receptors in the absence of Ca2+ feedback," *Biophysical Journal*, vol. 93, pp. 1151–1162, Aug. 2007.

[314] J. Sneyd and J.-F. Dufour, "A dynamic model of the type-2 inositol trisphosphate receptor," *Proceedings of the National Academy of Sciences*, vol. 99, pp. 2398–2403, Feb. 2002.

[315] G. Ullah and P. Jung, "Modeling the Statistics of Elementary Calcium Release Events," *Biophysical Journal*, vol. 90, pp. 3485–3495, May 2006.

[316] J. W. Shuai, D. P. Yang, J. E. Pearson, and S. Rüdiger, "An investigation of models of the IP3r channel in Xenopus oocyte.," *Chaos (Woodbury, N.Y.), Chaos*, vol. 19, 19, pp. 037105–037105, Sept. 2009.

[317] Y. X. Li, S. S. Stojilković, J. Keizer, and J. Rinzel, "Sensing and refilling calcium stores in an excitable cell," *Biophysical Journal*, vol. 72, pp. 1080–1091, Mar. 1997.

[318] J. Wagner, Y.-X. Li, J. Pearson, and J. Keizer, "Simulation of the Fertilization Ca2+ Wave in Xenopus laevis Eggs," *Biophysical Journal*, vol. 75, pp. 2088–2097, Oct. 1998.

[319] Y.-X. Li, "Tango waves in a bidomain model of fertilization calcium waves," *Physica D: Nonlinear Phenomena*, vol. 186, pp. 27–49, Dec. 2003.

[320] S. Schuster, M. Marhl, and T. Höfer, "Modelling of simple and complex calcium oscillations," *European Journal of Biochemistry*, vol. 269, no. 5, pp. 1333–1355, 2002.

[321] G. Dupont, M. Falcke, V. Kirk, and J. Sneyd, *Models of Calcium Signalling*, vol. 43 of *Interdisciplinary Applied Mathematics*. Cham: Springer International Publishing, 2016.

[322] G. Ullah, P. Jung, and A. H. Cornell-Bell, "Anti-phase calcium oscillations in astrocytes via inositol (1, 4, 5)-trisphosphate regeneration," *Cell Calcium*, vol. 39, pp. 197–208, Mar. 2006.

[323] M. Lavrentovich and S. Hemkin, "A mathematical model of spontaneous calcium(II) oscillations in astrocytes," *Journal of Theoretical Biology*, vol. 251, pp. 553–560, Apr. 2008.

[324] S. Zeng, B. Li, S. Zeng, and S. Chen, "Simulation of Spontaneous Ca2+ Oscillations in Astrocytes Mediated by Voltage-Gated Calcium Channels," *Biophysical Journal*, vol. 97, pp. 2429–2437, Nov. 2009.

[325] F. Oschmann, K. Mergenthaler, E. Jungnickel, and K. Obermayer, "Spatial separation of two different pathways accounting for the generation of calcium signals in astrocytes," *PLOS Computational Biology*, vol. 13, p. e1005377, Feb. 2017.

[326] I. Goto, S. Kinoshita, and K. Natsume, "The model of glutamate-induced intracellular Ca2+ oscillation and intercellular Ca2+ wave in brain astrocytes," *Neurocomputing - IJON*, vol. 58, pp. 461–467, June 2004.

[327] M. Stamatakis and N. V. Mantzaris, "Modeling of ATP-mediated signal transduction and wave propagation in astrocytic cellular networks," *Journal of Theoretical Biology*, vol. 241, pp. 649–668, Aug. 2006.

[328] F. Wei and J. Shuai, "Intercellular calcium waves in glial cells with bistable dynamics," *Physical biology*, vol. 8, p. 026009, Mar. 2011.

[329] A. Di Garbo, M. Barbi, S. Chillemi, S. Alloisio, and M. Nobile, "Calcium signalling in astrocytes and modulation of neural activity," *Biosystems*, vol. 89, pp. 74–83, May 2007.

[330] M. D. Pittà, V. Volman, H. Berry, and E. Ben-Jacob, "A Tale of Two Stories: Astrocyte Regulation of Synaptic Depression and Facilitation," *PLOS Computational Biology*, vol. 7, p. e1002293, Dec. 2011.

[331] M. R. Bennett, L. Farnell, and W. G. Gibson, "Origins of blood volume change due to glutamatergic synaptic activity at astrocytes abutting on arteriolar smooth muscle cells," *Journal of Theoretical Biology*, vol. 250, pp. 172–185, Jan. 2008.

[332] J. Riera, R. Hatanaka, T. Uchida, T. Ozaki, and R. Kawashima, "Quantifying the Uncertainty of Spontaneous Ca2+ Oscillations in Astrocytes: Particulars of Alzheimer's Disease," *Biophysical Journal*, vol. 101, pp. 554–564, Aug. 2011.

[333] M. De Pittà, M. Goldberg, V. Volman, H. Berry, and E. Ben-Jacob, "Glutamate regulation of calcium and IP3 oscillating and pulsating dynamics in astrocytes," *Journal of Biological Physics*, vol. 35, pp. 383–411, Oct. 2009.

[334] M. De Pittà, E. Ben-Jacob, and H. Berry, "G Protein-Coupled Receptor-Mediated Calcium Signaling in Astrocytes," in *Computational Glioscience* (M. De Pittà and H. Berry, eds.), Springer Series in Computational Neuroscience, pp. 115–150, Cham: Springer International Publishing, 2019.

[335] J. Lallouette, *Modélisation des réponses calciques de réseaux d'astrocytes : Relations entre topologie et dynamiques*. thesis, Lyon, INSA, Dec. 2014.

[336] Y. Tang, J. L. Stephenson, and H. G. Othmer, "Simplification and analysis of models of calcium dynamics based on IP3-sensitive calcium channel kinetics," *Biophysical Journal*, vol. 70, pp. 246–263, Jan. 1996.

[337] T. Höfer, L. Venance, and C. Giaume, "Control and Plasticity of Intercellular Calcium Waves in Astrocytes: A Modeling Approach," *Journal of Neuroscience*, vol. 22, pp. 4850–4859, June 2002.

[338] U. Kummer, L. F. Olsen, C. J. Dixon, A. K. Green, E. Bornberg-Bauer, and G. Baier, "Switching from Simple to Complex Oscillations in Calcium Signaling," *Biophysical Journal*, vol. 79, pp. 1188–1195, Sept. 2000.

[339] R. Thul, T. C. Bellamy, H. L. Roderick, M. D. Bootman, and S. Coombes, "Calcium Oscillations," in *Cellular Oscillatory Mechanisms* (M. Maroto and N. A. M. Monk, eds.), Advances in Experimental Medicine and Biology, pp. 1–27, New York, NY: Springer New York, 2009.

[340] G. Dupont and J. Sneyd, "Recent developments in models of calcium signalling," *Current Opinion in Systems Biology*, vol. 3, pp. 15–22, June 2017.

[341] I. Siekmann, P. Cao, J. Sneyd, and E. J. Crampin, "Data-driven modelling of the inositol trisphosphate receptor (IPR) and its role in calcium induced calcium release (CICR)," *ResearchGate*, July 2015.

[342] K. Hituri and M.-L. Linne, "Comparison of Models for IP3 Receptor Kinetics Using Stochastic Simulations," *PLOS ONE*, vol. 8, p. e59618, Apr. 2013.

[343] Y. Togashi and K. Kaneko, "Transitions Induced by the Discreteness of Molecules in a Small Autocatalytic System," *Physical Review Letters*, vol. 86, pp. 2459–2462, Mar. 2001.

[344] N. M. Shnerb, Y. Louzoun, E. Bettelheim, and S. Solomon, "The importance of being discrete: Life always wins on the surface," *Proceedings of the National Academy of Sciences*, vol. 97, pp. 10322–10324, Sept. 2000.

[345] D. Frigola, L. Casanellas, J. M. Sancho, and M. Ibañes, "Asymmetric Stochastic Switching Driven by Intrinsic Molecular Noise," *PLOS ONE*, vol. 7, p. e31407, Feb. 2012.

[346] D. T. Gillespie, "Exact stochastic simulation of coupled chemical reactions," *The Journal of Physical Chemistry*, vol. 81, pp. 2340–2361, Dec. 1977.

[347] N. G. V. Kampen, *Stochastic Processes in Physics and Chemistry*. Elsevier, Aug. 2011.

[348] A. B. Bortz, M. H. Kalos, and J. L. Lebowitz, "A new algorithm for Monte Carlo simulation of Ising spin systems," *Journal of Computational Physics*, vol. 17, pp. 10–18, Jan. 1975.

[349] P. Kratzer, "Monte Carlo and kinetic Monte Carlo methods," *arXiv:0904.2556 [cond-mat, physics:physics]*, Apr. 2009. arXiv: 0904.2556.

[350] J. R. Winkler, "Numerical recipes in C: The art of scientific computing, second edition," *Endeavour*, vol. 17, p. 201, Jan. 1993.

[351] D. J. Wilkinson, *Stochastic Modelling for Systems Biology*. CRC Press, Nov. 2011. Google-Books-ID: 7jnNBQAAQBAJ.

[352] Singh Abhyudai and Hespanha João P., "Stochastic hybrid systems for studying biochemical processes," *Philosophical Transactions of the Royal Society A: Mathematical, Physical and Engineering Sciences*, vol. 368, pp. 4995–5011, Nov. 2010.

[353] D. Higham., "An Algorithmic Introduction to Numerical Simulation of Stochastic Differential Equations," *SIAM Review*, vol. 43, pp. 525–546, Jan. 2001.

[354] P. E. Kloeden and E. Platen, "Stochastic Differential Equations," in *Numerical Solution of Stochastic Differential Equations* (P. E. Kloeden and E. Platen, eds.), Applications of Mathematics, pp. 103–160, Berlin, Heidelberg: Springer Berlin Heidelberg, 1992.

[355] D. T. Gillespie, "Stochastic simulation of chemical kinetics," *Annual Review of Physical Chemistry*, vol. 58, pp. 35–55, 2007.

[356] D. Higham, "Modeling and Simulating Chemical Reactions," *SIAM Review*, vol. 50, pp. 347–368, Jan. 2008.

[357] D. T. Gillespie and E. Seitaridou, *Simple Brownian Diffusion: An Introduction to the Standard Theoretical Models*. OUP Oxford, 2013.

[358] M. A. Gibson and J. Bruck, "Efficient exact stochastic simulation of chemical systems with many species and many channels," *The Journal of Physical Chemistry A*, vol. 104, no. 9, pp. 1876–1889, 2000.

[359] Y. Cao, D. Gillespie, and L. Petzold, "Multiscale stochastic simulation algorithm with stochastic partial equilibrium assumption for chemically reacting systems," *Journal of Computational Physics*, vol. 206, pp. 395–411, July 2005.

[360] W. E, D. Liu, and E. Vanden-Eijnden, "Nested stochastic simulation algorithms for chemical kinetic systems with multiple time scales," *Journal of Computational Physics*, vol. 221, pp. 158–180, Jan. 2007.

[361] E. L. Haseltine and J. B. Rawlings, "Approximate simulation of coupled fast and slow reactions for stochastic chemical kinetics," *The Journal of Chemical Physics*, vol. 117, pp. 6959–6969, Sept. 2002.

[362] D. T. Gillespie and L. R. Petzold, "Improved leap-size selection for accelerated stochastic simulation," *The Journal of Chemical Physics*, vol. 119, pp. 8229–8234, Oct. 2003.

[363] T. Tian and K. Burrage, "Binomial leap methods for simulating stochastic chemical kinetics," *The Journal of Chemical Physics*, vol. 121, pp. 10356–10364, Nov. 2004.

[364] J. Pahle, "Biochemical simulations: stochastic, approximate stochastic and hybrid approaches," *Briefings in Bioinformatics*, vol. 10, pp. 53–64, Jan. 2009.

[365] J. Goutsias and G. Jenkinson, "Markovian dynamics on complex reaction networks," *Physics Reports*, vol. 529, pp. 199–264, Aug. 2013.

[366] A. Skupin, H. Kettenmann, U. Winkler, M. Wartenberg, H. Sauer, S. C. Tovey, C. W. Taylor, and M. Falcke, "How Does Intracellular Ca2+ Oscillate: By Chance or by the Clock?," *Biophysical Journal*, vol. 94, pp. 2404–2411, Mar. 2008.

[367] M. Perc, A. K. Green, C. J. Dixon, and M. Marhl, "Establishing the stochastic nature of intracellular calcium oscillations from experimental data," *Biophysical Chemistry*, vol. 132, pp. 33–38, Jan. 2008.

[368] J. S. Marchant and I. Parker, "Role of elementary Ca2+ puffs in generating repetitive Ca2+ oscillations," *The EMBO Journal*, vol. 20, pp. 65–76, Jan. 2001.

[369] J. W. Shuai and P. Jung, "Optimal ion channel clustering for intracellular calcium signaling," *Proceedings of the National Academy of Sciences*, vol. 100, pp. 506–510, Jan. 2003.

[370] A. Skupin and M. Falcke, "From puffs to global Ca2+ signals: how molecular properties shape global signals," *Chaos (Woodbury, N.Y.)*, vol. 19, p. 037111, Sept. 2009.

[371] K. Thurley, S. C. Tovey, G. Moenke, V. L. Prince, A. Meena, A. P. Thomas, A. Skupin, C. W. Taylor, and M. Falcke, "Reliable encoding of stimulus intensities within random sequences of intracellular Ca2+ spikes," *Science Signaling*, vol. 7, p. ra59, June 2014.

[372] G. Dupont, L. Combettes, G. S. Bird, and J. W. Putney, "Calcium Oscillations," *Cold Spring Harbor Perspectives in Biology*, vol. 3, Mar. 2011.

[373] J.-W. Shuai and P. Jung, "Stochastic Properties of Ca2+ Release of Inositol 1,4,5-Trisphosphate Receptor Clusters," *Biophysical Journal*, vol. 83, pp. 87–97, July 2002.

[374] G. Dupont, A. Abou-Lovergne, and L. Combettes, "Stochastic Aspects of Oscillatory Ca2+ Dynamics in Hepatocytes," *Biophysical Journal*, vol. 95, pp. 2193–2202, Sept. 2008.

[375] D.-O. D. Mak, S. M. J. McBride, and J. K. Foskett, "Spontaneous Channel Activity of the Inositol 1,4,5-Trisphosphate (InsP3) Receptor (InsP3r). Application of Allosteric Modeling to Calcium and InsP3 Regulation of InsP3r Single-channel Gating," *The Journal of General Physiology*, vol. 122, pp. 583–603, Nov. 2003.

[376] I. Baran, "Integrated Luminal and Cytosolic Aspects of the Calcium Release Control," *Biophysical Journal*, vol. 84, pp. 1470–1485, Mar. 2003.

[377] M. Falcke, L. Tsimring, and H. Levine, "Stochastic spreading of intracellular Ca(2+) release," *Physical Review. E, Statistical Physics, Plasmas, Fluids, and Related Interdisciplinary Topics*, vol. 62, pp. 2636–2643, Aug. 2000.

[378] M. Bär, M. Falcke, H. Levine, and L. S. Tsimring, "Discrete stochastic modeling of calcium channel dynamics," *Physical Review Letters*, vol. 84, pp. 5664–5667, June 2000.

[379] D.-O. D. Mak, J. E. Pearson, K. P. C. Loong, S. Datta, M. Fernández-Mongil, and J. K. Foskett, "Rapid ligand-regulated gating kinetics of single inositol 1,4,5-trisphosphate receptor Ca2+ release channels," *EMBO reports*, vol. 8, pp. 1044–1051, Nov. 2007.

[380] E. Gin, M. Falcke, L. E. Wagner, D. I. Yule, and J. Sneyd, "A Kinetic Model of the Inositol Trisphosphate Receptor Based on Single-Channel Data," *Biophysical Journal*, vol. 96, pp. 4053–4062, May 2009.

[381] I. Siekmann, L. Wagner, D. Yule, E. Crampin, and J. Sneyd, "A Kinetic Model for Type I and II IP3r Accounting for Mode Changes," *Biophysical Journal*, vol. 103, pp. 658–668, Aug. 2012.

[382] G. Ullah, D.-O. D. Mak, and J. E. Pearson, "A data-driven model of a modal gated ion channel: The inositol 1,4,5-trisphosphate receptor in insect Sf9 cells," *The Journal of General Physiology*, vol. 140, pp. 159–173, Aug. 2012.

[383] I. Bezprozvanny, "The inositol 1,4,5-trisphosphate receptors," *Cell Calcium*, vol. 38, pp. 261–272, Sept. 2005.

[384] S. Rüdiger, "Excitability in a stochastic differential equation model for calcium puffs," *Physical Review E*, vol. 89, June 2014.

[385] V. Nguyen, R. Mathias, and G. D. Smith, "A stochastic automata network descriptor for Markov chain models of instantaneously coupled intracellular Ca2+ channels," *Bulletin of Mathematical Biology*, vol. 67, pp. 393–432, May 2005.

[386] G. Dupont, M. Falcke, V. Kirk, and J. Sneyd, "Hierarchical and Stochastic Modelling," in *Models of Calcium Signalling* (G. Dupont, M. Falcke, V. Kirk, and J. Sneyd, eds.), Interdisciplinary Applied Mathematics, pp. 163–205, Cham: Springer International Publishing, 2016.

[387] H. Li, Z. Hou, and H. Xin, "Internal noise stochastic resonance for intracellular calcium oscillations in a cell system," *Physical Review E*, vol. 71, p. 061916, June 2005.

[388] C.-l. Zhu, Y. Jia, Q. Liu, L.-j. Yang, and X. Zhan, "A mesoscopic stochastic mechanism of cytosolic calcium oscillations," *Biophysical Chemistry*, vol. 125, pp. 201–212, Jan. 2007.

[389] A. Tilūnaitė, W. Croft, N. Russell, T. C. Bellamy, and R. Thul, "A Bayesian approach to modelling heterogeneous calcium responses in cell populations," *PLOS Computational Biology*, vol. 13, p. e1005794, Oct. 2017.

[390] M. Falcke, M. Moein, A. Tilunaite, R. Thul, and A. Skupin, "On the phase space structure of IP3 induced Ca2+ signalling and concepts for predictive modeling," *Chaos*, vol. 28, Mar. 2018.

[391] M. Falcke, "On the Role of Stochastic Channel Behavior in Intracellular Ca2+ Dynamics," *Biophysical Journal*, vol. 84, pp. 42–56, Jan. 2003.

[392] S. Rüdiger and J. Shuai, "Modeling of Stochastic ca^{2+} Signals," in *Computational Glioscience* (M. De Pittà and H. Berry, eds.), Springer Series in Computational Neuroscience, pp. 91–114, Cham: Springer International Publishing, 2019.

[393] M. De Pittà and N. Brunel, "Modulation of Synaptic Plasticity by Glutamatergic Gliotransmission: A Modeling Study," *Neural Plasticity*, vol. 2016, 2016.

[394] A. M. Turing, "The chemical basis of morphogenesis," *Philosophical Transactions of the Royal Society of London. Series B, Biological Sciences*, vol. 237, pp. 37–72, Aug. 1952.

[395] C. Nicholson, K. C. Chen, S. Hrabětová, and L. Tao, "Diffusion of molecules in brain extracellular space: theory and experiment," in *Progress in Brain Research*, vol. 125 of *Volume Transmission Revisited*, pp. 129–154, Elsevier, Jan. 2000.

[396] N. J. Eungdamrong and R. Iyengar, "Computational approaches for modeling regulatory cellular networks," *Trends in Cell Biology*, vol. 14, pp. 661–669, Dec. 2004.

[397] G. D. Smith, *Numerical Solution of Partial Differential Equations: Finite Difference Methods*. Clarendon Press, 1985. Google-Books-ID: hDpvljaHOrMC.

[398] B. M. Slepchenko, J. C. Schaff, I. Macara, and L. M. Loew, "Quantitative cell biology with the Virtual Cell," *Trends in Cell Biology*, vol. 13, pp. 570–576, Nov. 2003.

[399] F. Sayyid and S. Kalvala, "On the importance of modelling the internal spatial dynamics of biological cells.," *Bio Systems*, vol. 145, pp. 53–66, July 2016.

[400] J. M. Bower and D. Beeman, *The Book of GENESIS: Exploring Realistic Neural Models with the GEneral NEural SImulation System*. Springer Science & Business Media, Dec. 2012. Google-Books-ID: f4PTBwAAQBAJ.

[401] K. T. Blackwell and J. H. Kotaleski, "Modeling The Dynamics of Second Messenger Pathways," in *Neuroscience Databases: A Practical Guide* (R. Kötter, ed.), pp. 63–79, Boston, MA: Springer US, 2003.

[402] S. Ray and U. S. Bhalla, "PyMOOSE: interoperable scripting in Python for MOOSE," *Frontiers in Neuroinformatics*, vol. 2, 2008.

[403] M. L. Hines and N. T. Carnevale, "Neuron: A Tool for Neuroscientists," *The Neuroscientist*, vol. 7, pp. 123–135, Apr. 2001.

[404] A. J. H. Newton, R. A. McDougal, M. L. Hines, and W. W. Lytton, "Using NEURON for Reaction-Diffusion Modeling of Extracellular Dynamics," *Frontiers in Neuroinformatics*, vol. 12, 2018.

[405] L. P. Savtchenko, L. Bard, T. P. Jensen, J. P. Reynolds, I. Kraev, N. Medvedev, M. G. Stewart, C. Henneberger, and D. A. Rusakov, "Disentangling astroglial physiology with a realistic cell model in silico," *Nature Communications*, vol. 9, no. 1, p. 3554, 2018.

[406] R. A. McDougal, R. Wang, T. M. Morse, M. Migliore, L. Marenco, T. Carnevale, M. Hines, and G. M. Shepherd, "ModelDB," in *Encyclopedia*

of Computational Neuroscience (D. Jaeger and R. Jung, eds.), pp. 1–4, New York, NY: Springer New York, 2013.

[407] B. M. Slepchenko, J. C. Schaff, J. H. Carson, and L. M. Loew, "Computational Cell Biology: Spatiotemporal Simulation of Cellular Events," *Annual Review of Biophysics and Biomolecular Structure*, vol. 31, no. 1, pp. 423–441, 2002.

[408] Chen Xi, Guo Liang, Kang Jianhong, Huo Yunlong, Wang Shiqiang, and Tan Wenchang, "Calcium waves initiating from the anomalous subdiffusive calcium sparks," *Journal of The Royal Society Interface*, vol. 11, p. 20130934, Feb. 2014.

[409] G. Weng, U. S. Bhalla, and R. Iyengar, "Complexity in Biological Signaling Systems," *Science*, vol. 284, pp. 92–96, Apr. 1999.

[410] J. T. Koivumäki, T. Korhonen, and P. Tavi, "Impact of Sarcoplasmic Reticulum Calcium Release on Calcium Dynamics and Action Potential Morphology in Human Atrial Myocytes: A Computational Study," *PLOS Computational Biology*, vol. 7, p. e1001067, Jan. 2011.

[411] S. R. Neves and R. Iyengar, "Models of Spatially Restricted Biochemical Reaction Systems," *Journal of Biological Chemistry*, vol. 284, pp. 5445–5449, Feb. 2009.

[412] M. J. Berridge, "Elementary and global aspects of calcium signalling.," *The Journal of Physiology*, vol. 499, pp. 291–306, Mar. 1997.

[413] J. Marchant, N. Callamaras, and I. Parker, "Initiation of IP3 mediated Ca2+ waves in Xenopus oocytes," *The EMBO Journal*, vol. 18, pp. 5285–5299, Oct. 1999.

[414] J. Keizer and G. D. Smith, "Spark-to-wave transition: saltatory transmission of calcium waves in cardiac myocytes," *Biophysical Chemistry*, vol. 72, pp. 87–100, May 1998.

[415] S. P. Dawson, J. Keizer, and J. E. Pearson, "Fire–diffuse–fire model of dynamics of intracellular calcium waves," *Proceedings of the National Academy of Sciences*, vol. 96, pp. 6060–6063, May 1999.

[416] S. Coombes, "The Effect of Ion Pumps on the Speed of Travelling Waves in the Fire-diffuse-fire Model of Ca2+Release," *Bulletin of Mathematical Biology*, vol. 63, pp. 1–20, Jan. 2001.

[417] R. Thul, G. D. Smith, and S. Coombes, "A bidomain threshold model of propagating calcium waves," *Journal of Mathematical Biology*, vol. 56, pp. 435–463, Apr. 2008.

[418] R. Thul, S. Coombes, and G. D. Smith, "Sensitisation waves in a bidomain fire-diffuse-fire model of intracellular Ca2+ dynamics," *Physica D: Nonlinear Phenomena*, vol. 238, pp. 2142–2152, Nov. 2009.

[419] B. Pando, J. Pearson, and S. Ponce Dawson, "Sheet Excitability and Nonlinear Wave Propagation," *Physical review letters*, vol. 91, p. 258101, Jan. 2004.

[420] C. C. Fink, B. Slepchenko, I. I. Moraru, J. Watras, J. C. Schaff, and L. M. Loew, "An Image-Based Model of Calcium Waves in Differentiated Neuroblastoma Cells," *Biophysical Journal*, vol. 79, pp. 163–183, July 2000.

[421] K. Samanta, P. Kar, G. Mirams, and A. Parekh, "Ca2+ Channel Relocalization to Plasma-Membrane Microdomains Strengthens Activation of Ca2+-Dependent Nuclear Gene Expression," *Cell Reports*, vol. 12, pp. 203–216, July 2015.

[422] E. McIvor, S. Coombes, and R. Thul, "Three-dimensional spatio-temporal modelling of store operated Ca2+ entry: Insights into ER refilling and the spatial signature of Ca2+ signals," *Cell Calcium*, vol. 73, Apr. 2018.

[423] D. E. Postnov, R. N. Koreshkov, N. A. Brazhe, A. R. Brazhe, and O. V. Sosnovtseva, "Dynamical patterns of calcium signaling in a functional model of neuron–astrocyte networks," *Journal of Biological Physics*, vol. 35, pp. 425–445, Oct. 2009.

[424] M. Kang and H. G. Othmer, "Spatiotemporal characteristics of calcium dynamics in astrocytes," *Chaos*, vol. 19, Jan. 2009.

[425] M. Goldberg, M. D. Pittà, V. Volman, H. Berry, and E. Ben-Jacob, "Nonlinear Gap Junctions Enable Long-Distance Propagation of Pulsating Calcium Waves in Astrocyte Networks," *PLOS Computational Biology*, vol. 6, p. e1000909, Aug. 2010.

[426] J. Lallouette, M. De Pittà, E. Ben-Jacob, and H. Berry, "Sparse short-distance connections enhance calcium wave propagation in a 3d model of astrocyte networks," *Frontiers in Computational Neuroscience*, vol. 8, p. 45, 2014.

[427] A. R. Brazhe, D. E. Postnov, and O. Sosnovtseva, "Astrocyte calcium signaling: Interplay between structural and dynamical patterns," *Chaos: An Interdisciplinary Journal of Nonlinear Science*, vol. 28, p. 106320, Oct. 2018.

[428] S. Y. Gordleeva, S. A. Lebedev, M. A. Rumyantseva, and V. B. Kazantsev, "Astrocyte as a Detector of Synchronous Events of a Neural Network," *JETP Letters*, vol. 107, pp. 440–445, Apr. 2018.

[429] K. Breslin, J. J. Wade, K. Wong-Lin, J. Harkin, B. Flanagan, H. V. Zalinge, S. Hall, M. Walker, A. Verkhratsky, and L. McDaid, "Potassium and sodium microdomains in thin astroglial processes: A computational model study," *PLOS Computational Biology*, vol. 14, p. e1006151, May 2018.

[430] P. Montes de Oca Balderas and H. Montes de Oca Balderas, "Synaptic neuron-astrocyte communication is supported by an order of magnitude analysis of inositol tris-phosphate diffusion at the nanoscale in a model of peri-synaptic astrocyte projection," *BMC Biophysics*, vol. 11, p. 3, Feb. 2018.

[431] T. Mazel, R. Raymond, M. Raymond-Stintz, S. Jett, and B. S. Wilson, "Stochastic Modeling of Calcium in 3d Geometry," *Biophysical Journal*, vol. 96, pp. 1691–1706, Mar. 2009.

[432] P. K. Maini, K. J. Painter, and H. N. P. Chau, "Spatial pattern formation in chemical and biological systems," *Journal of the Chemical Society, Faraday Transactions*, vol. 93, pp. 3601–3610, Jan. 1997.

[433] A. H. Elcock, "Models of Macromolecular Crowding Effects & the Need for Quantitative Comparisons with Experiment," *Current opinion in structural biology*, vol. 20, pp. 196–206, Apr. 2010.

[434] M. Tomita, "Whole-cell simulation: a grand challenge of the 21st century," *Trends in Biotechnology*, vol. 19, pp. 205–210, June 2001.

[435] D. Fange and J. Elf, "Noise-Induced Min Phenotypes in E. coli," *PLOS Computational Biology*, vol. 2, p. e80, June 2006.

[436] K. Lipkow, S. S. Andrews, and D. Bray, "Simulated Diffusion of Phosphorylated CheY through the Cytoplasm of Escherichia coli," *Journal of Bacteriology*, vol. 187, pp. 45–53, Jan. 2005.

[437] K. Takahashi, S. Tanase-Nicola, and P. R. ten Wolde, "Spatio-temporal correlations can drastically change the response of a MAPK pathway," *Proceedings of the National Academy of Sciences of the United States of America*, vol. 107, pp. 2473–2478, Feb. 2010.

[438] T. Erdmann, M. Howard, and P. R. ten Wolde, "Role of Spatial Averaging in the Precision of Gene Expression Patterns," *Physical Review Letters*, vol. 103, p. 258101, Dec. 2009.

[439] J. S. van Zon, M. J. Morelli, S. Tănase-Nicola, and P. R. ten Wolde, "Diffusion of transcription factors can drastically enhance the noise in gene expression," *Biophysical Journal*, vol. 91, pp. 4350–4367, Dec. 2006.

[440] K. Burrage, P. M. Burrage, A. Leier, T. Marquez-Lago, and D. V. Nicolau, "Stochastic Simulation for Spatial Modelling of Dynamic Processes in a Living Cell," in *Design and Analysis of Biomolecular Circuits: Engineering Approaches to Systems and Synthetic Biology* (H. Koeppl, G. Setti, M. di Bernardo, and D. Densmore, eds.), pp. 43–62, New York, NY: Springer New York, 2011.

[441] S. Smith and R. Grima, "Spatial Stochastic Intracellular Kinetics: A Review of Modelling Approaches," *Bulletin of Mathematical Biology*, May 2018.

[442] K. Takahashi, S. N. V. Arjunan, and M. Tomita, "Space in systems biology of signaling pathways – towards intracellular molecular crowding in silico," *FEBS Letters*, vol. 579, no. 8, pp. 1783–1788, 2005.

[443] C. Lemerle, B. D. Ventura, and L. Serrano, "Space as the final frontier in stochastic simulations of biological systems," *FEBS Letters*, vol. 579, no. 8, pp. 1789–1794, 2005.

[444] S. A. Isaacson and D. Isaacson, "The Reaction-Diffusion Master Equation, Diffusion Limited Reactions, and Singular Potentials," *Physical Review. E, Statistical, Nonlinear, and Soft Matter Physics*, vol. 80, p. 066106, Dec. 2009.

[445] L. Boulianne, S. Al Assaad, M. Dumontier, and W. J. Gross, "GridCell: a stochastic particle-based biological system simulator," *BMC Systems Biology*, vol. 2, p. 66, July 2008.

[446] S. Wils and E. De Schutter, "STEPS: Modeling and Simulating Complex Reaction-Diffusion Systems with Python," *Frontiers in Neuroinformatics*, vol. 3, p. 15, 2009.

[447] I. Hepburn, R. Cannon, and E. De Schutter, "Efficient calculation of the quasi-static electrical potential on a tetrahedral mesh and its implementation in STEPS," *Frontiers in Computational Neuroscience*, vol. 7, Oct. 2013.

[448] R. Erban, "From molecular dynamics to Brownian dynamics," *Proc. R. Soc. A*, vol. 470, p. 20140036, July 2014.

[449] A. Ghosh, A. Leier, and T. T. Marquez-Lago, "The Spatial Chemical Langevin Equation and Reaction Diffusion Master Equations: moments and qualitative solutions," *Theoretical Biology & Medical Modelling*, vol. 12, Feb. 2015.

[450] R. Erban and S. J. Chapman, "Stochastic modelling of reaction–diffusion processes: algorithms for bimolecular reactions," *Physical Biology*, vol. 6, p. 046001, Aug. 2009.

[451] I. C. Agbanusi and S. A. Isaacson, "A Comparison of Bimolecular Reaction Models for Stochastic Reaction–Diffusion Systems," *Bulletin of Mathematical Biology*, vol. 76, pp. 922–946, Apr. 2014.

[452] R. Grima and S. Schnell, "A systematic investigation of the rate laws valid in intracellular environments," *Biophysical Chemistry*, vol. 124, pp. 1–10, Oct. 2006.

[453] S. S. Andrews, N. J. Addy, R. Brent, and A. P. Arkin, "Detailed Simulations of Cell Biology with Smoldyn 2.1," *PLOS Computational Biology*, vol. 6, p. e1000705, Mar. 2010.

[454] J. S. van Zon and P. R. ten Wolde, "Green's-function reaction dynamics: A particle-based approach for simulating biochemical networks in time and space," *The Journal of Chemical Physics*, vol. 123, p. 234910, Dec. 2005.

[455] S. S. Andrews, "Particle-Based Stochastic Simulators," in *Encyclopedia of Computational Neuroscience* (D. Jaeger and R. Jung, eds.), pp. 1–5, New York, NY: Springer New York, 2018.

[456] S. Engblom, L. Ferm, A. Hellander, and P. Lötstedt, "Simulation of Stochastic Reaction-Diffusion Processes on Unstructured Meshes," *SIAM Journal on Scientific Computing*, vol. 31, pp. 1774–1797, Jan. 2009.

[457] R. Erban, J. Chapman, and P. Maini, "A practical guide to stochastic simulations of reaction-diffusion processes," *arXiv:0704.1908 [physics, q-bio]*, Apr. 2007. arXiv: 0704.1908.

[458] S. Isaacson and C. Peskin, "Incorporating Diffusion in Complex Geometries into Stochastic Chemical Kinetics Simulations," *SIAM Journal on Scientific Computing*, vol. 28, pp. 47–74, Jan. 2006.

[459] S. Hellander, A. Hellander, and L. Petzold, "Reaction-diffusion master equation in the microscopic limit," *Physical Review E*, vol. 85, p. 042901, Apr. 2012.

[460] U. S. Bhalla, "Multiscale Modeling and Synaptic Plasticity," *Progress in Molecular Biology and Translational Science*, vol. 123, pp. 351–386, Jan. 2014.

[461] A. Leier and T. T. Marquez-Lago, "Correction factors for boundary diffusion in reaction-diffusion master equations," *The Journal of Chemical Physics*, vol. 135, p. 134109, Oct. 2011.

[462] S. Isaacson, "The Reaction Diffusion Master Equation as an Asymptotic Approximation of Diffusion to a Small Target," *SIAM Journal on Applied Mathematics*, vol. 70, pp. 77–111, Jan. 2009.

[463] T. T. Marquez-Lago and K. Burrage, "Binomial tau-leap spatial stochastic simulation algorithm for applications in chemical kinetics," *The Journal of Chemical Physics*, vol. 127, p. 104101, Sept. 2007.

[464] M. B. Flegg, S. J. Chapman, and R. Erban, "The two-regime method for optimizing stochastic reaction-diffusion simulations., The two-regime method for optimizing stochastic reaction–diffusion simulations," *Journal of the Royal Society, Interface, Journal of the Royal Society Interface*, vol. 9, 9, pp. 859, 859–868, May 2012.

[465] S. N. V. Arjunan and M. Tomita, "A new multicompartmental reaction-diffusion modeling method links transient membrane attachment of E. coli MinE to E-ring formation," *Systems and Synthetic Biology*, vol. 4, pp. 35–53, Mar. 2010.

[466] K. T. Blackwell, "Approaches and tools for modeling signaling pathways and calcium dynamics in neurons," *Journal of Neuroscience Methods*, vol. 220, pp. 131–140, Nov. 2013.

[467] C. A. Smith and C. A. Yates, "Spatially extended hybrid methods: a review," *Journal of the Royal Society, Interface*, vol. 15, no. 139, 2018.

[468] M. Dobrzyński, J. V. Rodríguez, J. A. Kaandorp, and J. G. Blom, "Computational methods for diffusion-influenced biochemical reactions," *Bioinformatics*, vol. 23, pp. 1969–1977, Aug. 2007.

[469] J. Schöneberg, A. Ullrich, and F. Noé, "Simulation tools for particle-based reaction-diffusion dynamics in continuous space," *BMC Biophysics*, vol. 7, p. 11, Oct. 2014.

[470] S. Anders, D. Minge, S. Griemsmann, M. K. Herde, C. Steinhäuser, and C. Henneberger, "Spatial properties of astrocyte gap junction coupling in the rat hippocampus," *Philosophical Transactions of the Royal Society B: Biological Sciences*, vol. 369, Oct. 2014.

[471] J. Hattne, D. Fange, and J. Elf, "Stochastic reaction-diffusion simulation with MesoRD," *Bioinformatics*, vol. 21, pp. 2923–2924, June 2005.

[472] M. Tomita, K. Hashimoto, K. Takahashi, T. S. Shimizu, Y. Matsuzaki, F. Miyoshi, K. Saito, S. Tanida, K. Yugi, J. C. Venter, and C. A. Hutchison, "E-CELL: software environment for whole-cell simulation.," *Bioinformatics*, vol. 15, pp. 72–84, Jan. 1999.

[473] K. Takahashi, K. Kaizu, B. Hu, and M. Tomita, "A multi-algorithm, multi-timescale method for cell simulation," *Bioinformatics*, vol. 20, pp. 538–546, Mar. 2004.

[474] B. Drawert, S. Engblom, and A. Hellander, "URDME: a modular framework for stochastic simulation of reaction-transport processes in complex geometries," *BMC Systems Biology*, vol. 6, p. 76, 2012.

[475] I. Hepburn, W. Chen, S. Wils, and E. De Schutter, "STEPS: efficient simulation of stochastic reaction–diffusion models in realistic morphologies," *BMC Systems Biology*, vol. 6, no. 1, p. 36, 2012.

[476] S. J. Plimpton and A. Slepoy, "ChemCell : a particle-based model of protein chemistry and diffusion in microbial cells.," Tech. Rep. SAND2003-4509, Sandia National Laboratories, Dec. 2003.

[477] R. Kerr, T. Bartol, B. Kaminsky, M. Dittrich, J. Chang, S. Baden, T. Sejnowski, and J. Stiles, "Fast Monte Carlo Simulation Methods for Biological Reaction-Diffusion Systems in Solution and on Surfaces," *SIAM Journal on Scientific Computing*, vol. 30, pp. 3126–3149, Jan. 2008.

[478] C. Sanford, M. L. K. Yip, C. White, and J. Parkinson, "Cell++—simulating biochemical pathways," *Bioinformatics*, vol. 22, pp. 2918–2925, Dec. 2006.

[479] J. Schöneberg and F. Noé, "ReaDDy - A Software for Particle-Based Reaction-Diffusion Dynamics in Crowded Cellular Environments," *PLOS ONE*, vol. 8, p. e74261, Sept. 2013.

[480] N. B. Thillaiappan, A. Chavda, S. Tovey, D. Prole, and C. Taylor, "Ca2+ signals initiate at immobile IP3 receptors adjacent to ER-plasma membrane junctions," *Nature Communications*, vol. 8, Dec. 2017.

[481] S. M. Wiltgen, I. F. Smith, and I. Parker, "Superresolution localization of single functional IP3r channels utilizing Ca2+ flux as a readout," *Biophysical Journal*, vol. 99, pp. 437–446, July 2010.

[482] I. F. Smith and I. Parker, "Imaging the quantal substructure of single IP3r channel activity during Ca2+ puffs in intact mammalian cells," *Proceedings of the National Academy of Sciences*, vol. 106, pp. 6404–6409, Apr. 2009.

[483] M. Kraus, B. Wolf, and B. Wolf, "Crosstalk between cellular morphology and calcium oscillation patterns Insights from a stochastic computer model," *Cell Calcium*, vol. 19, pp. 461–472, June 1996.

[484] H. Anwar, I. Hepburn, H. Nedelescu, W. Chen, and E. D. Schutter, "Stochastic Calcium Mechanisms Cause Dendritic Calcium Spike Variability," *Journal of Neuroscience*, vol. 33, pp. 15848–15867, Oct. 2013.

[485] P. Smolen, D. A. Baxter, and J. H. Byrne, "Molecular Constraints on Synaptic Tagging and Maintenance of Long-Term Potentiation: A Predictive Model," *PLOS Computational Biology*, vol. 8, p. e1002620, Aug. 2012.

[486] S. Khan, Y. Zou, A. Amjad, A. Gardezi, C. L. Smith, C. Winters, and T. S. Reese, "Sequestration of CaMKII in dendritic spines in silico," *Journal of Computational Neuroscience*, vol. 31, pp. 581–594, Nov. 2011.

[487] B. Kim, S. L. Hawes, F. Gillani, L. J. Wallace, and K. T. Blackwell, "Signaling Pathways Involved in Striatal Synaptic Plasticity are Sensitive to Temporal Pattern and Exhibit Spatial Specificity," *PLOS Computational Biology*, vol. 9, p. e1002953, Mar. 2013.

[488] C. M. Simon, I. Hepburn, W. Chen, and E. D. Schutter, "The role of dendritic spine morphology in the compartmentalization and delivery of surface receptors," *Journal of Computational Neuroscience*, vol. 36, pp. 483–497, June 2014.

[489] R. L. Winslow, A. Tanskanen, M. Chen, and J. L. Greenstein, "Multiscale Modeling of Calcium Signaling in the Cardiac Dyad," *Annals of the New York Academy of Sciences*, vol. 1080, no. 1, pp. 362–375, 2006.

[490] N. Wieder, R. Fink, and F. von Wegner, "Exact Stochastic Simulation of a Calcium Microdomain Reveals the Impact of Ca2+ Fluctuations on IP3r Gating," *Biophysical Journal*, vol. 108, pp. 557–567, Feb. 2015.

[491] U. Dobramysl, S. Rüdiger, and R. Erban, "Particle-Based Multiscale Modeling of Calcium Puff Dynamics," *Multiscale Modeling & Simulation*, pp. 997–1016, Jan. 2016.

[492] S. Coombes and Y. Timofeeva, "Sparks and waves in a stochastic fire-diffuse-fire model of ${\mathrm{Ca}}^{2+}$ release," *Physical Review E*, vol. 68, p. 021915, Aug. 2003.

[493] A. Calabrese, D. Fraiman, D. Zysman, and S. Ponce Dawson, "Stochastic fire-diffuse-fire model with realistic cluster dynamics," *Physical Review. E, Statistical, Nonlinear, and Soft Matter Physics*, vol. 82, p. 031910, Sept. 2010.

[494] M. Arizono, H. Bannai, K. Nakamura, F. Niwa, M. Enomoto, T. Matsu-ura, A. Miyamoto, M. W. Sherwood, T. Nakamura, and K. Mikoshiba, "Receptor-Selective Diffusion Barrier Enhances Sensitivity of Astrocytic Processes to Metabotropic Glutamate Receptor Stimulation," *Sci. Signal.*, vol. 5, pp. ra27–ra27, Apr. 2012.

[495] L. Lencesova, A. O'Neill, W. G. Resneck, R. J. Bloch, and M. P. Blaustein, "Plasma membrane-cytoskeleton-endoplasmic reticulum complexes in neurons and astrocytes," *The Journal of Biological Chemistry*, vol. 279, pp. 2885–2893, Jan. 2004.

[496] S. H. Weerth, L. A. Holtzclaw, and J. T. Russell, "Signaling proteins in raft-like microdomains are essential for Ca2+ wave propagation in glial cells," *Cell Calcium*, vol. 41, pp. 155–167, Feb. 2007.

[497] L. Buscemi, V. Ginet, J. Lopatar, V. Montana, L. Pucci, P. Spagnuolo, T. Zehnder, V. Grubišić, A. Truttman, C. Sala, L. Hirt, V. Parpura, J. Puyal, and P. Bezzi, "Homer1 Scaffold Proteins Govern Ca2+ Dynamics in Normal and Reactive Astrocytes," *Cerebral Cortex (New York, N.Y.: 1991)*, Apr. 2016.

[498] E. Cresswel-Clay, N. Crock, J. Tabak, and G. Erlebacher, "A Compartmental Model to Investigate Local and Global Ca2+ Dynamics in Astrocytes," *Frontiers in Computational Neuroscience*, vol. 12, 2018.

[499] S. Winkelmann and C. Schütte, "Hybrid models for chemical reaction networks: Multiscale theory and application to gene regulatory systems," *The Journal of Chemical Physics*, vol. 147, p. 114115, Sept. 2017.

[500] A. Hellander and P. Lötstedt, "Hybrid method for the chemical master equation," *Journal of Computational Physics*, vol. 227, pp. 100–122, Nov. 2007.

[501] A. Duncan, R. Erban, and K. Zygalakis, "Hybrid framework for the simulation of stochastic chemical kinetics," *Journal of Computational Physics*, vol. 326, pp. 398–419, Dec. 2016.

[502] M. H. A. Davis, "Piecewise-Deterministic Markov Processes: A General Class of Non-Diffusion Stochastic Models," *Journal of the Royal Statistical Society. Series B (Methodological)*, vol. 46, no. 3, pp. 353–388, 1984.

[503] F. von Wegner, N. Wieder, and R. H. A. Fink, "Simulation strategies for calcium microdomains and calcium-regulated calcium channels," *Advances in Experimental Medicine and Biology*, vol. 740, pp. 553–567, 2012.

[504] Y. Cao, D. T. Gillespie, and L. R. Petzold, "The slow-scale stochastic simulation algorithm," *The Journal of Chemical Physics*, vol. 122, p. 014116, Dec. 2004.

[505] A. Crudu, A. Debussche, and O. Radulescu, "Hybrid stochastic simplifications for multiscale gene networks," *BMC Systems Biology*, vol. 3, p. 89, Sept. 2009.

[506] H. Salis and Y. Kaznessis, "Accurate hybrid stochastic simulation of a system of coupled chemical or biochemical reactions," *The Journal of Chemical Physics*, vol. 122, p. 054103, Jan. 2005.

[507] A. Alfonsi, E. Cancès, G. Turinici, B. Di Ventura, and W. Huisinga, "Adaptive simulation of hybrid stochastic and deterministic models for biochemical systems," *ESAIM: Proceedings*, vol. 14, pp. 1–13, Sept. 2005.

[508] A. Ganguly, D. Altintan, and H. Koeppl, "Jump-Diffusion Approximation of Stochastic Reaction Dynamics: Error Bounds and Algorithms," *Multiscale Modeling & Simulation*, vol. 13, pp. 1390–1419, Jan. 2015.

[509] K. Vasudeva and U. S. Bhalla, "Adaptive stochastic-deterministic chemical kinetic simulations," *Bioinformatics*, vol. 20, pp. 78–84, Jan. 2004.

[510] S. Zeiser, U. Franz, and V. Liebscher, "Autocatalytic genetic networks modeled by piecewise-deterministic Markov processes," *Journal of Mathematical Biology*, vol. 60, p. 207, Feb. 2010.

[511] S. Zeiser, U. Franz, O. Wittich, and V. Liebscher, "Simulation of genetic networks modelled by piecewise deterministic Markov processes," *IET Systems Biology*, vol. 2, pp. 113–135, May 2008.

[512] Yates Christian A. and Flegg Mark B., "The pseudo-compartment method for coupling partial differential equation and compartment-based models of diffusion," *Journal of The Royal Society Interface*, vol. 12, p. 20150141, May 2015.

[513] L. Ferm, A. Hellander, and P. Lötstedt, "An adaptive algorithm for simulation of stochastic reaction–diffusion processes," *Journal of Computational Physics*, vol. 229, pp. 343–360, Jan. 2010.

[514] C. Nagaiah, S. Rüdiger, G. Warnecke, and M. Falcke, "Adaptive space and time numerical simulation of reaction–diffusion models for intracellular calcium dynamics," *Applied Mathematics and Computation*, vol. 218, pp. 10194–10210, June 2012.

[515] S. Engblom, A. Hellander, and P. Lötstedt, "Multiscale Simulation of Stochastic Reaction-Diffusion Networks," in *Stochastic Processes, Multiscale Modeling, and Numerical Methods for Computational Cellular Biology* (D. Holcman, ed.), pp. 55–79, Cham: Springer International Publishing, 2017.

[516] J. C. Schaff, F. Gao, Y. Li, I. L. Novak, and B. M. Slepchenko, "Numerical Approach to Spatial Deterministic-Stochastic Models Arising in Cell Biology," *PLOS Computational Biology*, vol. 12, p. e1005236, Dec. 2016.

[517] N. Dudani, U. S. Bhalla, and S. Ray, "MOOSE, the Multiscale Object-Oriented Simulation Environment," in *Encyclopedia of Computational Neuroscience* (D. Jaeger and R. Jung, eds.), pp. 1–4, New York, NY: Springer New York, 2013.

[518] M. Robinson, S. S. Andrews, and R. Erban, "Multiscale reaction-diffusion simulations with Smoldyn," *Bioinformatics*, vol. 31, pp. 2406–2408, July 2015.

[519] B. Franz, M. Flegg, S. Chapman, and R. Erban, "Multiscale Reaction-Diffusion Algorithms: PDE-Assisted Brownian Dynamics," *SIAM Journal on Applied Mathematics*, vol. 73, pp. 1224–1247, Jan. 2013.

[520] M. Djurfeldt, J. Hjorth, J. M. Eppler, N. Dudani, M. Helias, T. C. Potjans, U. S. Bhalla, M. Diesmann, J. Hellgren Kotaleski, and O. Ekeberg, "Run-Time Interoperability Between Neuronal Network Simulators Based on the MUSIC Framework," *Neuroinformatics*, vol. 8, pp. 43–60, Mar. 2010.

[521] M. Brandi, E. Brocke, H. Talukdar, M. Hanke, U. S. Bhalla, J. Kotaleski, and M. Djurfeldt, "Connecting MOOSE and NeuroRD through MUSIC: towards a communication framework for multi-scale modeling," *BMC Neuroscience*, vol. 12, no. Suppl 1, p. P77.

[522] R. Hinch, J. L. Greenstein, A. J. Tanskanen, L. Xu, and R. L. Winslow, "A simplified local control model of calcium-induced calcium release in cardiac ventricular myocytes," *Biophysical Journal*, vol. 87, pp. 3723–3736, Dec. 2004.

[523] M. D. Stern, L. S. Song, H. Cheng, J. S. Sham, H. T. Yang, K. R. Boheler, and E. Ríos, "Local control models of cardiac excitation-contraction coupling. A possible role for allosteric interactions between ryanodine receptors," *The Journal of General Physiology*, vol. 113, pp. 469–489, Mar. 1999.

[524] M. Rückl, I. Parker, J. S. Marchant, C. Nagaiah, F. W. Johenning, and S. Rüdiger, "Modulation of Elementary Calcium Release Mediates a Transition from Puffs to Waves in an IP3r Cluster Model," *PLOS Computational Biology*, vol. 11, p. e1003965, Jan. 2015.

[525] M. Rückl and S. Rüdiger, "Calcium waves in a grid of clustered channels with synchronous IP3 binding and unbinding," *The European Physical Journal E*, vol. 39, p. 108, Nov. 2016.

[526] J. W. Shuai and P. Jung, "Optimal Intracellular Calcium Signaling," *Physical Review Letters*, vol. 88, p. 068102, Jan. 2002.

[527] S. Rüdiger, J. W. Shuai, and I. M. Sokolov, "Law of mass action, detailed balance, and the modeling of calcium puffs," *Physical Review Letters*, vol. 105, p. 048103, July 2010.

[528] L. Diambra and J. S. Marchant, "Inositol (1,4,5)-Trisphosphate Receptor Microarchitecture Shapes Ca2+ Puff Kinetics," *Biophysical Journal*, vol. 100, pp. 822–831, Feb. 2011.

[529] G. S. B. Williams, E. J. Molinelli, and G. D. Smith, "Modeling local and global intracellular calcium responses mediated by diffusely distributed inositol 1,4,5-trisphosphate receptors," *Journal of Theoretical Biology*, vol. 253, pp. 170–188, July 2008.

[530] A. Skupin, H. Kettenmann, and M. Falcke, "Calcium Signals Driven by Single Channel Noise," *PLoS computational biology*, vol. 6, Aug. 2010.

[531] S. Rüdiger, J. W. Shuai, W. Huisinga, C. Nagaiah, G. Warnecke, I. Parker, and M. Falcke, "Hybrid stochastic and deterministic simulations of calcium blips," *Biophysical Journal*, vol. 93, pp. 1847–1857, Sept. 2007.

[532] S. Swillens, G. Dupont, L. Combettes, and P. Champeil, "From calcium blips to calcium puffs: theoretical analysis of the requirements for interchannel communication," *Proceedings of the National Academy of Sciences of the United States of America*, vol. 96, pp. 13750–13755, Nov. 1999.

[533] A. Skupin and M. Falcke, "The role of IP3r clustering in Ca2+ signaling," *Genome Informatics. International Conference on Genome Informatics*, vol. 20, pp. 15–24, 2008.

[534] S. Braichenko, A. Bhaskar, and S. Dasmahapatra, "Phenomenological cluster-based model of ${\text{Ca}}^{2+}$ waves and oscillations for inositol 1,4,5-trisphosphate receptor (${\mathrm{IP}}_{3}\mathrm{R}$) channels," *Physical Review E*, vol. 98, p. 032413, Sept. 2018.

[535] J. W. Shuai, Y. D. Huang, and S. Rüdiger, "Puff-wave transition in an inhomogeneous model for calcium signals," *Physical Review. E, Statistical, Nonlinear, and Soft Matter Physics*, vol. 81, p. 041904, Apr. 2010.

[536] S. Means, A. J. Smith, J. Shepherd, J. Shadid, J. Fowler, R. J. H. Wojcikiewicz, T. Mazel, G. D. Smith, and B. S. Wilson, "Reaction Diffusion Modeling of Calcium Dynamics with Realistic ER Geometry," *Biophysical Journal*, vol. 91, pp. 537–557, July 2006.

[537] G. E. P. Box, "Sampling and Bayes' Inference in Scientific Modelling and Robustness," *Journal of the Royal Statistical Society: Series A (General)*, vol. 143, no. 4, pp. 383–404, 1980.

[538] G. Dupont and H. Croisier, "Spatiotemporal organization of Ca2+ dynamics: A modeling based approach," *HFSP Journal*, vol. 4, pp. 43–51, Apr. 2010.

[539] S. Rüdiger, "Stochastic models of intracellular calcium signals," *Physics Reports*, vol. 534, pp. 39–87, Jan. 2014.

[540] T. Manninen, R. Havela, and M.-L. Linne, "Reproducibility and Comparability of Computational Models for Astrocyte Calcium Excitability," *Frontiers in Neuroinformatics*, vol. 11, 2017.

[541] A. Panatier, M. Arizono, and U. V. Nägerl, "Dissecting tripartite synapses with STED microscopy," *Phil. Trans. R. Soc. B*, vol. 369, p. 20130597, Oct. 2014.

[542] I. F. Smith, S. M. Wiltgen, and I. Parker, "Localization of puff sites adjacent to the plasma membrane: Functional and spatial characterization of Ca2+ signaling in SH-SY5y cells utilizing membrane-permeant caged IP3," *Cell Calcium*, vol. 45, pp. 65–76, Jan. 2009.

[543] M. B. Flegg, S. Rüdiger, and R. Erban, "Diffusive spatio-temporal noise in a first-passage time model for intracellular calcium release," *The Journal of Chemical Physics*, vol. 138, p. 154103, Apr. 2013.

[544] B. Pando, S. P. Dawson, D.-O. D. Mak, and J. E. Pearson, "Messages diffuse faster than messengers," *Proceedings of the National Academy of Sciences*, vol. 103, pp. 5338–5342, Apr. 2006.

[545] S. Rüdiger, C. Nagaiah, G. Warnecke, and J. Shuai, "Calcium Domains around Single and Clustered IP3 Receptors and Their Modulation by Buffers," *Biophysical Journal*, vol. 99, pp. 3–12, July 2010.

[546] D. Fraiman and S. P. Dawson, "Buffer regulation of calcium puff sequences," *Physical Biology*, vol. 11, p. 016007, Feb. 2014.

[547] M. Falcke, "Buffers and oscillations in intracellular Ca2+ dynamics," *Biophysical Journal*, vol. 84, pp. 28–41, Jan. 2003.

[548] J. Shuai, J. E. Pearson, and I. Parker, "Modeling Ca2+ Feedback on a Single Inositol 1,4,5-Trisphosphate Receptor and Its Modulation by Ca2+ Buffers," *Biophysical Journal*, vol. 95, pp. 3738–3752, Oct. 2008.

[549] B. A. Bicknell and G. J. Goodhill, "Emergence of ion channel modal gating from independent subunit kinetics," *Proceedings of the National Academy of Sciences*, vol. 113, pp. E5288–E5297, Sept. 2016.

[550] T. Oura, K. Murata, T. Morita, A. Nezu, M. Arisawa, S. Shuto, and A. Tanimura, "Highly Sensitive Measurement of Inositol 1,4,5-Trisphosphate by Using a New Fluorescent Ligand and Ligand Binding Domain Combination," *Chembiochem: A European Journal of Chemical Biology*, vol. 17, no. 16, pp. 1509–1512, 2016.

[551] K. Zheng, L. Bard, J. P. Reynolds, C. King, T. Jensen, A. Gourine, and D. Rusakov, "Time-Resolved Imaging Reveals Heterogeneous Landscapes of Nanomolar Ca2+ in Neurons and Astroglia," *Neuron*, vol. 88, pp. 277–288, Oct. 2015.

[552] H. Tu, Z. Wang, and I. Bezprozvanny, "Modulation of Mammalian Inositol 1,4,5-Trisphosphate Receptor Isoforms by Calcium: A Role of Calcium Sensor Region," *Biophysical Journal*, vol. 88, pp. 1056–1069, Feb. 2005.

[553] E. C. Thrower, R. E. Hagar, and B. E. Ehrlich, "Regulation of Ins(1,4,5)P3 receptor isoforms by endogenous modulators," *Trends in Pharmacological Sciences*, vol. 22, pp. 580–586, Nov. 2001.

[554] N. L. Allbritton, T. Meyer, and L. Stryer, "Range of messenger action of calcium ion and inositol 1,4,5-trisphosphate," *Science (New York, N.Y.)*, vol. 258, pp. 1812–1815, Dec. 1992.

[555] B. Schwaller, "Cytosolic Ca2+ buffers," *Cold Spring Harbor Perspectives in Biology*, vol. 2, p. a004051, Nov. 2010.

[556] B. S. Wilson, J. R. Pfeiffer, A. J. Smith, J. M. Oliver, J. A. Oberdorf, and R. J. H. Wojcikiewicz, "Calcium-dependent Clustering of Inositol 1,4,5-Trisphosphate Receptors," *Molecular Biology of the Cell*, vol. 9, pp. 1465–1478, June 1998.

[557] T. Rahman, "Dynamic clustering of IP $_3$ receptors by IP $_3$," *Biochemical Society Transactions*, vol. 40, pp. 325–330, Apr. 2012.

[558] I. Smith, D. Swaminathan, G. Dickinson, and I. Parker, "Single-Molecule Tracking of Inositol Trisphosphate Receptors Reveals Different Motilities and Distributions," *Biophysical Journal*, vol. 107, pp. 834–845, Aug. 2014.

[559] H. Tu, Z. Wang, E. Nosyreva, H. De Smedt, and I. Bezprozvanny, "Functional Characterization of Mammalian Inositol 1,4,5-Trisphosphate Receptor Isoforms," *Biophysical Journal*, vol. 88, pp. 1046–1055, Feb. 2005.

[560] W. Chen and E. De Schutter, "Parallel STEPS: Large Scale Stochastic Spatial Reaction-Diffusion Simulation with High Performance Computers," *Frontiers in Neuroinformatics*, vol. 11, 2017.

[561] D. Swaminathan and P. Jung, "The Role of agonist-independent conformational transformation (AICT) in IP3 cluster behavior," *Cell Calcium*, vol. 49, pp. 145–152, Mar. 2011.

[562] R. A. McDougal, T. M. Morse, T. Carnevale, L. Marenco, R. Wang, M. Migliore, P. L. Miller, G. M. Shepherd, and M. L. Hines, "Twenty years of ModelDB and beyond: building essential modeling tools for the future of neuroscience," *Journal of Computational Neuroscience*, vol. 42, pp. 1–10, Feb. 2017.

[563] J. L. Stobart, K. D. Ferrari, M. J. P. Barrett, M. J. Stobart, Z. J. Looser, A. S. Saab, and B. Weber, "Long-term In Vivo Calcium Imaging of Astrocytes Reveals Distinct Cellular Compartment Responses to Sensory Stimulation," *Cerebral Cortex (New York, N.Y.: 1991)*, vol. 28, pp. 184–198, Jan. 2018.

[564] L.-J. Pilaz, A. L. Lennox, J. P. Rouanet, and D. L. Silver, "Dynamic mRNA Transport and Local Translation in Radial Glial Progenitors of the Developing Brain," *Current Biology*, vol. 26, pp. 3383–3392, Dec. 2016.

[565] R. Thomsen, J. Pallesen, T. F. Daugaard, A. D. Børglum, and A. L. Nielsen, "Genome wide assessment of mRNA in astrocyte protrusions by direct RNA sequencing reveals mRNA localization for the intermediate filament protein nestin," *Glia*, vol. 61, pp. 1922–1937, Nov. 2013.

[566] Z. Wang, M. Tymianski, O. T. Jones, and M. Nedergaard, "Impact of Cytoplasmic Calcium Buffering on the Spatial and Temporal Characteristics of Intercellular Calcium Signals in Astrocytes," *Journal of Neuroscience*, vol. 17, pp. 7359–7371, Oct. 1997.

[567] S. Zeller, S. Rüdiger, H. Engel, J. Sneyd, G. Warnecke, I. Parker, and M. Falcke, "Modeling of the modulation by buffers of Ca2+ release through clusters of IP3 receptors," *Biophysical Journal*, vol. 97, pp. 992–1002, Aug. 2009.

[568] V. C. Jones, L. McKeown, A. Verkhratsky, and O. T. Jones, "LV-pIN-KDEL: a novel lentiviral vector demonstrates the morphology, dynamics and continuity of the endoplasmic reticulum in live neurones," *BMC Neuroscience*, vol. 9, p. 10, Jan. 2008.

[569] J. Nixon-Abell, C. J. Obara, A. V. Weigel, D. Li, W. R. Legant, C. S. Xu, H. A. Pasolli, K. Harvey, H. F. Hess, E. Betzig, C. Blackstone, and J. Lippincott-Schwartz, "Increased spatiotemporal resolution reveals highly dynamic dense tubular matrices in the peripheral ER," *Science*, vol. 354, p. aaf3928, Oct. 2016.

[570] M. Brunstein, K. Wicker, K. Hérault, R. Heintzmann, and M. Oheim, "Full-field dual-color 100-nm super-resolution imaging reveals organization and dynamics of mitochondrial and ER networks," *Optics Express*, vol. 21, pp. 26162–26173, Nov. 2013.

[571] B. G. Kopek, M. G. Paez-Segala, G. Shtengel, K. A. Sochacki, M. G. Sun, Y. Wang, C. S. Xu, S. B. van Engelenburg, J. W. Taraska, L. L. Looger, and H. F. Hess, "Diverse protocols for correlative super-resolution fluorescence imaging and electron microscopy of chemically fixed samples," *Nature protocols*, vol. 12, pp. 916–946, May 2017.

[572] M.-Y. Sun, P. Devaraju, A. X. Xie, I. Holman, E. Samones, T. R. Murphy, and T. A. Fiacco, "Astrocyte calcium microdomains are inhibited by Bafilomycin A1 and cannot be replicated by low-level Schaffer collateral stimulation in situ," *Cell Calcium*, vol. 55, pp. 1–16, Jan. 2014.

[573] A. Agarwal, P.-H. Wu, E. G. Hughes, M. Fukaya, M. A. Tischfield, A. J. Langseth, D. Wirtz, and D. E. Bergles, "Transient Opening of the Mitochondrial Permeability Transition Pore Induces Microdomain Calcium Transients in Astrocyte Processes," *Neuron*, vol. 93, pp. 587–605.e7, Feb. 2017.

[574] C. Mauvezin and T. P. Neufeld, "Bafilomycin A1 disrupts autophagic flux by inhibiting both V-ATPase-dependent acidification and Ca-P60a/SERCA-dependent autophagosome-lysosome fusion," *Autophagy*, vol. 11, no. 8, pp. 1437–1438, 2015.

[575] G. Roest, R. M. La Rovere, G. Bultynck, and J. B. Parys, "IP3 Receptor Properties and Function at Membrane Contact Sites," *Advances in Experimental Medicine and Biology*, vol. 981, pp. 149–178, 2017.

[576] J. Marchaland, C. Calì, S. M. Voglmaier, H. Li, R. Regazzi, R. H. Edwards, and P. Bezzi, "Fast Subplasma Membrane Ca2+ Transients Control Exo-Endocytosis of Synaptic-Like Microvesicles in Astrocytes," *Journal of Neuroscience*, vol. 28, pp. 9122–9132, Sept. 2008.

[577] M. M Wu, E. D Covington, and R. Lewis, "Single-molecule analysis of diffusion and trapping of STIM1 and Orai1 at ER-plasma membrane junctions," *Molecular biology of the cell*, vol. 25, July 2014.

[578] Y. Elbaz and M. Schuldiner, "Staying in touch: the molecular era of organelle contact sites," *Trends in Biochemical Sciences*, vol. 36, pp. 616–623, Nov. 2011.

[579] H. Wu, P. Carvalho, and G. K. Voeltz, "Here, there, and everywhere: The importance of ER membrane contact sites," *Science*, vol. 361, p. eaan5835, Aug. 2018.

[580] J. T. Smyth, W. I. DeHaven, G. S. Bird, and J. W. Putney, "Ca2+-store-dependent and -independent reversal of Stim1 localization and function," *J Cell Sci*, vol. 121, pp. 762–772, Mar. 2008.

[581] T. A. Fiacco and K. D. McCarthy, "Intracellular Astrocyte Calcium Waves In Situ Increase the Frequency of Spontaneous AMPA Receptor Currents in CA1 Pyramidal Neurons," *Journal of Neuroscience*, vol. 24, pp. 722–732, Jan. 2004.

[582] R. Yuste, A. Majewska, and K. Holthoff, "From form to function: calcium compartmentalization in dendritic spines," *Nature Neuroscience*, vol. 3, pp. 653–659, July 2000.

[583] N. Korogod, C. C. Petersen, and G. W. Knott, "Ultrastructural analysis of adult mouse neocortex comparing aldehyde perfusion with cryo fixation," *eLife*, vol. 4, p. e05793, 2015.

[584] X. Li, Y. Tao, R. Bradley, Z. Du, Y. Tao, L. Kong, Y. Dong, J. Jones, Y. Yan, C. R. K. Harder, L. M. Friedman, M. Bilal, B. Hoffmann, and S.-C. Zhang, "Fast Generation of Functional Subtype Astrocytes from Human Pluripotent Stem Cells," *Stem Cell Reports*, vol. 11, pp. 998–1008, Oct. 2018.

[585] H. Cang, Z. Tong, P. Beuzer, Q. Ye, J. Axelrod, and Z. Hong, "Ex-STORM: Expansion Single Molecule Nanoscopy," *bioRxiv*, p. 049403, Apr. 2016.

[586] M. Gao, R. Maraspini, O. Beutel, A. Zehtabian, B. Eickholt, A. Honigmann, and H. Ewers, "Expansion Stimulated Emission Depletion Microscopy (ExSTED)," *ACS Nano*, vol. 12, pp. 4178–4185, May 2018.

[587] A. R. Halpern, G. C. M. Alas, T. J. Chozinski, A. R. Paredez, and J. C. Vaughan, "Hybrid Structured Illumination Expansion Microscopy Reveals Microbial Cytoskeleton Organization," *ACS Nano*, vol. 11, pp. 12677–12686, Dec. 2017.

[588] Y. Wang, Z. Yu, C. K. Cahoon, T. Parmely, N. Thomas, J. R. Unruh, B. D. Slaughter, and R. S. Hawley, "Combined expansion microscopy with structured illumination microscopy for analyzing protein complexes," *Nature Protocols*, vol. 13, p. 1869, Aug. 2018.

[589] M. U. Khalid, A. Tervonen, I. Korkka, J. Hyttinen, and K. Lenk, "Geometry-based Computational Modeling of Calcium Signaling in an Astrocyte," in *EMBEC & NBC 2017*, IFMBE Proceedings, pp. 157–160, Springer, Singapore, June 2017.

[590] E. Nordlie, M.-O. Gewaltig, and H. E. Plesser, "Towards Reproducible Descriptions of Neuronal Network Models," *PLOS Computational Biology*, vol. 5, p. e1000456, Aug. 2009.

[591] S. M. Crook, A. P. Davison, and H. E. Plesser, "Learning from the Past: Approaches for Reproducibility in Computational Neuroscience," in *20 Years of Computational Neuroscience* (J. M. Bower, ed.), Springer Series in Computational Neuroscience, pp. 73–102, New York, NY: Springer New York, 2013.

[592] S. Crook, "Model Reproducibility: Overview," in *Encyclopedia of Computational Neuroscience* (D. Jaeger and R. Jung, eds.), pp. 1–3, New York, NY: Springer New York, 2013.

[593] M. Migliore, T. M. Morse, A. P. Davison, L. Marenco, G. M. Shepherd, and M. L. Hines, "ModelDB," *Neuroinformatics*, vol. 1, pp. 135–139, Mar. 2003.

[594] N. L. Novère, A. Finney, M. Hucka, U. S. Bhalla, F. Campagne, J. Collado-Vides, E. J. Crampin, M. Halstead, E. Klipp, P. Mendes, P. Nielsen, H. Sauro, B. Shapiro, J. L. Snoep, H. D. Spence, and B. L. Wanner, "Minimum information requested in the annotation of biochemical models (MIRIAM)," *Nature Biotechnology*, vol. 23, pp. 1509–1515, Dec. 2005.

[595] M. Hucka, A. Finney, H. M. Sauro, H. Bolouri, J. C. Doyle, H. Kitano, A. P. Arkin, B. J. Bornstein, D. Bray, A. Cornish-Bowden, A. A. Cuellar, S. Dronov, E. D. Gilles, M. Ginkel, V. Gor, I. I. Goryanin, W. J. Hedley, T. C. Hodgman, J.-H. Hofmeyr, P. J. Hunter, N. S. Juty, J. L. Kasberger, A. Kremling, U. Kummer, N. Le Novère, L. M. Loew, D. Lucio, P. Mendes, E. Minch, E. D. Mjolsness, Y. Nakayama, M. R. Nelson, P. F. Nielsen, T. Sakurada, J. C.

Schaff, B. E. Shapiro, T. S. Shimizu, H. D. Spence, J. Stelling, K. Takahashi, M. Tomita, J. Wagner, and J. Wang, "The systems biology markup language (SBML): a medium for representation and exchange of biochemical network models," *Bioinformatics*, vol. 19, pp. 524–531, Mar. 2003.

[596] A. P. Davison, D. Brüderle, J. M. Eppler, J. Kremkow, E. Muller, D. Pecevski, L. Perrinet, and P. Yger, "PyNN: a common interface for neuronal network simulators," *Frontiers in Neuroinformatics*, vol. 2, 2009.

[597] S. Crook, P. Gleeson, F. Howell, J. Svitak, and R. A. Silver, "MorphML: Level 1 of the NeuroML Standards for Neuronal Morphology Data and Model Specification," *Neuroinformatics*, vol. 5, pp. 96–104, Apr. 2007.

[598] S. M. T. Hernández-Sotomayor, C. D. L. Santos-Briones, J. A. Muñoz-Sánchez, and V. M. Loyola-Vargas, "Kinetic Analysis of Phospholipase C from Catharanthus roseus Transformed Roots Using Different Assays," *Plant Physiology*, vol. 120, pp. 1075–1082, Aug. 1999.

[599] J. Akerboom, T.-W. Chen, T. J. Wardill, L. Tian, J. S. Marvin, S. Mutlu, N. C. Calderón, F. Esposti, B. G. Borghuis, X. R. Sun, A. Gordus, M. B. Orger, R. Portugues, F. Engert, J. J. Macklin, A. Filosa, A. Aggarwal, R. A. Kerr, R. Takagi, S. Kracun, E. Shigetomi, B. S. Khakh, H. Baier, L. Lagnado, S. S.-H. Wang, C. I. Bargmann, B. E. Kimmel, V. Jayaraman, K. Svoboda, D. S. Kim, E. R. Schreiter, and L. L. Looger, "Optimization of a GCaMP calcium indicator for neural activity imaging," *The Journal of Neuroscience: The Official Journal of the Society for Neuroscience*, vol. 32, pp. 13819–13840, Oct. 2012.

[600] A. Michailova, F. Del Principe, M. Egger, and E. Niggli, "Spatiotemporal Features of Ca2+ Buffering and Diffusion in Atrial Cardiac Myocytes with Inhibited Sarcoplasmic Reticulum," *Biophysical journal*, vol. 83, pp. 3134–51, Jan. 2003.

Appendix A

Supplemental methods and model validation

> *"There is always time for another last minute"*
> Terry Pratchett

A.1 Parameter values

Table A.1 presents the parameter values that have been used in the "GCaMP", "No-GCaMP", "GCaMP6f" and "Lck-GCaMP6f" 3D models (see section V.1). Table A.2 presents the additional parameter values that were added in the "GC+Buf" model, which accounts for endogenous Ca^{2+} buffers, their diffusion and interactions with Ca^{2+} ions (see section V.1 and Fig V.1).

A.2 Validation of modeling strategies

A.2.1 Study of the effect of endogenous buffers on the effective D_{Ca}

A.2.1.1 Mean field model of Ca^{2+} buffering

In the 2D implementation of the model, the effect of Ca^{2+} buffers has been accounted by decreasing the effective Ca^{2+} coefficient of diffusion, D_{Ca} (see Chap-

Table A.1: Parameter values and initial conditions of the 3D model. The parameter values of the 3D model listed here correspond to the "GCaMP" model. The parameter values for the "No-GCaMP" model, devoid of GCaMP, are the same except that [GCaMP6s] = 0 nM. In "GCaMP6f" and "Lck-GCaMP6f" models, $\text{Gcamp}_f = 1.05 \times 10^7 M^{-1}.s^{-1}$ and $\text{Gcamp}_b = 3.93 s^{-1}$. Parameter values have been adjusted to optimize the match with experimental data (see Fig V.2). Note that the values for Ca^{2+} and IP_3 binding or unbinding to IP_3R, i.e. the a_i's and b_j's parameters below, are smaller in our model than in the literature, probably because our model is not cooperative. For GCaMP6s and cytosolic GCaMP6f, we used the diffusion coefficient of calmodulin. The initial number of Ca^{2+} ions was adjusted so that the measured basal GCaMP6s-Ca concentration was around 300nM [177, 551].

Parameter	Description	Value in 3D GCaMP model	Reference
V	Cell volume	2.81×10^{-17} L	[32]
IP$_3$ dynamics			
IP_0	Initial IP$_3$ number/conc	3 molec. i.e 177 nM	[550]
D_{IP3}	IP$_3$ diffusion	280 $\mu m^2.s^{-1}$	[554]
N_{plc}	PLCδ number/conc.	1696 molec. i.e 100 μM	[598]
δ	PLCδ max rate	1 s^{-1}	-
β	IP$_3$ decay	1.2×10^{-4} s^{-1}	-
Ca^{2+} dynamics			
Ca_0	Initial Ca^{2+} number/conc.	5 molec. i.e 295 nM	[551]
D_{Ca}	Ca^{2+} diffusion	13 $\mu m^2.s^{-1}$	[554]
μ	Ca^{2+} flux through open IP$_3$R	6×10^3 s^{-1}	-
γ	Cytosolic Ca^{2+} influx	1.5×10^{-7} s^{-1}	-
α	Ca^{2+} decay rate	30 s^{-1}	-
GCaMP6s			
C_{GCa}	GCaMP6s conc.	169 molec. i.e 10 μM	[599, 163]
D_{GCaMP}	GCaMP6s diffusion	50 $\mu m^2.s^{-1}$	[600]
Gcamp$_f$	GCaMP6s Ca binding rate	7.78×10^6 M$^{-1}.s^{-1}$	[185]
Gcamp$_b$	GCaMP6s-Ca dissociation rate	1.12 s^{-1}	[185]
IP$_3$R			
$N_{\text{IP}_3\text{R}}$	IP$_3$R number	50 molec.	[481]
$d_{\text{IP}_3\text{R}}$	IP$_3$R interact. distance	1 mesh triangle	-
IP$_3$R binding			
a_1	First Ca	1.2×10^6 M$^{-1}.s^{-1}$	-
a_2	IP$_3$	4.1×10^7 M$^{-1}.s^{-1}$	-
a_3	Second Ca	1.6×10^4 M$^{-1}.s^{-1}$	-
IP$_3$R dissociation			
b_1	First Ca	50 s^{-1}	-
b_2	IP$_3$	400 s^{-1}	-
b_3	Second Ca	100 s^{-1}	-

Table A.2: Parameter values and initial conditions associated to endogenous buffers in the 3D "GC+Buf" model. Parameter values for the "GC+Buf" 3D model (Fig V.1) are the same as in "GCaMP" model (Table A.1). Parameter values associated with the kinetics and diffusion of endogenous buffers were taken from a study that modeled Ca^{2+} dynamics in dendrites [484]. Note that total endogenous buffer concentration in our model is 2 orders of magnitude lower than in this study.

Parameter	Description	Value in 3D	Reference
C_{PV}	Initial PV conc.	260 nM	[484]
C_{PVCa}	Initial PV-Ca conc.	400 nM	[484]
D_{PV}	PV diffusion	43 $\mu m^2.s^{-1}$	[484]
PV_f	PV Ca binding rate	10.7×10^7 $M^{-1}.s^{-1}$	[484]
PV_b	PV-Ca dissociation rate	0.95 s^{-1}	[484]
C_{CBs}	Initial CBs conc.	110 nM	[484]
C_{CBsCa}	Initial CBsCa conc.	200 nM	[484]
C_{CBsCa2}	Initial CBsCa2 conc.	200 nM	[484]
D_{CBs}	CBs diffusion	28 $\mu m^2.s^{-1}$	[484]
CBs_f	CBs Ca binding rate	5.5×10^6 $M^{-1}.s^{-1}$	[484]
CBs_b	CBs-Ca dissociation rate	2.6 s^{-1}	[484]
$CBsCa_f$	CBs-Ca Ca binding rate	5.5×10^6 $M^{-1}.s^{-1}$	[484]
$CBsCa_b$	CBs-Ca2 dissociation rate	2.6 s^{-1}	[484]
C_{CBf}	Initial CBf conc.	110 nM	[484]
C_{CBfCa}	Initial CBfCa conc.	200 nM	[484]
C_{CBfCa2}	Initial CBfCa2 conc.	200 nM	[484]
D_{CBf}	CBf diffusion	28 $\mu m^2.s^{-1}$	[484]
CBf_f	CBf Ca binding rate	4.35×10^7 $M^{-1}.s^{-1}$	[484]
CBf_b	CBf-Ca dissociation rate	35.8 s^{-1}	[484]
$CBfCa_f$	CBf-Ca Ca binding rate	4.35×10^7 $M^{-1}.s^{-1}$	[484]
$CBfCa_b$	CBf-Ca2 dissociation rate	35.8 s^{-1}	[484]

Table A.3: Parameter values and initial conditions of the ODE model of Ca^{2+} buffering. Table presenting parameter values of the ODE model of Ca^{2+} buffering, presented in Fig A.1A. a.u : arbitrary unit.

| Parameter	Description	Value in ODE model
	Ca^{2+} dynamics	
Ca_0	Initial Ca^{2+} number	50 molec.
α	cytosolic Ca^{2+} influx	50 a.u
β	Ca^{2+} decay rate	1.0 a.u
	Buffers dynamics	
nb_{buf}	Total number of buffers	varied
$CaBuf_0$	Initial number of Ca^{2+}-bound buffers	0 molec.
D_{buf}	Coefficient of diffusion of buffers	0.1 a.u
k_{on}	Ca^{2+} binding rate	3.5 a.u
k_{off}	CaBuf dissociation rate	0.05 a.u

ter IV), which thus lumps together Ca^{2+} buffering by mobile endogenous buffers as well as the diffusion of these buffers. In order to better understand the dynamics of our model when Ca^{2+} buffers are explicitly added in the model, we have developed a simple mean field (ODE) model of Ca^{2+} buffering. The reactions of the model and the corresponding ODEs are presented in Fig A.1A. Fig A.1B presents the Ca^{2+} response to an injection of 100 Ca^{2+} ions in the system at t=150 dt. Results suggest that an increase in the number of buffers leads to a slight decrease of Ca^{2+} peak amplitude. Interestingly, we show that the basal concentration of Ca^{2+} remains unchanged (Fig A.1B) while the concentration of Ca-bound buffers (CaBuf) increases linearly with the number of buffers (Fig A.1C). Finally, peak amplitude of CaBuf (which is what is measured with fluorescent Ca^{2+} indicators) decreases exponentially with the number of Buf molecules (Fig A.1D). This result is due to the fact that peak amplitude is measured as $\Delta F/F$ ratio, which decreases exponentially with the number of buffer molecules. Those preliminary results have helped us better understand the dynamics of Ca^{2+} buffering.

A.2.1.2   2D model of Ca^{2+} buffering

To test whether adding explicitly buffers in the model yields effects similar to a decrease of Ca^{2+} diffusion coefficient D_{Ca} (see Chapter IV), we have added buffers to the 2D implementation of the model, which kinetic scheme is presented in Fig IV.1. The kinetic scheme of the 2D model with explicit Ca^{2+} buffering is presented in Fig A.2A and the associated parameter values are presented in Table A.4. We com-
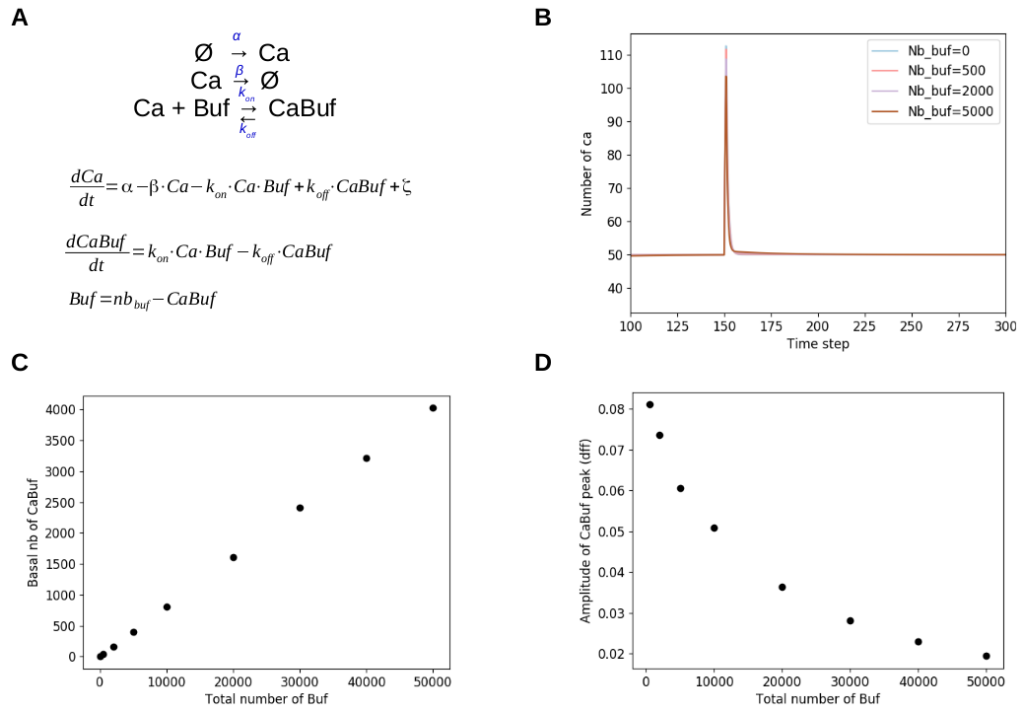
Figure A.1: Mean field study of the effect of Ca^{2+} **buffering.** (*A*) Reactions of the model and the corresponding ODEs for the 3 variables: the concentration of Ca^{2+}, Ca, the concentration of Ca^{2+}-bound buffers, CaBuf and the concentration of unbound buffers, Buf. Ca^{2+} enters the cytosol with rate α. Likewise, cytosolic Ca^{2+} exits the cytosol at rate β. Ca^{2+} and Buf molecules bind at rate k_{on} to form CaBuf molecules. CaBuf molecules dissociate into Ca^{2+} and Buf molecules at rate k_{off}. ξ term is the Ca^{2+} injection term, corresponding to an addition of 100 Ca^{2+} ions in the system at time t=150 dt. nb_{buf} corresponds to the total number of buffers, including both bound and unbound molecules. Parameter values are presented in Table A.3

pared Ca^{2+} dynamics in the reference model presented in Chapter IV with this 2D Ca^{2+} buffering model. The buffering model is characterized by a faster Ca^{2+} ions diffusion but a lower CaBuf diffusion coefficient (see Fig A.2 and Table A.4). No significant effect of the number of buffers was observed on basal Ca^{2+} concentration (Fig A.2B), peak amplitude (Fig A.2C) and frequency (Fig A.2D) compared to simulations in which the effect of buffers was accounted for by a decreased effective D_{Ca}. Those results suggest that simulating Ca^{2+} diffusion in our 2D implementation of the model with a decreased effective coefficient of diffusion is equivalent to explicitly adding endogenous buffers in the system.
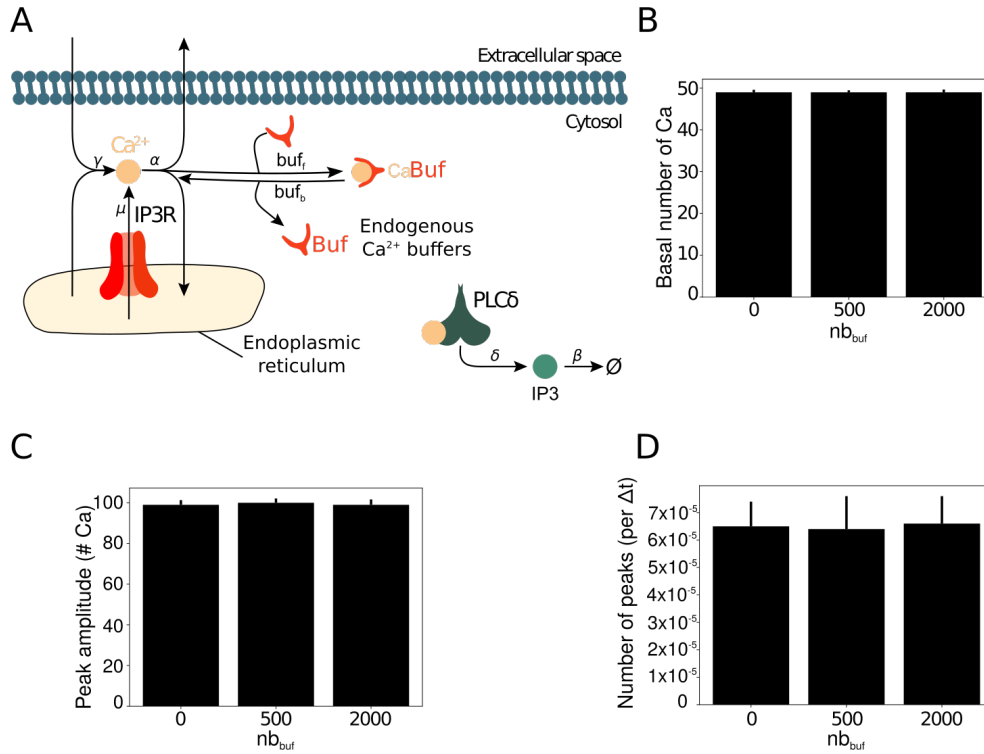
Figure A.2: Effect of adding buffers to the 2D particle-based model. (*A*) Biochemical reactions and regulatory interactions modeled in the 2D Ca^{2+} buffering model. Reactions are the same as the ones described in Fig IV.1, except that Buf particles were added. Parameter values are presented in Table A.4. The binding rate and dissociation constant associated with the binding of Ca^{2+} to Buf correspond respectively to buf_f and buf_b. Different amounts of buffers nb_{buf} were added to the model (500 or 2000), with the following diffusion coefficients: $D_{buf} = 0.1$ a.u and $D_{Ca} = 0.8$ a.u. Those simulations were compared to our reference model (Chapter IV), which contains 0 Buf particles but in which $D_{Ca} = 0.1$ a.u, corresponding to an effective lower D_{Ca}. No significant difference between simulations with a number of Buf of 0, 500 or 2000 is observed regarding basal Ca^{2+} concentration (B), peak amplitude (C) or peak frequency (D). Note that we refer here to free Ca^{2+} peaks and not to CaBuf peaks.

Table A.4: Parameter values and initial conditions of the 2D model of Ca^{2+} **buffering**. Table presenting parameter values of the 2D model of Ca^{2+} buffering, presented in Fig A.2A. Parameter values were the same as the model presented in Chapter IV (Table IV.1). The additional parameter values associated with buffers and their interactions with Ca^{2+} ions are presented below. a.u : arbitrary unit.

Parameter	Description	Value in 2D model
V	Cell volume	200×200 a.u.
	Ca^{2+} dynamics	
Ca_0	Initial Ca^{2+} number	50 molec.
α	cytosolic Ca^{2+} influx	50 a.u
β	Ca^{2+} decay rate	1.0 a.u
	Buffer dynamics	
nb_{buf}	Total number of buffers	varied
$CaBuf_0$	Initial number of Ca^{2+}-bound buffers	0 molec.
buf_f	Ca^{2+} binding rate	3.5 a.u
buf_b	CaBuf dissociation rate	0.05 a.u

A.2.2   Validation of the 3D model implemented in STEPS

As explained in section V.1, the parameters used in our 3D model were based on values extracted from experimental data whenever available and the other parameters were adjusted to fit experimental recordings of Ca^{2+} dynamics. In order to validate the 3D voxel-based model presented in section V.1, we have compared its Ca^{2+} dynamics to that of the 2D particle-based implementation of the model, presented in Chapter IV. To do so, we have built a sheet-like 3D geometry (Fig A.3A) in which simulations with similar parameter values to that of the 2D model (see Table IV.1) were performed. The evolution of [IP$_3$] and [Ca^{2+}] displayed Ca^{2+} dynamics that was similar to that of the 2D particle-based implementation of the model (Fig A.3B) and reproduced the main results from section IV.2 (Fig A.3C). Those results validate the implementation of our 3D voxel-based model.
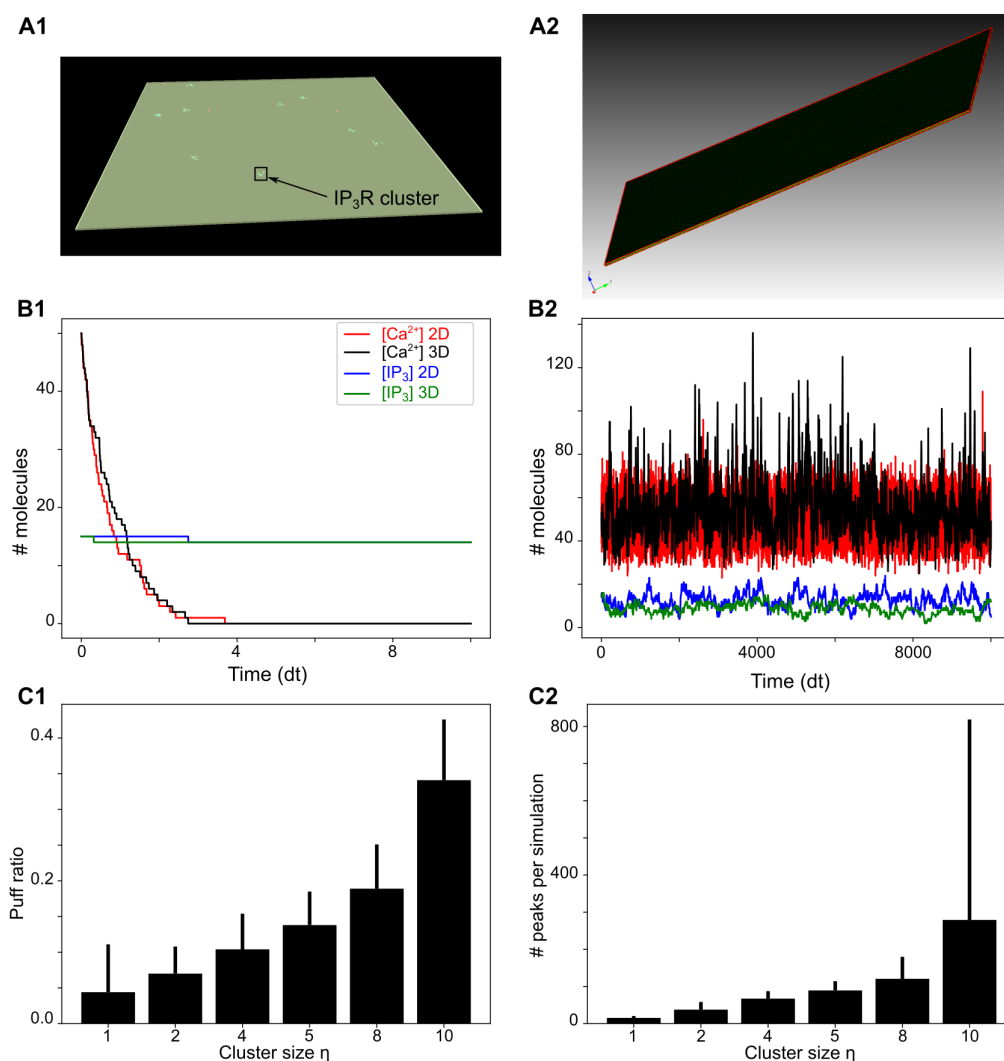
Figure A.3: Validation of the 3D model. (*A*) Geometry that was designed for comparing the behavior of the 2D (Chapter IV) and of the 3D (Chapter V) implementations of the model. The geometry corresponds to a sheet of size 200 x 200 x 1 nm^3. Panel *A1* presents a screenshot of a representative simulation, displaying IP_3R clusters of size η=4 on the membrane. Panel *A2* presents a screenshot that reveals the sheet-like geometry of the mesh used in this study. (*B1*) Representative simulation traces displaying the evolution of the number of IP_3 and of Ca^{2+} particles over time in a model of IP_3 and Ca^{2+} degradation. Simulations in the 2D particle-based (red and blue for Ca^{2+} and IP_3, respectively) and in the 3D voxel-based implementation of the model (black and green for Ca^{2+} and IP_3, respectively) were compared. (*B2*) Representative simulation traces of the complete reference model presented in Chapter IV, with either a 2D particle-based (red and blue for Ca^{2+} and IP_3 respectively) or a 3D voxel-based implementation of the model (black and green for Ca^{2+} and IP_3 respectively). (*C*) Similarly to the 2D model (Fig IV.5), increasing IP_3R cluster size η resulted in an increase of puff ratio (*C1*) and of the number of peaks during simulation time (*C2*). Data are presented as mean $\pm$ standard deviation over 20 simulations.

FOLIO ADMINISTRATIF

THESE DE L'UNIVERSITE DE LYON OPEREE AU SEIN DE L'INSA LYON

NOM : DENIZOT   DATE de SOUTENANCE : 08/11/2019

Prénoms : Audrey

TITRE : Simulation de la signalisation calcique dans les prolongements fins astrocytaires

NATURE : Doctorat   Numéro d'ordre : 2019LYSEI093

Ecole doctorale : École Doctorale Informatique et Mathématiques (ED512)

Spécialité : Informatique

RESUME :

Les astrocytes ont récemment été identifiés comme partenaires essentiels des neurones pour le traitement de l'information dans le cerveau. Les astrocytes répondent à une stimulation neuronale par des variations de concentration en calcium, ce qui entraîne une modulation de l'efficacité de la communication neuronale. Ces interactions sont essentielles aux fonctions cérébrales et sont altérées dans les maladies du cerveau, comme le cancer, l'épilepsie et les maladies neurodégénératives. La modélisation est cruciale pour étudier ces signaux, car la plupart d'entre eux se produisent dans des ramifications cellulaires qui sont trop fines pour être résolues par les techniques de microscopie optique classiques. Des études en microscopie électronique ont révélé une grande diversité des géométries de ces ramifications. Les rôles fonctionnels de cette diversité géométrique n'ont cependant pas été étudiés car les modèles d'astrocytes actuellement disponibles ne permettent pas une modélisation spatiale au sein de petits volumes. Cette thèse vise à fournir des modèles stochastiques réalistes d'un point de vue biologique afin de simuler le traitement de l'information par les astrocytes et d'étudier l'influence de la géométrie cellulaire sur les signaux calciques. Dans l'ensemble, cette recherche contribuera à une meilleure compréhension de l'intégration spatio-temporelle des signaux calciques astrocytaires, une condition préalable à la compréhension de la communication neurones-astrocytes et de son influence sur les fonctions cérébrales.

MOTS-CLÉS : Astrocytes, signalisation calcique, neurosciences computationnelles, réaction-diffusion, géométrie,

Laboratoire (s) de recherche :
Laboratoire d'Informatique en Image et Systèmes d'information
LIRIS CNRS UMR5205

Directeur de thèse: Hugues Berry, INRIA
Président de jury : Laurent Venance, INSERM

Composition du jury :
Geneviève Dupont (Directeur de Recherche ULB, rapportrice)
Leonid Savtchenko (Senior Research Scientist , rapporteur)
Laurent Venance (Directeur de Recherche INSERM, examinateur)
Aude Panatier (Chargée de Recherche CNRS, examinatrice)
Christian Henneberger (Assistant Professor Uni. Bonn, examinateur)
Guillaume Beslon (Professeur INSA, examinateur)
Hédi Soula (Professeur UPMC, co-directeur de thèse, invité)
Hugues Berry (Directeur de recherche INRIA, directeur de thèse)